ISBN 978-82-326-2991-6 (printed ver.)
ISBN 978-82-326-2990-9 (electronic ver.)
ISSN 1503-8181

Aksel Fenerci

Doctoral thesis

Doctoral theses at NTNU, 2018:100

Aksel Fenerci

# Full-scale investigation of the effects of wind turbulence characteristics on dynamic behavior of long-span cable-supported bridges in complex terrain

Doctoral theses at NTNU, 2018:100

NTNU
Norwegian University of Science and Technology

Thesis for the Degree of Philosophiae Doctor

NTNU

NTNU
Norwegian University of Science and Technology

NTNU
Norwegian University of Science and Technology

Aksel Fenerci

# Full-scale investigation of the effects of wind turbulence characteristics on dynamic behavior of long-span cable-supported bridges in complex terrain

Thesis for the Degree of Philosophiae Doctor

Trondheim, April 2018

Norwegian University of Science and Technology
Faculty of Engineering
Department of Structural Engineering

NTNU
Norwegian University of
Science and Technology

**NTNU**
Norwegian University of Science and Technology

Thesis for the Degree of Philosophiae Doctor

Faculty of Engineering
Department of Structural Engineering



ISBN 978-82-326-2990-9 (printed ver.)
ISBN 978-82-326-2991-6 (electronic ver.)
ISSN 1503-8181

IMT-report 2018:100

Doctoral theses at NTNU, 2018:100

Printed by NTNU Grafisk senter

# Abstract

The global demand for long-span cable-supported bridges are emerging. Impressive number of projects have been realized in the last two decades and many more projects are in their planning, design or construction phases today. Recently, the Norwegian Public Roads Administration took the initiative and started a project to replace ferries along Norway's coastal E39 highway by fixed links. This requires crossing of wide and deep straits by bridges in the wind-prone Norwegian fjords, where the terrain is mountainous and complex. Some of the straits extend up to 3-5 kilometers, which demand novel bridge designs. Accomplishment of such bridge projects is only possible with a deep understanding of the wind environment, terrain-induced effects, wind-structure interaction and the uncertainties involved in analytical methodologies. In this context, Hardanger Bridge, currently the longest suspension bridge in Norway (main span 1308 meters), has been instrumented to investigate characteristics of the turbulent wind environment and the dynamic response of the bridge.

In this thesis, large amount of data collected from the Hardanger Bridge monitoring system over a period of almost four years are analyzed to study the wind characteristics and dynamic response of the bridge. Response surface analyses is employed to examine the wind-response relationship from a statistical point-of-view. Analytical predictions of the dynamic response are carried out using multimode buffeting theory and compared with the measurements. The measurement data are then used to deduce a probabilistic turbulence model that can be used in long-term extreme response estimation and reliability based and probabilistic analyses.

The investigations surfaced that the wind-induced response of the Hardanger Bridge showed significant variability, implying significant amount of uncertainty inherently present in the dynamic response analyses. To a large extent, this is found to root from the variable wind turbulence field. Therefore. It is stressed that this variability might cause unfavorable designs and should be handled rationally. In light of these findings and using field measurements, a probabilistic turbulence model is devised and its ability to represent the measured turbulence field is shown.

Prediction of the wind-induced dynamic response of a cable-supported bridge is a complex problem, involving characterization of the turbulence field, determination of structural, dynamic and aerodynamic properties of the structure and modeling of the fluid-structure interaction. Consequently, analytical treatment of such a problem involves a great deal of modeling and parametric uncertainties, and requires validation by full-scale measurements. Comparison of the analytical predictions with full-scale measurements remains as the most reliable approach for evaluation of performance of the available analytical tools. The comparisons throughout the thesis indicates discrepancies between

measurements and analytical results, where the sources of which are difficult to identify. Further research is needed that will aid in calibration or improvement of the available tools.

# Acknowledgements

Above others, I would like to express my sincere gratitude to my main supervisor Ole Øiseth, who gave me this opportunity and guided me through the process with utter generosity and devotion. I am also indebted to my co-supervisor Anders Rønnquist for all his support, wisdom and friendship.

I am grateful to the Norwegian Public Roads Administration for the financial support they have provided to realize this research and the eco-system that they have created for the E39 project.

I would like to thank Knut Andreas Kvåle, Øyvind Wiig Petersen and Tor Martin Lystad for their co-operation in the project. I was lucky to have worked with such excellent engineers.

Thanks are extended to the past and present members of the structural dynamics group: Gunnstein Thomas Frøseth, Petter Nåvik, Yuwang Xu, Randi Nøhr Møller, Michael Stryk Andersen, Henrik Skyvulstad, Tore Helgedagsrud, Bjørn Svendsen, Heidi Kvåle, Daniel Cantero and Stefano Derosa for the inspiring conversations (and also for the not so inspiring ones) during the coffee breaks. They definitely created a warm work environment in this cold country.

Many thanks to Bartosz (the Bartek) Siedziako for being an excellent office mate and friend. I would also like to state that I wrote his name without cheating.

I would also like to thank all my friends for their support and the great times we had.

Finally, I would like to express my deepest gratitude for the support of my family. I am truly blessed to have Tülay Fenerci and Can Fenerci, Medya and Køfte in my life. This work would not have been possible without their unconditional love and support.

# Preface

This thesis is submitted in partial fulfilment of the requirements for the degree Philosophiae Doctor at the Norwegian University of Science and Technology (NTNU). The work has been carried out at the Department of Structural Engineering, Faculty of Engineering and funded by the Norwegian Public Roads Administration (NPRA).

Associate Professor Ole Øiseth, Professor Anders Rönnquist and Bjørn Isaksen from the NPRA have supervised the work.

The thesis is composed of four papers either published in or submitted to international peer-reviewed scientific journals and one paper presented in an international conference, following an introductory part.

Aksel Fenerci
Trondheim, Norway
December 2017

# List of appended papers

I. Fenerci A, Øiseth O, Rønnquist A. Long-term monitoring of wind field characteristics and dynamic response of a long-span suspension bridge in complex terrain. Eng Struct 2017;147:269–84. doi:10.1016/j.engstruct.2017.05.070.

II. Fenerci A, Øiseth O. Measured Buffeting Response of a Long-Span Suspension Bridge Compared with Numerical Predictions Based on Design Wind Spectra. J Struct Eng (United States) 2017;143. doi:10.1061/(ASCE)ST.1943-541X.0001873.

III. Fenerci A, Øiseth O. Evaluation of wind-induced response predictions of a long-span suspension bridge using full-scale measurements. 7th Eur. African Conf. Wind Eng. (EACWE 2017), Liege, Belgium, 2017.

IV. Fenerci A, Øiseth O. Strong wind characteristics and dynamic response of a long-span suspension bridge during a storm. J Wind Eng Ind Aerodyn 2018:116–38. doi:10.1016/j.jweia.2017.10.030.

V. Fenerci A, Øiseth O. Site-specific data-driven probabilistic wind field modeling for wind-induced response prediction of cable-supported bridges. Submitted for journal publication.

# Other scientific contributions

I. Fenerci A, Øiseth O. Full-Scale Measurements on the Hardanger Bridge During Strong Winds. In: Pakzad S, Juan C, editors. Dyn. Civ. Struct. Vol. 2 Proc. 34th IMAC, A Conf. Expo. Struct. Dyn. 2016, Cham: Springer International Publishing; 2016, p. 237–45. doi:10.1007/978-3-319-29751-4_24.

II. Fenerci A, Øiseth O. Wind Field Characteristics at the Hardanger Bridge Site. Proc. 12th UK Conf. Wind Eng., Nottingham, UK: 2016.

III. Fenerci A, Øiseth O. Full-scale measurement and analysis of wind-induced vibrations of a long-span suspension bridge in complex terrain. In: Rupakhety, Rajesh, Olafsson S, editor. Earthq. Eng. Struct. Dyn. Mem. Ragnar Sigbjörnsson Sel. Top. 1st ed., Springer International Publishing; 2018, p. in publication. doi:10.1007/978-3-319-62099-2.

IV. Fenerci A, Øiseth O. The Hardanger Bridge monitoring project: Long-term monitoring results and implications on bridge design. Procedia Eng 2017;199:3115–20. doi:https://doi.org/10.1016/j.proeng.2017.09.576.

V. Lystad TM, Fenerci A, Øiseth O. Wind field characteristics at the Hardanger Bridge site: comparison of wind tunnel terrain model tests with full-scale measurements. 7th Eur. African Conf. Wind Eng. (EACWE 2017), Liege, Belgium, 2017.

# Contents

# 1. Introduction

## 1.1. Background and Motivation

### 1.1.1. Toward longer and more slender bridges

Throughout history, road bridges have been an integral component of civilization. They have stimulated economic growth by connecting human populations and aiding in transport of commercial goods and services. As the world population and economy continue to grow, the global demand for bridges, especially long spanning bridges increases. So far, cable-supported bridges have been used as the dominating solution for such long spans without supports. According to the configuration of their cable-system, they can be classified in three main types: suspension, cable-stayed and hybrid cable-stayed suspension bridges [1]. Although the concept can be traced back further, the early examples of cable-supported road bridges were built mostly in 19$^{th}$ century, where the maximum span length was around 500 meters. First long-span cable-supported bridges appeared in 1930s (George Washington Bridge, 1067 m, Golden Gate Bridge. 1280 m) in the United States. The number of such bridges increased gradually until the 1980s and then skyrocketed. Especially, the amount of long span cable-supported bridges built in China over the last two decades is remarkable. Currently, the longest suspension bridge in the world is the Akashi-Kaikyo Suspension Bridge in Japan since its opening in 1998, with its 1991 main span. The longest cable-stayed bridge is the Russky Bridge in Russia (1104 m main span) which was built in 2012 and it is followed closely by the Stonecutters Bridge (1018 m main span) in China. Recently, a hybrid cable-stayed suspension bridge was constructed in Turkey. The bridge has an impressive main span of 1408 meters crossing the Bosphorus, and it was named as the Yavuz Sultan Selim Bridge after the Ottoman Emperor. It seems possible that this previously not so popular concept will be used more commonly in the future in crossing of the wide straits. The vast number of projects that have been carried out in recent years resulted into an accumulation of experience and knowledge on the subject for the aforementioned span lengths.

In recent years, there has also been initiatives to build super long-span suspension bridges, with spans exceeding 2000 meters. Two famous examples are the proposed bridges for the 3300 meters Messina Strait [2] and the 5000 m Gibraltar strait [3]. These projects have not been realized yet, mainly due to their massive costs and political reasons. However, they stimulated research and initiated discussion on the possibility and feasibility of such projects. More recently, an even more ambitious project was initiated in Norway by the Norwegian Public Roads Administration (NPRA). The Norwegian government has the desire to have a continuous highway along its highly economically active west coast, which is dominated by fjords and mountains. In the current state of the Coastal Highway E39, seven ferries operate along the highway in crossing of the fjords, which results in an extended travel

time of approximately 21 hours along the highway. Replacing the ferries by fixed links will reduce this travel time to about 11 hours, which is a substantial reduction with potential economic impacts. However, the unique topography of the Norwegian fjords makes this challenging. The fjords crossings are usually longer than the span of the Akashi-Kaikyo Bridge and the seabed is very deep, not allowing any mid-supports. Therefore, bridges with so far unmatched scale will have to be designed and built to realize the project. Alternative to the classical single-span suspension bridges, multi-span suspension bridges with floating towers, floating pontoon bridges or submerged floating tunnels are also considered. The fjord crossings are listed in Table 1 with the bridge solutions considered so far by the NPRA. It can be seen that for most of the crossings, suspension bridges are considered as either primary or viable options and if realized, they will most likely break the world record by a significant margin.

Table 1 List of fjord crossings in Ferry-Free E39 Project

| Fjord crossing | Length (km) | Depth (m) | Considered solution |
|---|---|---|---|
| Halsafjorden | 2 | 600 | single-span susp. bridge/floating pontoon bridge/ submerged floating tunnel/ multi-span susp. bridge with floating pylons |
| Julsundet | 1.6 | 600 | single-span susp. bridge |
| Vartdalsfjorden | 2.1 | 600 | single-span susp. bridge/floating pontoon bridge |
| Sulafjorden | 3.8 | 500 | single-span susp. bridge/ multi-span susp. bridge/ multi-span susp. bridge with floating pylons/ floating pontoon bridge |
| Nordfjorden | 1.5 | 500 | single-span susp. bridge |
| Sognefjorden | 3.7 | 1250 | single-span susp. bridge/ submerged floating tunnel/ floating pontoon bridge/ multi-span susp. bridge with floating pylons |
| Bjørnafjorden | 5 | 600 | multi-span susp. bridge with floating towers /floating pontoon bridge/ submerged floating tunnel |
| Langenuen | 1.3 | 500 | single-span susp. bridge |

As the span length of cable-supported bridges increases, wind effects on them becomes a major concern. The geographical area where the future bridges will be located is exposed to strong European windstorms. Experience suggests that if not carefully handled, wind loading on such slender structures might be critical or even catastrophic [4,5]. Therefore, methods used in analytical prediction of the wind effects should be revisited to evaluate their performance. The challenges posed by the particular terrain specific to the Norwegian fjords should also be investigated. Perhaps one of the best ways to

achieve these is to carry out full-scale measurements on existing long-span cable-supported bridges under similar conditions. Such an approach will aid in qualitative and quantitative evaluation of the overall uncertainty and lead to safer and more reliable designs.

### 1.1.2. Structural monitoring of cable supported bridges

Today, extensive monitoring systems are installed on many long-span cable-supported bridges around the world. It is every engineer's desire to know if the built structure fulfills the performance goals set in the design of the structure throughout its life span. This being the main idea behind it, full-scale monitoring of cable-supported bridges have been conducted for nearly a century [6,7] and such efforts gained significant momentum in the last couple of decades. Nowadays, all such efforts are termed as "Structural Health Monitoring (SHM)". By SHM campaigns, it is aimed to detect changes in the structural system such as structural damage, settlement, time dependent changes, etc. SHM systems are not standardized yet. Since the expected outcome from every project is different, the amount and location of sensors, data acquisition and processing systems are decided according the nature, budget and scale of the project by experience or using rough guidelines. It should be noted that SHM is a separate and broad research topic on its own [8–10]. In case of long-span bridges, detecting minor structural damage does not seem likely for now; however, major structural change or damage after an extreme event, such as an earthquake or a hurricane should be possible to detect. It is also expected that having permanent SHM systems installed on long span bridges should reduce the effort and cost in inspection, maintenance and rehabilitation of these structures, which require substantial allocation of resources. Another common reason for SHM is to determine the dynamic properties of the structure using operational modal analysis (OMA) [11], and use the input in updating of analytical models and methods. These are usually conducted using temporary systems and short term campaigns. Currently, most long-span cable-supported bridges around the world are equipped with permanent monitoring systems that do real-time monitoring of the bridge response, environmental factors and structural loads. There is also a modern trend that the newly built bridges have monitoring systems embedded from the construction stage. It is advantageous if the monitoring system is designed along with the bridge itself [10,12].

In Table 2, some information on monitoring efforts on prominent cable-supported bridges around the world are given. These include both permanent systems and short term monitoring campaigns. It can be seen that accelerometers and anemometers are the most commonly used sensors. This is not surprising given that accelerometers are most commonly used to obtain modal properties of the structure, which is one of the primary objectives of SHM studies, where anemometers are used to learn about the wind environment and loading, which is usually the most important hazard for long-span bridges. Most monitoring systems also contain other sensors, such as GNSS sensors, strain gauges,

temperature sensors, inclinometers, etc. Although having more sensors is beneficial in terms of detecting damage or unusual activity and consequently provides more control, the management of the system and the resulting data requires more workforce as the system grows. Nevertheless, the trend seems to be toward extensive and continuous monitoring systems embedded into the design of such bridges to detect unusual behavior, damage or deterioration through its life span.

Table 2 Prominent long-span cable-supported bridges with monitoring systems

| opening year | bridge | type | span length | location | sensors | purpose |
|---|---|---|---|---|---|---|
| 1937 | Golden Gate Bridge [7,13,14] | suspension | 1280 m | USA | accelerometers | OMA |
| 1964 | Forth Road Bridge [15] | suspension | 1006 m | UK | GNSS, acceleration, wind | SHM, research |
| 1973 | Bosphorus Bridge [16,17] | suspension | 1074 m | Turkey | accelerometers, laser displacement, thermocouple, GPS, strain gage, tiltmeter, weather station | real-time monitoring of condition and environment, post-earthquake performance |
| 1981 | Humber Bridge [11,18] | suspension | 1410 m | UK | accelerometers, anemometers, video, GPS | OMA, research |
| 1988 | Fatih Sultan Mehmet Bridge [16,19] | suspension | 1090 m | Turkey | accelerometers, seismometer, GPS, displacement transducers | real-time monitoring of condition and environment, post-earthquake performance |
| 1988 | Akashi-Kaikyo Bridge [20,21] | suspension | 1911 m | Japan | accelerometers, anemometers, seismometers, velocity gauge. GPS, temperature, stress | real-time monitoring of condition and environment, post-earthquake performance |
| 1996 | Second Severn Crossing [22] | cable-stayed | 456 m longest span (5.13 km total) | UK | accelerometers, anemometers, displacement transducers, temperature, vision-based | SHM, research |
| 1997 | Tsing Ma Bridge [23] | suspension | 1377 m | Hong Kong | accelerometers, anemometers, displacement transducer, level sensing strain gauges, GPS, weigh in motion | real-time monitoring of condition and environment |
| 1998 | Great Belt Bridge [24] | suspension | 1624 m | Denmark | accelerometers, anemometers, rain | SHM, vortex-induced vibrations |
| 1999 | Jiangyin Bridge [25] | suspension | 1385 m | China | accelerometers, anemometers, displacement transducers, fiber optic strain, temperature, GPs | real-time monitoring of condition and environment |
| 2005 | Runyang Suspension Bridge (South Bridge) [26,27] | suspension | 1490 m | China | accelerometers, anemometers, GPS,temperature, strain gauge | real-time monitoring of condition and environment |
| 2008 | Sutong Bridge [28] | cable-stayed | 1088 m | China | accelerometers, anemometers, temperature, displacement, weigh-in- | real-time monitoring of condition and environment |

| | | | | | | |
|---|---|---|---|---|---|---|
| | | | | | motion, strain gauges, GPS, corrosion | |
| 2009 | Stonecutters Bridge [29,30] | cable-stayed | 1078 m | Hong Kong | ~1500 sensors (wind, acceleration, GPS, corrosion, strain gages, temperature, dynamic weigh-in motion, rain etc.) | extensive real-time monitoring of condition and environment |
| 2009 | Xihoumen Bridge [31] | suspension | 1650 m | China | accelerometers, anemometers, GPS, wind pressure sensors | SHM, typhoons, vortex-induced vibrations |
| 2012 | Russky Bridge [32] | cable-stayed | 1104 m | Russia | accelerometers, anemometers, temperature, displacement, strain gauges, GPS, corrosion, weather, visual based | real-time monitoring of condition and the environment, reducing maintenance costs |
| 2013 | Hardanger Bridge [33] | suspension | 1310 m | Norway | accelerometers, anemometers | OMA, research |
| 2016 | Yavuz Sultan Selim Bridge [16] | hybrid cable-stayed suspension | 1408 m | Turkey | accelerometers, GPS, strain gages, tiltmeter | real-time monitoring of condition and environment, post-earthquake performance |
| 2016 | Osman Gazi Bridge [16] | suspension | 1550 m | Turkey | 386 sensors (accelerometers, temperature, anemometers fibre-optic strain, inclinometer, rain, etc.) | extensive real-time monitoring of condition and the environment |
| 2017 | Queensferry Crossing [12] | cable-stayed | 650 m longest span (total 2.7 km) | UK | ~1500 sensors (wind, acceleration, GPS, corrosion, strain gages, temperature, dynamic weigh-in motion, etc.) | extensive real-time monitoring of condition and the environment |

In the context of the Ferry-Free E39 project described in the previous section, a monitoring system was installed on the Hardanger Bridge [33] consisting of accelerometers and anemometers. The system was installed solely for research purposes; therefore, it is not aimed that the system serves as a permanent health monitoring system. When the future E39 bridges are concerned, full-scale monitoring of existing bridges are expected to aid in new design by condensing the experience from earlier designs. Valuable knowledge such as the validity of the models and assumptions involved in design of such structures are sought after. Additionally, since the environmental conditions of the future E39 bridges will be similar to that of the Hardanger Bridge, information on environmental factors such as wind characteristics will be of utmost value.

### 1.1.3. Buffeting of cable-supported bridge decks

Long-span cable-supported structures are flexible, light-weight structures with low damping, therefore are susceptible to wind actions. As the spans get longer, the wind-effects get more profound. Wind actions on such bridges result in aerodynamic forces acting on the structure that may cause instability phenomena such as galloping, vortex-shedding and flutter or vibrations (buffeting) of the deck due to the turbulence in the atmospheric boundary layer. The so-called buffeting response of a long-span cable-

supported bridge may become important since violent vibrations of the bridge deck can cause discomfort or instability of pedestrians and passing vehicles, fatigue problems and even exceedance of the ultimate strength of structural members. Therefore, accurate prediction of the buffeting response is vitally important for reliable design of these structures.

Stochastic methods for analytical prediction of the buffeting response of cable-supported bridge decks was first introduced by Davenport [34–36]. Based on the theory of random vibrations [37], Davenport's buffeting theory allowed calculation of the stochastic dynamic response of a bridge deck under random turbulence loading by means of spectral analysis. The theory was based on a set of assumptions, such as stationary and Gaussian turbulence that is small compared to the mean speed, uncoupled modes, and small deflections that allow linearization. For bluff-bodies, unsteadiness of the flow could be taken into account by the so-called aerodynamic admittance functions and a joint acceptance function in case of buffeting forces, where in case of self-excited forces, a quasi-steady approach needed to be adopted. Later, Scanlan and his co-workers introduced the frequency dependent aerodynamic (flutter) derivatives (ADs) that could include the fluid memory effect in modeling of the self-excited forces [38].

In the earlier practice, a mode-by-mode approach was used by the researchers, where the modal responses were combined post analysis by a modal combination approach, such as the square-root-of-sum-of-squares (SRSS) [39,40]. However, aerodynamic coupling between modes might be profound for long-span bridges, where closely spaced modes are commonly encountered. Consequently, neglecting the modal coupling might result into inaccurate predictions of the multimode response. Therefore, a multimode coupled approach is frequently used today in calculation of the buffeting response [41–45]. In a frequency domain approach, aerodynamic forces are linearized with respect to the effective angle-of-attack. In cases where the aerodynamic coefficients of the bridge deck shows high sensitivity against the angle-of-attack, a time-domain approach [46–50] should be adopted, where the nonlinearities can be included. In frequency domain, the equation of motion can be formulized in generalized coordinates to reduce the expressional complexity. The global displacement vector (Fig. 1) reads

$$\mathbf{r}(x,t) = \begin{bmatrix} r_y & r_z & r_\theta \end{bmatrix}^T, \ \mathbf{r}(x,t) = \mathbf{\Phi}(x)\boldsymbol{\eta}(t) \tag{1}$$

where $\boldsymbol{\eta}(t)$ is the generalized displacement vector and $\mathbf{\Phi}(x)$ is a matrix composed of mode shapes. These are further expressed as

$$\begin{aligned} &\mathbf{\Phi}(x) = \begin{bmatrix} \boldsymbol{\varphi}_1 & \boldsymbol{\varphi}_2 & \dots & \boldsymbol{\varphi}_N \end{bmatrix}, \ \boldsymbol{\varphi}_i = \begin{bmatrix} \phi_y & \phi_z & \phi_\theta \end{bmatrix} \\ &\boldsymbol{\eta}(t) = \begin{bmatrix} \eta_1 & \eta_2 & \dots & \eta_N \end{bmatrix} \end{aligned} \tag{2}$$

where N is the number of mode shapes to be included in the analysis. Having established the generalized displacement vector, the corresponding generalized aeroelastic matrices and the generalized buffeting

load vector remains to be formed. The aeroelastic stiffness ($\mathbf{K}_{ae}$) and damping ($\mathbf{C}_{ae}$) matrices are written in global coordinates as

$$\mathbf{K}_{ae} = \frac{\rho B^2}{2}\omega^2 \begin{bmatrix} P_4^* & P_6^* & BP_3^* \\ H_6^* & H_4^* & BH_3^* \\ BA_6^* & BA_4^* & B^2A_3^* \end{bmatrix}, \quad \mathbf{C}_{ae} = \frac{\rho B^2}{2}\omega \begin{bmatrix} P_1^* & P_5^* & BP_2^* \\ H_5^* & H_1^* & BH_2^* \\ BA_5^* & BA_1^* & B^2A_2^* \end{bmatrix} \tag{3}$$

where , $P_{1,2,..,6}^*$ , $H_{1,2,..,6}^*$ , $A_{1,2,..,6}^*$ denote the dimensionless aerodynamic derivatives, B is the width of the girder, $\omega$ is the frequency and ρ is the air density. The generalized matrices then read

$$\begin{aligned} \tilde{\boldsymbol{K}}_{ae}(U,\omega) &= \int_L (\boldsymbol{\Phi}^T \boldsymbol{K}_{ae}(U,\omega)\,\boldsymbol{\Phi})dx \\ \tilde{\boldsymbol{C}}_{ae}(U,\omega) &= \int_L (\boldsymbol{\Phi}^T \boldsymbol{C}_{ae}(U,\omega)\,\boldsymbol{\Phi})dx \end{aligned} \tag{4}$$

after the coordinate transformation.

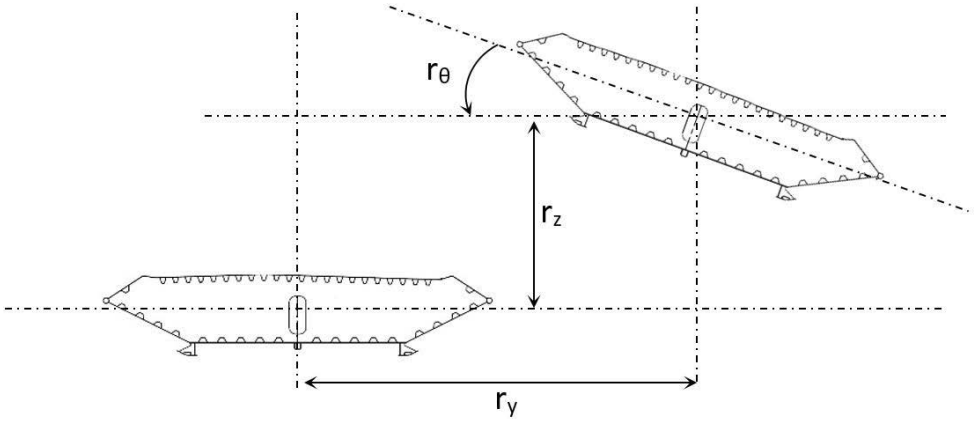


Fig. 1 Global deflections of the bridge cross-section

Again in generalized coordinates, the buffeting force matrix can be obtained after the following integration:

$$\boldsymbol{S}_{Q_{buff}}(\omega) = \int_L \int_L \boldsymbol{\Phi}^T(x_1)\mathbf{B}(\omega)\mathbf{S}_V(x_1,x_2,\omega)\mathbf{B}^T(\omega)\boldsymbol{\Phi}(x_2)dx_1dx_2 \tag{5}$$

where $\mathbf{S}_V(x_1,x_2,\omega)$ is the cross-spectral density matrix of turbulence, which reads

$$\mathbf{S}_V(x_1,x_2,\omega) = \begin{bmatrix} S_{uu}(x_1,x_2,\omega) & S_{uw}(x_1,x_2,\omega) \\ S_{uw}(x_1,x_2,\omega) & S_{ww}(x_1,x_2,\omega) \end{bmatrix} \tag{6}$$

and $\mathbf{B}(\omega)$ is the aerodynamic matrix, that reads

$$\mathbf{B}_q(\omega) = \frac{\rho UB}{2} \begin{bmatrix} 2(D/B)\bar{C}_D\chi_{yu} & ((D/B)C'_D - \bar{C}_L)\chi_{yw} \\ 2\bar{C}_L\chi_{zu} & (C'_L + (D/B)\bar{C}_D)\chi_{zw} \\ 2B\bar{C}_M\chi_{\theta u} & BC'_M\,\chi_{\theta w} \end{bmatrix} \tag{7}$$

In the cross-spectral density matrix, the diagonal terms denote the two-point cross-spectral densities of the same turbulence components, where the cross terms denote the two-point cross-spectral densities of different turbulence components. The along-wind turbulence component is denoted with u, where the vertical turbulence component is denoted with w. In the aerodynamic matrix, $\bar{C}_D$, $\bar{C}_L$ and $\bar{C}_M$ are the mean values of the steady-state force coefficients associated with the drag, lift and moment, respectively, $C'_D$, $C'_L$ and $C'_M$ are the corresponding derivatives, and D denotes the girder height. The remaining six terms ( $\chi_{yu}, \chi_{zu}, \chi_{\theta u}, \chi_{yw}, \chi_{zw}, \chi_{\theta w}$ ) are the aerodynamic admittance functions.

Then, the equation of motion can be written

$$\tilde{\mathbf{M}}_0\mathbf{G}_{\ddot{\eta}}(\omega)+(\tilde{\mathbf{C}}_0-\tilde{\mathbf{C}}_{ae}(U,\omega))\mathbf{G}_{\dot{\eta}}(\omega)+(\tilde{\mathbf{K}}_0-\tilde{\mathbf{K}}_{ae}(U,\omega))\mathbf{G}_{\eta}(\omega)=\mathbf{G}_{\mathbf{Q}_{buff}}(\omega) \tag{8}$$

where $\tilde{\mathbf{M}}_0$, $\tilde{\mathbf{K}}_0$ and $\tilde{\mathbf{C}}_0$ are the generalized mass, stiffness and damping matrices in still-air, respectively and $\mathbf{G}_{\ddot{\eta}}$, $\mathbf{G}_{\dot{\eta}}$ and $\mathbf{G}_{\eta}$ denote the Fourier transforms of the acceleration, velocity and displacement responses in generalized coordinates, respectively. Given the frequency domain equation of motion, the spectral density matrix of the generalized displacement response can be obtained by spectral analysis [37]:

$$\begin{aligned}\tilde{\mathbf{S}}_R(\omega)&=\left[\mathbf{H}^{-1}(\omega)\mathbf{S}_{\mathbf{Q}_{buff}}(\omega)\mathbf{H}^{-1*}(\omega)\right]\\ \mathbf{H}(\omega)&=\left[-\tilde{\mathbf{M}}_0\omega^2+(\tilde{\mathbf{C}}_0-\tilde{\mathbf{C}}_{ae}(U,\omega))i\omega+(\tilde{\mathbf{K}}_0-\tilde{\mathbf{K}}_{ae}(U,\omega))\right]\end{aligned} \tag{9}$$

Finally, the root-mean-square (RMS) of the displacement response can be obtained by calculating the area under the response spectra in global coordinates by integration and taking the square root

$$\sigma_R(x)=\sqrt{\int_0^{\infty}S_R(\omega)d\omega},\quad S_R(\omega)=\mathbf{\Phi}(x)\tilde{S}_R(\omega)\mathbf{\Phi}^T(x) \tag{10}$$

The above formulation assumes that the mean wind direction coincides with the axis perpendicular to the bridge longitudinal direction. In case of winds attacking the bridge with a yaw-angle, it is customary to decompose the wind velocity vector into a perpendicular and a parallel component to the bridge axis. Although the approach seems intuitive, it poses problems in decomposition of the turbulence components and also taking into account the response caused by the parallel component, which is usually neglected. In light of these, Xu and his co-workers [1,51–55] proposed a finite-element-model (FEM) based formulation of the theory to take into account the skew-winds (yaw-winds). In this method, the full set of equations of motion are formed and solved in the global coordinates of a full finite element model of the bridge. The method requires wind tunnel testing of oblique cross-sections for obtaining ADs for skew-winds, which might be cumbersome. On the other hand, other bridge components, such as the cables and towers are easily taken into account, since a complete finite element model of the bridge is used.

The mean wind speed and turbulence intensities along the bridge are generally assumed as uniform; since information on span-wise distribution of such quantities are seldom available. However, in case of large variations of the wind turbulence characteristics along the bridge girder [56], which might be the case for very long-span bridges, the effect on the buffeting response prediction might be significant, If profound non-uniform profiles are present and sufficient information on the profiles are available from wind tunnel terrain model tests or anemometric data, it is possible to include this effect using the above formulation by modifying the cross-spectral density matrix [57–59].

Rather recently, a number of studies [41,57,60,61] focused on non-stationary buffeting response of cable-supported bridges that are mostly located in typhoon-prone regions. It is observed that non-stationary features are present in wind recordings that are collected from different bridge sites, which challenges the common practice, where the wind is assumed as stationary. Considering this, recent studies conducted buffeting analysis of bridges removing the stationary assumption. This implies that the wind field is characterized by a slowly-varying static wind component and time-varying turbulence statistics. Although some studies pointed out differences between the stationary and non-stationary responses [41], further investigation and comparison with full-scale data is needed to reach to more concrete conclusions. It is also a question how this approach can be incorporated into the design process.

In this thesis, when needed, the buffeting response of the Hardanger Bridge (HB) is calculated in frequency domain using the multimode coupled buffeting theory, which is described through Eqns. (1) -(10). The analyses are conducted using the traditional stationary wind model. Skew-winds are not taken into account and the wind velocity vector is not decomposed into perpendicular and parallel components. The aerodynamic derivatives and static force coefficients for the HB section are taken from the forced vibration wind tunnel tests of Siedziako et al. [62]. The aerodynamic admittance functions are taken as unity, due to lack of experimental data. The span-wise correlation of the buffeting forces are assumed to be identical to the correlation structure of the incoming turbulence. The combination of these two assumptions are expected to give a conservative prediction in the end [4,63]. The cross-spectral density of u and w turbulence components is neglected in the analyses, since the contribution is small. Non-uniform profiles of wind speed and turbulence intensity are taken into account when considerable differences are present along the bridge.

### 1.1.4. Modeling of the atmospheric turbulence

The methods described in the previous section provide means for prediction of wind-induced dynamic response of long-span cable-supported bridges. However, accurate predictions are only possible with a good description of the aerodynamic loads acting on the structure. These are simply the buffeting and self-excited forces when only the dynamic response is considered. A good description of the buffeting

loading then relies on the modeling of the atmospheric turbulence. The structural dynamic response of the bridge is associated with the wind speed fluctuations (gusts). Therefore, the wind velocity vector is usually decomposed to its mean and three orthogonal fluctuating components aligned in the mean wind direction, which are termed as the along-wind, cross-wind and vertical turbulence components. The cross-wind component is usually neglected in case of horizontal line-like structures, where the other two components cause the buffeting response. In a frequency domain buffeting analysis, the effect of turbulence is represented by means of a cross-spectral density matrix, which contains temporal and spatial characteristics of turbulence components. The cross-spectral density matrix, already given in Eqn. (6), is composed of two parts: an auto-spectral density $S_{nm}(x,\omega)$ and a normalized cross-spectrum $C_{nm}(\Delta x,\omega)$ which are related as follows:

$$S_{nm}(x_1,x_2,\omega)=\sqrt{S_{nm}(x_1,\omega)S_{nm}(x_2,\omega)}C_{nm}(\Delta x,\omega),\quad n,m=u,w \tag{11}$$

The auto-spectrum gives the energy content of turbulence at a single point, where the normalized cross-spectrum gives the correlation information of the same component between two points along the structure. The former is usually approximated by a smooth curve with a single maximum when plotted as $\omega S_{nm}(x_1,\omega)$ *vs.* $\log\omega$. The latter has both real and imaginary parts, where the imaginary part is usually neglected for perpendicular winds [64]. The real part is called the normalized co-spectra, and can be thought of as a frequency dependent correlation coefficient, therefore it assumes values between -1 and 1, where values close to unity implies strong correlation. Typically, the correlation of turbulence components gets smaller when the separation distance or the frequency increases (smaller eddies). Therefore, when plotted against a non-dimensional frequency ($\omega\Delta x/U$), the normalized co-spectra constitutes a decaying function. The illustrations of both are given in Fig. 2

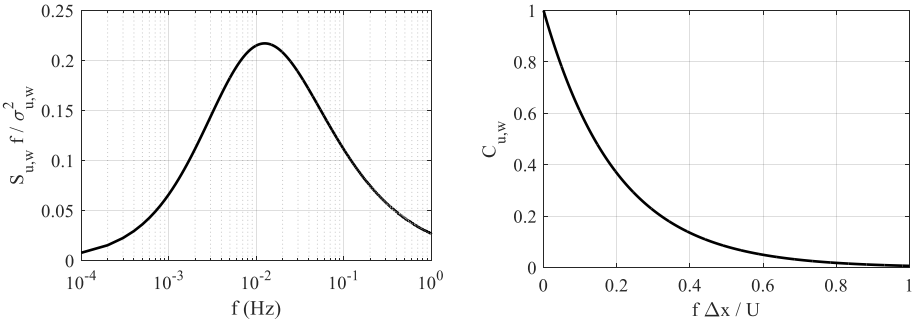


Fig. 2 Illustrations of auto-spectrum (on the left) and normalized co-spectra (on the right) of turbulence

Substantial amount of models have been proposed for the turbulence (gust, micrometeorological) spectra [65–77] and the normalized co-spectra [66,75,78–81] (root coherence or co-coherence if absolute value is taken) by researchers based on wind tunnel or field measurements or theoretical derivations. For a comprehensive critical review of different models in literature, the reader may refer

to the papers of Solari [82,83]. One of the earlier models for the auto-spectra was proposed by von Karman [67], as a result of his measurements in the wind tunnel for grid-generated turbulence. The von Karman spectra for the along-wind (u) and vertical (w) turbulence spectra reads:

$$\frac{f\,S_u(f)}{\sigma_u^{\,2}} = \frac{4.\frac{L_u \cdot f}{U}}{\left[1+70.8\left(\frac{L_u \cdot f}{U}\right)^2\right]^{5/6}}, \quad \frac{f.S_w(f)}{\sigma_w^{\,2}} = \frac{4.\frac{L_w \cdot f}{U}\left[1+755\left(\frac{L_w \cdot f}{U}\right)^2\right]}{\left[1+283\left(\frac{L_w \cdot f}{U}\right)^2\right]^{11/6}} \tag{12}$$

where $L_{u,w}$ denote the integral length scales. The von Karman model is written in terms of standard deviations of velocity fluctuations and integral length scales, parameters that are difficult to forecast due to their significant variability and site-dependence, which makes it hard to use it as a universal spectrum. Moreover, it is known that integral length scales estimated by exploiting Taylor's hypothesis of frozen turbulence cause fallacious estimates of the von Karman spectrum. For that reason, ESDU [84] proposes a modified spectral formula based on von Karman's original formulation. Another spectral model proposed by Davenport [85] had apparently been used in practice by wind engineers in the earlier days, but abandoned due to discrepancies observed with the field measurements [73]. Other family of models usually assume the following form:

$$\frac{f\,S_{u,w}(f)}{u_*^{\,2}} = \frac{Af_z^{\,\gamma}}{\left(C+Bf_z^{\,\alpha}\right)^{\beta}}, \quad f_z = fz/U \tag{13}$$

where $u_*$ is the friction velocity and z is the height. Other letters denote parameters that are determined by field observations. Several criteria are sought in determination of the parameters, such as the spectra should agree with the Kolmogorov law [72,86] in the inertial subrange (the frequency range of eddies where inertial forces dominate the fluid motion) and the maximum point, peak frequency and area under the spectra should match the observations. For flat homogenous terrain and stable or neutral atmospheric conditions, the model takes the more specific form:

$$\frac{f\,S_{u,w}(f)}{u_*^{\,2}} = \frac{Af_z}{\left(1+Bf_z\right)^{5/3}} \tag{14}$$

which is called a blunt model and usually shows satisfactory agreement with the measurements; however, may not always match well in complex terrain.

The normalized co-spectra is usually represented sufficiently well by an exponentially decaying curve, which is a function of the non-dimensional frequency. A simple expression proposed by Davenport is commonly used, which reads:

$$C_{u,w}(\Delta x, f) = \exp\left(-K_{u,w}\frac{\Delta x f}{U}\right) \tag{15}$$

where $K_{u,w}$ is known as the decay coefficient, which is also determined by field observations. This model has some well-known weaknesses. The first is the normalized co-spectra always assumes the value of 1 when frequency goes to zero, which is not the case in reality, since turbulence components at different points are not fully coherent. Secondly, the model does not allow negative values of the normalized co-spectra. Despite these, the expression is still frequently used due to its simplicity and the fact that the discrepancies are contained only in the very low frequency range, which is lower than the fundamental natural frequency of most land-based structures. More advanced models are also available in the literature [75,78,80,87]. It is also possible to use expressions similar to the decaying function with more parameters that allow the necessary alterations [58,88]. Regarding the spectra measured at the Hardanger Bridge site, the following expressions are found satisfactory in terms practicality and correctness:

$$\frac{f\,S_{u,w}(f)}{{\sigma_{u,w}}^2} = \frac{Af_z}{\left(1+1.5Af_z\right)^{5/3}}, \quad C_{u,w}(\Delta x, f) = \exp\left(-K_{u,w}\frac{\Delta x f}{U}\right) \tag{16}$$

Although it seems like the auto-spectra and normalized co-spectra of turbulence components are described reasonably well with such basic models, it is seen that the parameters of models show significant variation between measurements at different sites [83]. Site-specific features such as the terrain characteristics makes it difficult to describe the spectra with the above models and a few basic parameters such as the height above the ground or the roughness coefficient. Moreover, a considerable amount of data have been presented lately on wind characteristics at long-span bridge sites, as a result of structural health monitoring systems [28,33,89–97]. The long-term measurement results at specific sites also indicate that the turbulence parameters also exhibit variability at the same site. Uncertainty in the turbulence is inherent as a result of the terrain effects, variable atmospheric conditions and the nature of the upcoming winds.

The traditional design practice ignores this variability, since deterministic turbulence parameters are often used to deduce the cross-spectral density matrix of turbulence. The mean wind speed is usually treated as the sole design parameter, and for a given return period such as 50-100 years, the extreme value of which is used to calculate the extreme response, where the turbulence field is deduced using deterministic parameters, some of which are functions of the mean wind speed. In modern engineering design, such uncertainties should be taken into account for more refined and reliable designs. Probabilistic design and analysis methods are quite common in wind engineering. In case of the buffeting response of a cable-supported bridge, the parametric uncertainties can be listed as the uncertainty in the wind environment (mean wind and turbulence parameters), wind-structure interaction (aerodynamic properties of the bridge deck) and structural properties (damping, material and modal parameters, etc.). Probability based frameworks such as reliability analysis [98–103], probabilistic

response analysis [104–108], performance based design [109,110], fragility assessment [111–113] or long-term extreme value response analysis [114,115] all require probabilistic description of the uncertain parameters. The studies so far have been concerned about the last two, where the uncertainty in the turbulence parameters were generally overlooked. Although it was pointed out extensively that the turbulence parameters exhibit significant uncertainty and should be taken into account, very few studies addressed this in their probabilistic analyses.

Solari and Piccardo [83] proposed a probabilistic turbulence model that is based on random Gaussian turbulence parameters, which are defined through their first and second statistical moments obtained from a collection of field data presented in the literature. The model can be easily implemented in any probabilistic framework through Monte Carlo simulations. Such a model is useful in propagating the uncertainty in the turbulence parameters into the response estimates. However, the considered variability might be too high, since it covers a wide range of measurements, and the model is restricted to flat homogenous terrain, so the applicability in complex terrain is a question mark.

In the case of the Hardanger Bridge, analysis of long-term data indicates that most of the variability in the response is due to the variability in the turbulence parameters. Therefore, consideration of the parameter uncertainty in turbulence modeling is essential for such complex terrain. For this purpose, performance of current models need to be evaluated and improvements should be made toward a competent probabilistic description of the turbulence field to be used in such applications.

## 1.2. Objectives and scope

### 1.2.1. Objectives of the research

This doctoral study aims to assess the performance of state-of-the-art methodology and the degree of uncertainty involved in wind-resistant design and analytical prediction of wind-induced dynamic response of cable-supported bridges in complex terrain, by using long-term monitoring data of wind velocities and accelerations from the Hardanger Bridge (HB) as a case study. To that extent, the following research objectives can be listed:

- **Present one-point and two-point turbulence characteristics at the bridge site**

The terrain at the HB site is quite particular and representative of the conditions at the future bridge sites in Norway. It is important to have an extensive database on one-point and two-point turbulence statistics from such terrain and extra-tropical wind conditions, which are not commonly encountered in the literature. It is also aimed that the data are used not only to present the averaged wind characteristics, but also the variability of turbulence statistics at the site.

- **Study the variability in dynamic response of the HB using statistical and analytical tools**

The wind-induced dynamic response of the HB deck shows significant variability. The causes of this with reference to the turbulence characteristics at the site shall be investigated by utilizing both statistical and analytical tools.

- **Assess the performance of state-of-the-art methods in predicting the wind-induced dynamic response of the HB**

The studies comparing buffeting response predictions with full-scale measurements in literature are rather scarce, so here it is aimed to assess the accuracy of analytical predictions through such comparisons and investigate the degree of uncertainty involved.

- **Investigate the possibility of using probabilistic turbulence models in design and response analysis**

A deterministic description of the turbulence field along a cable-supported bridge deck, which is the current practice, is an oversimplification that neglects the inherent variability of the wind field at the site. The uncertainty caused by this is expected to be more severe in complex terrain. Here, instead of a deterministic model, the possibility of using probabilistic models in describing the atmospheric turbulence in buffeting response predictions shall be assessed.

### 1.2.2. Scope

The results obtained in the course of this thesis are representative for the specific case of the HB; however, generalization of the results for other sites and structures is not possible without further investigation.

In the wind characterization study, the traditional stationary Gaussian turbulence model is used. Nonstationary & non-Gaussian models and methods of analyses are considered out of scope of this thesis.

Only buffeting response of the HB deck is considered in the study. Traffic-induced vibrations, cable and hanger vibrations or vibration of the concrete pylons are not studied. As for the vibrations of the deck, vortex-induced vibrations, flutter and other instability phenomena are also considered out of scope of this thesis and will not be addressed here.

In buffeting response analyses, state-of-the-art methodology is used to predict the dynamic response [44]. The aerodynamic properties of the bridge section are taken from the tests results of Siedziako et

al. [62]. Wind tunnel testing, identification of aerodynamic parameters and assessment of adequacy of motion-induced load models are not addressed in this thesis, as these are subjects of another doctoral study being conducted at the department [62].

Aerodynamic admittance functions are taken as unity and the spatial correlation of the buffeting forces are assumed to be the same as the incoming turbulence throughout the study, due to lack of experimental data on those matters.

Buffeting loads on bridge cables and towers are not included in the analyses, since measurements on the turbulence characteristics at these locations were not available and since the main goal of the thesis is to investigate the effects of turbulence modeling. Necessary discussions on the implications of these matters are included in the appended papers.

Modal properties of the bridge are obtained from a finite element model of the bridge supplied by the NPRA, which shows reasonable agreement with the operational modal analysis results of [116]. Further investigation of the modal properties are therefore considered out of scope.

Lastly, the probabilistic approach presented here is based on a large amount of data. Although physically consistent models are used to represent the turbulence, a purely statistical approach is adopted in its derivation. The physical interpretation of the results are not addressed in this study.

### 1.3. Structure of the thesis

The next chapter (Chapter 2) explains in detail the Hardanger Bridge monitoring project, which has been going on for about 4 years. The workings of the monitoring system and data handling are addressed in more detail than it was done in the appended papers. It is then followed by Chapter 3, which gives a summary of the investigations and main findings of the appended papers. Chapter 4 and 5 presents the conclusions of the thesis and suggestions for future work, respectively. The final chapter, Chapter 6 contains three published journal papers, a conference paper and a manuscript that is submitted for journal publication. According to their subjects, the papers may further be divided into the following subtopics:

- Relationship between variable turbulence characteristics and dynamic response (Papers 1 & 2)
- Comparison of measured and predicted response (Papers 3 & 4)
- Probabilistic modeling of the turbulence field (Paper 5)

# 2. Hardanger Bridge Monitoring Project

## 2.1. The Hardanger Bridge and its surroundings

The Hardanger Bridge (Fig. 3) is currently the longest suspension bridge in Norway with its single span of 1308 meters. It crosses the Hardangerfjord in the western coast of Norway and connects the two small towns: Vallavik in the north and Bu in the south and it is an important part of the highway from Bergen to Oslo. It is located in a region known for its unique topography, where narrow and deep fjords with tall mountains are common. A map showing the local topography surrounding the Hardanger Bridge is given in Fig. 4. On the map, steep mountain sides to the north and the south ends of the bridge are noticed, as well as the mountains reaching up to 1100 meters in the east and 1600 meters in the west.

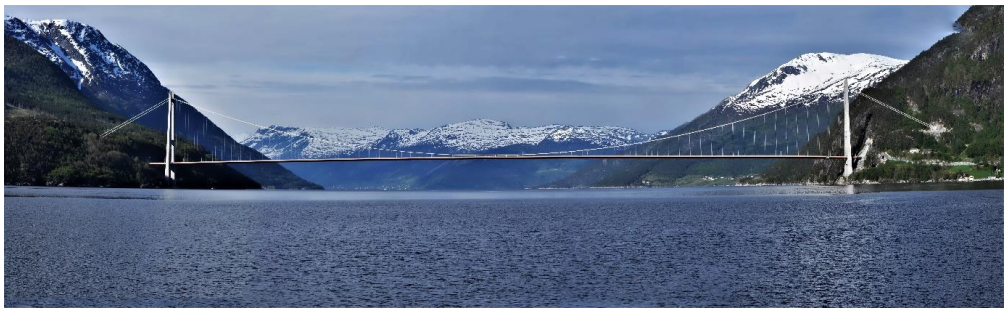

Fig. 3 Panorama view of the Hardanger Bridge. In the background, the tall mountains to the west can be observed. Mount Oksen stands on the right side i.e. the north end of the bridge, reaching up to 1000-1100 meters. (Photography by Aksel Fenerci/NTNU)

Hardanger Bridge supports two traffic lanes, one in each direction and a bicycle lane on its girder; therefore, it is exceptionally slender compared to other bridges of similar scale (Fig. 5). The bridge deck section is an aerodynamically designed streamlined box section, which is 3.2 meters high and 18.3 meters wide. The deck is curved with a radius of curvature of 20,000 meters (Fig. 6) A technical drawing of the section is provided in Fig. 7. As seen in the drawings, the deck section is equipped with guide vanes which were installed underneath the girder. These were designed to mitigate vortex-induced vibrations detected during the wind tunnel tests prior to the construction of the bridge. The girder is composed of 60 meters long sections, which were individually lifted to place and attached to the hangers of the bridge. In total, the bridge girder is supported by 2 main cables through 130 straight hangers, where the shortest one is 2 meters and the longest one is 128 meters long. The massive pylons on either side sit on rock foundations and reach around 200 meters.

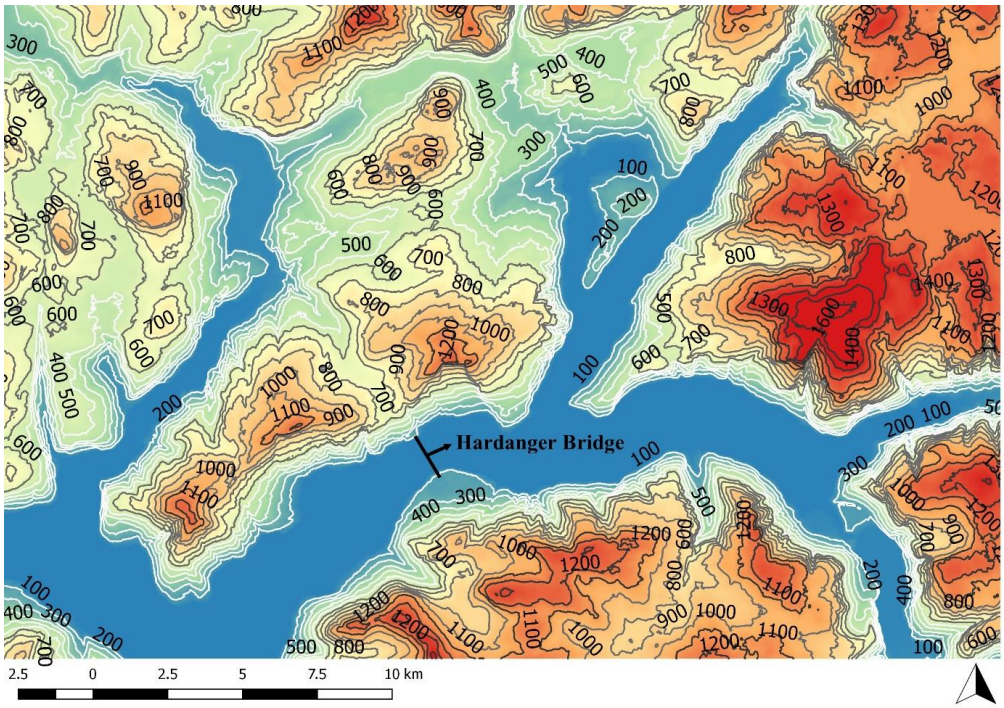


Fig. 4 Local topography surrounding the Hardanger Bridge (contour lines show 100 m elevation difference) (map data from ®Kartverket, Norwegian Mapping Authority)

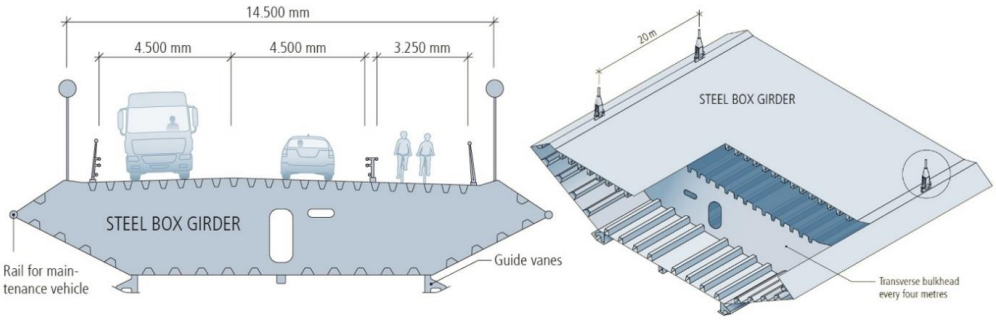


Fig. 5 The Hardanger Bridge girder: the girder supports two traffic lanes and a bicycle lane. The streamlined box girder and the guide vanes underneath it are shown (Illustration courtesy of NPRA)

Fig. 6 On the deck of Hardanger Bridge: the curvature of the deck is visible

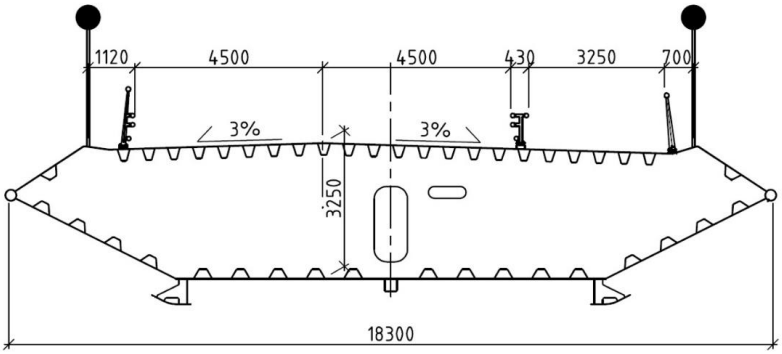


Fig. 7 Technical drawing of the Hardanger Bridge deck cross-section, all units in mm (courtesy of NPRA)

## 2.2. Project overview

Hardanger Bridge was opened to traffic on August 2013 after a 3.5 year construction period. Shortly after its opening, a research project has been initiated by the structural dynamics group at the Norwegian University of Science and Technology (NTNU) aiming to conduct long-term monitoring of wind velocities and deck accelerations along the bridge span. In context with the Ferry-Free Coastal Highway E39, the aim of the project and the measurement campaign was to provide data on wind characteristics and dynamic response of a long-span suspension bridge in Norwegian Fjords. This would aid in validation and applicability of the state-of-the-art methodology for the unique terrain where the future bridges are planned to be built, as well as quantitative and qualitative evaluation of the uncertainty imposed into dynamic response prediction.

The monitoring system, consisting of wind and acceleration sensors was designed to serve the needs of the research project, not as a structural health monitoring system, which is the common practice. The

monitoring system was installed by a team from NTNU. An overview of the monitoring system is shown in Fig. 8. The coordinates of the sensors are given in Table 1, where the origin of the coordinate system is taken at the midspan of the bridge and positive x-axis is toward the Bu side. As indicated in the figure, eight of the anemometers are distributed along the girder, attached to the hangers of the bridge at a height of 8 meters above the deck (Fig. 9) to avoid disturbance of the wind flow due to the deck itself or the overflowing traffic. The remaining anemometer is located at the top of the Vallavik (north) tower. The deck anemometers are located on the side of the bridge facing the east because of the ease of access provided by the pedestrian lane, except for the anemometer A6, which is attached to a light pole around midspan on the west side. The anemometers are WindMaster Pro 3D ultrasonic type from Gill Instruments. The sensors measure in 0-65 m/s range with 0.001 m/s resolution with a maximum sampling rate of 32 Hz. Among 20 accelerometers, 16 of them are installed inside the girder at the bulkheads. Among which, 14 of the sensors are located on either side of the cross-section with approximately 13 meters apart from each other (Fig. 10), where the remaining two were installed without pairs. The remaining four is at the tower tops, two at each tower and one on each side. The sensors are of type CUSP-3D series triaxial strong motion accelerographs from Canterbury Seismic Instruments. They can measure in ±4g range with a maximum sampling rate of 200 Hz.

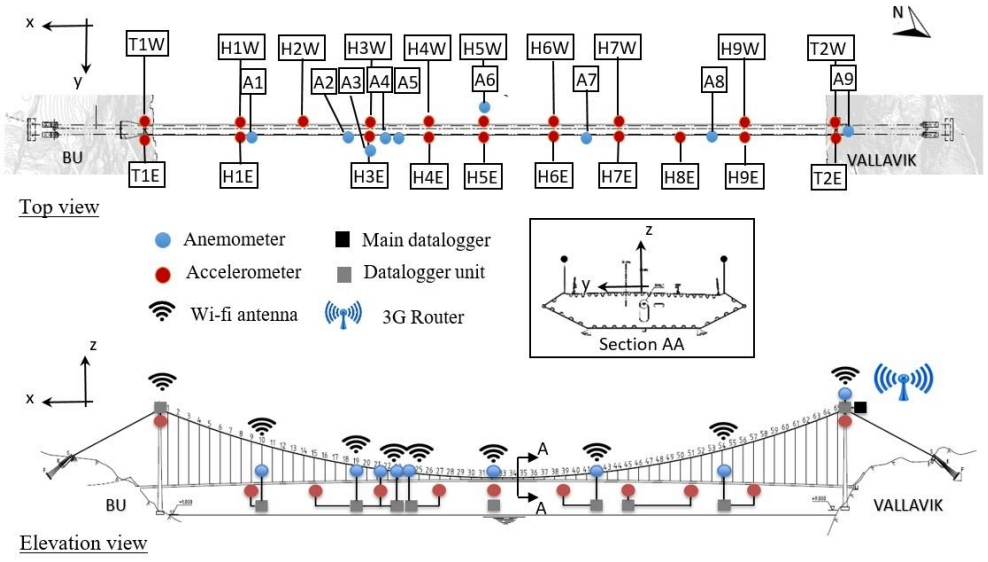


Fig. 8 Overview of the Hardanger Bridge monitoring system: the system consists of 9 wind sensors (anemometers), 20 accelerometers, 10 wi-fi antennas, 10 GPS sensors and 11 dataloggers.

Table 3 Sensor names and coordinates: the origin of the coordinate system is the midspan of the bridge and positive x-direction points to the south (Bu) end of the bridge

| Wind sensors | | | | Accelerometers | | | |
|---|---|---|---|---|---|---|---|
| Name | x (m) | y (m) | z (m) | Name | x (m) | y (m) | z (m) |
| A1 | 460 | 7.25 | 0.3 | H1E/H1W | 480 | 6.33/-6.64 | -8.38 |
| A2 | 280 | 7.25 | 3.2 | H2W | 360 | -6.64 | -6.41 |
| A3 | 240 | 7.25 | 3.9 | H3E/H3W | 240 | 6.33/-6.64 | -4.45 |
| A4 | 200 | 7.25 | 4.6 | H4E/H4W | 120 | 6.33/-6.64 | -2.48 |
| A5 | 180 | 7.25 | 4.9 | H5E/H5W | -7 | 6.33/-6.64 | -0.4 |
| A6 | -10 | -7.25 | 8 | H6E/H6W | -120 | 6.33/-6.64 | -2.25 |
| A7 | -180 | 7.25 | 5.2 | H7E/H7W | -240 | 6.33/-6.64 | -4.22 |
| A8 | -420 | 7.25 | 1.2 | H8E | -360 | 6.33 | -6.18 |
| A9 | -655 | 4.5 | 140 | H9E/H9W | -480 | 6.33/-6.64 | -8.15 |
| | | | | T1E/T1W | 655 | 4.5/-4.5 | 120.5 |
| | | | | T2E/T2W | -655 | 4.5/-4.5 | 120.5 |

Fig. 9 Triaxial sonic anemometers installed on the Hardanger Bridge: the anemometers extend one meter to the side of the hangers by a steel bar to avoid disturbance of the wind flow. On the right, anemometer A6 is shown. It is attached to a light pole around midspan.

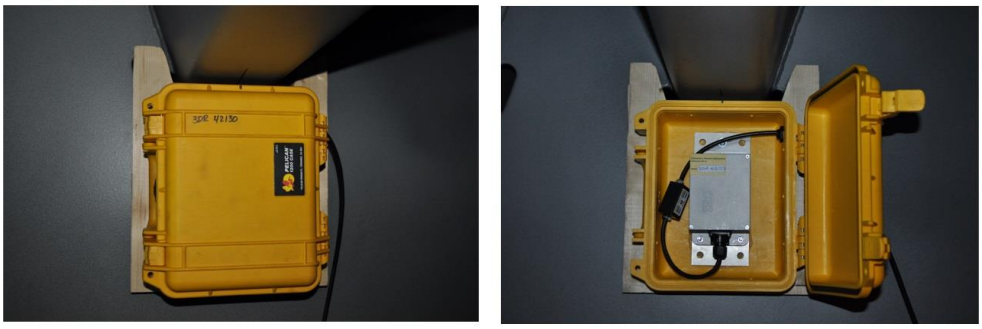

Fig. 10 Triaxial accelerometers inside the Hardanger Bridge deck. The sensors are attached to the bulkheads with a wood block in between to provide better traction.

The wind and acceleration sensors are connected by wire to the local datalogger units placed in close vicinity of the sensors inside the bridge deck (Fig. 11). These loggers are of CUSP-Ms type from Canterbury Seismic Instruments. A main datalogger (CUSP-Me) is situated at the top of the Vallavik Tower (Fig. 11). There, all the data is collected from the local loggers by wireless communication. This is achieved by wi-fi antennas connected to each local logger unit (Fig. 12). The time synchronization of the data between loggers is achieved using GPS sensors at each logger unit (Fig. 12).

Fig. 11 Dataloggers at the Hardanger Bridge: on the left, two logger units at the Vallavik Tower are shown. The other loggers are placed inside the girder, close to sensors.

Fig. 12 Other instruments of the monitoring system: wi-fi antennas and GPS sensors are attached to hangers and connected to each logger unit. In both pictures, the antennas are on the left and the GPS sensors are on the right.

## 2.3. Operation, maintenance and data acquisition

The monitoring system is operational at all times, unless there is a technical problem. Although the sensors measure data continuously, the dataloggers do not always record data. The system is set in such a way that the dataloggers are triggered to record data only in case of strong winds. When the mean wind velocity in any of the sensors exceeds a trigger value of 15 m/s averaged over 1 minute, all of the dataloggers record data from all of the sensors in the system for a duration of 30 minutes. The sensors are set to measure with their highest possible sampling rates, which are 32 Hz for the anemometers and 200 Hz for the accelerometers. By means of the wi-fi antennas, the data from each of the local loggers then get transformed to the main datalogger at the tower. Here the datalogger is connected to an ADSL router and the data is automatically uploaded to and stored securely in servers located at NTNU with the UTC timestamp.

Regular maintenance checks of the measurement system were conducted only once a year, prior to the storm season, which usually starts in December for Norway. These regular checks included inspection of the physical health of the sensors and connections, as well as the data acquisition system. Remote access to the system settings is provided by a web interface through the internet connection. This allows changing the settings, remote manual triggering of the system, rebooting of individual loggers or rebooting of all loggers. The conncetion is checked regularly by pinging the IP numbers of the wireless sensors inside the local network. In case of a connection failure, the project members are notified via e-mail and the issue is due further inspection. In the event of a sensor or connection failure which cannot be handled remotely, additional maintenance trips had to be performed to the site. During the 4 year monitoring period, accelerometers did not experience any failure. The wifi-antennas and anemometers, on the other hand, were more vulnerable; since they are located out in the open and exposed to environmental effects such as wind, ice snow, rain, bird impact, etc. Although not frequent, failure of the wind sensors, wi-fi antennas and malfunction of the dataloggers and the ADSL router were experienced during the course of the 4 year measurement campaign. Any malfunction of the dataloggers were usually possible to be fixed with a remote reboot; however, a hard reboot in the box was sometimes necessary. Two of the anemometers and one wi-fi antenna had to be replaced by new ones, due to permanent sensor failures. One of the anemometers was physically broken, possibly due to fatigue, induced by high frequency vortex-induced vibration of the hanger [117]. In the case of a router or wireless sensor failure, no data is lost. The data cannot be transferred but still locally recorded and can be retrieved later. Unavoidably, in case of sensor failures or failure of local loggers, the data from local sensors are lost. In the case of failure of the main logger, all data is still logged in the local units. If the router does not work, the data cannot be transferred from the main logger, but still recorded there until its capacity (50 gigabytes) is full.

Fig. 13 Anemometer failure. The picture on the left shows the broken sensor. The head of the sensor is completely detached from its body; however, it is hanging on to the bottom plate by pure luck. The failure is believed to have happened due to fatigue caused by wild vortex-induced vibrations of the hanger. On the right: PhD candidates Øyvind Wiig Petersen and Tor Martin Lystad are working hard to replace the broken sensor.

## 2.4. Database for bridge monitoring projects

The comprehensive monitoring system has a dense sensor network and as mentioned earlier, high sampling rates were imposed, which inevitably results into large amount of data accumulation, especially in the long term. A 30-minute long recording outputs approximately 600 MB of data in the comma-separated-values (.csv) file format, which is the default format in the system for the raw and uncompressed data. The large amount of data makes storage, organization, sharing and processing of the data rather challenging. Therefore, it is required that the data is handled in a systematic but practical way.

In parallel to the Hardanger Bridge, two other bridges in Norway, namely the Gjemnessund Bridge, a suspension bridge (623 m main span, 1257 m in total) and the Bergsøysund Bridge [118], an end-supported pontoon bridge (930 m) are being monitored by the structural dynamics group at NTNU. Therefore, it was desired to have a common database for all bridge monitoring data acquired during these campaigns. To that end, it was decided to collect the data into Matlab data structures [119] with ".mat" extension in a predefined structure common for all projects. The file format was chosen due to its ease of use and well integration into commonly used computation and analysis software such as Matlab [119] or Python [120]. It was also preferred that the 30-minute recordings kept in separate files, to avoid excessive file sizes that require sizeable memory allocation.

A computer program was written in Matlab in collaboration with PhD candidate Knut Andreas Kvåle to automate the collection of the data into the desired format, as the monitoring project continues. This

way, a new recording is automatically detected by a workstation dedicated to this particular job and the data is stored in mat-files after preliminary signal processing. The resulting files contain general information about the recording (such as the coordinate system, sensor locations, duration of the recording, etc.), raw data, adjusted data (after signal processing) and some basic statistics. The organization of a single mat-file is given in Fig. 14. A mat-file for a 30 minutes long recording takes around 300 MB of space. It is possible to further compress this [119]; however, the loading time for the compressed file would be longer.

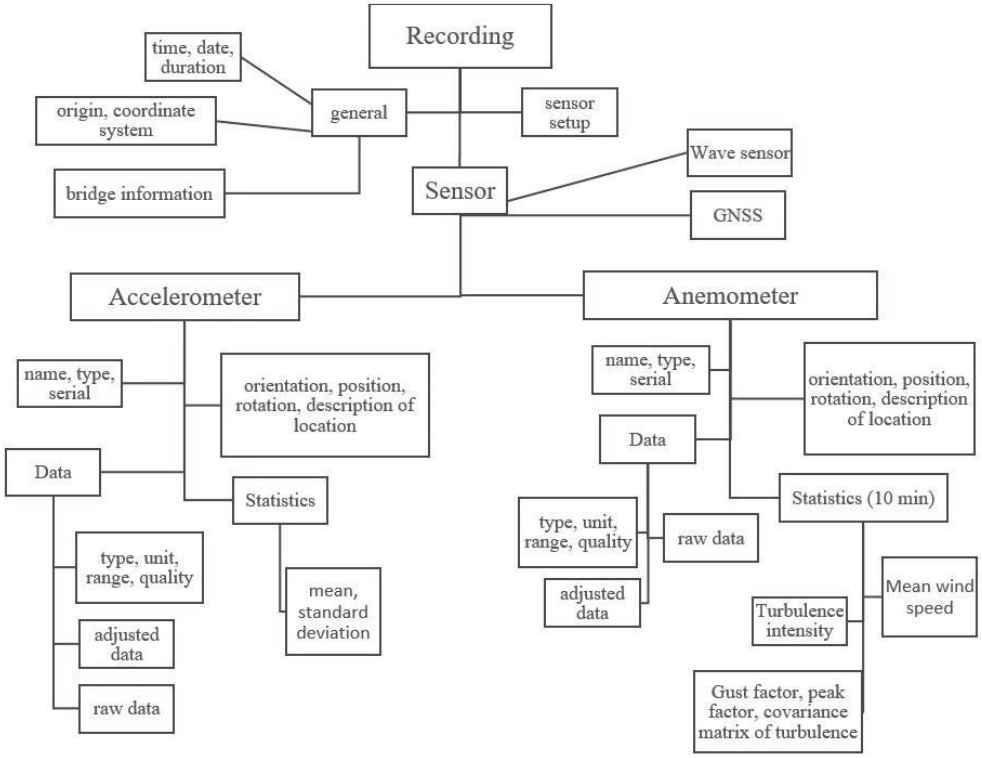


Fig. 14 Organization of the data structure for a single 30-minute recording: the file contains general information on the recordings and sensors, raw and adjusted data and simple sensor-specific statistics.

The workflow in creating a mat-file following a recording at the bridge site is illustrated in Fig. 15. Along with the ".csv" output from the system, the program requires other input files in the ".xml" file format. Among which, the "system setup" file incorporates information about the sensor setup and sampling frequencies, valid measurement ranges, etc. and shall be left unchanged unless there is a change in the configuration of the system. The "sensor info" file contains information on the sensor types such as accelerometers and wind sensors. This file requires updating if there is an addition of new sensor types to the system. The remaining "metadata" is supplied by the monitoring system as a bi-

product and contains information about the recording and system settings. Having the necessary input, the program compiles all information into a single file with the raw data and the so-called “adjusted data”. The latter consists of data that are downsampled and cleaned from error values (the sensors commonly output large values as errors) of values outside valid limits and necessary transformations made. An example recording is presented in Fig. 16 to highlight differences between raw and adjusted data.

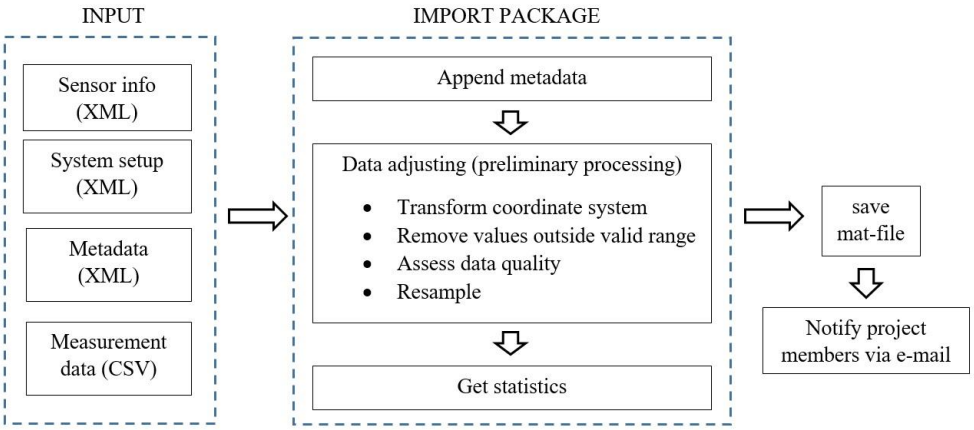


Fig. 15 Workflow of the data import package

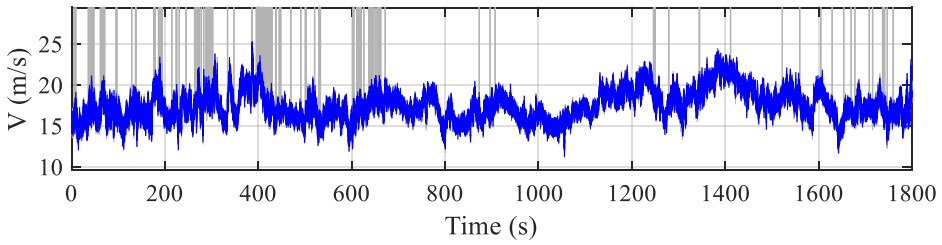


(a)

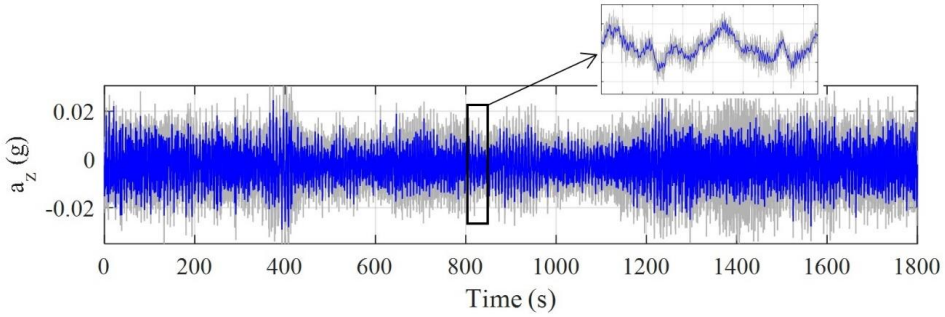


(b)

Fig. 16 Raw vs. adjusted data for a 30-minute long recording: (a) Magnitude of the velocity vector in the horizontal plane (sensor A6) and (b) vertical acceleration signal (sensor H8E). The gray lines show the raw data, where blue is for the adjusted data. The large error values in (a) was removed by preliminary signal processing. The data is also resampled to 20 Hz.

It is also beneficial that the data structure contains simple statistics from the recording, which shall be quickly accessed. These are the mean, standard deviation and higher order moments for the accelerometers and the turbulence statistics for the anemometers. Since, anemometers sample data in polar coordinates, a coordinate transformation had to be performed to obtain the mean wind velocity and the turbulence components. Given the outputs V(t) the magnitude of the wind velocity on the horizontal plane, $\phi$(t) the wind direction and W(t) the vertical wind velocity, the transformation reads

$$\begin{aligned} &U = \overline{V_\phi(t)}, \;\; V_\phi(t) = V(t)\cos\left(\phi(t) - \overline{\phi(t)}\right) \\ &u(t) = V_\phi(t) - U, \;\; v(t) = V(t)\sin\left(\phi(t) - \overline{\phi(t)}\right), \;\; w(t) = W(t) - \overline{W(t)} \end{aligned} \tag{17}$$

where the bar denotes time averaging, U the mean wind speed and u(t), v(t) and w(t) the along-wind, cross-wind and vertical turbulence components, respectively. Using these turbulence components, statistics such as the mean wind speed and direction, turbulence intensity and covariance of turbulence components are obtained and appended to the data structures.

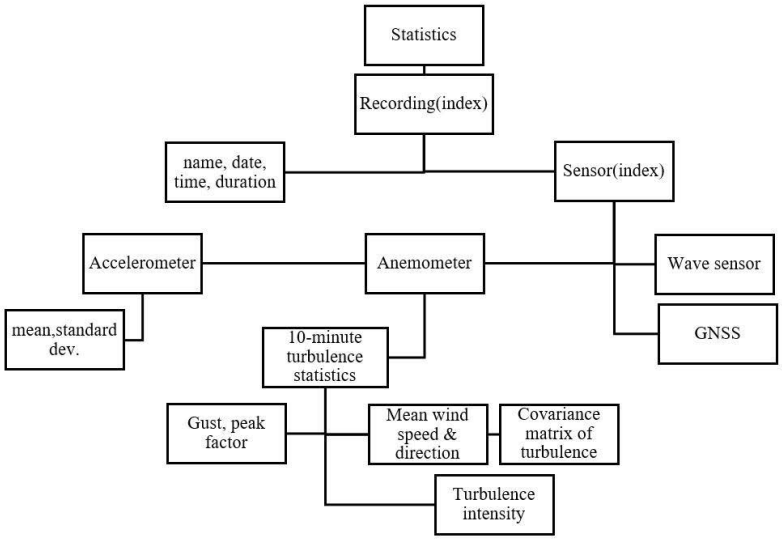


Fig. 17 Organization of the statistical information file

After appending the statistics, the file is complete; therefore, it is saved to the database and the project members are notified with an e-mail. However, it is of practical advantage if the statistics from each recording can be accessed easily without having to load the entire database to the computer memory. This was achieved by creating a separate file called the “statistical info” file, where the statistics from all recordings are collected without the data itself. The organization chart for this file is given in Fig. 17. The file is updated after each recording and it contains essentially the same statistical information as the individual recording files. The database is formed by a combination of the individual recording

files and the statistics file. Together, they provide practical means for assessing data and searching through the large database.

# 3. Summary of appended papers

## 3.1. Declaration of authorship

First of all, it is deemed important to state that PhD candidate Aksel Fenerci did not take part in the planning and installation of the monitoring system. The system was designed mainly by Dr. Ole Øiseth and the installation was done in 2013 by contribution of several PhD candidates, master students and technicians from the Department of Structural Engineering at NTNU. Therefore, the system was already operational when the doctoral study started. The PhD candidate had the primary role in maintenance, control and data handling during the project, together with PhD candidates Knut Andreas Kvåle and Øyvind Wiig Petersen.

PhD candidate Aksel Fenerci is the first author of all the appended papers. In Paper 1, Aksel Fenerci and Ole Øiseth did the planning, where Aksel Fenerci conducted the numerical study and wrote the manuscript with frequent discussion with Ole Øiseth. Both Anders Rønnquist and Ole Øiseth contributed with proof-reading and general suggestions.

In Paper 2, Aksel Fenerci and Ole Øiseth established the framework. Aksel Fenerci conducted the numerical study based on a buffeting response routine written by Ole Øiseth. Aksel Fenerci wrote the manuscript, where Ole Øiseth contributed with suggestions, which improved the overall scientific quality of the paper.

In Papers 3, 4 and 5, Aksel Fenerci did most of the planning, implemented the necessary computational tools and wrote the manuscripts, with close communication with Ole Øiseth, who did the proof-reading and suggested corrections and improvements that lead to better manuscripts.

## 3.2. **Paper 1** [121]

*Fenerci A, Øiseth O, Rønnquist A. Long-term monitoring of wind field characteristics and dynamic response of a long-span suspension bridge in complex terrain. Engineering Structures 2017;147:269–84.*

The first paper presents long-term data of wind characteristics at the bridge site and dynamic response of the bridge deck. The results showed large scatter in both. The relationship of the two are then studied using response surface methodology. Simple wind related parameters such as the mean wind speed, the yaw-angle, turbulence intensities and length scales are used to describe the wind turbulence field. It is seen that the variability observed in the dynamic response is attributable to the variability present in the

wind field to a significant extent. The mean wind speed and the three turbulence parameters are found critically important in describing the wind-induced dynamic response, from the statistical point of view.

### 3.3. **Paper 2** [122]

*Fenerci A, Øiseth O. Measured Buffeting Response of a Long-Span Suspension Bridge Compared with Numerical Predictions Based on Design Wind Spectra. Journal of Structural Engineering (United States) 2017;143.*

Having reached the conclusion that the dynamic response of the HB shows significant variability caused by the variable turbulence filed, it is desired to test how this is reflected into the current design practice, where the turbulence parameters are usually treated in a deterministic manner. Using the N400 [123] (Norwegian guidelines for bridge design) and the basis wind characteristics at the HB site used in design [124], the dynamic response of the HB deck is calculated using multimode buffeting theory in frequency domain. When compared with full-scale measurements, the analytical predictions gave design curves approximately in the middle of the scatter. This means that the design approach is successful in capturing and average of the measured response. However, the scatter in the dynamic response is neglected by the design method due to deterministic treatment of the turbulence characteristics. That way, the design curves get exceeded frequently by measurements. As a conservative and illustrative approach, the analyses are repeated using $95^{th}$ percentiles of turbulence characteristics. The analyses resulted into more satisfactory design curves, encompassing most of the measurement data. Therefore, it is shown that the effect of variability in turbulence parameters can and should be accounted for in the analytical predictions.

### 3.4. **Paper 3** [125]

*Fenerci A, Øiseth O. Evaluation of wind-induced response predictions of a long-span suspension bridge using full-scale measurements. 7th Eur. African Conf. Wind Eng. (EACWE 2017), Liege, Belgium, 2017.*

In the global analyses of papers 1 & 2, it was found that the variability in the turbulence characteristics of HB site should be taken into account for reliable design and buffeting response analysis. However, it is also important to investigate how well the analytical predictions correspond with the measured response. This short paper presents a straight-forward comparison of measured and predicted responses for a 1 hour recording that was taken at the HB site. Intentionally, an exceptionally stationary 1-hour long recording with 14.3 m/s wind speed and steady perpendicular (to the bridge longitudinal axis) wind direction was selected from the database. Comparison of the buffeting response in terms of root-mean-square accelerations along the girder and the corresponding response spectra pointed out significant discrepancies. The vertical response was under-predicted by the analysis, where the torsional response

was highly overestimated. Although the exact reason of the discrepancy could not be pin-pointed, the study shows that the uncertainty is quite high, even when the turbulence field is modeled with maximum possible accuracy and the wind is stationary and perpendicular to the bridge.

### 3.5. Paper 4 [126]

*Fenerci A, Øiseth O. Strong wind characteristics and dynamic response of a long-span suspension bridge during a storm. Journal of Wind Engineering and Industrial Aerodynamics 2018:116–38.*

In this paper, the investigations of the third paper is extended for an entire storm event with a duration of 13.5 hours. Here, it was found that an averaging interval of 1-hour was not appropriate, since nonstationary features were present in wind signals. Using 10-minute averaging intervals, an extensive wind characteristics study is conducted and the measurement results are used to model the turbulence field. The predicted buffeting response is compared with measurements in terms of root-mean-square acceleration and displacement responses. Span-wise non-uniformity of the wind field is also modeled in the analyses. Reasonable predictions for the lateral and the torsional responses were achieved, where the vertical response was again under-predicted. The discrepancies found in papers 3 & 4 indicate that there is also considerable uncertainty in the buffeting response estimates, resulting from sources other than the turbulence modeling. This suggests that improvements on the current methodology or use of more sophisticated methods are needed for more accurate estimations.

### 3.6. Paper 5

*Fenerci A, Øiseth O. Site-specific data-driven probabilistic wind field modeling for wind-induced response prediction of cable-supported bridges. Submitted for journal publication.*

In light of the findings of paper 1 & 2, it is made clear that the variability in the wind field should be taken into account in design and buffeting response predictions carried out for such complex terrain. This implies that a probabilistic turbulence model have to be used instead of the common practice, where the turbulence field is described through deterministic parameters obtained by either averaging the measurements or directly from code recommendations. In this paper, using long-term data from the HB site, the wind turbulence field is modeled using six parameters, which are treated as correlated random variables. The probability distributions and correlation structures of the parameters are established conditional to the mean wind speed and direction. Simulations of the turbulence field are conducted using random number generators and compared with the measurement data through auto-spectra and normalized co-spectra of turbulence. It is founded that the turbulence field at the HB can be modeled probabilistically with the use of six log-normally distributed correlated random variables. Such

a model is suitable to be used in reliability analyses or long term extreme response estimation of the HB against turbulent wind loading.

# 4. Conclusions

Analysis of extensive amount of data on wind field characteristics and bridge accelerations collected from a measurement system installed in the HB showed significant scatter, conflicting the current design approach. The most prominent contribution of this thesis is perhaps the elaborate presentation of this variability, investigation of the effects of turbulence parameters on it and suggestions toward probabilistic modeling of the turbulence field for long-span cable-supported bridges located in complex terrain. In further detail, following conclusions are reached in light of the presented study:

Wind field characteristics in complex terrain

- The wind filed at the HB site exhibits variable turbulence characteristics. In general, the wind is not strictly stationary and not homogenous along the bridge. The turbulence components show reasonably Gaussian behavior, except for the cross-wind component, which is of minor importance in case of a horizontal line-like structure.
- Integral length scale estimates show severe scatter. The estimations are very sensitive to nonstationary features and the estimation method adopted. Therefore, it is recommended that the use of deterministic length scales as design parameters should be avoided when possible.
- For the case of the HB site, a Kaimal-type of formula for the auto-spectra of turbulence components and Davenport's expression for the normalized co-spectra are found satisfactory in modeling the turbulence field. For super long-span bridges, it is likely that Davenport's formula is no more suitable, due to its weakness in modeling low-frequency behavior. In that case, more advanced models, or multiple-parameter expressions have to be used.

Response surface analysis

- Response surface methodology is used to estimate the relationship between wind characteristics at the site and the wind-induced dynamic response of the bridge in a statistical framework. It is found that most of the variability observed in dynamic response roots from the variable turbulence characteristics.
- Response surface analyses allow further elaboration of the underlying relationships between individual turbulence parameters and dynamic response components, and also their interactions with each other.
- The statistical tool is found useful in understanding such complex physical phenomena. However, it should be handled carefully since there is no integral physical model in the analysis. If successfully applied, valuable information about overall uncertainty of the process and sensitivity to different parameters can be extracted. It might also be possible to integrate the

framework in structural health monitoring applications, where identification of unexpected behavior is the ultimate goal.

Buffeting analysis of the HB deck

- Throughout the thesis, buffeting response of the HB deck was calculated several times using the multimode buffeting theory applied in frequency domain. The results indicate considerable discrepancies between measured and predicted responses.
- The aim of the analyses was to apply and test the performance of the common practice; therefore, a study toward improvement of these predictions were not conducted. Calculations and discussions are provided for the buffeting loads on bridge cables and span-wise non-uniform winds are given in the papers.
- The discrepancy is not likely to be due to parameter and model uncertainties in the turbulence model. Large discrepancies are also not expected due to presence of skew winds or nonstationary trends. Since the considered wind speed range is far from flutter conditions, the self-excited forces are thought to be modeled with reasonable accuracy. The investigations of paper 3 also imply that the vertical angle-of-attack cannot explain these discrepancies.
- For better evaluation of the performance of methods and predictions, it is recommended that the effect of nonlinear buffeting forces is established, which requires a time-domain analysis. Better estimations for aerodynamic admittance functions and span-wine correlation of buffeting loads are also needed, which require further wind tunnel testing. Lastly, better estimations of the in-wind modal properties, especially damping, would be useful.

Probabilistic modeling of the turbulence field

- The turbulence field along the HB deck is successfully modeled by a set of log-normally distributed and correlated turbulence parameters.
- The site-specific model represents the wind field with good accuracy in the measurement range.
- If a frequency domain approach is adopted, such a model is fast, easy to use and suitable for use in reliability analyses, performance-based design or long term extreme response analysis.

# 5. Suggestions for future work

- Nonstationary features are captured in some of the wind recordings. Although the strong winds in extra-tropical conditions are rather stationary, the built-up parts of storms seem to accommodate trends in the mean wind speed. Terrain-induced effects are also possible. Therefore, nonstationary analyses should be conducted to test the validity of the stationarity assumption.
- Fast Fourier Transform (FFT) based spectral estimation methods result into large variance in the estimates, which might increase possible signal processing and modeling errors. Parametric spectral estimation methods [127] might offer a practical alternative.
- For a more elaborate study on the buffeting response, more sophisticated analysis techniques may be sought. Inclusion of the effect of skew-winds, vertical angle-of-attack and correct aerodynamic admittance and span-wise correlation of buffeting forces all require extensive wind tunnel testing.
- The effect of the nonlinear buffeting forces can be investigated using time-domain simulations.
- The in-wind modal properties of the bridge should be studied further to better simulate the modal behavior. Especially, accurate modeling of damping is prominent for more satisfactory predictions. If these factors are found to be of critical importance in prediction of the buffeting response, the methods should be standardized to be used in design.
- The probabilistic model derived for the HB site should be tested in frameworks such as reliability analysis and long-term extreme response analysis. Work is also needed toward incorporating these techniques into the design phase, given that the analyses provide satisfactory results.

# 6. References


[1] Xu Y-L. Wind Effects on Cable-Supported Bridges. John Wiley & Sons; 2013.

[2] Diana G, Fiammenghi G, Belloli M, Rocchi D. Wind tunnel tests and numerical approach for long span bridges: The Messina bridge. J Wind Eng Ind Aerodyn 2013;122:38–49. doi:10.1016/j.jweia.2013.07.012.

[3] Lin TY, Chow P. Gibraltar strait crossing-a challenge to bridge and structural engineers. Struct Eng Int 1991;1:53–8.

[4] Larsen A, Larose GL. Dynamic wind effects on suspension and cable-stayed bridges. J Sound Vib 2015;334:2–28. doi:10.1016/j.jsv.2014.06.009.

[5] Miyata T. Historical view of long-span bridge aerodynamics. J Wind Eng Ind Aerodyn 2003;91:1393–410. doi:10.1016/j.jweia.2003.09.033.

[6] Brownjohn JMW. Structural health monitoring of civil infrastructure. Philos Trans R Soc London, Ser A, Math Phys Sci 2007;365:589–622. doi:10.1098/rsta.2006.1925.

[7] Carder D. Observed vibrations of bridges. Bul Seismol Soc Am 1937;27:267–303.

[8] Worden K, Farrar CR, Manson G, Park G. The fundamental axioms of structural health monitoring. Proc R Soc A Math Phys Eng Sci 2007;463:1639–64. doi:10.1098/rspa.2007.1834.

[9] Cunha A, Caetano E, Magalhães F, Moutinho C. Recent perspectives in dynamic testing and monitoring of bridges. Struct Control Heal Monit 2013;20:853–77. doi:10.1002/stc.1516.

[10] Wong K-Y. Instrumentation and health monitoring of cable-supported bridges. Struct Control Heal Monit 2004;11:91–124. doi:10.1002/stc.33.

[11] Brownjohn JMW, Magalhaes F, Caetano E, Cunha A. Ambient vibration re-testing and operational modal analysis of the Humber Bridge. Eng Struct 2010;32:2003–18. doi:10.1016/j.engstruct.2010.02.034.

[12] Carney C, Scullion A, Faulkner P, Carr J. Structural Health Monitoring System installation and use on the Queensferry Crossing. 9th Int. Cable Support. Bridg. Oper. Conf. June 19-22, Halifax, Nov. Scotia, Canada, 2016.

[13] Tanaka H, Davenport AG. Wind-Induced Response of Golden Gate Bridge. J Eng Mech 1983;109:296–312. doi:10.1061/(ASCE)0733-9399(1983)109:1(296).

[14] Abdel-Ghaffar AM, Scanlan RH. Ambient Vibration Studies of Golden Gate Bridge: I. Suspended Structure. J Eng Mech 1985;111(4).

[15] Owen JS, Meng X. Field Monitoring of the Forth Road Bridge. 7th Eur. African Conf. Wind Eng. (EACWE 2017), Liege, Belgium, 2016.

[16] Bas S, Apaydin NM, Ilki A, Catbas FN. Structural health monitoring system of the long-span bridges in Turkey. Struct Infrastruct Eng 2017:1–20. doi:10.1080/15732479.2017.1360365.

[17] Brownjohn JMW, Dumanoglu AA, Severn RT, Blakeborough A. Ambient vibration survey of

the bosporus suspension bridge. Earthq Eng Struct Dyn 1989;18:263–83. doi:10.1002/eqe.4290180210.

[18] Brownjohn JMW, Bocciolone M, Curami A, Falco M, Zasso A. Humber bridge full-scale measurement campaigns 1990-1991. J Wind Eng Ind Aerodyn 1994;52:185–218. doi:10.1016/0167-6105(94)90047-7.

[19] Brownjohn JMW, Dumanoglu AA, Severn RT. Ambient vibration survey of the fatih sultan mehmet (second Bosporus) suspension bridge. Earthq Eng Struct Dyn 1992;21:907–24. doi:10.1002/eqe.4290211005.

[20] Miyata T, Yamada H, Katsuchi H, Kitagawa M. Full-scale measurement of Akashi-Kaikyo Bridge during typhoon. J Wind Eng Ind Aerodyn 2002;90:1517–27. doi:10.1016/S0167-6105(02)00267-2.

[21] Sumitoro S, Matsui Y, Kono M, Okamoto T, Fujii K. Long span bridge health monitoring system in Japan. 6th Annu Int Symp NDE Heal Monit Diagnostics 2001;4337:517–24. doi:10.1117/12.435628.

[22] Macdonald JHG, Dagless EL, Thomas BT. Dynamic measurements of the Second Severn Crossing. Proc Instn Civ Engrs, Transp 1997;123:241–8.

[23] Xu YL, Zhu LD, Wong KY, Chan KWY. Field measurement results of Tsing Ma suspension bridge during typhoon Victor. Struct Eng Mech 2001;10:545–59.

[24] Larsen A, Esdahl S., Jacob Anderson, Vejrum T. Storebælt Suspension Bridge-Vortex Shedding Excitation and Mitigation by Guide Vanes. J Wind Eng Ind Aerodyn 2000;88:283–96.

[25] Zhou HF, Ni YQ, Ko JM. Structural health monitoring of the Jiangyin Bridge: system upgrade and data analysis. Smart Struct Syst 2013;11:637–62. doi:10.12989/sss.2013.11.6.637.

[26] Wang H, Li A, Guo T, Tao T. Establishment and Application of the Wind and Structural Health Monitoring System for the Runyang Yangtze River Bridge. Shock Vib 2014;2014:1–15. doi:10.1155/2014/421038.

[27] Wang H, Li A, Guo T, Xie J. Field measurement on wind characteristic and buffeting response of the Runyang Suspension Bridge during typhoon Matsa 2009;52:1354–62. doi:10.1007/s11431-008-0238-y.

[28] Wang H, Wu T, Tao T, Li A, Kareem A. Measurements and analysis of non-stationary wind characteristics at Sutong Bridge in Typhoon Damrey. J Wind Eng Ind Aerodyn 2016;151:100–6. doi:10.1016/j.jweia.2016.02.001.

[29] Hui MCH, Larsen A, Xiang HF. Wind turbulence characteristics study at the Stonecutters Bridge site: Part I-Mean wind and turbulence intensities. J Wind Eng Ind Aerodyn 2009;97:22–36. doi:10.1016/j.jweia.2008.11.002.

[30] Hui MCH, Larsen A, Xiang HF. Wind turbulence characteristics study at the Stonecutters Bridge site: Part II: Wind power spectra, integral length scales and coherences. J Wind Eng Ind Aerodyn 2009;97:48–59. doi:10.1016/j.jweia.2008.11.003.

[31] Liu M, Liao H, Li M, Ma C, Yu M. Long-term field measurement and analysis of the natural wind characteristics at the site of Xi-hou-men Bridge. J Zhejiang Univ Sci A 2012;13:197–207. doi:10.1631/jzus.A1100178.

[32] Syrkov A V., Krutikov O V. Lifecycle optimization for Vladivostok-Russky isle bridge by means of risk analysis and monitoring. Autom Remote Control 2014;75:2217–24. doi:10.1134/S000511791412011X.

[33] Fenerci A, Øiseth O, Rønnquist A. Long-term monitoring of wind field characteristics and dynamic response of a long-span suspension bridge in complex terrain. Eng Struct 2017;147:269–84. doi:10.1016/j.engstruct.2017.05.070.

[34] Davenport AG. Buffeting of a suspension bridge by storm winds. J Struct Div 1962;88:233–68. doi:10.4319/lo.2013.58.2.0489.

[35] Davenport AG. The application of statistical concepts to the wind loading of structures. Proc Inst Civ Eng Struct Build 1961;19:449–72.

[36] Davenport AG. Response of Slender Line Like Structures to a Gusty Wind. Inst Civ Engrs, Proc 1963;23:389–408.

[37] Wirsching PH, Paez TL, Ortiz K. Random Vibrations: Theory and Practice. Dover Publications; 2006.

[38] Scanlan RH, Tomko JJ. Airfoil and Bridges Deck Flutter Derivatives. J Eng Mech Div 1971;97:1717–37.

[39] Scanlan RH. The action of flexible bridges under wind, II: Buffeting theory. J Sound Vib 1978;60:187–99. doi:10.1016/S0022-460X(78)80029-7.

[40] Lin YK, Yang JN. Multimode Bridge Response to Wind Excitations. J Eng Mech 1983;109:586–603. doi:10.1061/(ASCE)0733-9399(1983)109:2(586).

[41] Chen X. Analysis of multimode coupled buffeting response of long-span bridges to nonstationary winds with force parameters from stationary wind. J Struct Eng (United States) 2015;141:1–14. doi:10.1061/(ASCE)ST.1943-541X.0001078.

[42] Chen X, Kareem A, Matsumoto M. Multimode coupled flutter and buffeting analysis of long span bridges. J Wind Eng Ind Aerodyn 2001;89:649–64. doi:10.1016/S0167-6105(01)00064-2.

[43] Jain A, Jones NP, Scanlan RH. Coupled Flutter and Buffeting Analysis of Long-Span Bridges. J Struct Eng 1996;122:716–25. doi:10.1061/(ASCE)0733-9445(1996)122:7(716).

[44] Katsuchi H, Jones NP, Scanlan RH, Akiyama H. Multi-mode flutter and buffeting analysis of the Akashi-Kaikyo bridge. J Wind Eng Ind Aerodyn 1998;77–78:431–41. doi:10.1016/S0167-6105(98)00162-7.

[45] Øiseth O, Rönnquist A, Sigbjørnsson R. Simplified prediction of wind-induced response and stability limit of slender long-span suspension bridges, based on modified quasi-steady theory: A case study. J Wind Eng Ind Aerodyn 2010;98:730–41. doi:10.1016/j.jweia.2010.06.009.

[46] Costa C, Borri C, Flamand O, Grillaud G. Time-domain buffeting simulations for wind-bridge

interaction. J Wind Eng Ind Aerodyn 2007;95:991–1006. doi:10.1016/j.jweia.2007.01.026.

[47] Caracoglia L, Jones NP. Time domain vs. frequency domain characterization of aeroelastic forces for bridge deck sections. J Wind Eng Ind Aerodyn 2003;91:371–402. doi:10.1016/S0167-6105(02)00399-9.

[48] Øiseth O, Rönnquist A, Sigbjörnsson R. Time domain modeling of self-excited aerodynamic forces for cable-supported bridges: A comparative study. Comput Struct 2011;89:1306–22. doi:10.1016/j.compstruc.2011.03.017.

[49] Petrini F, Giuliano F, Bontempi F. Comparison of time domain techniques for the evaluation of the response and the stability in long span suspension bridges. Comput Struct 2007;85:1032–48. doi:http://dx.doi.org/10.1016/j.compstruc.2006.11.015.

[50] Chen X, Matsumoto M, Kareem A. Time Domain Flutter and Buffeting Response Analysis of Bridges. J Eng Mech 2000;126:7–16. doi:10.1061/(ASCE)0733-9399(2000)126:1(7).

[51] Zhu LD, Xu YL. Buffeting response of long-span cable-supported bridges under skew winds . Part 1 : theory. J Sound Vib 2005;281:647–73. doi:10.1016/j.jsv.2004.01.026.

[52] Xu YL, Zhu LD, Xiang HF. Buffeting response of long suspension bridges to skew winds. Wind Struct An Int J 2003;6:179–96. doi:10.1296/WAS2003.06.03.01.

[53] Xu YL, Zhu LD. Buffeting response of long-span cable-supported bridges under skew winds. Part 2: case study. J Sound Vib 2005;281:675–97. doi:10.1016/j.jsv.2004.01.025.

[54] Xu YL, Sun DK, Ko JM, Lin JH. Buffeting analysis of long span bridges: a new algorithm. Comput Struct 1998;68:303–13. doi:10.1016/S0045-7949(98)00072-8.

[55] Zhu L. Buffeting response of long span cable-supported bridges under skew winds: field measurement and analysis 2002.

[56] Li Y, Hu P, Xu X, Qiu J. Wind characteristics at bridge site in a deep-cutting gorge by wind tunnel test. J Wind Eng Ind Aerodyn 2017;160:30–46. doi:10.1016/j.jweia.2016.11.002.

[57] Hu L, Xu Y-L, Zhu Q, Guo A, Kareem A. Tropical Storm–Induced Buffeting Response of Long-Span Bridges: Enhanced Nonstationary Buffeting Force Model. J Struct Eng 2017. doi:http://dx.doi.org/10.1061/(ASCE)ST.1943-541X.0001745#sthash.NxH6qIhi.dpuf.

[58] Fenerci A, Øiseth O. Strong wind characteristics and dynamic response of a long-span suspension bridge during a storm. J Wind Eng Ind Aerodyn 2018:116–38. doi:10.1016/j.jweia.2017.10.030.

[59] Zhang X. Influence of some factors on the aerodynamic behavior of long-span suspension bridges. J Wind Eng Ind Aerodyn 2007;95:149–64. doi:10.1016/j.jweia.2006.08.003.

[60] Hu L, Xu Y-L. Extreme value of typhoon-induced non-stationary buffeting response of long-span bridges. Probabilistic Eng Mech 2014;36:19–27. doi:10.1016/j.probengmech.2014.02.002.

[61] Hu L, Xu Y-L, Huang W-F. Typhoon-induced non-stationary buffeting response of long-span bridges in complex terrain. Eng Struct 2013;57:406–15. doi:http://dx.doi.org/10.1016/j.engstruct.2013.09.044.

[62] Siedziako B, Øiseth O, Rønnquist A. An enhanced forced vibration rig for wind tunnel testing of bridge deck section models in arbitrary motion. J Wind Eng Ind Aerodyn 2017;164:152–63. doi:10.1016/j.jweia.2017.02.011.

[63] Larose GL, Mann J. Gust loading on streamlined bridge decks. J Fluids Struct 1998;12:511–36.

[64] ESDU 086010. Characteristics of atmospheric turbulence near the ground Part 3: variations in space and time for strong winds (neutral atmosphere). 2008th ed. London: ESDU International plc; 2001.

[65] Panofsky HA, McCormick RA. The spectrum of vertical velocity near the surface. Q J R Meteorol Soc 1960;86:495–503. doi:10.1002/qj.49708637006.

[66] Davenport AG. The spectrum of horizontal gustiness near the ground in high winds. Q J R Meteorol Soc 1961;87:194–211. doi:10.1002/qj.49708737208.

[67] von Karman T. Progress in the statistical theory of turbulence. Proc Natl Acad Sci U S A 1948;34:530–9. doi:10.1073/pnas.34.11.530.

[68] Busch NE, Panofsky HA. Recent spectra of atmospheric turbulence. Q J R Meteorol Soc 1968;94:132–48. doi:10.1002/qj.49709440003.

[69] Panofsky HA, Tennekes H, Lenschow DH, Wyngaard JC. The characteristics of turbulent velocity components in the surface layer under convective conditions. Boundary-Layer Meteorol 1977;11:355–61. doi:10.1007/BF02186086.

[70] Teunissen HW. Structure of mean winds and turbulence in the planetary boundary layer over rural terrain. Boundary-Layer Meteorol 1980;19:187–221. doi:10.1007/BF00117220.

[71] Panofsky HA, Larko D, Lipschutz R, Stone G, Bradley EF, Bowen AJ, et al. Spectra of velocity components over complex terrain. Q J R Meteorol Soc 1982;108:215–30. doi:10.1002/qj.49710845513.

[72] Simiu E, Scanlan RH. Winds Effects on Structures: Fundamentals and Applications to Design. 3rd ed. Wiley; 1996.

[73] Tieleman HW. Universality of velocity spectra. J Wind Eng Ind Aerodyn 1995;56:55–69. doi:10.1016/0167-6105(94)00011-2.

[74] Tieleman HW. Wind characteristics in the surface layer over heterogeneous terrain. J Wind Eng Ind Aerodyn 1992;41:329–40. doi:10.1016/0167-6105(92)90427-C.

[75] Mann J. The spatial structure of neutral atmospheric surface-layer turbulence. J Fluid Mech 1994;273:141. doi:10.1017/S0022112094001886.

[76] Olesen HR, Larsen SE, Højstrup J. Modelling velocity spectra in the lower part of the planetary boundary layer. Boundary-Layer Meteorol 1984;29:285–312. doi:10.1007/BF00119794.

[77] Naito G. Spatial structure of surface wind over the ocean. J Wind Eng Ind Aerodyn 1983;13:67–76. doi:10.1016/0167-6105(83)90129-0.

[78] Kristensen L, Jensen NO. Lateral coherence in isotropic turbulence and in the natural wind. Boundary-Layer Meteorol 1979;17:353–73. doi:10.1007/BF00117924.

[79] Kristensen L, Panofsky HA, Smith SD. Lateral coherence of longitudinal wind components in strong winds. Boundary-Layer Meteorol 1981;21:199–205. doi:10.1007/BF02033937.

[80] Krenk S. Wind Field Coherence And Dynamic Wind Forces. In: Naess A, Krenk S, editors. IUTAM Symp. Adv. Nonlinear Stoch. Mech. Proc. IUTAM Symp. held Trondheim, Norway, 3--7 July 1995, Dordrecht: Springer Netherlands; 1996, p. 269–78. doi:10.1007/978-94-009-0321-0_25.

[81] Mann J. The spectral velocity tensor in moderately complex terrain. J Wind Eng Ind Aerodyn 2000;88:153–69. doi:https://doi.org/10.1016/S0167-6105(00)00046-5.

[82] Solari G. Turbulence Modeling for Gust Loading. J Struct Eng 1987;113:1550–69. doi:10.1061/(ASCE)0733-9445(1987)113:7(1550).

[83] Solari G, Piccardo G. Probabilistic 3-D turbulence modeling for gust buffeting of structures. Probabilistic Eng Mech 2001;16:73–86. doi:10.1016/S0266-8920(00)00010-2.

[84] ESDU 85020. Characteristics of atmospheric turbulence near groud Part 2: signle point data for strong winds (neutral atmosphere). London: ESDU International plc; 2001.

[85] Davenport AG. The Spectrum of Horizontal Gustiness Near the Ground in High Winds. J R Meteorol Soc 1961;87:194–211.

[86] Tennekes H, Lumley JL. A First Course in Turbulence. Cambridge: The MIT Press; 1999.

[87] Kristensen L, Jensen NO. Lateral coherence in isotropic turbulence and in the natural wind. Boundary-Layer Meteorol 1979;17:353–73. doi:10.1007/BF00117924.

[88] Cheynet E, Jakobsen JB, Snæbjørnsson J. Buffeting response of a suspension bridge in complex terrain. Eng Struct 2016;128:474–87. doi:10.1016/j.engstruct.2016.09.060.

[89] Chen J, Hui MCH, Xu YL. A comparative study of stationary and non-stationary wind models using field measurements. Boundary-Layer Meteorol 2007;122:105–21. doi:10.1007/s10546-006-9085-1.

[90] Hui MCH, Larsen A, Xiang HF. Wind turbulence characteristics study at the Stonecutters Bridge site: Part II: Wind power spectra, integral length scales and coherences. J Wind Eng Ind Aerodyn 2009;97:48–59. doi:10.1016/j.jweia.2008.11.003.

[91] Hui MCH, Larsen A, Xiang HF. Wind turbulence characteristics study at the Stonecutters Bridge site: Part I-Mean wind and turbulence intensities. J Wind Eng Ind Aerodyn 2009;97:22–36. doi:10.1016/j.jweia.2008.11.002.

[92] Wang H, Li A, Niu J, Zong Z, Li J. Long-term monitoring of wind characteristics at Sutong Bridge site. J Wind Eng Ind Aerodyn 2013;115:39–47. doi:10.1016/j.jweia.2013.01.006.

[93] Tao T, Asce SM, Wang H, Asce M, Wu T, Asce AM. Comparative Study of the Wind Characteristics of a Strong Wind Event Based on Stationary and Nonstationary Models. J Struct Eng 2015:1–16. doi:10.1061/(ASCE)ST.1943-541X.0001725.

[94] Wang H, Guo T, Tao T-Y, Li A-Q. Study on Wind Characteristics of Runyang Suspension Bridge Based on Long-Term Monitored Data. Int J Struct Stab Dyn 2015;16:1640019.

doi:10.1142/S0219455416400198.

[95] Yang D-H, Yi T-H, Li H-N, Zhang Y-F. Monitoring-based analysis of the static and dynamic characteristic of wind actions for long-span cable-stayed bridge. J Civ Struct Heal Monit 2017:1–11. doi:10.1007/s13349-017-0257-0.

[96] Ye XW, Xi PS, Su YH. Analysis of non-stationary wind characteristics at an arch bridge using structural health monitoring data. J Civ Struct Heal Monit 2017;7:573–87. doi:10.1007/s13349-017-0244-5.

[97] He X, Qin H, Tao T, Liu W, Wang H. Measurement of Non-Stationary Characteristics of a Landfall Typhoon at the Jiangyin Bridge Site. Sensors 2017;17:2186. doi:10.3390/s17102186.

[98] Davenport AG. The relationship of reliability to wind loading. J Wind Eng Ind Aerodyn 1983;13:3–27. doi:https://doi.org/10.1016/0167-6105(83)90125-3.

[99] Zhang L, Li J, Peng Y. Dynamic response and reliability analysis of tall buildings subject to wind loading. J Wind Eng Ind Aerodyn 2008;96:25–40. doi:https://doi.org/10.1016/j.jweia.2007.03.001.

[100] Davenport AG. On the assessment of the reliability of wind loading on low buildings. J Wind Eng Ind Aerodyn 1983;11:21–37. doi:10.1016/0167-6105(83)90088-0.

[101] Pagnini L. Reliability analysis of wind-excited structures. J Wind Eng Ind Aerodyn 2010;98:1–9. doi:https://doi.org/10.1016/j.jweia.2009.08.010.

[102] Su C, Chen X, Luor J. Buffeting reliability of bridges with structural uncertainties 2014:30–42. doi:10.1680/bren.12.00024.

[103] Pourzeynali S, Datta TK. Reliability Analysis of Suspension Bridges against Fatigue Failure from the Gusting of Wind. J Bridg Eng 2005;10:262–71. doi:10.1061/(ASCE)1084-0702(2005)10:3(262).

[104] Minciarelli F, Gioffrè M, Grigoriu M, Simiu E. Estimates of extreme wind effects and wind load factors: influence of knowledge uncertainties. Probabilistic Eng Mech 2001;16:331–40. doi:https://doi.org/10.1016/S0266-8920(01)00024-8.

[105] Solari G. Wind-excited response of structures with uncertain parameters. Probabilistic Eng Mech 1997;12:75–87. doi:10.1016/S0266-8920(96)00027-6.

[106] Caracoglia L. Influence of uncertainty in selected aerodynamic and structural parameters on the buffeting response of long-span bridges. J Wind Eng Ind Aerodyn 2008;96:327–44. doi:10.1016/j.jweia.2007.08.001.

[107] Mannini C, Bartoli G. Aerodynamic uncertainty propagation in bridge flutter analysis. Struct Saf 2015;52:29–39. doi:10.1016/j.strusafe.2014.07.005.

[108] Kareem A. Aerodynamic response of structures with parametric uncertainties. Struct Saf 1988;5:205–25. doi:10.1016/0167-4730(88)90010-0.

[109] Spence SMJ, Kareem A. Performance-based design and optimization of uncertain wind-excited dynamic building systems. Eng Struct 2014;78:133–44.

doi:https://doi.org/10.1016/j.engstruct.2014.07.026.

[110] Ciampoli M, Petrini F, Augusti G. Performance-Based Wind Engineering: Towards a general procedure. Struct Saf 2011;33:367–78. doi:https://doi.org/10.1016/j.strusafe.2011.07.001.

[111] Smith MA, Caracoglia L. A Monte Carlo based method for the dynamic "fragility analysis" of tall buildings under turbulent wind loading. Eng Struct 2011;33:410–20. doi:10.1016/j.engstruct.2010.10.024.

[112] Li Y, Ellingwood BR. Hurricane damage to residential construction in the US: Importance of uncertainty modeling in risk assessment. Eng Struct 2006;28:1009–18. doi:10.1016/j.engstruct.2005.11.005.

[113] Seo DW, Caracoglia L. Statistical buffeting response of flexible bridges influenced by errors in aeroelastic loading estimation. J Wind Eng Ind Aerodyn 2012;104–106:129–40. doi:10.1016/j.jweia.2012.03.036.

[114] Giske F-IG, Leira BJ, Øiseth O. Full long-term extreme response analysis of marine structures using inverse FORM. Probabilistic Eng Mech 2017;50:1–8. doi:https://doi.org/10.1016/j.probengmech.2017.10.007.

[115] Xu Y, Øiseth O, Naess A, Moan T. Prediction of long-term extreme load effects due to wind for cable-supported bridges using time-domain simulations. Eng Struct 2017;148:239–53. doi:10.1016/j.engstruct.2017.06.051.

[116] Petersen ØW, Øiseth O. Finite element model updating of a long span suspension bridge. Int. Conf. Earthq. Eng. Struct. Dyn. Reykjavik, Icel., 2017.

[117] Cantero D, Øiseth O, Rønnquist A. Indirect monitoring of vortex-induced vibration of suspension bridge hangers. Struct Heal Monit 2017:1475921717721873. doi:10.1177/1475921717721873.

[118] Kvåle KA, Øiseth O. Structural monitoring of an end-supported pontoon bridge. Mar Struct 2017;52:188–207. doi:https://doi.org/10.1016/j.marstruc.2016.12.004.

[119] The Mathworks Inc. MATLAB (R2015a). MathWorks Inc 2015. doi:10.1007/s10766-008-0082-5.

[120] Python Software Foundation. Python Language Reference, version 2.7. Python Softw Found 2013. doi:https://www.python.org/.

[121] Fenerci A, Øiseth O, Rønnquist A. Long-term monitoring of wind field characteristics and dynamic response of a long-span suspension bridge in complex terrain. Eng Struct 2017;147. doi:10.1016/j.engstruct.2017.05.070.

[122] Fenerci A, Øiseth O. Measured Buffeting Response of a Long-Span Suspension Bridge Compared with Numerical Predictions Based on Design Wind Spectra. J Struct Eng (United States) 2017;143. doi:10.1061/(ASCE)ST.1943-541X.0001873.

[123] Statens-Vegvesen. N400 Handbook for bridge design. 2009.

[124] Statens-Vegvesen. The Hardanger Bridge design basis - wind characteristics. 2006.

[125] Fenerci A, Øiseth O. Strong wind characteristics and dynamic response of a long-span suspension bridge during a storm. J Wind Eng Ind Aerodyn 2018;172:116–38.

[126] Fenerci A, Øiseth O. Evaluation of wind-induced response predictions of a long-span suspension bridge using full-scale measurements. 7th Eur. African Conf. Wind Eng. (EACWE 2017), Liege, Belgium, 2017.

[127] Kay SM. Modern Spectral Estimation: Theory and Application. Michigan, USA: PTR Prentice Hall; 1988.

# Paper I

Aksel Fenerci, Ole Øiseth, Anders Rønnquist

*Long-term monitoring of wind field characteristics and dynamic response of a long-span suspension bridge in complex terrain*

*Engineering Structures 2017;147:269–84*

Engineering Structures 147 (2017) 269–284

Contents lists available at ScienceDirect

Engineering Structures

journal homepage: www.elsevier.com/locate/engstruct

# Long-term monitoring of wind field characteristics and dynamic response of a long-span suspension bridge in complex terrain

Aksel Fenerci *, Ole Øiseth, Anders Rønnquist

*Department of Structural Engineering, Norwegian University of Science and Technology, Trondheim, Norway*

ARTICLE INFO

*Article history:*
Received 18 August 2016
Revised 4 May 2017
Accepted 8 May 2017

*Keywords:*
Suspension bridge
Bridge monitoring
Field measurement
Wind characteristics
Response surface methodology
Complex terrain
Bridge dynamic response

ABSTRACT

Long-term monitoring data of wind velocities and accelerations on the Hardanger Bridge are used to investigate the relationship between the wind-loading and response processes. The extensive measurement system consisting of 20 accelerometers and 9 anemometers is described as well as the local topography of the site. The wind and response characteristics are presented using scatter plots and wind rose diagrams. The considerable variability observed in the bridge dynamic response is investigated by utilizing response surface methodology. Simple parameters of the wind field are selected as the predictor variables in the analyses. The variability in response is attributed to the variable wind field, and the effects of the significant parameters on the response are presented in a statistical framework. The agreement of the findings with previous considerations and the implications on the design of long-span suspension bridges are discussed.



## 1. Introduction

The Norwegian Public Roads Administration (NPRA) is currently seeking solutions to replace several ferry connections along Norway's coastal highway E39 with road transportation. The extraordinary terrain typical of the west coast of Norway, famous for its fjords and tall mountains, requires crossing straits up to 5 km long and 2 km deep, which manifests a challenging task for bridge engineers. The growing demand for longer suspension bridges around the world calls for relatively lighter and slenderer bridge structures, which will be prone to excessive wind excitation. To this day, many bridges exhibited unexpected behavior due to different wind-related phenomena, such as flutter [1], vortex shedding [2] and excessive cable vibrations [1,3], which revealed gaps in the knowledge of loading mechanisms on such structures. To diagnose and minimize these unexpected effects, monitoring of existing structures and analysis of field data are deemed essential [4].

Accurate prediction of wind-induced response of suspension bridges is vitally important for reliable design and assessment of such structures. Predicting the dynamic response, however, accommodates uncertainties due to many sources, including the modeling of gust loading. Following the work of Davenport [5], the dynamic load effects caused by atmospheric turbulence are traditionally described using power spectral densities (PSDs) and coherences of turbulence [6–9]. Consequently, several expressions have been suggested for the spectral densities over the years [6,10,11], which in general depend on basic parameters of the wind field. The results of the recent bridge monitoring efforts [12–16] reveal that the wind field characteristics exhibit variability from site to site. Therefore, the spectral expressions need to be adjusted for the site in question using field measurements [13,17]. The site-specific spectra are generally deduced from single events such as typhoons or averaged over a number of recordings. However, neither approach seems to reflect the actual variability of the wind field present at the particular site, making it difficult to establish design spectra, even for a specific site. Solari and Piccardo [18] presented a collection of wind field statistics taken from field measurement results in the literature. The variability of the results presented by [18], as well as the random and site-dependent nature of wind loading on suspension bridges, encourage a probabilistic description of the wind field [19–21].

The field measurement results of wind statistics and structural responses were reported by several researchers as the outcomes of large measurement campaigns to investigate the effect of wind loading on bridge response and modal properties [4,14,22–24] or to verify numerical simulations [17,25–27]. The studies showed that reasonable predictions of dynamic response can be achieved using the measured turbulence spectra. Other works showed that the spectra can accommodate significant uncertainty and that

* Corresponding author.
*E-mail address:* aksel.fenerci@ntnu.no (A. Fenerci).

http://dx.doi.org/10.1016/j.engstruct.2017.05.070
0141-0296/

the selection can significantly influence the response estimations [9,28].

In complex terrain, the wind field is expected to be variable and not homogenous. However, modeling the wind field using state-of-the-art methods will not reflect this variability in the dynamic response predictions. Consequently, safety concerns may arise when designing very long suspension bridges. The present study aims to put forth the actual relationship between wind and the response parameters of a long-span suspension bridge located in complex terrain using long-term field data. The thorough analysis of wind field parameters and their effects on the dynamic response will provide insight into the uncertainties involved in wind field modeling and response prediction. For this purpose, field measurement results are presented from an extensive monitoring system installed on the Hardanger Bridge in Norway. The wind and response characteristics for the measurement period are presented. The influence of the wind field on the dynamic response is studied in a statistical framework, using response surface methodology (RSM) with basic wind-related parameters from measurements. The significance of the parameters is assessed using hypothesis testing techniques. Finally, the effects of the significant wind field parameters are presented in the form of two-dimensional surface plots.

## 2. The Hardanger Bridge and its surroundings

The Hardanger Bridge (Fig. 1) crosses the Hardangerfjord in Hordaland county of Norway, connecting the small towns of Bu and Vallavik (Fig. 2). Since its completion in 2013, it remains the longest suspension bridge in Norway with its slender main span of 1310 m. The bridge deck has a well-streamlined box shape and guide vanes were installed underneath the deck to mitigate vortex-induced vibrations. The bridge girder is 18.5 meters wide and 3.2 meters high, supporting two traffic lanes and a bicycle lane, making the bridge exceptionally slender compared to existing structures with similar scales. The bridge direction deviates approximately 25° from the north-south direction, towards the west, perpendicular to the fjord. The bridge is surrounded by steep mountains (1000–1500 m high) to the north and the south. The view of the surrounding fjords and mountains is shown Fig. 3.

The dynamic characteristics of the Hardanger Bridge, namely its natural frequencies and mode shapes are extracted from a finite element (FE) model of the bridge through eigenvalue analysis. The FE model was provided by NPRA. According to the analysis, the first lateral symmetric mode occurs at 0.05 Hz, followed by an antisymmetric lateral mode at 0.098 Hz. The first vertical asymmetric and symmetric frequencies of the structure were calculated as 0.11 Hz and 0.14 Hz, respectively. The first torsional vibration frequency was 0.36 Hz. The fundamental frequencies of the structure under 16 m/s wind were also identified by [29], using Operational Modal Analysis (OMA). The results were similar to the FE analysis.

## 3. The measurement system

The Hardanger Bridge was instrumented with an extensive monitoring system after its completion to measure the wind veloc-

**Fig. 1.** The Hardanger Bridge.

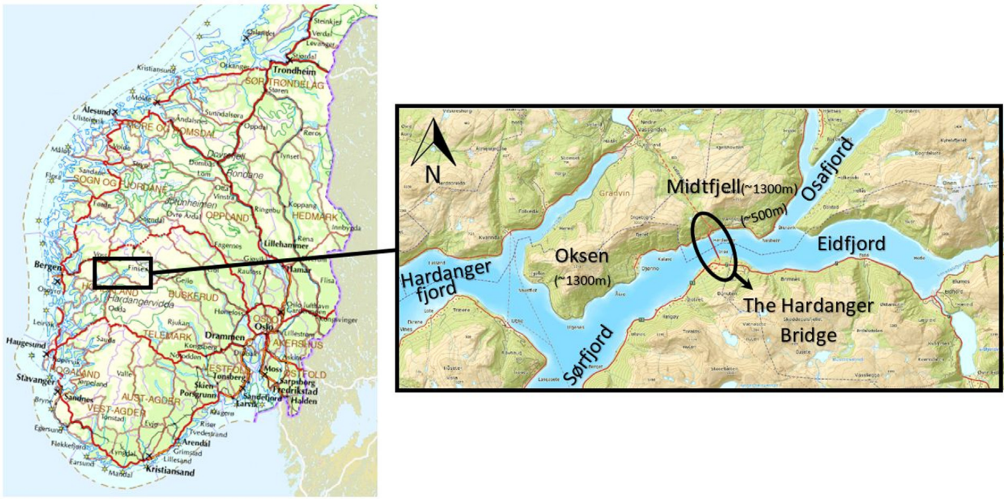


**Fig. 2.** Location and local topography (map images from Kartverket©).

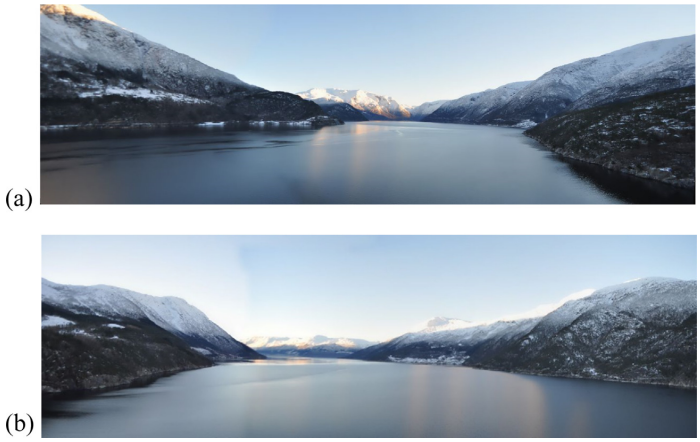


**Fig. 3.** View from the Hardanger Bridge (a) towards the east and (b) towards the west.

ities and dynamic excitation at several locations on the bridge girder and the bridge towers. The monitoring system is shown in Fig. 4 on a scale drawing of the Hardanger Bridge. The sensor network consists of 9 sonic anemometers and 20 triaxial accelerometers. WindMaster Pro 3D anemometers were used to measure the wind speeds; these are robust triaxial ultrasonic anemometers capable of measuring wind gusts up to 65 m/s. CUSP-3D series strong motion accelerometers with a ±4 g measurement range were used for the acceleration measurements. The names and coordinates of all the sensors are listed in Table 1; the midspan of the bridge was selected as the origin of the coordinate system. 16 of the accelerometers are located inside the bridge girder, attached on bulkheads on both sides of the girder to capture the torsional motion, while the remaining 4 are located inside the bridge towers. Anemometers A1-8 are attached to bridge hangers at a height of 8 meters above the girder, except for one anemometer (A6) that is attached to a light pole at the midspan. As shown by the sensor layout presented in Fig. 4, the accelerometers were distributed uniformly along the bridge girder, whereas the anemometers were unevenly distributed. This layout was intentionally selected to extract more information about the spatial structure of the wind field at the site. The final anemometer (A9) is located at the top of the Vallavik (North) Tower.

Each sensor is connected to a datalogger unit, where the data are recorded locally, then the data are transferred to a main datalogger located at the top of the Vallavik Tower (Fig. 4) by wireless communication. A CUSP-Me series recorder was used for the main datalogger, while the other dataloggers were of type CUSP-Ms. Both types are suitable for working with a variety of different sensors. The time synchronization of the data was ensured by using

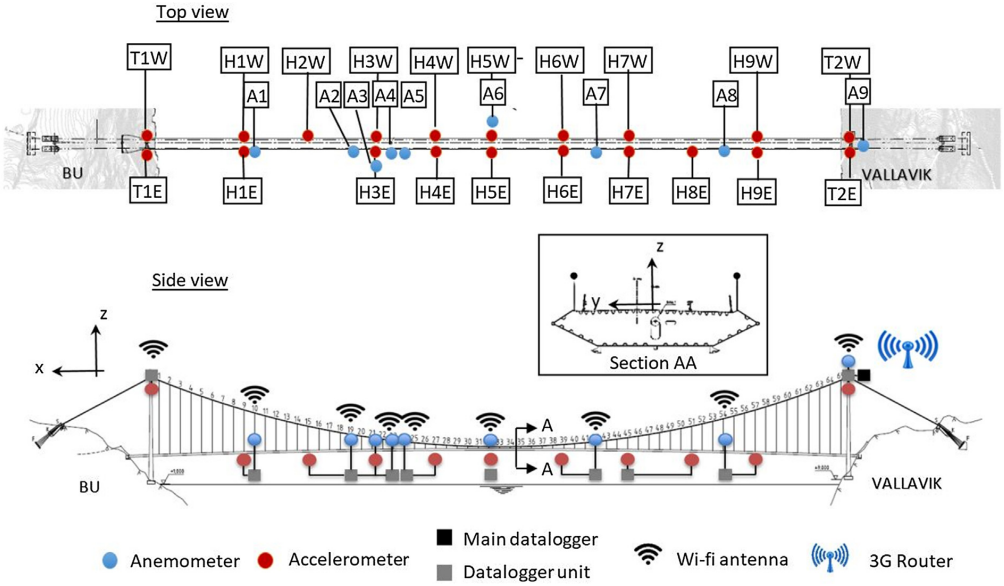


**Fig. 4.** The measurement system.

**Table 1**
Sensor names and coordinates.

| Wind sensors | | | | Accelerometers | | | |
|---|---|---|---|---|---|---|---|
| Name | x (m) | y (m) | z (m) | Name | x (m) | y (m) | z (m) |
| A1 | 460 | 7.25 | 0.3 | H1E/H1 W | 480 | 6.33/−6.64 | −8.38 |
| A2 | 280 | 7.25 | 3.2 | H2 W | 360 | −6.64 | −6.41 |
| A3 | 240 | 7.25 | 3.9 | H3E/H3 W | 240 | 6.33/−6.64 | −4.45 |
| A4 | 200 | 7.25 | 4.6 | H4E/H4 W | 120 | 6.33/−6.64 | −2.48 |
| A5 | 180 | 7.25 | 4.9 | H5E/H5 W | −7 | 6.33/−6.64 | −0.4 |
| A6 | −10 | −7.25 | 8 | H6E/H6 W | −120 | 6.33/−6.64 | −2.25 |
| A7 | −180 | 7.25 | 5.2 | H7E/H7 W | −240 | 6.33/−6.64 | −4.22 |
| A8 | −420 | 7.25 | 1.2 | H8E | −360 | 6.33 | −6.18 |
| A9 | −655 | 4.5 | 140 | H9E/H9 W | −480 | 6.33/−6.64 | −8.15 |
| | | | | T1E/T1 W | 655 | 4.5/−4.5 | 120.5 |
| | | | | T2E/T2 W | −655 | 4.5/−4.5 | 120.5 |

GPS time. The data collected at the main logger unit are then transferred to servers at the Norwegian University of Science and Technology (NTNU) via an internet connection and are stored there. Pictures of sensors are shown in Fig. 5.

The wind velocities and accelerations at the Hardanger Bridge site were recorded starting from December 2013, and the monitoring campaign is still ongoing. This study considers recordings from December 2013 to March 2016, corresponding to a total of 28 months. During this period, the sensors were operational; however, the data were only stored after a triggering wind speed of 15 m/s was exceeded in any of the wind sensors. After the system was triggered, the accelerations and wind velocities were recorded for a duration of 30 min. The system was also triggered manually several times in a random manner during this period, to include recordings with lower wind speeds in the dataset. The dataset which will be used throughout the rest of the paper consists of 9590 10-min long recordings. A histogram showing the distribution of recordings according to the mean wind velocity is given in Fig. 6.

## 4. Wind characteristics

### 4.1. Data handling

The wind velocities at the Hardanger Bridge site were recorded in polar coordinates with a sampling frequency of 32 Hz using the nine anemometers mentioned above. The wind data were then resampled to 20 Hz and decomposed into static (mean wind velocity, U) and dynamic (wind velocity fluctuations) components considering a 10-min averaging interval, where the wind process was assumed to be stationary [6,8]. The three wind velocity fluctuations are referred as the along-wind (u), cross-wind (v) and vertical (w) turbulence components. All the one-point statistics used to characterize the wind field are calculated using the wind measurements at the midspan (sensor A6).

Sample time series of the turbulence components and wind direction are given in Fig. 7 for a 10-min interval, which was recorded on January 12, 2015, starting at 17.43 local time. The turbulence spectra of the along-wind and the vertical components are estimated using the same 10-min recording. Welch spectral estimation method is used with 8 data segments with 50% overlap. A Hamming window is applied to each segment prior to averaging. The respective von Karman spectra [11] are also calculated and both spectra are given in Fig. 8 to present the diversity of the spectral shapes. It is observed that the von Karman spectra represents the along-wind turbulence reasonably well, where some discrepancies are present for the vertical turbulence. The measured vertical turbulence is rather flat in the 0.1–1 Hz frequency range, which is observed commonly in the rest of the database; however, the slope of the two spectra agrees for higher frequencies. To avoid any disturbance of the wind flow due to the presence of the bridge deck and the vehicles on travelling on it, the anemometers were installed 8 meters above the deck. It is also important to ensure that the wind speed measurements are not affected by the structural vibrations of the bridge deck. Any such effect would be detectable as peaks on the wind spectra at the locations of the natural frequencies of the bridge. Looking at the measured wind spectra (Fig. 8), no such peaks were observed, even for high response levels. Furthermore, the maximum instantaneous velocity of the girder was calculated approximately as 0.5 m/s by integrating the accelerometer signals for the highest measured response.

A running mean is also plotted on the time series to highlight any non-stationary behavior. It is observed that the along-wind turbulence component exhibits non-stationary behavior, which is frequently observed also in the rest of the data. Although non-stationary models can also be used to study the wind characteristics [30–32], the traditional stationary wind model is preferred

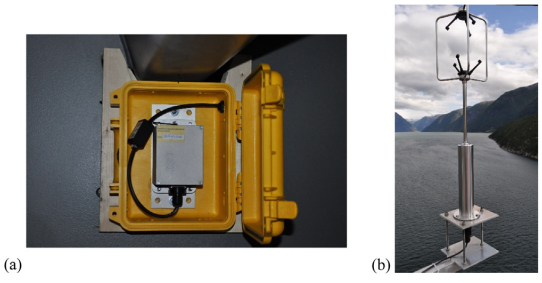


**Fig. 5.** Instruments on the bridge: (a) triaxial accelerometer inside the bridge deck and (b) anemometer attached to the hanger.

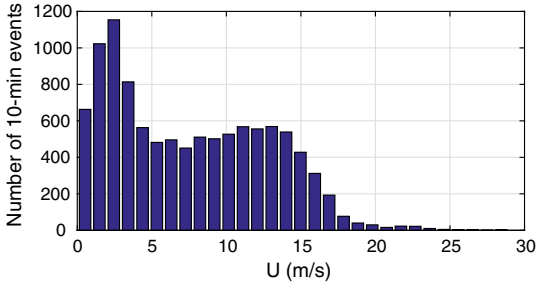


**Fig. 6.** Histogram of 10-min recordings.

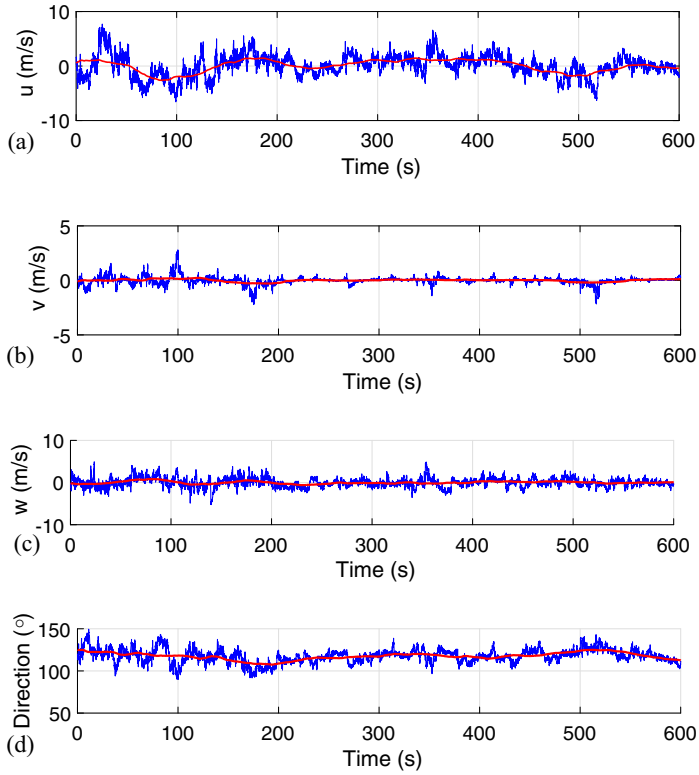


**Fig. 7.** Sample time series of wind measurements (U = 15.6 m/s) recorded on 12/1/2015: (a) along-wind turbulence (b) cross-wind turbulence (c) vertical turbulence and (d) wind direction.

here due to its common use in practice. Recent case studies based on typhoon winds [30,32] also show that if there is no sudden change in the wind direction or no rapid increase or decrease is present in the wind speed (such as in the build-up phase of a storm), the difference between stationary and non-stationary wind characteristics is not significant. For the strong winds recorded at the Hardanger Bridge, 10 min duration is sufficient to exclude such variations in the wind speed and the wind direction is usually steady.

### 4.2. Mean wind speed and direction

The mean wind velocities (U) were calculated for 10-min intervals for all recordings using the sensor at the midspan (A6) and are presented in the wind rose plot shown in Fig. 9, using a threshold wind speed of 3 m/s. The wind rose was plotted on top of the topographical map of the bridge site to show the influence of local topography on the wind conditions. The 0° direction shown in Fig. 9 is the bridge direction. The results suggest that the wind was approaching from either the east or the west and was mainly perpendicular to the bridge girder. The easterly winds approached the bridge from a wider directional range compared to the westerly winds. The directions of the easterly winds were bounded by the surrounding mountains; the highest mean speeds from this direction were approximately 18 m/s, and no significant directional dependence was observed. The westerly winds, on the other hand, had higher mean speeds of up to 30 m/s with mean directions almost perpendicular to the bridge direction.

### 4.3. Turbulence intensity

The turbulence intensity is a simple indicator of the intensity of the atmospheric turbulence. For the three turbulence components (u, v, w), the turbulence intensity is defined as

$$I_u = \frac{\sigma_u}{U}, I_v = \frac{\sigma_v}{U}, I_w = \frac{\sigma_w}{U} \quad (1)$$

where $\sigma_u$, $\sigma_v$ and $\sigma_w$ denote the standard deviations of the turbulence components. The turbulence intensity factors for each of the three turbulence components were calculated for the 10-min intervals, and wind rose plots were generated as shown in Fig. 10. The plots reveal that for the lower speed winds, the results are rather arbitrary, and the turbulence intensities are scattered randomly. This is due to the fact that the lower wind speeds accommodate more non-stationary behavior due to sudden changes in the wind direction and mean wind speed. In addition, since the wind speed fluctuations are divided by the mean wind speed in calculation of the turbulence intensity, similar variations in wind fluctuations result into larger scatter in case of low wind speeds. However, when strong winds are considered, the scatter is much smaller, and more dependence on the wind direction is observed. The along-wind turbulence intensity ($I_u$) ranges between 10% and 35% for strong winds (U > 12 m/s) from either direction. The cross-wind ($I_v$) and vertical ($I_w$) turbulence intensities exhibited much smaller values, ranging between 0 and 15% for the strong winds. The vertical turbulence intensity is more dependent on the wind direction than the along-wind turbulence (Fig. 10c). For the easterly winds, the 60°–

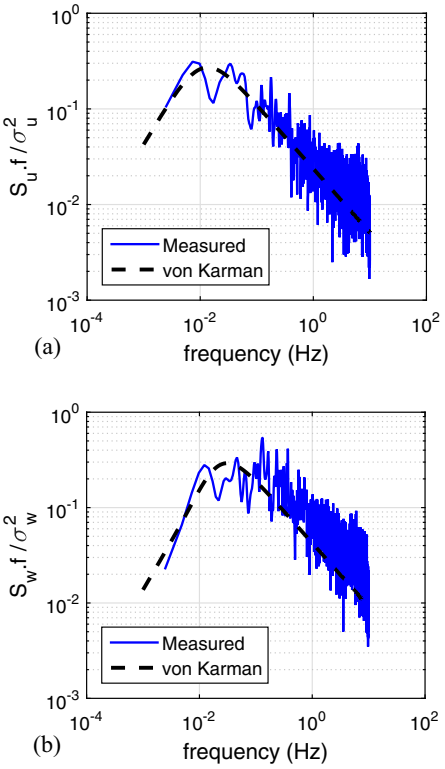


**Fig. 8.** Spectral density estimates of turbulence components for a 10-min recording on 12/1/2015: (a) along-wind turbulence and (b) vertical turbulence.

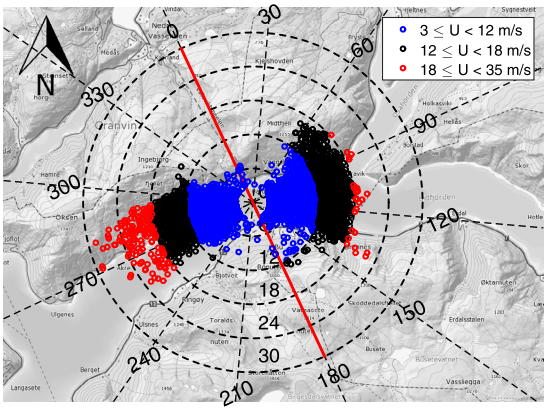


**Fig. 9.** Wind Rose plot of 10-min mean wind velocity (m/s).

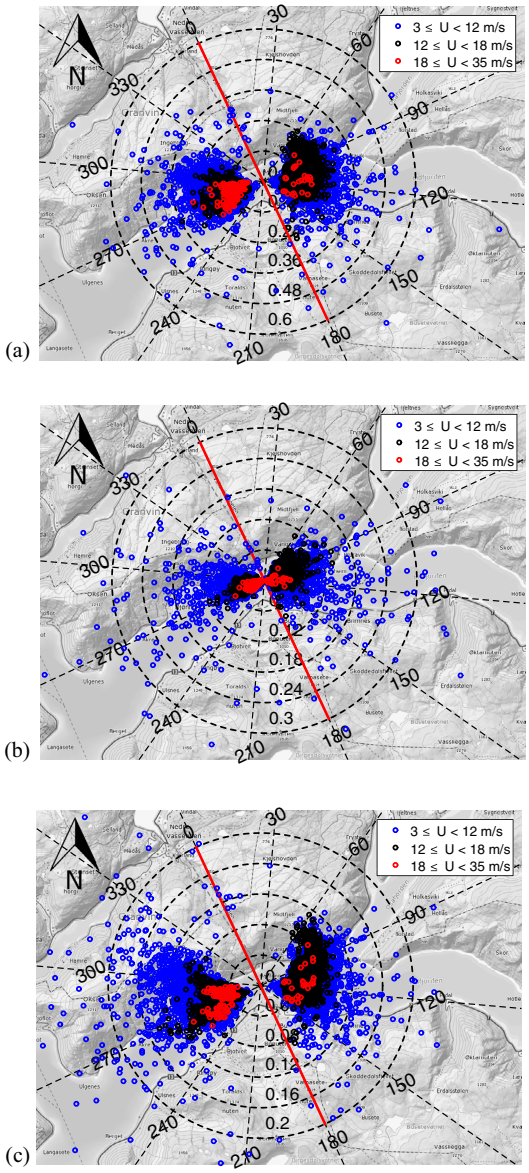


**Fig. 10.** Wind rose plots of turbulence intensities: (a) along-wind turbulence intensity, (b) cross-wind turbulence intensity and (c) vertical turbulence intensity.

90° range, where the wind flow had passed over a hill, generated the most turbulent flows. For the westerly winds, the winds blowing along the fjord, which were believed to be disturbed previously by the foothills of Mountain Oksen, had more vertical turbulence intensity (Fig. 2).

The covariance of the u and w turbulence components were plotted similar to the turbulence intensities (Fig. 11). Covariance of the turbulence components were calculated using

$$\mathrm{cov}(u,w) = \frac{1}{N-1}\sum_{i=1}^{N}(u_i - \mu_u) * (w_i - \mu_w) \tag{2}$$

where N denotes the number of observations, $\mu_{u,w}$ denote the mean of turbulence components and $*$ denotes the complex conjugate operation. The wind rose diagrams were separated into positive and negative correlations; most of the data indicated positive correlation of the two components, contradicting previous theoretical considerations [10,33]. However, similar observations have been reported previously [34,35]. For the westerly winds, the covariance term was positive for the winds blowing along the fjord (240–270°)

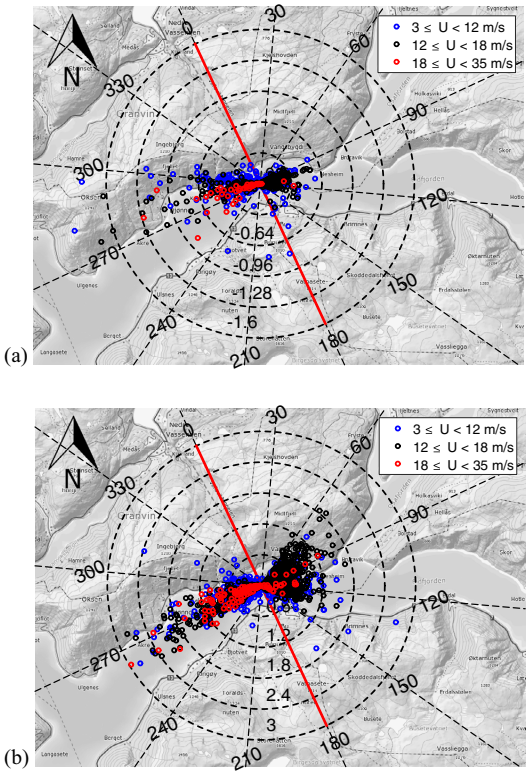


**Fig. 11.** Wind rose plots of the covariance term of longitudinal (u) and vertical (w) turbulence components (a) negative correlation (b) positive correlation.

and negative for the winds from the mountain direction (270–300°), demonstrating good separation. Smaller values were generally obtained from the easterly winds, for which no directional dependence was observed.

### 4.4. Turbulence length scale

The turbulence length scale or the integral length scale ($L_{u,v,w}$) represents the spectral content of the turbulence and can therefore be interpreted as the average eddy size of the turbulence. Theoretically, nine different length scales, three for each of the turbulence components, can be defined for the three-dimensional atmospheric turbulence. The length scale for the u-component in the along-wind direction can be written as [6]

$$L_u = \frac{1}{\sigma_u^2}\int_0^\infty R_{uu}(x)dx \tag{3}$$

where $R_{uu}(x)$ is the spatial cross-covariance function of the u-component. The same definition applies to the other turbulence components. Due to their physical interpretation, the length scales are essential parameters for describing atmospheric turbulence. In practice, the length scales cannot be calculated using Eq. (3), so they have to be estimated using approximate techniques [6]. However, estimating length scales from field data appears to be troublesome; the length scale estimates reported by previous studies show enormous variability in magnitude. After studying many field estimates of length scales in near-neutral atmospheric conditions, Solari [18] reported that the variability was not solely due to the terrain of interest, but also due to the estimation approach adopted. To examine the variability of estimates for the site in question, two practical estimation methods were adopted in this study. The first method (method 1) calculates the length scale by aligning the peak of the measured turbulence spectrum with the von Karman spectrum [11], which was given as

$$\frac{fS_u(f)}{\sigma_u^2} = \frac{4\frac{L_u f}{U}}{\left[1+70.8\left(\frac{L_u f}{U}\right)^2\right]^{5/6}}, \quad \frac{f.S_w(f)}{\sigma_w^2} = \frac{4\frac{L_w f}{U}\left[1+755\left(\frac{L_w f}{U}\right)^2\right]}{\left[1+283\left(\frac{L_w f}{U}\right)^2\right]^{11/6}} \tag{4}$$

for the along-wind and vertical turbulence components. The second method (method 2) integrates the auto-covariance function of the turbulence component up to the first zero crossing, assuming that Taylor's hypothesis is valid [6]. The relation for the longitudinal length scale then becomes

$$L_u = \frac{U}{\sigma_u^2}\int_0^\infty R_{uu}(\tau)d\tau, \quad R_{uu}(\tau) = \lim_{T\to\infty}\frac{1}{T}\int_{-T/2}^{T/2} u(t)u(t+\tau)d\tau \tag{5}$$

where $R_{uu}(\tau)$ is the cross-covariance function of the turbulence component in time. Fig. 12 shows the wind rose plots of the longitudinal length scales for 10-min intervals obtained using both methods, and the vertical length scale estimates are given in Fig. 13. Although estimating the length scales is fundamentally important for describing the atmospheric turbulence, the results indicate significant discrepancy in terms of magnitudes. The estimates of method 2 are systematically larger than those of method

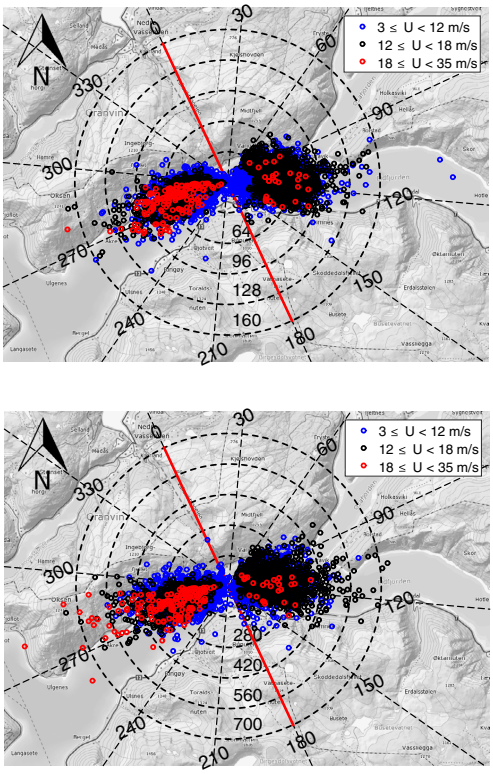


**Fig. 12.** Wind roses of the longitudinal length scale ($L_u$) estimates (in meters): (a) method 1 and (b) method 2.

1. The patterns in Fig. 12a and b, on the other hand, are in reasonable agreement with only minor differences. The general trends in Fig. 13a and b are also reasonably similar. The estimations of method 1 were clearly larger for the winds travelling along the fjord, where the winds were bounded by the mountains, while method 2 gave relatively more scattered results. Considering the values obtained using method 2, the longitudinal length scale of the strongest winds varies between 200 and 700 m, and the vertical length scale varies between 100 and 250 m. The length scale magnitudes obtained using method 2 show better agreement with the previously reported values [6]. In general, the longitudinal length scale was approximately 2–2.5 times the vertical length scale for both methods, which was in agreement with the observations of [8]. The wide range of the calculated length scale values, even for similar wind speeds and directions, implies that the spectral content of the turbulence varied randomly and therefore cannot be represented by a deterministic length scale value.

### 4.5. Angle of attack

The vertical angle of attack (β) is the angle between the mean wind velocity vector and the horizontal plane. Since the vertical inclination of the wind can influence the structural response, a brief description of the conditions at the site is useful. The angle of attack was calculated for each 10-min interval, and a wind rose plot was generated to present the results (Fig. 14). Negligible number of recordings exhibited negative angles with small amplitudes; therefore, only positive angles (mean wind velocity pointing upwards) are included in the figure. The results show that the mean wind velocity vector was generally inclined slightly upwards with angles of 1–5° for the strong winds.

## 5. Response characteristics

### 5.1. Data handling

The accelerations of the bridge girder were measured with a 200 Hz sampling frequency at 16 locations along the girder, as highlighted in Fig. 4. The acceleration data were then downsampled to 20 Hz, after applying a low-pass filter to avoid aliasing. The accelerometer pair located approximately at the midspan, namely H5E and H5W (Table 1), were selected to study the wind-induced dynamic response of the bridge girder. The vertical and lateral accelerations of the bridge girder were obtained by averaging the measurements from the two sensors, and the torsional response was obtained by dividing the difference of the two signals by the distance between the sensors. 10-min long recordings, same as for the wind records, were used to calculate the RMS values of the acceleration components.

To effectively study the wind-induced response, other sources of vibration, such as traffic-induced vibrations, should be excluded from the analysis. Because the wind-induced response of a suspension bridge is typically in the 0–1 Hz frequency range [14,17,32], the vertical high frequency vibrations are expected to increase when there is traffic loading on the bridge [14]. Examining the acceleration data indicated that the dynamic response was dominated by low-frequency vibrations (below 1 Hz) when the wind speed was above 8 m/s. The recordings with low wind speed (U < 8 m/s) and high frequency content were removed from the dataset, assuming that the vibrations were induced by other sources such as the overflowing traffic and are therefore outside of the scope of our analyses. Although the traffic density on Hardanger Bridge is typically low and the dynamic response is mainly due to wind (when wind speed is reasonably high), the effects of traffic loading could not be completely removed from the data. Therefore, other sources of vibration may still contribute to the overall variability in the results; however, this impact is expected to be negligible.

Spectral density estimations are given in Fig. 15 for the three response components for a 10-min recording recorded on 12/1/2015, for which the wind time series were already given in Fig. 7. The spectra are estimated using Welch [36] spectral estimation method. Spectral estimates of 8 data segments with 50% over-

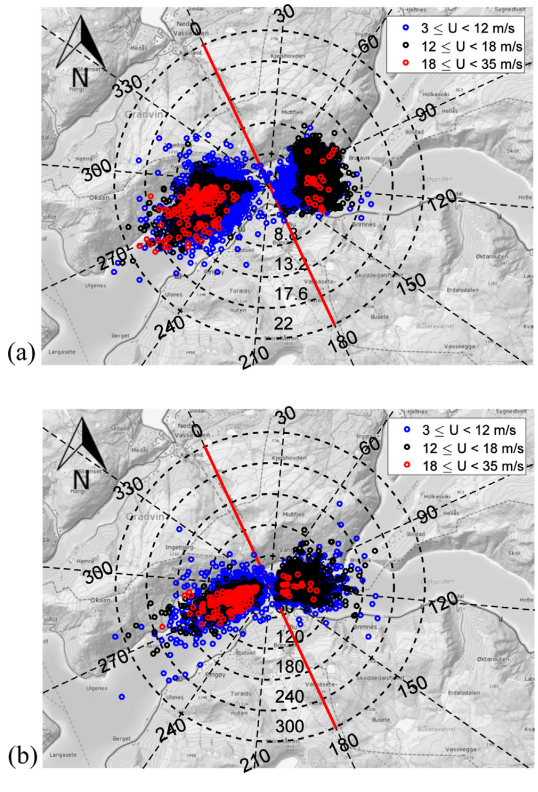


**Fig. 13.** Wind roses of the vertical length scale ($L_w$) estimates (in meters): (a) method 1 and (b) method 2.

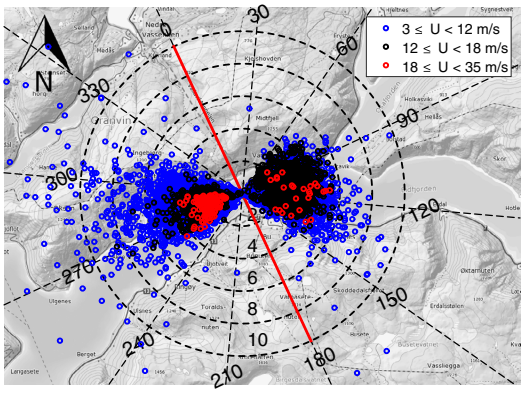


**Fig. 14.** Wind rose plot of the vertical angle-of-attack (β) in degrees.

lap are computed using Fast Fourier Transform (FFT) and averaged after applying a Hamming window to each segment. It is seen that the responses are dominated by the fundamental modes, with some contribution from the higher modes. The lateral response spectra exhibits similar results for the rest of the database, with a typical large peak at the first symmetric lateral frequency (0.05 Hz) of the structure. On the other hand, significant contributions from several modes are commonly observed in case of the vertical and torsional responses.

### 5.2. Dynamic response due to wind

The measured root mean square (RMS) values for the lateral, vertical and torsional accelerations are presented in Fig. 16 in the form of wind rose diagrams. The easterly winds showed consistent patterns for the three response components. The dynamic response was usually higher for higher mean wind speeds and the perpendicular wind direction. Westerly winds, on the other hand, showed peculiar response characteristics. The lateral and vertical acceleration responses induced by the westerly winds were generally smaller than the vibrations measured for the easterly winds, where the torsional response was high but severely scattered. The largest measured torsional vibrations were caused by moderate winds (12 < U < 18 m/s) from the east. The most critical wind direction was apparently the range of 60°–90°, where the winds passed over a hill approximately 500–600 meters high (Fig. 2). The winds approaching from this range typically had high vertical turbulence (Fig. 10c) and small length scales (Fig. 12), likely due to the interaction with the terrain. This observation indicates the effect of the relatively high surface roughness along the 60°–90° directional range on the response. However, the easterly winds travelling along the fjord with higher length scales did not cause large vibrations.

The three response components were then plotted against mean wind velocity to demonstrate the general trend and the variability in the measurements (Fig. 17). The results indicate vast variability in the wind-induced dynamic response. The vertical response shows the least scatter and was greatly affected by the vertical turbulence intensity (Fig. 17a). More severe scatter is observed in the lateral response, which cannot be attributed to the variability in the along-wind turbulence alone (Fig. 17b). The torsional response shows the largest scatter of all (Fig. 17c), especially for winds with mean wind speeds exceeding 10 m/s In the moderate wind speed range (12–18 m/s), large torsional vibrations were observed. It is also seen that for high wind speeds, the

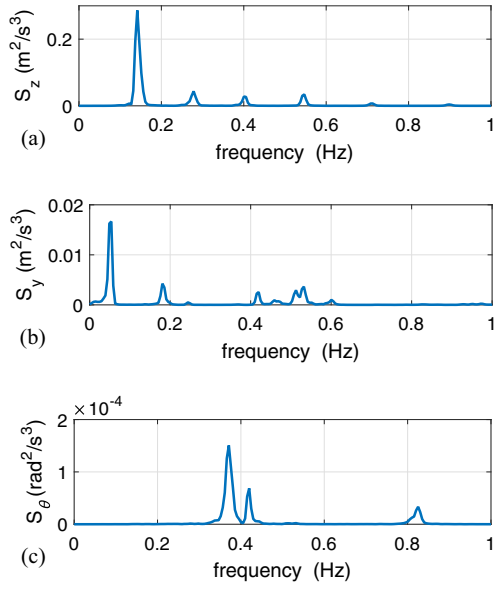


**Fig. 15.** Spectral density estimates of response components for a 10-min recording on 12/1/2015: (a) vertical acceleration, (b) lateral acceleration and (c) torsional acceleration.

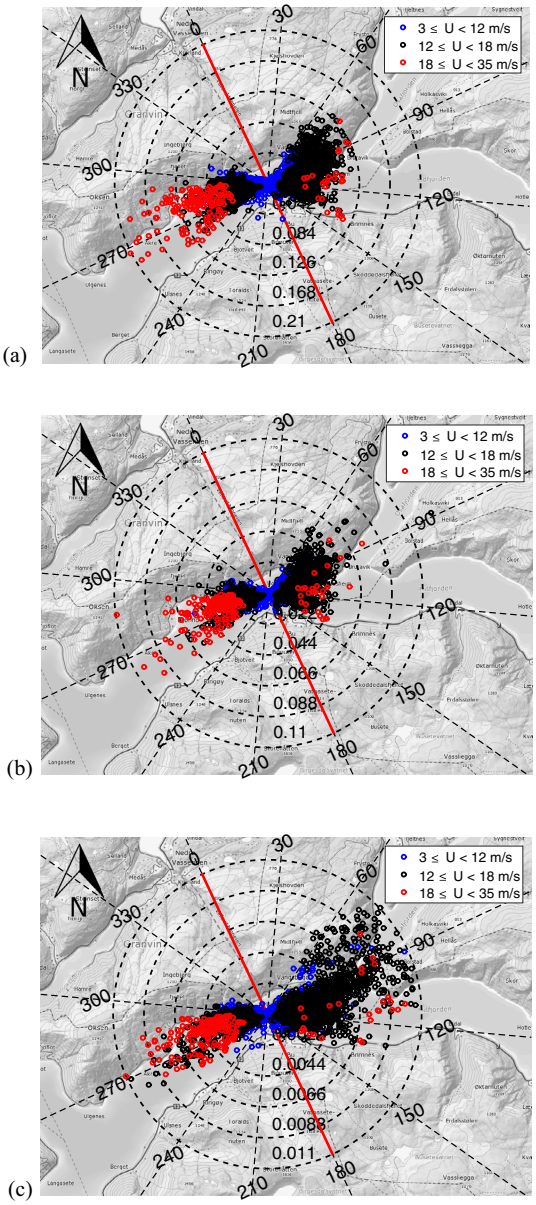


**Fig. 16.** Wind rose plots of the acceleration response: (a) RMS vertical acceleration (m/s$^2$) (b) RMS lateral acceleration (m/s$^2$) and (c) RMS torsional acceleration (rad/s$^2$).

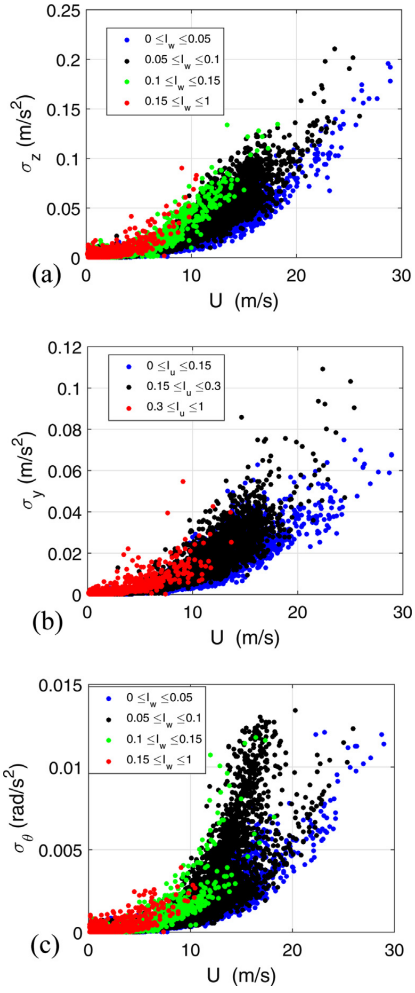


**Fig. 17.** RMS acceleration response plotted against mean wind velocity: (a) RMS vertical acceleration, (b) RMS lateral acceleration and (c) RMS torsional acceleration.

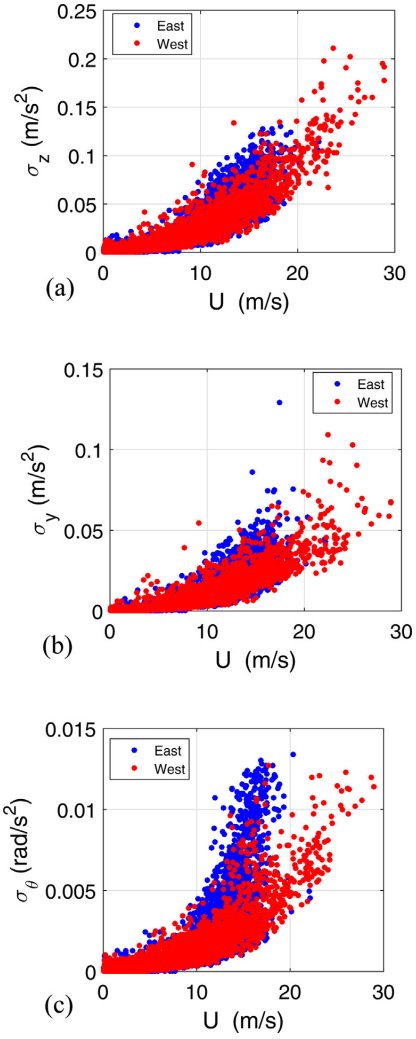


**Fig. 18.** RMS acceleration response vs. mean wind velocity for easterly and westerly winds: (a) RMS vertical acceleration, (b) RMS lateral acceleration and (c) RMS torsional acceleration.

torsional accelerations are separated. Higher torsional accelerations were recorded when the vertical turbulence was high, which was mostly the case for the easterly winds, especially the wind approaching from the 60°–100° range, where the wind flow is disturbed by the mountains. The three response components are plotted in Fig. 18 again with color-coding for the easterly and westerly winds. Distinctive torsional behavior was observed for the two different wind directions, whereas the lateral and vertical responses were essentially similar for the easterly and westerly winds. The difference between the torsional responses for the easterly and westerly directions is mainly attributed to the terrain effects. High turbulence levels generated by the upwind terrain in the east resulted into larger torsional vibrations of the Hardanger Bridge deck.

## 6. Influential factors for the dynamic response

The scatter plots given in Fig. 17 indicate severe variability in the wind-induced vibrations of the Hardanger Bridge. Since dynamic wind effects are crucially important in the design of slender cable-supported bridges, this variability should be further investigated. Identifying the sources of variability observed in the field measurements provide insight for evaluating the previously presented theoretical considerations. For this purpose, Response Surface Methodology (RSM), a well-known statistical tool [37], was utilized to study the relationship between the wind field parameters and the dynamic response.

Within the framework of RSM, the physical phenomenon of wind-induced bridge response can be treated as an empirical model where the response function, its functional form and the variables involved are unknown. Because wind effects are the primary focus in this study, several parameters related to the wind field characteristics (most of which are introduced in Section 2) were selected as the variables potentially influencing the dynamic response and were included in the analysis. These are listed as:

- the mean wind speed (U, averaged over 10 min)
- the wind yaw angle ($\alpha_{yaw}$)
- the standard deviations of the turbulence components ($\sigma_u$, $\sigma_v$, $\sigma_w$)
- the covariance of the u and w components of turbulence ($\sigma_{uw}$)
- the along-wind and the vertical turbulence length scales ($L_u$, $L_w$)
- the vertical angle of attack ($\beta$)
- the standard deviation of the mean wind speed values measured at eight locations along the bridge ($\sigma_{ms}$)
- Decay coefficients of coherence of turbulence components ($C_u$, $C_w$)

The decay coefficients are calculated by fitting Davenport's [38] coherence formula to the field data in least-squares sense. The coherence formula can be written as:

$$Coh_{u,w}(f,\Delta x) = \exp\left(-C_{u,w}\frac{f.\Delta x}{U}\right) \quad (6)$$

where f is frequency, $C_{u,w}$ are the decay coefficients and $\Delta x$ is the spanwise separation. The length scale parameters ($L_u$, $L_w$) used in the analyses were calculated using method 2 described in Section 4.4, due to its more common use in the practice. The final variable in the list was included to provide a crude representation of the inhomogeneity of the wind field. These variables are referred to as the predictor variables, adapting the terminology of RSM. Several sources of variability that were observed in the response measurement were not included in the analysis: the traffic loading, the spatial distribution of the wind turbulence effects, non-stationarity of the wind time series and cable vibrations. When standard stationarity tests such as the run test [39,40] are conducted on the entire data, it is found that very few recordings can be classified as stationary. Non-stationary winds can cause higher or lower bridge response compared to stationary winds with similar statistics, depending on the nature of the non-stationarity. This naturally imposes additional variability when assessing the wind and response relationship. However, analytical studies on non-stationary buffeting response of different bridge structures [41,42] show that the variations induced by non-stationary wind records are much smaller than the variability observed in the response of the Hardanger Bridge, which is mainly due to terrain effects. The wind rose plots of Fig. 16 show that the response was highly dependent on the mean wind direction, which was presumably a topographic influence on the wind field. Because this relationship between the mean wind direction and the response parameters could not be modeled using a quadratic response surface, the angle between the mean wind and the perpendicular bridge directions (yaw angle, $\alpha_{yaw}$) was used in the analysis to represent the directional effects. Although the effects of topography could not be fully represented by the yaw angle, they were partly represented by other parameters, such as the standard deviations of the turbulence and length scales, which are already dependent on the wind direction. The anemometer A6 and the accelerometer pair H5 were selected to study the wind field – bridge response relationship using response surface analysis, which are both located approximately at the midspan. However, when the analysis is repeated with another accelerometer pair, say at the quarter-span (H3 pair) considering that the first vertical mode is antisymmetric, very similar results were obtained.

A quadratic response surface including interaction terms was then fitted to the field data. The functional form of the model can be written as

$$y = \beta_0 + \sum_{i=1}^{n}\left(\beta_i x_i + \sum_{j=i+1}^{n}\beta_{ij}x_i x_j + \beta_{ii}x_i^2\right) \quad (7)$$

where n is the number of predictor variables and $\beta$ represents the coefficients to be determined by a least-squares fit to the measured response. The regression is still linear because the model is linear in the coefficients [33]. The unnecessary terms should be eliminated to obtain more significant and computationally efficient response surfaces. For this purpose, after an initial fit, the predictor variables, which had negligible effect on the regression, were determined through hypothesis tests on the regression coefficients. The null hypothesis of $H_0$: $\beta = 0$ (the term has no effect on the model) was tested for each parameter used in the model by a *t*-test, and the corresponding term was deleted from the model if the null hypothesis was not rejected at a 95% significance level.

The resulting response surfaces were then used to calculate the predicted response using the field data. A summary of the regression analyses results is given in Table 2. The results of the response surface prediction are given in Fig. 19 and are plotted against the mean wind velocity. The plots indicate that most of the variability observed in the measurement data (Fig. 17) can be explained by the variability in the wind field itself. The $R^2$ values of the regression were 0.95, 0.9 and 0.82 for the vertical, lateral and torsional acceleration responses, respectively, which supports the previous statement. Furthermore, the significance of the regression was assessed using an F-test with the null hypothesis of $H_0$: $\beta_1 = \beta_2 = \ldots = \beta_n = 0$. The null hypothesis states that there is no linear relationship between the response variable and any subset of the predictor variables. The F-statistics resulting from the tests on the vertical, lateral and torsional response surface fits were well above the test value corresponding to the 99% significance level, implying that the regressions were very significant.

It is also beneficial to elaborate on the factors that influence the response as well as their influence and interactions. Therefore, the significance of each term used in the final models was assessed, using an analysis of variance (ANOVA) procedure. The p-value approach is used to present the results instead of directly using the F-statistic due to its ease of interpretation. If the resulting p-value is less than the significance level ($\alpha$), then the null hypothesis will be rejected, meaning that the term is significant at that level. The p-values calculated for the terms in the three response surfaces are given in Table 3.

### 6.1. Mean wind velocity

The tests on parameter significance showed that the mean wind velocity was the most influential factor on the dynamic response, as expected. The response surface analyses indicate a quadratic relationship between the mean wind velocity and the response, as shown in the scatter plots of Fig. 17. However, considering the $R^2$ values, the mean speed alone can only explain 84%, 78% and 63% of the variability in the vertical, lateral and torsional acceleration response, respectively. Accordingly, including other variables in the analyses is necessary for better describing the dynamic response.

### 6.2. Turbulence

The effect of the turbulence components on the dynamic response was incorporated into the response surface analyses

**Table 2**
Summary of regression analyses.

| | Number of observations | $R^2$ value | F-statistic for model significance |
|---|---|---|---|
| Vertical acceleration | 9590 | 0.95 | $7.38 \times 10^3$ |
| Lateral acceleration | 9590 | 0.9 | $2.89 \times 10^3$ |
| Torsional acceleration | 9590 | 0.82 | $1.55 \times 10^3$ |

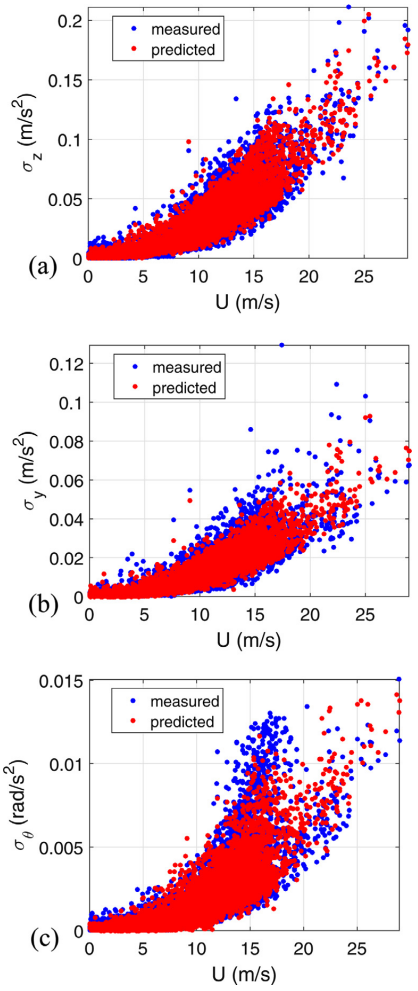


**Fig. 19.** Measured vs. predicted responses using the response surface models: (a) vertical response, (b) lateral response and (c) torsional response.

using the standard deviations of the three turbulence components ($\sigma_u$, $\sigma_v$, $\sigma_w$) along with the covariance of the along-wind and vertical turbulences ($\sigma_{uw}$). A quick inspection of the p-values shows that the vertical turbulence component had an important influence on all response components. The cross-wind turbulence appeared to be important only for the torsional response, whereas the along-wind turbulence was significant for both the lateral and vertical responses. The covariance term ($\sigma_{uw}$) was significant for the vertical and torsional responses but not for the lateral response.

After establishing the important terms, the effect of the four turbulence terms on the dynamic response can be investigated further. The dynamic response was predicted using the previously obtained response surfaces for a range of turbulence values. The results shown in Fig. 20 were obtained by changing only one variable while the other parameters in the model were taken as their mean values, except for the mean wind velocity, which was taken as 15 m/s and the wind yaw angle, which was taken as zero (perpendicular to the bridge). The confidence intervals (95%) for the predictions are also shown using dashed lines. The acceleration

**Table 3**
Significance of terms in response surface analyses.

| Vertical acceleration | | Lateral acceleration | | Torsional acceleration | |
|---|---|---|---|---|---|
| Term | p-value | Term | p-value | Term | p-value |
| $U.\sigma_w$ | 0 | $U.\sigma_w$ | 7.24E−206 | $U.\sigma_v$ | 2.35E−164 |
| U^2 | 2.26E−155 | $\alpha_{yaw}.\sigma_u$ | 6.97E−65 | $U^2$ | 4.25E−82 |
| $\sigma_w.\alpha_{yaw}$ | 8.59E−73 | $\sigma_w.L_u$ | 2.89E−33 | U | 1.18E−79 |
| $U.C_w$ | 1.46E−56 | $U.C_u$ | 8.65E−33 | $L_u.\sigma_v$ | 8.92E−70 |
| $\sigma_{uw}^2$ | 7.42E−40 | $U^2$ | 7.50E−25 | $\sigma_{uw}^2$ | 5.58E−63 |
| U | 1.97E−35 | $\sigma_w.\sigma_{ms}$ | 7.87E−24 | $U.C_w$ | 7.02E−58 |
| $\sigma_w.\sigma_{ms}$ | 4.62E−23 | $\sigma_{uw}^2$ | 4.35E−22 | $U.\sigma_w$ | 1.92E−52 |
| $\sigma_w.\sigma_v$ | 6.92E−23 | $\sigma_w.\sigma_u$ | 1.66E−21 | $U.\alpha_{yaw}$ | 1.02E−49 |
| $\alpha_{yaw}.L_w$ | 1.13E−16 | $\sigma_w.L_w$ | 2.01E−18 | $\sigma_u.\sigma_{uw}$ | 2.13E−37 |
| $L_w^2$ | 3.61E−16 | U.β | 1.30E−17 | $L_w.\sigma_v$ | 1.18E−27 |
| $\sigma_w.L_u$ | 3.87E−16 | $\alpha_{yaw}.\sigma_v$ | 2.28E−17 | $U.L_w$ | 8.04E−22 |
| $\sigma_w.L_w$ | 6.09E−14 | $\sigma_u.\sigma_{uw}$ | 4.15E−12 | $C_u$ | 1.95E−13 |
| $\sigma_v.\sigma_{ms}$ | 6.97E−13 | $C_w$ | 1.28E−10 | $C_u^2$ | 1.67E−12 |
| $C_w^2$ | 5.59E−12 | $L_w^2$ | 4.64E−10 | $L_u.L_w$ | 6.77E−12 |
| $\sigma_u.\sigma_{uw}$ | 9.86E−11 | $\alpha_{yaw}.L_w$ | 5.07E−10 | $\alpha_{yaw}^2$ | 2.44E−10 |
| $L_w$ | 3.27E−09 | $C_w^2$ | 7.91E−10 | $\alpha_{yaw}.L_u$ | 1.64E−09 |
| $U.L_w$ | 1.18E−05 | $C_u^2$ | 1.82E−08 | $\alpha_{yaw}$ | 3.40E−09 |
| $\sigma_{uw}$ | 3.38E−05 | $L_w$ | 2.06E−08 | $\sigma_w^2$ | 6.41E−09 |
| | | $\sigma_u.\beta$ | 1.56E−07 | $L_w^2$ | 2.11E−08 |
| | | $\alpha_{yaw}.L_u$ | 1.76E−07 | $C_w^2$ | 2.70E−06 |
| | | $\sigma_{uw}.C_w$ | 7.37E−07 | $\sigma_w.\sigma_u$ | 3.34E−06 |
| | | U | 1.07E−06 | $L_u.C_w$ | 1.01E−05 |
| | | $\sigma_{uw}$ | 9.97E−06 | | |

results were normalized with the maximum observed response during the field measurements. Although the actual behavior of the multivariate response surface model is more complex due to the interaction of several variables, certain inferences are possible using Fig. 20. The vertical turbulence clearly had the most profound impact on the response, while the cross-wind turbulence was equally important for the torsional response. Other turbulence components also showed a linear relationship with the response; however, their effects were much smaller in comparison. The covariance term also had a slight influence on the response. For the sake of discussion, the spectral densities of lateral, vertical and torsional forcing actions on the Hardanger Bridge section can be written using the buffeting theory [5,6] after inserting the bridge dimensions and the force coefficient terms previously obtained from wind tunnel tests [34,35] as

$$\begin{aligned} S_{yy} &= (\rho UB)^2[0.014S_{uu} + 0.03S_{uw} + 0.016S_{ww}] \\ S_{zz} &= (\rho UB)^2[0.064S_{uu} - 0.61S_{uw} + 1.62S_{ww}] \\ S_{\theta\theta} &= (\rho UB^2)^2[0.0001S_{uu} + 0.077S_{uw} + 0.143S_{ww}] \end{aligned} \tag{8}$$

In the equation, ρ denotes the air density, $S_{uu}$ and $S_{ww}$ denote the auto-spectral densities of the along-wind and vertical turbulences and $S_{uw}$ denotes the cross-spectral density of the u and w components and B is the width of the girder (18.3 m). The expressions for the buffeting actions suggest that the cross-wind turbulence does not contribute to loading; this conclusion was supported by the response surface predictions except for the torsional response. The cross-spectrum $S_{uw}$ is said to be much smaller in comparison and is usually neglected, which was also in agreement with the findings. Moreover, the expressions show that the vertical turbulence is the most influential parameter, which was also observed in the findings. The effect of the along-wind turbulence on the lateral response was small in the response surface predictions, whereas the expressions indicated that it would be more significant. It should also be noted that in addition to the one-point statistics, the spanwise correlation of the wind loads will also effect the dynamic response, which is included in the analysis with parameters $C_u$ and $C_w$. Moreover, due to the considerably long span of the bridge and the surrounding complex topography, wind loads

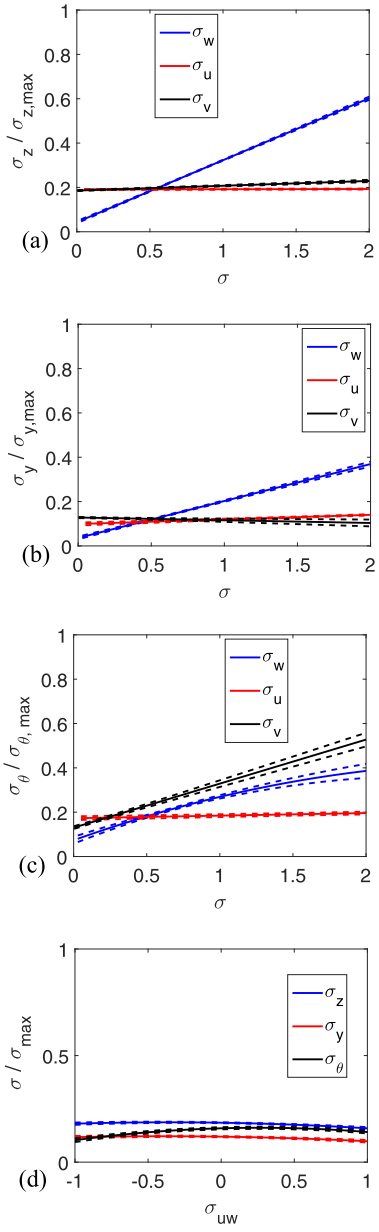


**Fig. 20.** Effects of turbulence on the dynamic response (the dashed lines represent 95% confidence intervals): (a) vertical response, (b) lateral response, (c) torsional response and (d) covariance of u and w components.

may vary along the span, due to nonhomogeneous wind conditions. This effect was attempted to be investigated using the parameter $\sigma_{ms}$.

In many cases, the turbulence terms seem to interact with each other and with other terms in the response surfaces (Table 3). Some of the important interactions are presented in Fig. 21 using three-dimensional surfaces. This time, the values of two variables were altered while all others remained fixed to obtain the results. The surfaces given in the plots were obtained by using the fitted response surfaces for a range of mean speed and turbulence values. The correlation between wind and response parameters were aimed to be presented using quadratic surfaces, therefore any marginal relationship or local effects may not be captured. Because the mean wind speed was the most significant variable in the model, the interactions of the turbulence terms with the wind speed are of particular interest. The surface plots support the relationships given in Fig. 21 for a wide range of mean speed values. All findings indicate that the wind velocity fluctuations had a crucial role in the dynamic excitation of the Hardanger Bridge.

### 6.3. Wind yaw angle

The strong winds attacked the Hardanger Bridge was not essentially perpendicular to the bridge axis. The mean wind directions averaged over 10-min intervals exhibited deviations from the perpendicular direction of up to 60° (Fig. 9). Traditionally, these skew-winds are treated as less critical events than the perpendicular winds [9,17]. This assumption relies on the decomposition of the mean wind vector to its components, which are parallel and perpendicular to the bridge axis. The effect of the parallel component to the bridge response is usually neglected where the perpendicular component is always smaller than the mean wind speed.

Instead of the traditional approach, the mean wind speed was included in the response surface analyses without any decomposition. The yaw angle ($\alpha_{yaw}$) is the angle between the mean wind direction and the axis perpendicular to the bridge direction and was therefore included in the analyses. However, recent studies indicated that similar response levels can be obtained under skew-winds and perpendicular winds with the same wind speeds [9]. The response surface predictions also showed similar response levels under skew-winds and perpendicular winds.

### 6.4. Other factors

The remaining factors, which have not been mentioned in the previous sections, are discussed here. The angle of attack almost completely disappeared from the response surface models after the parameter significance tests; therefore, no significant correlation could be extracted. The length scales, on the other hand, appeared in several model terms. The effect of the length scales on the response, however, was not profound, with the exception of the effect of the vertical length scale on the torsional response (Fig. 22). The models generally predicted higher responses for lower length scales, but the effect was minor. The last parameter considered in the analyses was the standard deviation of the mean wind speeds along the bridge. The effect of this parameter on the dynamic response was found to be negligible.

It is also seen that the spanwise correlation of the turbulence components, represented here by the decay coefficients, had influence on the measured responses (Fig. 23). An increase in the parameters $C_u$ and $C_w$ (smaller spanwise correlation of turbulence) are associated with lower lateral and vertical responses, respectively. A significant correlation between the torsional response component and the $C_w$ parameter is also observed (Fig. 23); however, with the opposite effect. When the recordings with both high $C_w$ values and high torsional response are inspected further, it is seen that the torsional responses in such events were not dominated by the fundamental symmetric torsional mode, but had significant contributions from multiple structural modes, especially the higher modes. Nevertheless, it should be noted that correlation does not necessarily imply causation in regression analysis.

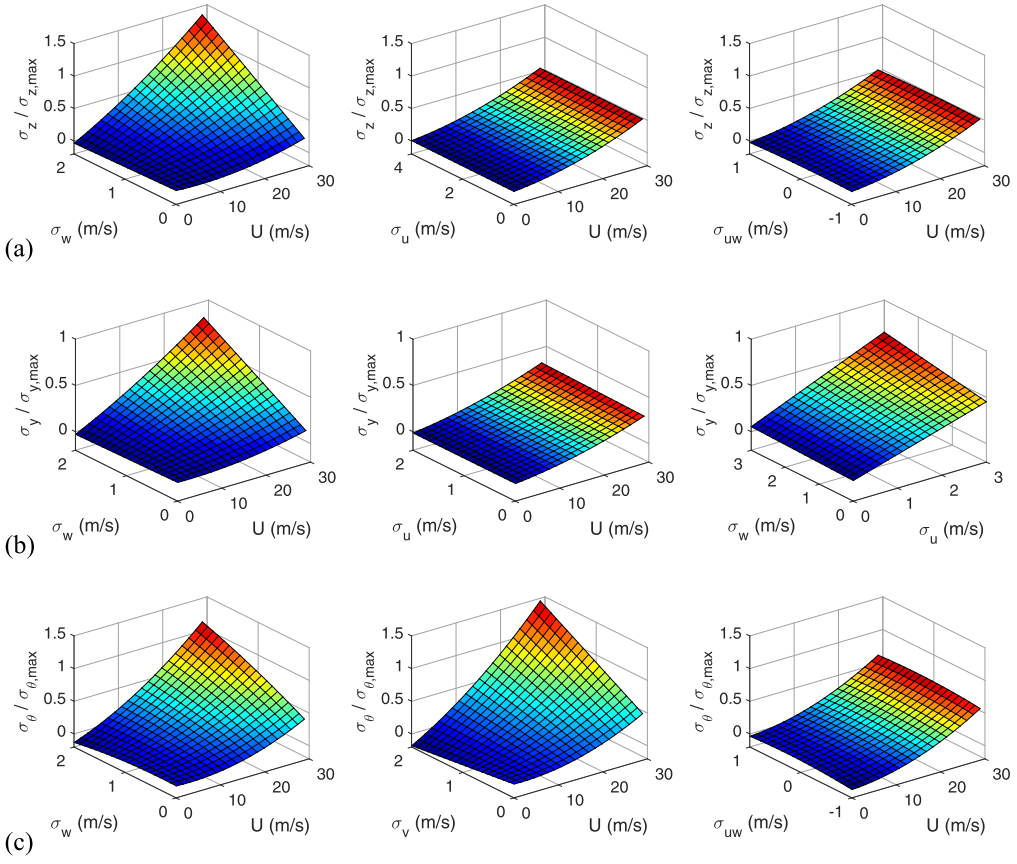


**Fig. 21.** Interaction effects of the turbulence components on the dynamic response: (a) vertical response, (b) lateral response and (c) torsional response.

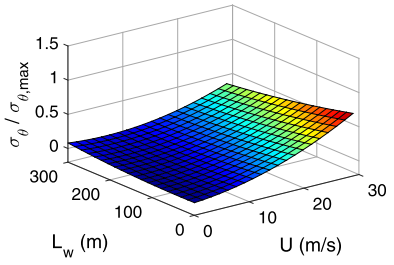


**Fig. 22.** Effect of the vertical length scale on the torsional response.

## 7. Conclusions

The wind and dynamic response characteristics of the Hardanger Bridge as well as their relationship were studied using field measurement data. The following conclusions were deduced from the results:

- The wind field showed large variability in the mean wind speed, mean wind direction, turbulence intensities and length scales.
- The dynamic response of the Hardanger Bridge was governed by the low-frequency vibrations induced by the wind effects when the mean wind speed was higher than 8 m/s. In case of lower wind speeds, the vibrations induced by traffic and other sources were relatively more significant.
- The measurement data and the complementary analyses showed that high response levels were reached also under skew-wind conditions. Such wind effects should be more carefully handled in the design stage, especially when complex topographical conditions are present.
- Response surface analyses showed that most of the variability observed in response was due to variability in the wind field itself. In general, the mean wind speed and the turbulence intensities are found critical to describe the response; however, other wind-related parameters also aided in explaining the variability.
- High mean wind speed and turbulent fluctuations were associated with higher bridge response. Spanwise correlation of turbulence were also found to be correlated with the bridge dynamic response, except for the torsional response, where an inverse correlation was observed.
- Although there is significant agreement between the findings here and the prediction methods used in practice, selection of the mean wind speed as the sole design parameter fails to capture the actual variability in the wind field. Therefore, the

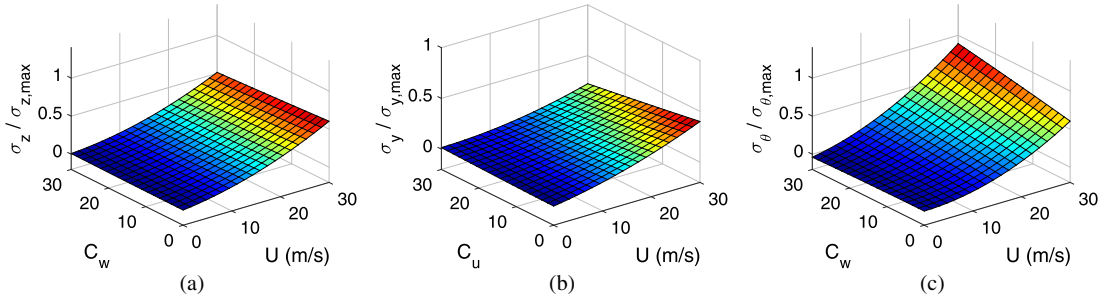


**Fig. 23.** Effect of decay coefficients on the dynamic response: (a) vertical response, (b) lateral response and (c) torsional response.

uncertainty in the description of the wind field is suggested to be considered when designing new bridges to achieve more reliable bridge designs.

- The present investigation provides insight into prediction discrepancies using Hardanger Bridge data as an example. Further research is needed to develop methods that incorporate uncertainty in both short- and long-term response estimation methods.

## Acknowledgments

The research described in this paper was financially supported by the Norwegian Public Roads Administration.

## References

[1] Miyata T. Historical view of long-span bridge aerodynamics. J Wind Eng Ind Aerodyn 2003;91:1393–410. http://dx.doi.org/10.1016/j.jweia.2003.09.033.
[2] Larsen A, Esdahl S, Andersen JE, Vejrum T. Storebælt suspension bridge – vortex shedding excitation and mitigation by guide vanes. J Wind Eng Ind Aerodyn 2000;88:283–96. http://dx.doi.org/10.1016/S0167-6105(00)00054-4.
[3] Larsen A, Larose GL. Dynamic wind effects on suspension and cable-stayed bridges. J Sound Vib 2015;334:2–28. http://dx.doi.org/10.1016/j.jsv.2014.06.009.
[4] Brownjohn JMW, Magalhaes F, Caetano E, Cunha A. Ambient vibration re-testing and operational modal analysis of the Humber Bridge. Eng Struct 2010;32:2003–18. http://dx.doi.org/10.1016/j.engstruct.2010.02.034.
[5] Davenport AG. Buffeting of a suspension bridge by storm winds. J Struct Div 1962;88:233–68. http://dx.doi.org/10.4319/lo.2013.58.2.0489.
[6] Simiu E, Scanlan RH. Winds effects on structures: fundamentals and applications to design. 3rd ed. Wiley; 1996.
[7] Mann J. The spatial structure of neutral atmospheric surface-layer turbulence. J Fluid Mech 2006;273:141. http://dx.doi.org/10.1017/S0022112094001886.
[8] Tamura Y, Kareem A. Advanced structural wind engineering. Japan: Springer; 2013.
[9] Xu Y-L. Wind effects on cable-supported bridges. John Wiley & Sons; 2013.
[10] Kaimal JCJ, Wyngaard JCJ, Izumi Y, Coté OR, Cote OR. Spectral characteristics of surface-layer turbulence. Q J R Meterol Soc 1972;98:563–89. http://dx.doi.org/10.1002/qj.49709841707.
[11] von Karman T. Progress in the statistical theory of turbulence. Proc Natl Acad Sci U S A 1948;34:530–9. http://dx.doi.org/10.1073/pnas.34.11.530.
[12] Hui MCH, Larsen A, Xiang HF. Wind turbulence characteristics study at the Stonecutters Bridge site: part I-mean wind and turbulence intensities. J Wind Eng Ind Aerodyn 2009;97:22–36. http://dx.doi.org/10.1016/j.jweia.2008.11.002.
[13] Hui MCH, Larsen A, Xiang HF. Wind turbulence characteristics study at the Stonecutters Bridge site: part II: wind power spectra, integral length scales and coherences. J Wind Eng Ind Aerodyn 2009;97:48–59. http://dx.doi.org/10.1016/j.jweia.2008.11.003.
[14] Brownjohn JMW, Bocciolone M, Curami A, Falco M, Zasso A. Humber bridge full-scale measurement campaigns 1990–1991. J Wind Eng Ind Aerodyn 1994;52:185–218. http://dx.doi.org/10.1016/0167-6105(94)90047-7.
[15] Wang H, Li A, Niu J, Zong Z, Li J. Long-term monitoring of wind characteristics at Sutong Bridge site. J Wind Eng Ind Aerodyn 2013;115:39–47. http://dx.doi.org/10.1016/j.jweia.2013.01.006.
[16] Cao S, Tamura Y, Kikuchi N, Saito M, Nakayama I, Matsuzaki Y. Wind characteristics of a strong typhoon. J Wind Eng Ind Aerodyn 2009;97:11–21. http://dx.doi.org/10.1016/j.jweia.2008.10.002.
[17] Xu YL, Zhu LD. Buffeting response of long-span cable-supported bridges under skew winds. Part 2: case study. J Sound Vib 2005;281:675–97. http://dx.doi.org/10.1016/j.jsv.2004.01.025.
[18] Solari G, Piccardo G. Probabilistic 3-D turbulence modeling for gust buffeting of structures. Probabilistic Eng Mech 2001;16:73–86. http://dx.doi.org/10.1016/S0266-8920(00)00010-2.
[19] Kareem A. Aerodynamic response of structures with parametric uncertainties. Struct Saf 1988;5:205–25. http://dx.doi.org/10.1016/0167-4730(88)90010-0.
[20] Solari G. Wind-excited response of structures with uncertain parameters. Probabilistic Eng Mech 1997;12:75–87. http://dx.doi.org/10.1016/S0266-8920(96)00027-6.
[21] Caracoglia L. Influence of uncertainty in selected aerodynamic and structural parameters on the buffeting response of long-span bridges. J Wind Eng Ind Aerodyn 2008;96:327–44. http://dx.doi.org/10.1016/j.jweia.2007.08.001.
[22] Cross EJ, Koo KY, Brownjohn JMW, Worden K. Long-term monitoring and data analysis of the Tamar Bridge. Mech Syst Signal Process 2013;35:16–34. http://dx.doi.org/10.1016/j.ymssp.2012.08.026.
[23] Peeters B, Couvreur G, Razinkov O, Kündig C, van der Auweraer H, de Roeck G. Continuous monitoring of the Øresund Bridge: system and data analysis. Struct Infrastruct Eng 2009;5:395–405. http://dx.doi.org/10.1080/15732470701478362.
[24] Caetano E, Cunha A, Moutinho C, Magalhães F. Dynamic characterization and continuous dynamic monitoring of long span bridges. Int. Conf. Multi-Span Large Bridg., Porto, Portugal. Balkema: CRC Press; 2015. p. 771–80.
[25] Wang H, Li A, Guo T, Xie J. Field measurement on wind characteristic and buffeting response of the Runyang Suspension Bridge during typhoon Matsa. Sci China Ser E Technol Sci 2009;52:1354–62. http://dx.doi.org/10.1007/s11431-008-0238-y.
[26] Wang H, Li A, Hu R. Comparison of ambient vibration response of the Runyang Suspension Bridge under skew winds with time-domain numerical predictions. J Bridg Eng 2011. http://dx.doi.org/10.1061/(ASCE)BE.1943-5592.0000168.
[27] Macdonald JHG. Evaluation of buffeting predictions of a cable-stayed bridge from full-scale measurements. J Wind Eng Ind Aerodyn 2003;91:1465–83. http://dx.doi.org/10.1016/j.jweia.2003.09.009.
[28] Wang H, Hu R, Xie J, Tong T, Li A. Comparative study on buffeting performance of sutong bridge based on design and measured spectrum. J Bridg Eng 2013;18:587–600. http://dx.doi.org/10.1061/(ASCE)BE.1943-5592.0000394.
[29] Øiseth O, Rönnquist A, Kvåle KA, Sigbjörnsson R. Monitoring wind velocities and dynamic response of the Hardanger Bridge. Conf ProcSoc Exp Mech Ser 2015;2:117–25. http://dx.doi.org/10.1007/978-3-319-15248-6_13.
[30] Wang H, Wu T, Tao T, Li A, Kareem A. Measurements and analysis of non-stationary wind characteristics at Sutong Bridge in Typhoon Damrey. J Wind Eng Ind Aerodyn 2016;151:100–6. http://dx.doi.org/10.1016/j.jweia.2016.02.001.
[31] Xu YL, Chen J. Characterizing nonstationary wind speed using empirical mode decomposition. J Struct Eng 2004;130:912–20.
[32] Chen J, Hui MCH, Xu YL. A comparative study of stationary and non-stationary wind models using field measurements. Boundary-Layer Meteorol 2007;122:105–21. http://dx.doi.org/10.1007/s10546-006-9085-1.
[33] Tennekes H, Lumley JL. A first course in turbulence. Cambridge: The MIT Press; 1999.
[34] Shuyang C, Nishi A, Hirano K, Ozono S, Miyagi H, Kikugawa H, et al. An actively controlled wind tunnel and its application to the reproduction of the atmospheric boundary layer. Boundary-Layer Meteorol 2001;101:61–76. http://dx.doi.org/10.1023/A:1019288828837.
[35] Øiseth O, Rönnquist A, Sigbjörnsson R. Effects of co-spectral densities of atmospheric turbulence on the dynamic response of cable-supported bridges: a case study. J Wind Eng Ind Aerodyn 2013;116:83–93. http://dx.doi.org/10.1016/j.jweia.2013.03.001.
[36] Welch PD. The Use of fast fourier transform for the estimation of power spectra: a method based on time averaging over short, modified periodograms. IEEE Trans Audio Electroacoust 1967;15:70–3. http://dx.doi.org/10.1109/TAU.1967.1161901.

[37] Myers RH, Montgomery DC, Anderson-Cook C. Response surface methodology: process and product optimization using designed experiments. Wiley Ser Probab Stat 2009:704. http://dx.doi.org/10.2307/1270613.
[38] Davenport AG. The spectrum of horizontal gustiness near the ground in high winds. Q J R Meteorol Soc 1961;87:194–211. http://dx.doi.org/10.1002/qj.49708737208.
[39] Bendat J, Piersol A. Random data analysis and measurement procedures. Meas Sci Technol 2000.
[40] Cao S, Tamura Y, Kikuchi N, Saito M, Nakayama I, Matsuzaki Y. A case study of gust factor of a strong typhoon. J Wind Eng Ind Aerodyn 2015;138:52–60. http://dx.doi.org/10.1016/j.jweia.2014.12.012.
[41] Chen X. Analysis of multimode coupled buffeting response of long-span bridges to nonstationary winds with force parameters from stationary wind. J Struct Eng (United States) 2015:141. http://dx.doi.org/10.1061/(ASCE)ST.1943-541X.0001078.
[42] Hu L, Xu Y-L, Huang W-F. Typhoon-induced non-stationary buffeting response of long-span bridges in complex terrain. Eng Struct 2013;57:406–15. http://dx.doi.org/10.1016/j.engstruct.2013.09.044.

# Paper II

Aksel Fenerci, Ole Øiseth

*Measured Buffeting Response of a Long-Span Suspension Bridge Compared with Numerical Predictions Based on Design Wind Spectra*

*Journal of Structural Engineering (United States) 2017;143. With permission from ASCE.*

# Paper III

Aksel Fenerci, Ole Øiseth

*Evaluation of wind-induced response predictions of a long-span suspension bridge using full-scale measurements*

*7th Eur. African Conf. Wind Eng. (EACWE 2017), Liege, Belgium, 2017.*

# Paper IV

Aksel Fenerci, Ole Øiseth

*Strong wind characteristics and dynamic response of a long-span suspension bridge during a storm*

*Journal of Wind Engineering and Industrial Aerodynamics 2018:116–38*

Journal of Wind Engineering & Industrial Aerodynamics 172 (2018) 116–138

Contents lists available at ScienceDirect

Journal of Wind Engineering & Industrial Aerodynamics

journal homepage: www.elsevier.com/locate/jweia

# Strong wind characteristics and dynamic response of a long-span suspension bridge during a storm

Aksel Fenerci *, Ole Øiseth

*Department of Structural Engineering, Norwegian University of Science and Technology, Trondheim, Norway*

ARTICLE INFO

*Keywords:*
Suspension bridge
Wind-induced vibration
Buffeting response
Extra-tropical cyclone
Field measurement
Turbulence characteristics

ABSTRACT

As Storm Tor struck the western coast of Norway, wind speeds and bridge deck accelerations along the Hardanger Bridge girder were recorded by the monitoring system installed on the bridge. Using 13.5 h of data, mean wind speed, turbulence intensities, gust factor, turbulence length scales, angle-of-attack, and one-point and two-point turbulence spectra are studied using 10-minute stationary averaging intervals. Using the measured turbulence statistics as inputs, the buffeting response of the bridge deck is calculated in the frequency domain. The calculated response is compared with the measured response in terms of the root-mean-square (RMS) of acceleration and displacement components and the power spectral density of the acceleration response. Significant discrepancies are found in the case of the vertical response. Predicting the spectral response is found to be more difficult than predicting the RMS response, in particular for high-frequency responses. Considering the spanwise non-uniformity of turbulence statistics did not affect the predictions significantly.

## 1. Introduction

In Norway, Coastal Highway E39 lies along the western coast and connects Trondheim to Kristiansand in southern Norway, eventually reaching Aalborg in Denmark. Today, a drive on the 1100 km highway from Trondheim to Kristiansand is interrupted by seven ferries, which results in a travel time of approximately 21 h. The western coast is the most economically active region of Norway, where the majority of export goods are transported along the E39 route. Therefore, it is desirable to decrease travel time by replacing the ferry connections with bridges or subsea tunnels. This would involve crossing seven fjords ranging between 1500 and 5000 meters wide and between 600 and 1500 meters deep; for this purpose, bridges of unmatched scale would have to be built. Feasibility studies concerning such large scale bridge projects are being conducted by the Norwegian Public Roads Administration (NPRA) (Ellevset and Skorpa, 2011). The focus is mainly given to the largest crossings (Sognefjørden 3.7 km, Bjørnafjørden 5 km). Different bridge concepts such as super long-span suspension bridges, multi-span suspension bridges with floating towers and pontoon bridges are being considered for the crossings. As the global demand for longer span cable-supported bridges grows, design of such structures against wind effects becomes increasingly important.

Field measurements of mean wind speed and turbulence are indispensable in characterization of the wind turbulence field for design of long-span bridges against gusty wind action. Owing to the increasing number of measurement campaigns (Brownjohn et al., 1994; Cao et al., 2009; Cheynet et al., 2016; Choi, 1978; Cross et al., 2013; Hui et al., 2009a,b; Macdonald, 2003; Miyata et al., 2002; Wang et al., 2017) and structural health monitoring projects with wind measurements (Wang et al., 2009, 2011, 2013, 2014; Xu, 2013) around the world, more and more data on wind turbulence characteristics have been presented by researchers (Harstveit, 1996; He et al., 2013; Hu and Ou, 2013; Li et al., 2015; Peng et al., 2013). Such works provide valuable information on the general characteristics of the wind field (stationarity, homogeneity, and one-point and two-point statistics) at specific sites. Information regarding site-specific features, terrain effects and variability of the wind field are also beneficial in understanding the nature of gust loading on such structures (Pagnini and Solari, 2002; Solari and Piccardo, 2001). However, most of the listed studies concentrate on the Asia and Pacific with a focus on typhoon winds. Therefore, more data on the strong wind characteristics of European windstorms from relevant sites, such as Norwegian fjords, are required.

Stochastic dynamic analysis of wind-induced vibrations of cable-supported bridges was first introduced by Davenport (1962) and then improved by Scanlan (1978) with the introduction of flutter derivatives in the description of self-excited forces (Scanlan and Tomko, 1971).

* Corresponding author.
*E-mail address:* aksel.fenerci@ntnu.no (A. Fenerci).

https://doi.org/10.1016/j.jweia.2017.10.030
Received 10 July 2017; Received in revised form 30 October 2017; Accepted 30 October 2017

**Fig. 1.** Panoramic view of the Hardanger Bridge toward the west (photograph by Aksel Fenerci/NTNU).

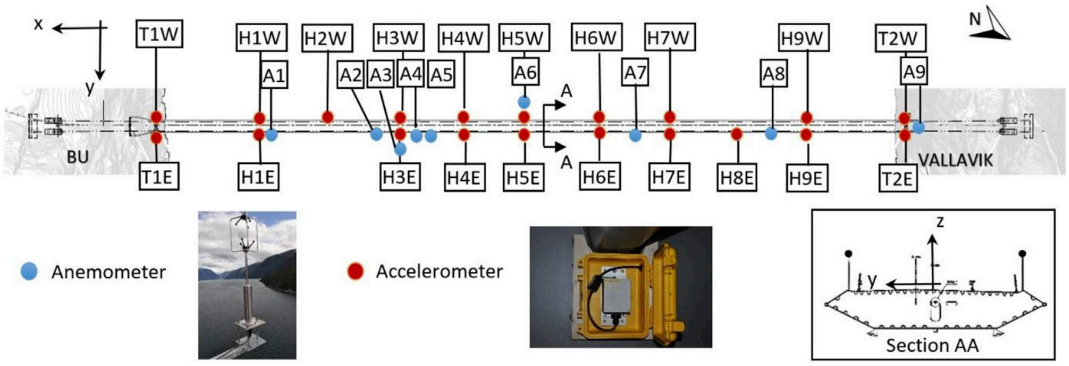


**Fig. 2.** The sensor layout.

Today, a multimode coupled approach (Chen et al., 2001; Jain et al., 1996; Katsuchi et al., 1998; Øiseth et al., 2010; Xu et al., 2000) is commonly used, where analysis may be conducted in either the frequency or time domain. Analyses considering skew-winds (Kimura and Tanaka, 1992; Wang et al., 2011; Xie et al., 1991; Xu et al., 2003; Xu and Zhu, 2005a; Zhu and Xu, 2005), full-bridge models (Xu et al., 2000) and spanwise non-uniform winds (Hu et al., 2017) were conducted by researchers. In recent years, non-stationary wind models have also been adopted by many (Chen et al., 2007; Chen, 2015; Hu et al., 2013, 2017; McCullough et al., 2014; Tao et al., 2017; Wang et al., 2016; Xu and Chen, 2004). Despite analytical efforts, few attempts have been made toward validation of these methods using full-scale measurements (Bietry et al., 1995; Cheynet et al., 2016; Macdonald, 2003; Park et al., 2012; Wang et al., 2011, 2013; Xu and Zhu, 2005b). Although satisfactory predictions were obtained by some, significant discrepancies were also observed, especially in the case of complex terrain, where the wind is variable, nonstationary and not homogenous. Moreover, the amount of data used for comparison is in general limited, especially under strong winds. Clearly, more comparisons, preferably from strong wind recordings, are needed for a better understanding of the limits of such analyses and the uncertainty involved, as well as the sources of uncertainty.

This paper concentrates on the strong wind characteristics and dynamic response of the Hardanger Bridge during a storm event. General information on wind conditions at the site and the bridge response were addressed in Fenerci et al. (2017), Fenerci and Øiseth (2017) and Fenerci and Øiseth (2016a,b). The wind speeds and accelerations at several locations along the bridge deck were measured by a dense sensor network. The wind turbulence statistics during the storm are presented using 10-sminute averaging intervals. Using the measured turbulence statistics, the wind field along the bridge is modeled separately for each interval, and the dynamic response is calculated accordingly. The measured and calculated dynamic responses are then compared, and the results are discussed.

**Table 1**
Sensor names and coordinates.

| Wind sensors | | | | Accelerometers | | | |
|---|---|---|---|---|---|---|---|
| Name | x (m) | y (m) | z (m) | Name | x (m) | y (m) | z (m) |
| A1 | 460 | 7.25 | 0.3 | H1E/H1W | 480 | 6.33/-6.64 | −8.38 |
| A2 | 280 | 7.25 | 3.2 | H2W | 360 | −6.64 | −6.41 |
| A3 | 240 | 7.25 | 3.9 | H3E/H3W | 240 | 6.33/-6.64 | −4.45 |
| A4 | 200 | 7.25 | 4.6 | H4E/H4W | 120 | 6.33/-6.64 | −2.48 |
| A5 | 180 | 7.25 | 4.9 | H5E/H5W | −7 | 6.33/-6.64 | −0.4 |
| A6 | −10 | −7.25 | 8 | H6E/H6W | −120 | 6.33/-6.64 | −2.25 |
| A7 | −180 | 7.25 | 5.2 | H7E/H7W | −240 | 6.33/-6.64 | −4.22 |
| A8 | −420 | 7.25 | 1.2 | H8E | −360 | 6.33 | −6.18 |
| A9 | −655 | 4.5 | 140 | H9E/H9W | −480 | 6.33/-6.64 | −8.15 |
| | | | | T1E/T1W | 655 | 4.5/-4.5 | 120.5 |
| | | | | T2E/T2W | −655 | 4.5/-4.5 | 120.5 |

## 2. Hardanger Bridge and the monitoring system

The Hardanger Bridge (HB) is currently the longest suspension bridge in Norway with a single span of 1308 meters (Fig. 1). It is located in mountainous terrain in Norwegian fjords and is subjected to strong European windstorms. The unique wind exposure of the site and the slender deck of the bridge make it an attractive case study when investigating the wind-induced dynamic response of long-span suspension bridges in such complex terrain. For this reason, shortly after the bridge was opened to the public in 2013, it was instrumented by a state-of-the-art monitoring system to measure wind velocities and accelerations along the girder. The system is comprised of 20 accelerations and 9 anemometers, where the data is transferred on the bridge by Wi-Fi and synced by GPS time. The sensor layout is shown in Fig. 2, and the coordinates of each sensor are listed in Table 1, where the origin of the coordinate system was taken as the midspan of the bridge. Detailed information on the HB and the workings of the monitoring system can be found in Fenerci and Øiseth (2017).

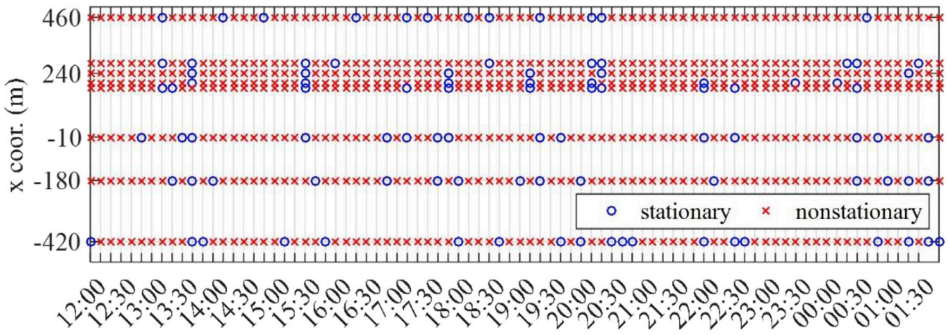


**Fig. 3.** Stationarity test on 10-minute recordings.

## 3. Storm Tor

On 29-30th January 2016, a European windstorm struck the coastline of Norway, Scotland and northern parts of Ireland and England. The extratropical cyclone was named and referred to as "Storm Tor" by the Norwegian Meteorological Institute, "Storm Gertrude" by the UK Met Office and Met Eirann of Ireland and "Storm Marita" by the Free University of Berlin in Germany. It will be referred to as "Storm Tor" here, adopting the Norwegian name. This severe storm affected several regions along the Norwegian coast, such as Sør-Trondelag, Møre og Romsdal, Sogn og Fjordane and also Hordaland, where the HB is located. The highest mean wind speed recorded during the storm was 48.9 m/s in a 10-minute averaging interval, and the highest measured gust was 61.7 m/s, both of which were recorded at a height of 75 m above ground at the Kråkenes Lighthouse in Møre og Romsdal. This was the highest wind speed officially recorded in Norway (Kristiansen et al., 2016). A public report by the Norwegian Meteoroligical Institute (2016) reported significant property damage (≈ 450 million NOK). Many regions were without power during the storm. The passage of the storm through the HB site has been successfully recorded by the HB monitoring system. The bridge was closed to traffic during most of the storm. Mean wind speeds of up to 30 m/s and wind gusts of up to 37 m/s were measured by the anemometers on the bridge, which were the highest recorded, during the first four-year period of the measurement campaign. Strong winds were recorded on both the 29th and 30th of January. However, in the rest of the paper, a continuous 13.5 h period will be considered from 29th January at 12:00 (UTC time) until 30th January 1.30, where the highest wind speeds were recorded.

## 4. Wind turbulence characteristics

### 4.1. General

The wind velocity data acquired through eight anemometers (A1-A8) located at the HB deck were used to study the wind characteristics of Storm Tor. All anemometers are attached to the hangers of the bridge at a height of 8 meters from the bridge girder to avoid the disturbance of the wind flow due to the bridge deck. It should be noted that the z-coordinates of the anemometers are not the same due to the curvature of the bridge. The wind data were initially sampled at 32 Hz in polar coordinates and then downsampled to 20 Hz to have a common sampling rate with the acceleration data. When studying wind turbulence characteristics relevant to the dynamic response of land-based structures, it is customary to decompose the wind speed to its mean and fluctuating components, considering a certain averaging interval. Depending on the region and nature of the wind, an averaging interval between 1 min and 1 h is generally adopted, where the wind flow is considered sufficiently stationary. Defining a new coordinate system aligned in the direction of the mean wind speed (U), three orthogonal fluctuating wind components, namely, the along-wind (u), cross-wind (v) and vertical (w) turbulences are defined. The three turbulence components are then assumed as zero-mean stationary Gaussian random processes.

It is important that these assumptions be reasonably valid since the classical methods of wind induced response analysis of structures rely on these assumptions. Methods such as the run test or the reverse arrangement test (Bendat and Piersol, 2000) were previously used on wind records to assess their stationarity (Cao et al., 2009, 2015; Tao et al., 2017). However, such methods provide an evaluation of randomness rather than stationarity and can be effective in highlighting underlying trends in wind records. A run test, following the work of Cao et al. (2015), was employed to assess the stationarity of 10-minute wind time series (U (t) + u (t)) obtained from the eight anemometers along the HB span, and the results are shown in Fig. 3. The majority of the recordings failed the test at a 5% significance level using 30 segments per signal, and no reasonable pattern of nonstationarity could be extracted. It is also observed that the test is highly dependent on the segment size and does not provide objective means for evaluation of stationarity. Recent studies

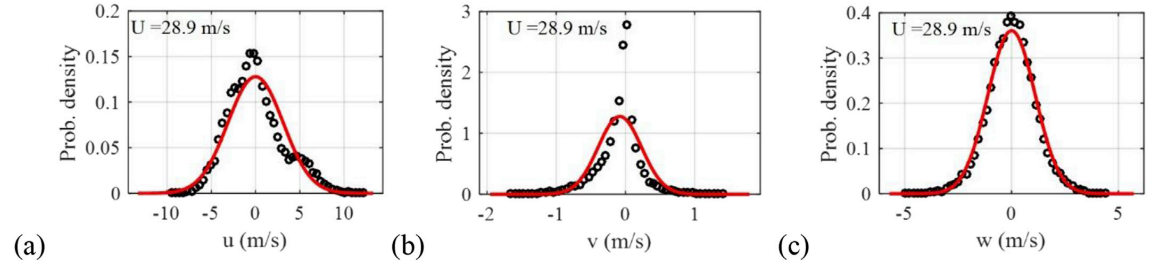


**Fig. 4.** Probability distributions of turbulence components for a 10-minute recording recoded on 29/01/2016 between 18:40 and 18:50: (a) along-wind, (b) cross-wind and (c) vertical components.

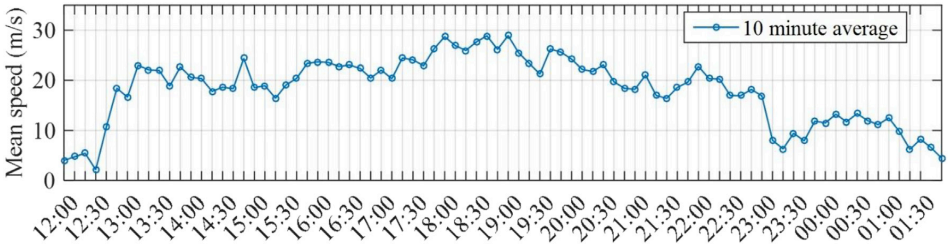


**Fig. 5.** Mean wind speed at the midspan (sensor A6).

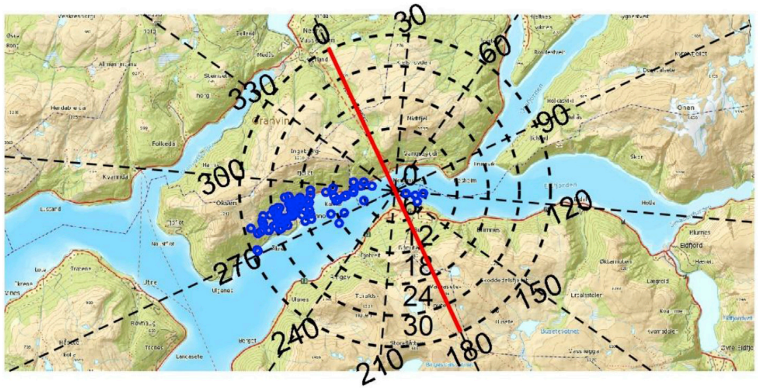


**Fig. 6.** Wind rose plot of 10-minute mean wind speed at the midspan (m/s) (base map courtesy of ©Kartverket, www.kartverket.no).

(Chen et al., 2007; Tao et al., 2017; Wang et al., 2016) also showed that when there is no abrupt change in the wind direction or speed in the considered averaging interval, the wind statistics obtained with stationary and nonstationary models do not vary significantly. It has been reported that the discrepancy is high in length scales and very low-frequency part of the along-wind turbulence spectra because these are sensitive to the slowly varying mean speed. It should be noted that such discrepancies are not important for the wind field model adopted here. Also, experience suggests that a 10-min averaging interval is appropriate to minimize such slowly varying components. Therefore, owing to its extensive use in practice and wind-resistant design codes, the traditional stationary wind model will be used in this study. Quantification of the uncertainty introduced by the nonstationarity of the wind time series on the wind statistics and response prediction requires a nonstationary analysis, which is considered out of scope for this paper, where the aim is to evaluate the performance of state-of-the-art methods.

Probability distributions of turbulence components for a 10-minute recording are plotted along with a normal distribution fit to demonstrate the normality of the data (Fig. 4). It is seen that the distributions of u and w components agree reasonably well with the Gaussian distribution, where the v component does not, presumably due to the effect of the mountains on either side of the bridge.

### 4.2. Mean wind speed and direction

The 10-minute mean wind speed during the storm is plotted in Fig. 5 using the data from the midspan sensor (A6). As is easily observed from the plot, the wind speed rapidly increased in the beginning of the storm and reached 20 m/s around 13.00. The strong winds were sustained until 23.00, where the wind speed decreased to approximately 10 m/s suddenly. In this ten-hour period, the wind speed was generally in the 20–25 m/s range, except for the one hour period between 18.00 and 19.00, where it reached its peak of approximately 30 m/s. Including the built-up phase and the end of the storm, a total of 13.5 h of well-acquired data are considered to study the storm. The mean wind speed data are also plotted in Fig. 6 in a wind rose on the topographical map of the

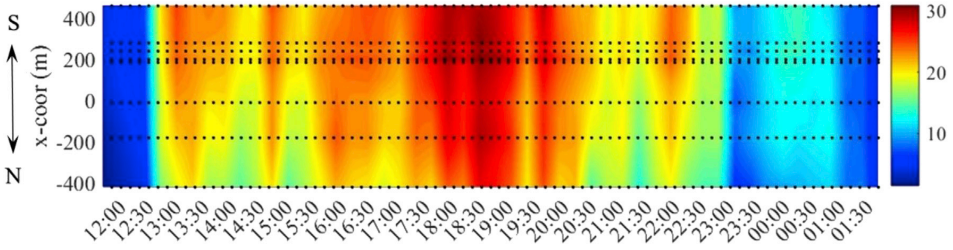


**Fig. 7.** Contour plot of mean wind speed.

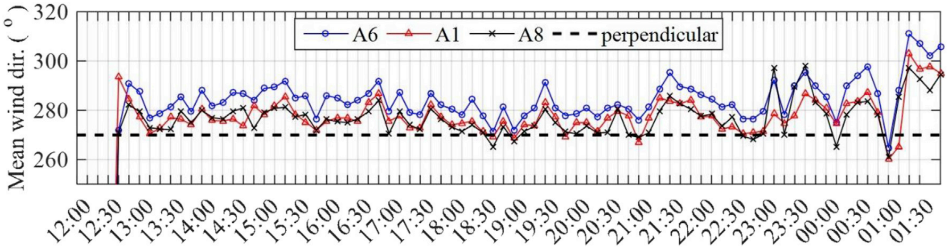


**Fig. 8.** Mean wind direction from anemometers A1, A6 and A8.

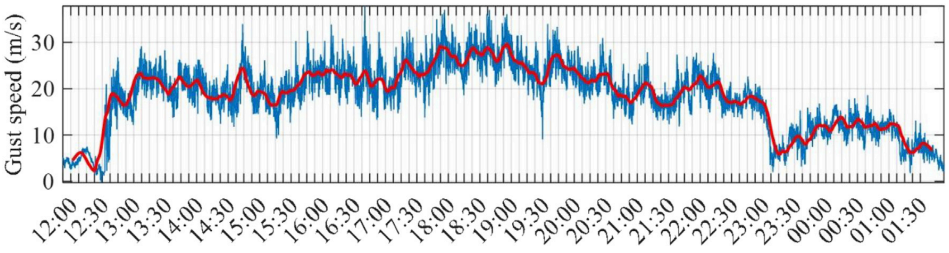


**Fig. 9.** Gust wind speed with 10-minute moving mean wind speed at the midspan (sensor A6).

region to show the direction of the wind and the upwind topographical conditions. As shown in the figure, the storm winds were nearly perpendicular to the bridge longitudinal axis, where the wind direction was sustained during the storm. A contour plot was also generated using the data from all sensors to show the variation of the wind speed along the bridge span (Fig. 7). The data points are highlighted in the plot, where the contour was obtained using linear interpolation between points. In general, higher mean wind speeds were measured toward the south end of the bridge during the storm. Finally, the time histories of wind directions shown in Fig. 8 are plotted for three anemometers: one at the midspan (A6) and two at either end of the bridge span (A1 & A8). It is seen that the wind direction measured at A1 and A8 were very close to each other, where slightly more skewed winds were measured at the midspan sensor.

### 4.3. Gust wind speed and gust factor

The gust wind speed is obtained by averaging the wind speed in a

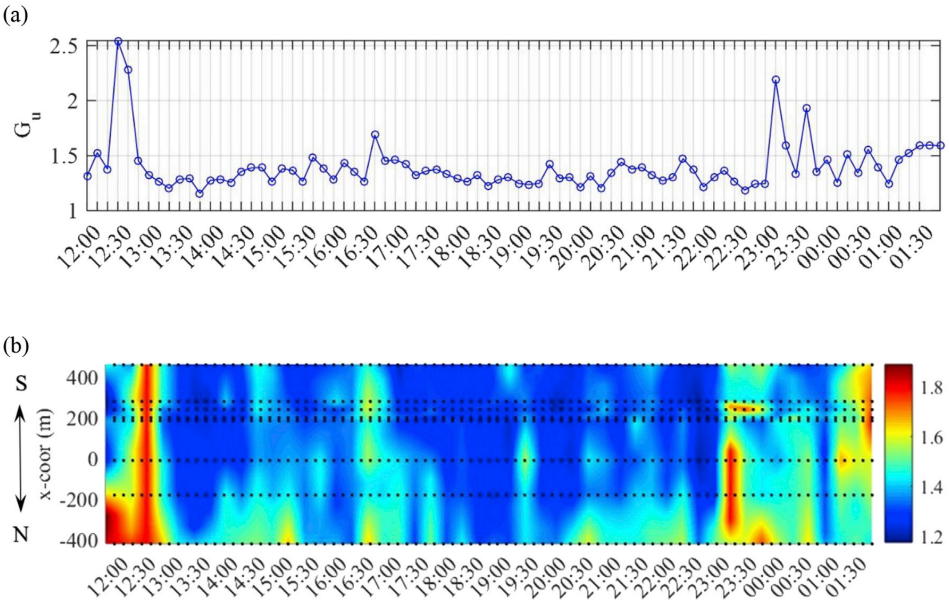


**Fig. 10.** Gust factor (a) at the midspan and (b) contour plot.

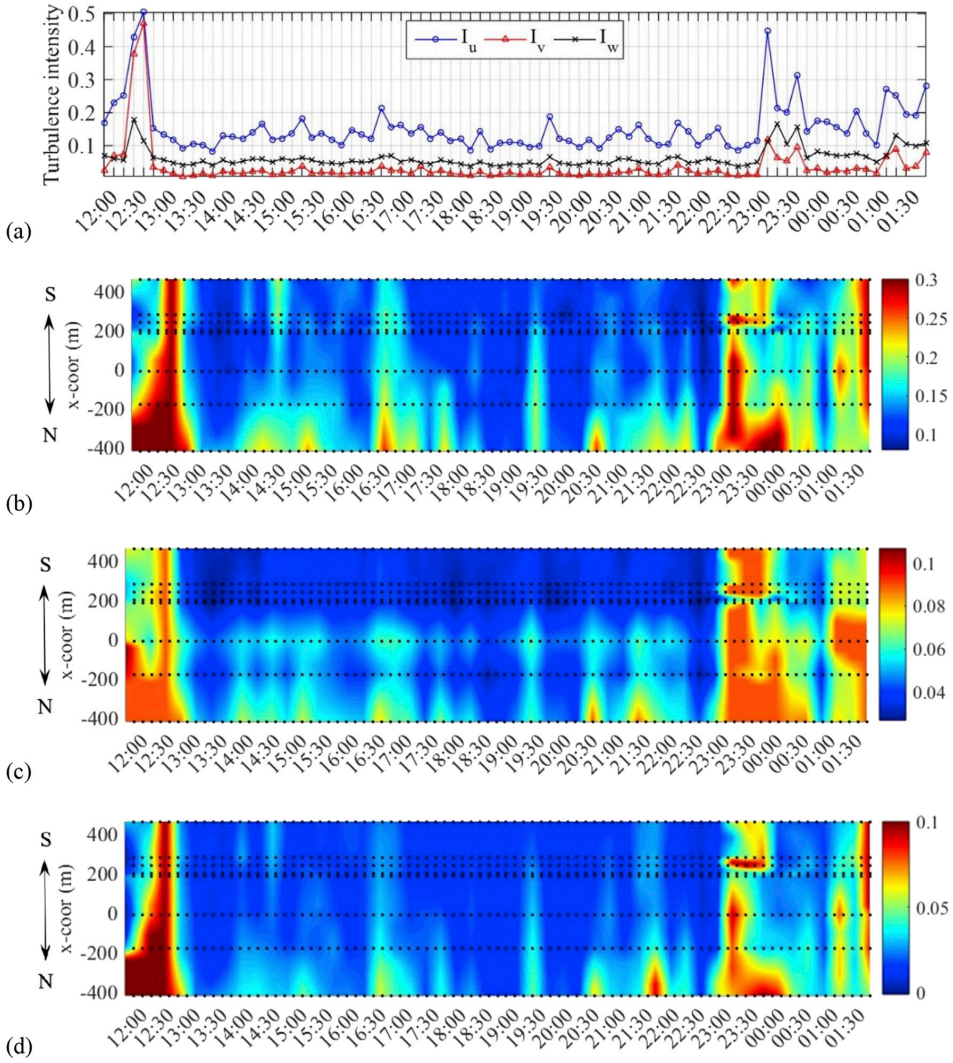


**Fig. 11.** Turbulence intensity (a) at the midspan and contour plots: (b) $I_u$ (c) $I_v$ (d) $I_w$.

much shorter interval than the mean wind speed and is used to represent sudden changes in wind speed (gusts), which are more closely related to the dynamic response of structures (Cao et al., 2015; Holmes, 2007; Krayer and Marshall, 1992; Kwon and Kareem, 2014; Shu et al., 2015). Typically, a gust averaging interval of 2–3 s is adopted to estimate the highest instantaneous wind speed. A gust factor is also commonly used to convert mean wind speed to gust wind speed, especially in the design of structures subjected to gusty winds. It can be written as

$$G_u = \frac{|u_t|_{\max}}{U_T} \tag{1}$$

where $u_t$ is the gust speed averaged over gust interval t and $U_T$ is the mean wind speed with averaging interval T. The gust wind speed and the gust factor for the 10-minute recordings of Storm Tor were calculated using a 3-second gust averaging interval and presented in Fig. 9. In the figure, a running 10-minute mean wind speed is also plotted on top of the gust speed to show the evolution of the 10-min mean wind speed. The maximum gust speed was around 37 m/s. The gust factor at the midspan is given in Fig. 10a. The gust factor seems sensitive to the stationarity of the signal. Typically, high gust factors were obtained when the wind speed or direction was changing rapidly; i.e., there is a profound trend in the time series. Discarding those, the gust factor was around 1.3–1.5 during the storm. A contour plot of the gust factor is also presented in Fig. 10b. The gust factor was in general larger at the north end of the bridge.

### 4.4. Turbulence intensity

Turbulence intensity is the ratio of the standard deviation of the turbulence components ($\sigma_u$, $\sigma_v$, $\sigma_w$) to the mean wind velocity (U), and it

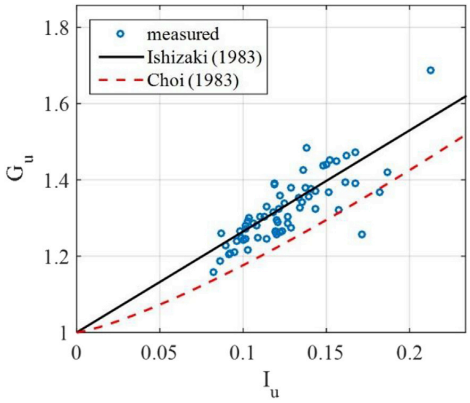


**Fig. 12.** Gust factor vs. along-wind turbulence intensity at the midspan.

is of vital importance in predicting the dynamic response since it is a direct measure of the energy content of turbulence. Turbulence intensities for the three turbulence components ($I_u$, $I_v$, $I_w$) are given in Fig. 11a for the midspan and Fig. 11b–d for all sensors using contour plots. Similar to the gust factor, high turbulence intensities were associated with the non-stationary signals. During the sustained part of the storm, along-wind turbulence intensity ($I_u$) varied between 10 and 20%, and vertical turbulence intensity ($I_w$) varied between 4 and 6%. Cross-wind turbulence intensity ($I_v$) was around 2%. The contour plots of turbulence intensities show a similar pattern to the gust factor (Fig. 10), with higher values toward the north. The ratio $I_u$:$I_v$:$I_w$ between the turbulence intensities is calculated as 1:0.14:0.4 using the mean values (0.125:0.018:0.051). Only recordings above 15 m/s were considered not to include the severely non-stationary recordings. The relation between turbulence intensity and gust factor is given in Fig. 12 along with two empirical models (Choi, 1983; Ishizaki, 1983). The correlation between two statistical parameters are apparent, and the model by Ishizaki (1983) gives a good approximation of the data for this particular storm.

### 4.5. Cross-correlation of u-w turbulence

The one-point correlation of the u and w turbulence components is assessed through the cross correlation coefficient, given as

$$\gamma_{uw} = \frac{\sigma_{uw}}{\sqrt{\sigma_u \sigma_w}}, \quad \sigma_{uw} = \frac{1}{N-1}\sum_{i=1}^{N}(u_i - \mu_u)^*(w_i - \mu_w) \tag{2}$$

where $\sigma_{uw}$denotes the cross-covariance of the turbulence components and $\sigma_u, \sigma_w$are the standard deviations. The cross-correlation coefficient will then assume a value between −1 and 1, and it relates to the vertical shear or energy loss of turbulence due to ground roughness. The cross-correlation coefficient of u and w components were calculated for all recordings, and they are presented in Fig. 13. It is observed that the correlation between the u and w components was in general positive, contradicting the theoretical consideration in flat homogenous terrain and the neutral boundary layer. The average cross-correlation coefficient was 0.067, where the corresponding cross-covariance was 0.17.

### 4.6. Turbulence length scale

The length scales of turbulence are the average length of turbulent eddies and hence give valuable information on the spectral content of the turbulence components. In the along-wind direction, three turbulence length scales ($L_u$, $L_v$, $L_w$) can be defined. If Taylor's hypothesis of frozen turbulence is assumed valid, the length scales in the along-wind direction can be estimated using the time auto-correlation of the turbulence components. The three length scales were calculated for the 10-minute recordings using the midspan sensor, and they are presented in Fig. 14 with recommendations of ESDU (2001a,b) and N400 (Norwegian bridge design handbook, Statens-Vegvesen, 2009). The estimated length scales show immense variability between 10-min recordings of the same storm, especially for the along-wind component, and the recommended values both by N400 (178:44:15 m) and ESDU (240:20:20 m) were in general much smaller compared to the calculated values. In this case, it should also be noted that since low frequency components in the turbulence recordings are of utmost importance in the calculation of the length scales, results are very sensitive to the signal stationarity and trends in the data. Since none of the recorded signals is strictly stationary, generally high values are obtained from measurements, with significant variability. This was also observed in the work of Tao et al. (2017), where a nonstationary analysis was carried out. Using average values, the $L_u$:$L_v$:$L_w$ ratio was around 1:0.3:0.2 (539:168:104 meters). Consequently, for the terrain in consideration, the use of length scales with the stationary wind model should be avoided when possible due to the randomness in field data and its sensitivity to signal stationarity.

Since a one-hour averaging interval is also commonly used in the calculation of length scales, one-hour length scales were also calculated for the sake of comparison. Considering only the strong wind part of the storm, length scales of 1900 meters and 138 meters were obtained in average for the along-wind and vertical turbulences, respectively. It is seen that the vertical length scales were more or less the same, but the along-wind length scales increased even more, where the variability in results persisted. This is due to the sensitivity of the auto-correlation function to the low-frequency components in the signals. Consequently, if there are slowly varying trends in the mean wind speed; it appears as a low-frequency correlation in the auto-correlation function, resulting into high estimates of the along-wind integral length scale. The difference can easily be observed in Fig. 15, where the autocorrelation function estimate for a 1-hour recording is compared with the average of estimates for 10-minute segments. It is apparent that the auto-correlation function is much higher for the longer recording, due to nonstationary components in the signal and this is consistent throughout the storm.

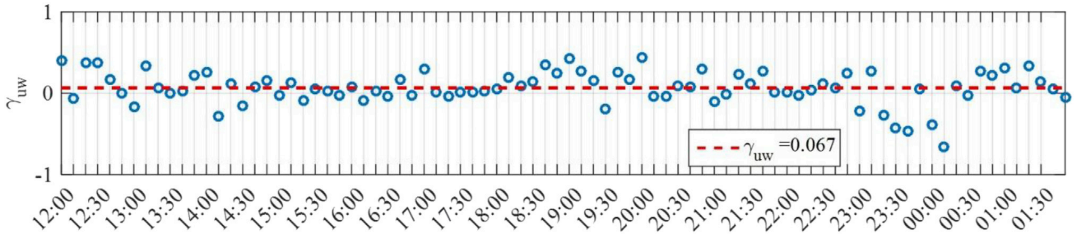


**Fig. 13.** Cross-correlation coefficient of u and w turbulence components at the midspan.

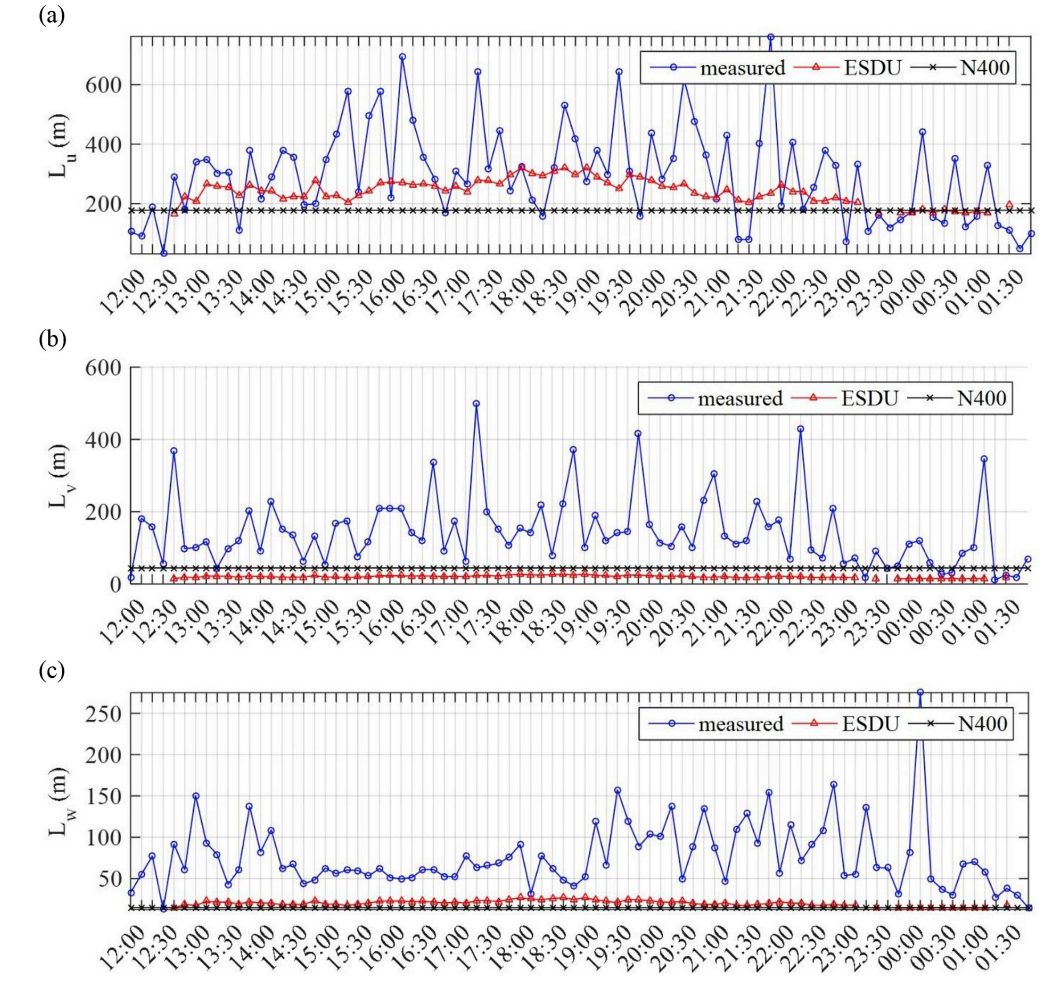


**Fig. 14.** Turbulence length scales: (a) along-wind (b) cross-wind and (c) vertical components.

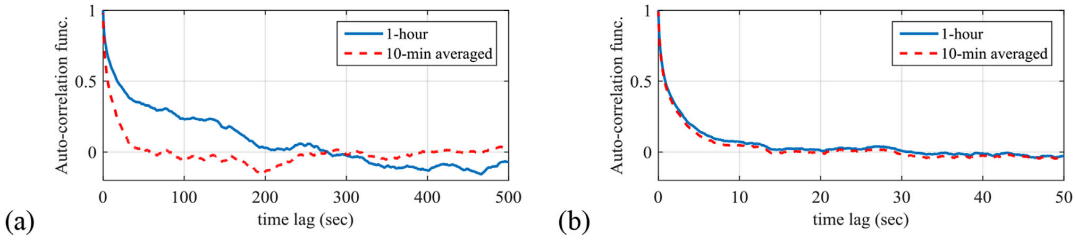


**Fig. 15.** The effect of averaging interval on the auto-correlation functions: (a) along-wind and (b) vertical turbulence.

### 4.7. Angle-of-attack

The angle-of-attack is defined here as the angle between the mean wind velocity vector and the horizontal plane. For the 10-minute recordings, the angle-of-attack was calculated using the midspan anemometer data, and the results are presented in Fig. 16. It is seen that the wind velocity vector was consistently inclined around 2.5° upwards on average during the whole storm.

### 4.8. One-point spectra of turbulence

In wind-induced dynamic response prediction of long-span cable-supported bridges, the buffeting load on the structure is generally described by a cross-spectral density matrix, including one-point and

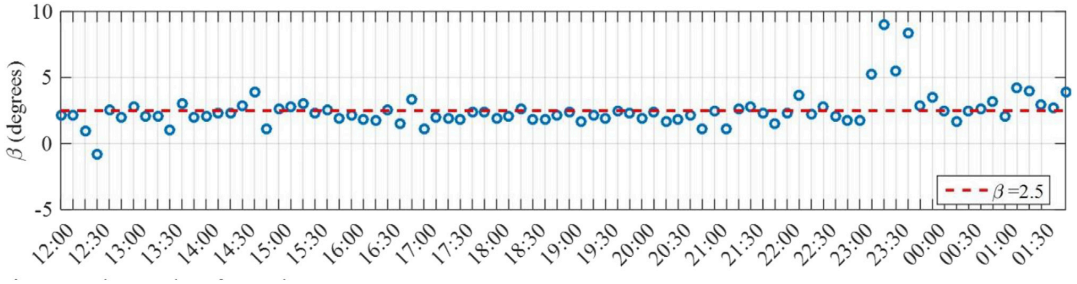


**Fig. 16.** The angle-of-attack.

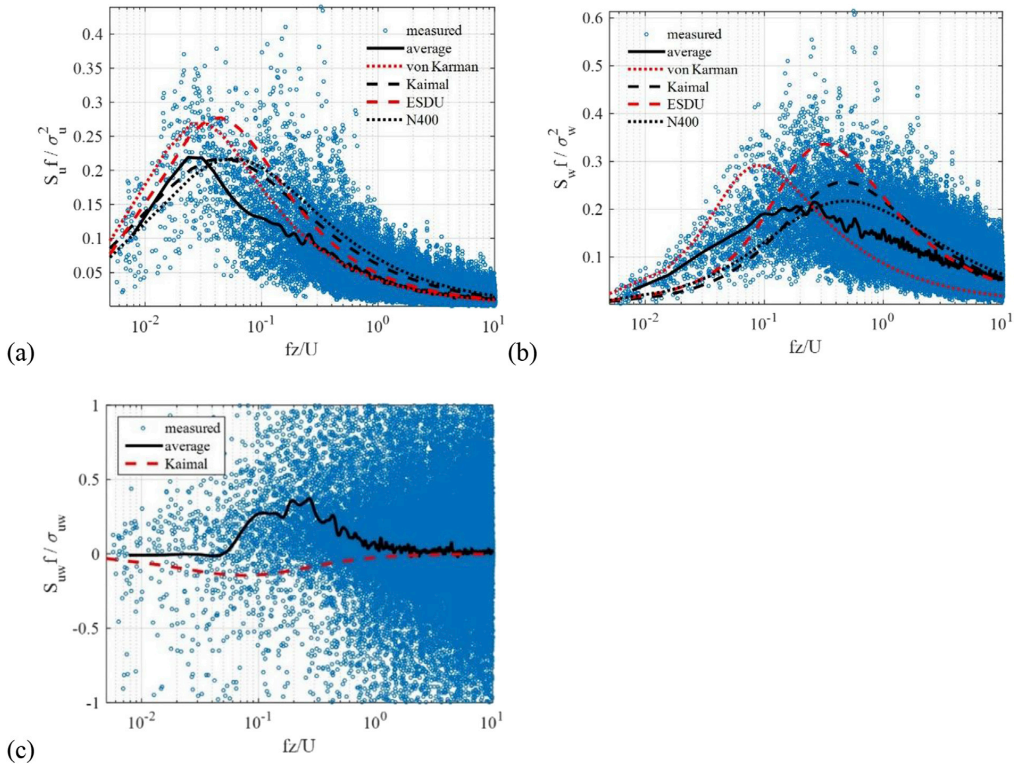


**Fig. 17.** One-point spectra of turbulence at the midspan: (a) auto-spectra of along-wind turbulence, (b) auto-spectra of vertical turbulence and (c) cross-spectra of along-wind and vertical turbulences.

two-point statistics of the along-wind and vertical turbulence components. Therefore, a good representation of spectral characteristics of turbulence is crucial for accurate response prediction. The one-point auto and cross spectra of the u and w components at the midspan were calculated for all recordings above a mean wind speed of 15 m/s using Welch's (1967) averaged periodogram method with eight segments and 50% overlap. The spectra are shown in Fig. 17. The scatter in the data can immediately be observed despite the averaging of the periodogram estimates. The average spectra of all recordings are also shown in Fig. 17, along with several analytical spectra given by Kaimal et al. (1972), von Karman (1948), ESDU (2001a,b) and N400 (Statens-Vegvesen, 2009). It is seen that in the average sense, the analytical spectra were not successful in capturing the peak of the along-wind turbulence spectra. The turbulence spectra were also estimated using a one-hour averaging interval. In this case, six segments with 75% overlap was used to average the periodogram estimates. This resulted in an increased frequency resolution of 0.0003052 Hz. In return, the estimates have larger variance due to lower number of averaged segments. The estimates are shown in Fig. 18. It is seen that the vertical turbulence spectra remained almost unchanged, where the peak of the along-wind turbulence spectra was moved to lower frequencies. This also roots from the fact that the signals are nonstationary and accommodate slowly varying trends. Nevertheless, it should be stressed again that the wind field model used here will not be affected greatly from such trends since it is not strongly dependent on the length scale estimates or the very low-frequency part of the turbulence spectra.

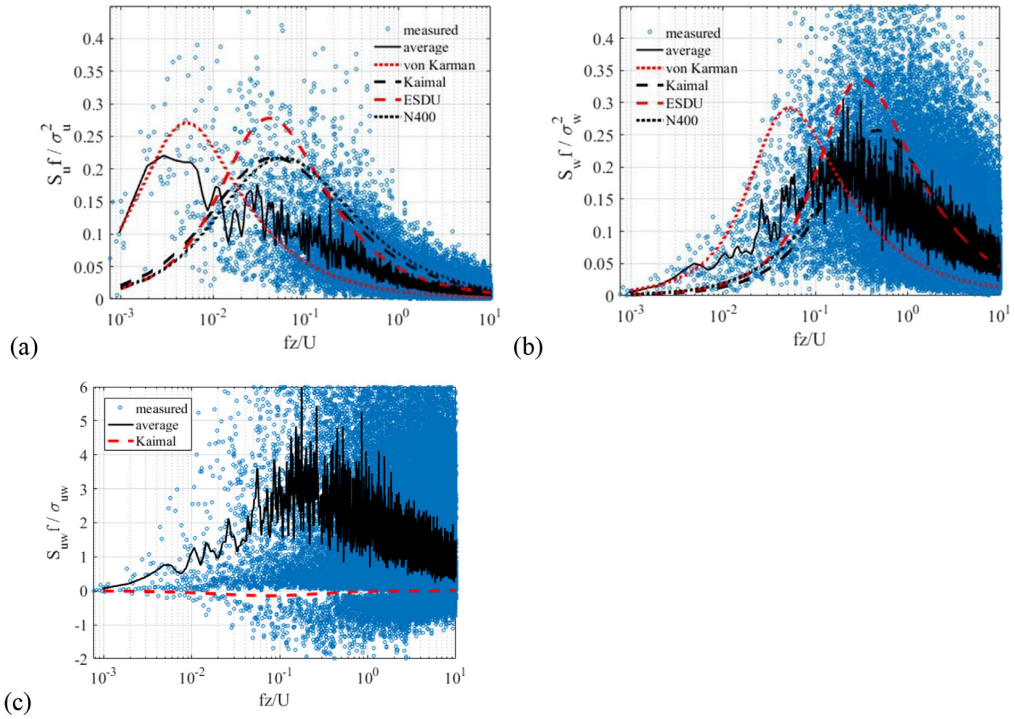


**Fig. 18.** One-point spectra of turbulence at the midspan using a one-hour averaging interval: (a) auto-spectra of along-wind turbulence, (b) auto-spectra of vertical turbulence and (c) cross-spectra of along-wind and vertical turbulences.

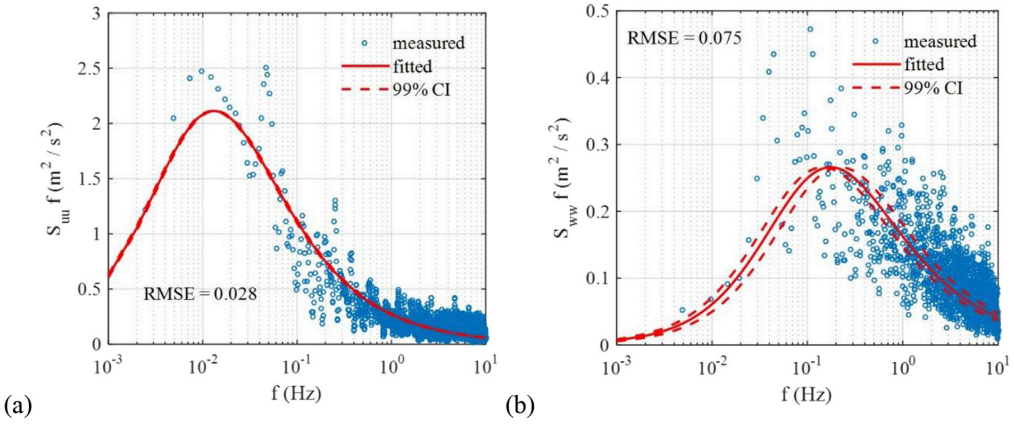


**Fig. 19.** Fitting of the one-point spectra using Eqn. (3) using a 10-minute recording recoded on 29/01/2016 between 18:40 and 18:50. ($A_u = 32.3$, $A_w = 2.42$, RMSE = root-mean-squared-error, CI = confidence interval) (a) auto-spectra of along-wind turbulence, (b) auto-spectra of vertical turbulence.

The measurement data also accommodate significant variability, making it difficult to deduce a single spectral expression for the entire storm. Therefore, a Kaimal-type expression (Kaimal et al., 1972; Solari and Piccardo, 2001) was fitted in the least-squares sense to the estimated 10-min spectra. The parametric spectral formula is written as

$$\frac{S_{u,w}f}{\sigma_{u,w}^2} = \frac{A_{u,w}f_z}{\left(1 + 1.5A_{u,w}f_z\right)^{5/3}}, \quad f_z = \frac{fz}{U} \tag{3}$$

where $A_{u,w}$ are the parameters to be fitted. In the expression, $S_{u,w}$ denote the auto-spectral densities, f denotes frequency in Hz and z denotes the height above ground (68 m for the midspan). An example fit is demonstrated in Fig. 19 with its 99% confidence intervals for a 10-min recording with 29 m/s mean wind velocity. The root-mean-square error (RMSE) values giving the standard error of the fit are also indicated in the figure. From visual observations and RMSE values, it can be stated that the fitted curves give a reasonable approximation of the measured

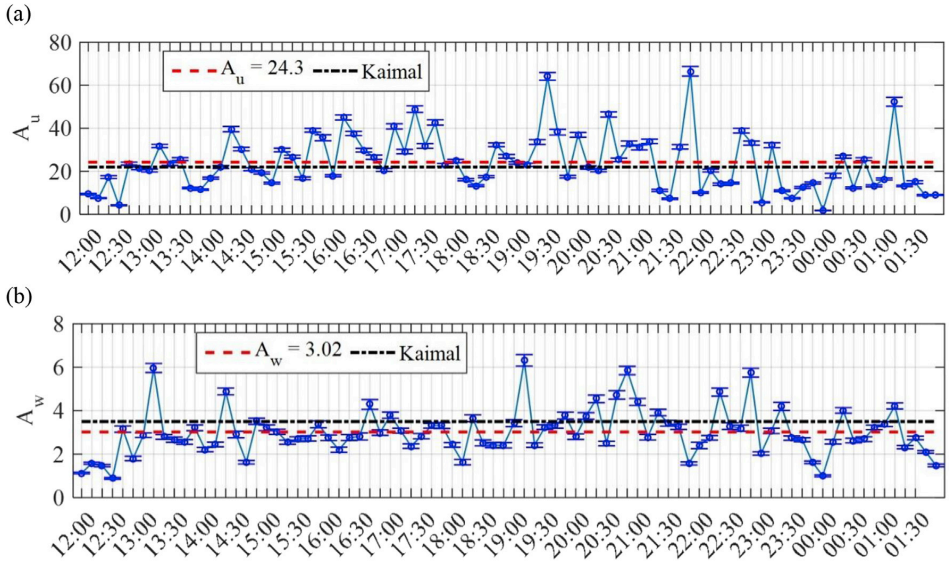


**Fig. 20.** Spectral parameters at the midspan: (a) $A_u$ and (b) $A_w$ (error bars show the 99% confidence intervals).

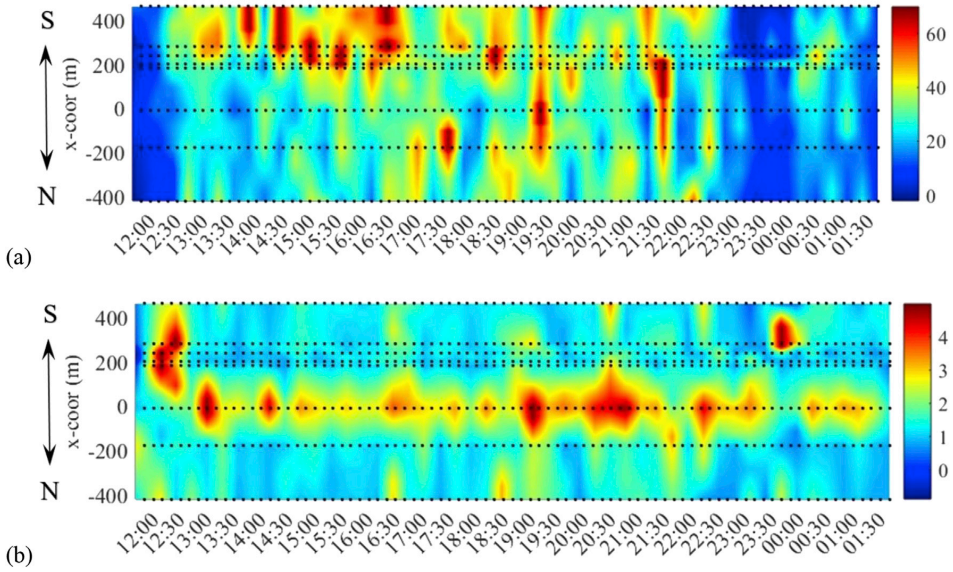


**Fig. 21.** Contour plots of spectral parameters: (a) $A_u$ and (b) $A_w$.

spectra. It should be noted that the fit is made only for the part of the spectra up to 1 Hz, which is considered the important frequency range for dynamic response calculations; however, reasonable agreement with the data is observed also in the higher frequency range.

The spectral parameters $A_{u,w}$ were then calculated for all 10-minute recordings. The results are presented for the midspan sensor in Fig. 20 and as contour plots in Fig. 21. 99% confidence intervals for the parameters are also shown in the figures using error bars. It is seen that the parameters showed variation between 10-minute recordings during the storm. The average values, which are also shown on the plots, were quite similar to the values of the Kaimal spectra. The parameter $A_w$ was relatively more stable compared to $A_u$ during the storm. The $A_u$ was in general higher toward the south side, where $A_w$ was consistently higher at the midspan of the bridge.

The parameters $A_{u,w}$ were then plotted against the previously obtained integral length scales for the recordings with mean speed higher than 15 m/s (Fig. 22). An apparent correlation is observed in the case of the along-wind component, where the measurements show random scatter for the vertical component.

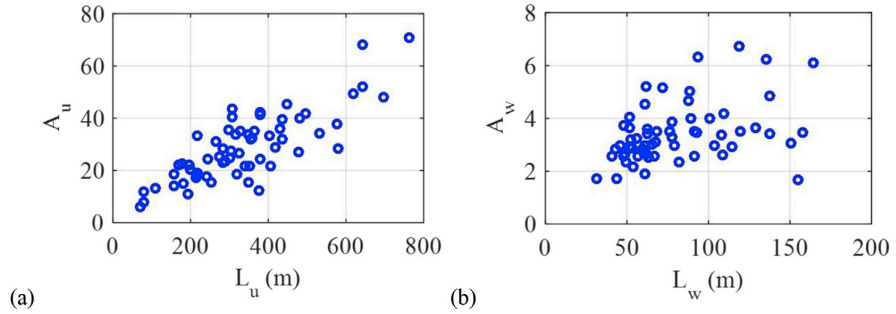


**Fig. 22.** Spectral parameter vs. length scale: (a) along-wind turbulence and (b) vertical turbulence.

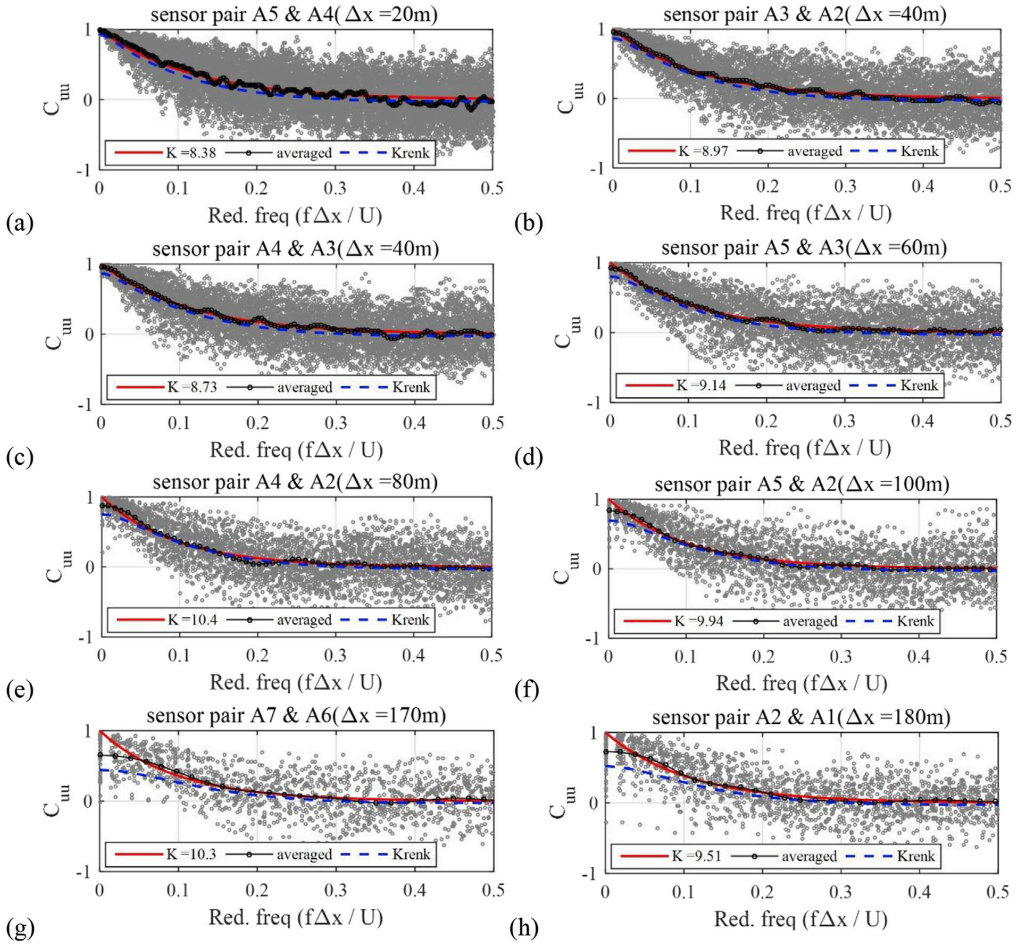


**Fig. 23.** Normalized cross-spectra of along-wind turbulence for several separation distances: (a) Δx = 20 m, (b) Δx = 40 m, (c) Δx = 40 m, (d) Δx = 60 m, (e) Δx = 80 m, (f) Δx = 100 m, (g) Δx = 170 m and (h) Δx = 180 m.

### *4.9. Normalized cross-spectra of turbulence*

In addition to the one-point statistics of turbulence, its spanwise correlation structure should be well defined for accurate prediction of the bridge dynamic response (Cheynet et al. 2016; Kristensen and Jensen 1979; Mann 2006; Toriumi et al. 2000). In the frequency domain, this is usually achieved with the help of a normalized cross-spectrum, which is essentially a frequency dependent cross-correlation coefficient. For two

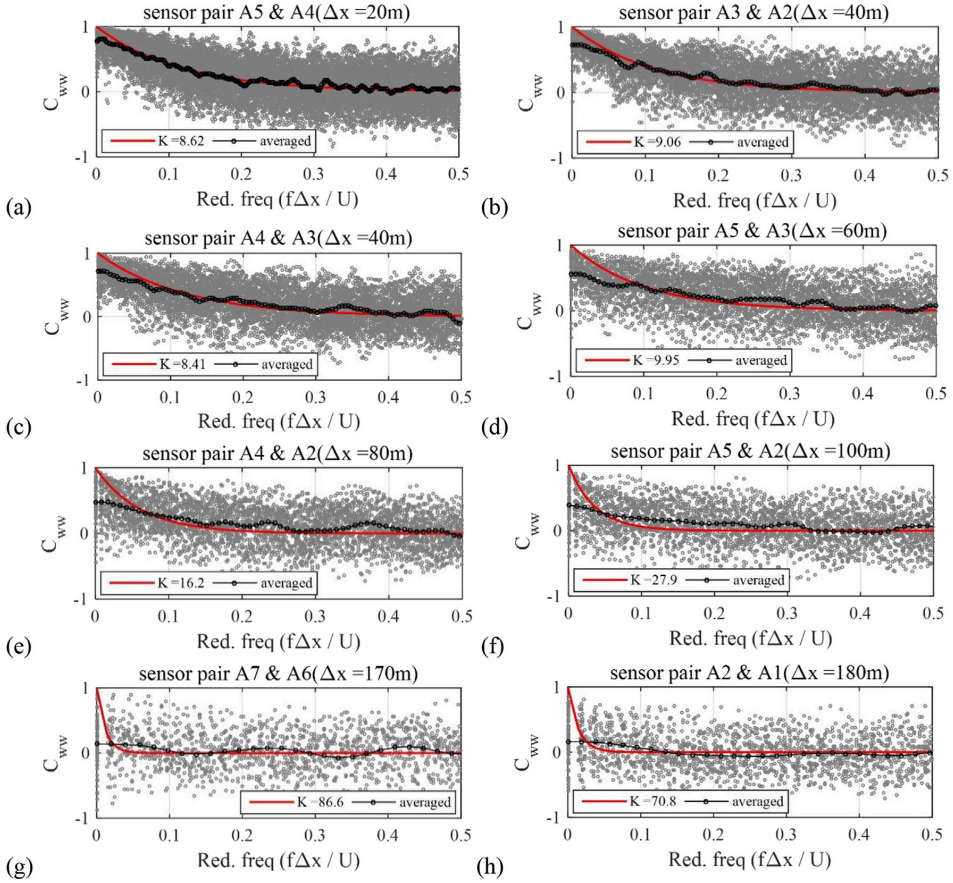


**Fig. 24.** Normalized cross-spectra of vertical turbulence for several separation distances: (a) Δx = 20 m, (b) Δx = 40 m, (c) Δx = 40 m, (d) Δx = 60 m, (e) Δx = 80 m, (f) Δx = 100 m, (g) Δx = 170 m and (h) Δx = 180 m.

points along the bridge separated by a distance Δx, the normalized cross-spectral density is defined as

$$C_{mn}(f,\Delta x) = \frac{S_{mn}(f)}{\sqrt{S_m(f)S_n(f)}},\quad n \in \{u,w\},\quad m \in \{u,w\} \tag{4}$$

where $S_{mn}$ is the cross-spectral density of turbulence at two points separated by Δx. Consequently, the normalized cross-spectral density can attain both negative and positive values and has real and imaginary parts. Its imaginary part includes the phase information and is usually neglected for separations normal to the wind direction (ESDU 2001a,b; Simiu and Scanlan 1996).

Owing to the dense wind sensor network along the bridge span, the normalized cross-spectra of turbulence can be calculated for many separation distances. Using eight different sensor pair combinations, the normalized cross-spectra were calculated for the 10-minute recordings during the strong wind part of the storm (U > 15 m/s). The estimates for different sensor pairs are plotted against a non-dimensional frequency (f Δx/U) and shown in Figs. 23–25. In the calculations, separation distances were taken as the distances between sensors, since wind direction was mostly perpendicular to the bridge longitudinal axis. Spectral estimations were carried out using Welch's method, as described in the previous

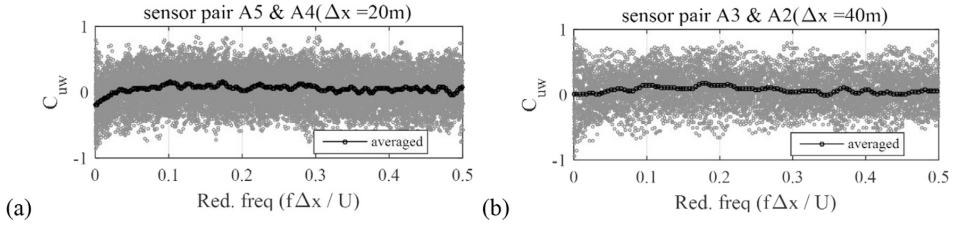


**Fig. 25.** Normalized cross-spectra of along-wind and vertical turbulence: (a) Δx = 20 m, (b) Δx = 40 m.

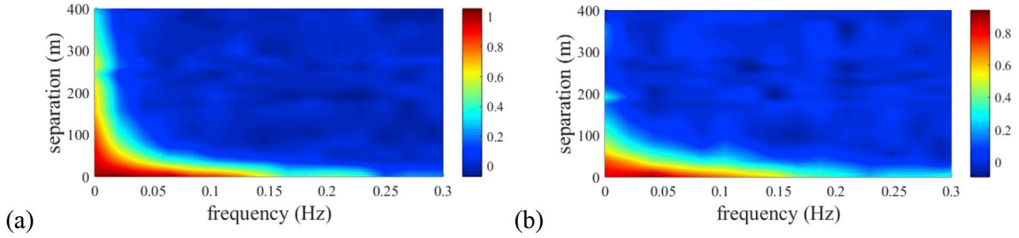


**Fig. 26.** Normalized cross-spectra of turbulence estimated from data (a) $C_{uu}$ and (b) $C_{ww}$.

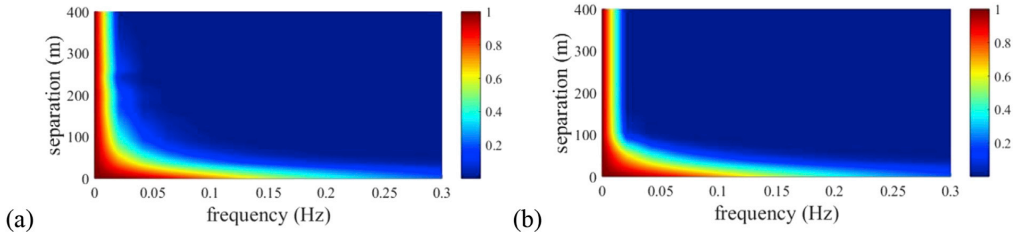


**Fig. 27.** Normalized cross-spectra of turbulence fitted to Davenport's formula in Eqn. (5): (a) $C_{uu}$ and (b) $C_{ww}$.

section, which inevitably results in high variance in the estimates. Relying on the assumption that the process is ergodic, variance can be reduced by averaging estimates from different recordings. The average curves are also shown in the figures. The variance can also be reduced by fitting a parametric function to the scattered data. Visual inspection of the data suggests that a simple exponentially decaying function, such as the one used by Davenport (1961), would be appropriate. The expression is written as

$$C_{uu,ww} = \exp\left(-K_{u,w}\frac{f\Delta x}{U}\right) \tag{5}$$

where K is commonly referred to as the decay coefficient. The curves were fitted to the scatter data in the least-squares sense, and they are shown along with the data. The resulting decay coefficients are also indicated in the figures. Finally, only for the u-component, a theoretical expression by Krenk (1996) is also plotted on the measurement data for the sake of comparison. In case of the along-wind turbulence component, both the fitted exponential curves and the theoretical curve by Krenk show good agreement with the averaged normalized cross-spectra for small separations. However, as the distance between the sensors increases, deviations are apparent in the low reduced frequency range. Davenport's expression assumes full correlation at zero frequency, which is a known drawback of the simple function. Krenk's formula, on the other hand, gave lower correlation in the low frequency range compared to the averaged data. The discrepancy between the fitted exponential curves and measurement data is more profound in the case of vertical turbulence. The normalized cross-spectrum of u and w components were essentially zero, even for small separations.

Although the use of a dimensionless frequency in the x-axis is very useful here, it makes the interpretation of the results rather difficult since engineers are more interested in the corresponding frequencies. Therefore, the same data are also plotted in Fig. 26 in the form of contour plots by linearly interpolating the average normalized cross-spectra. The decrease in correlation with increasing frequency and distance is immediately observed. Fitted normalized cross-spectra with Davenport's formula are also given in the same form in Fig. 27. Here, it is easily observed that the discrepancy is restricted to the low-frequency range, i.e., frequencies lower than the lowest natural frequency of HB (0.05 Hz). Moreover, to overcome this drawback of Davenport's formula, a surface fit was made to the data given in Fig. 28 using the following two-parameter expression, which was also used in the design basis of the HB in the form of Krenk's formula:

$$C_{uu,ww}(f,\Delta x) = \left(1-\frac{1}{2}\kappa\Delta x\right)\exp(-\kappa\Delta x), \quad \kappa = b_{u,w}\sqrt{\left(\frac{2\pi f}{U}\right)^2 + \left(\frac{1}{c_{u,w}L_u}\right)^2} \tag{6}$$

where $b_{u,w}$ and $c_{u,w}$ are parameters to be fitted. The resulting contour plot is shown in Fig. 28. A very good agreement with the measurement data is

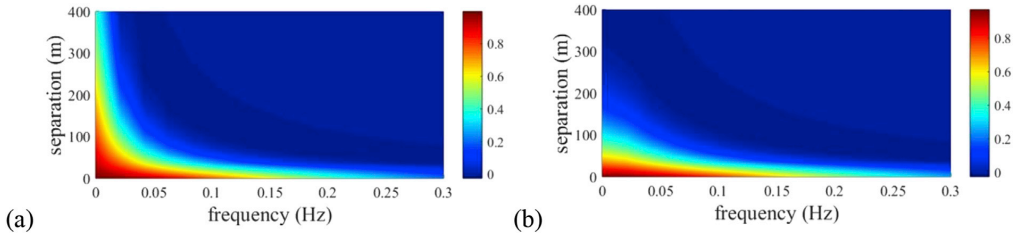


**Fig. 28.** Normalized cross-spectra of turbulence fitted to Krenk-type formula in Eqn. (6): (a) $C_{uu}$ and (b) $C_{ww}$ ($b_u = 0.79$, $c_u = 1.44$, $b_w = 0.72$, $c_w = 0.27$).

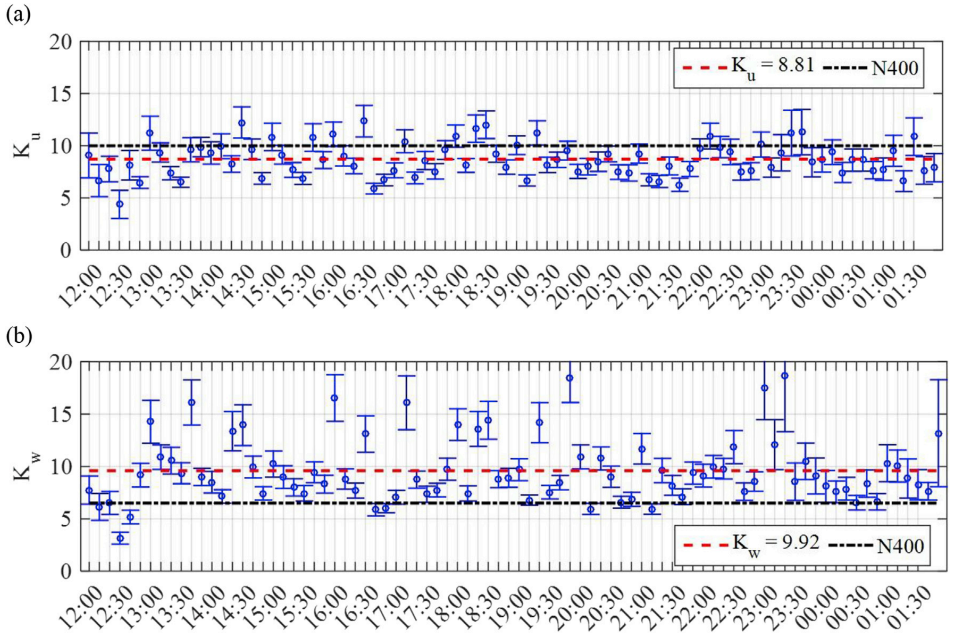


**Fig. 29.** Decay coefficients given in Eqn. (a) along-wind turbulence and (b) vertical turbulence.

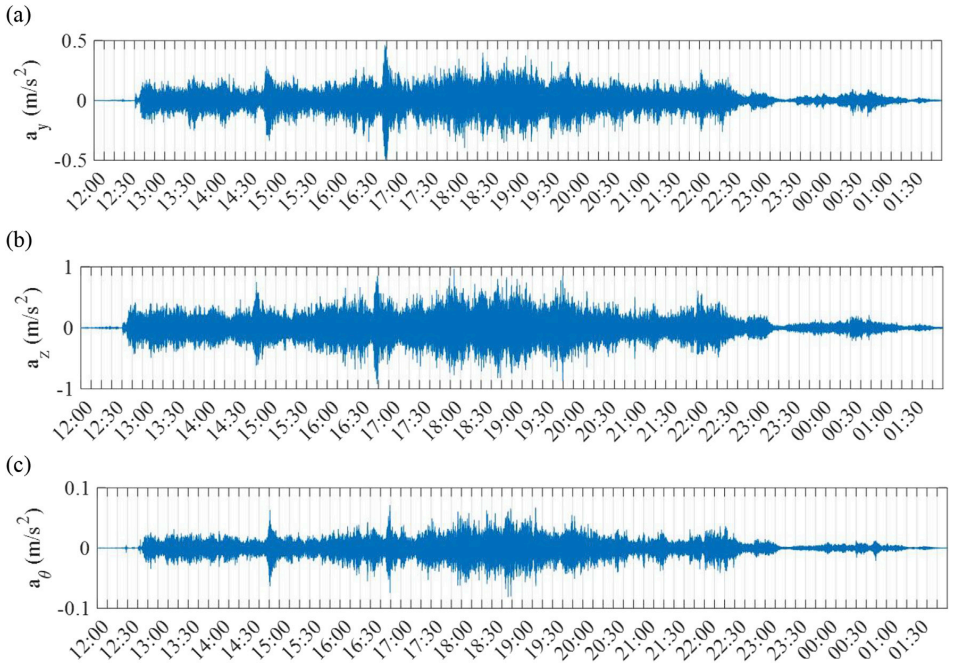


**Fig. 30.** Acceleration records at the quarter-span (using accelerometer pair H3) (a) lateral, (b) vertical and (c) torsional acceleration.

achieved using Eqn. (6).

Finally, the decay coefficients in Eqn. (5) were calculated for the 10-minute recordings separately using only the closely spaced sensor pairs. The results are presented in Fig. 29 with the 95% confidence intervals of the parameter estimates, where the mean value (for U > 15 m/s) and the N400 recommendation are also indicated. It is seen that the decay

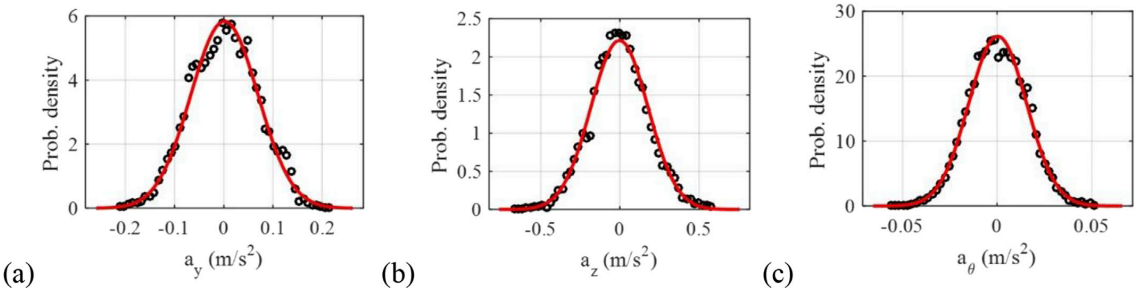


**Fig. 31.** Probability distributions of acceleration components at the midspan for a 10-minute recording recoded on 29/01/2016 between 18:40 and 18:50: (a) lateral, (b) vertical and (c) torsional components.

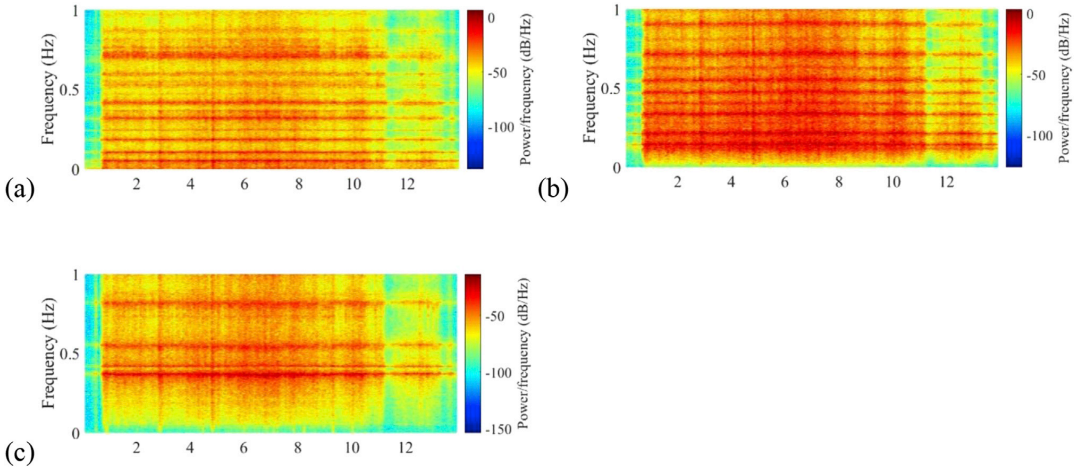


**Fig. 32.** Spectrogram of acceleration records at the quarter-span (using accelerometer pair H3): (a) lateral, (b) vertical and (c) torsional acceleration.

coefficients show random variation between 10-min recordings of the storm. The margin of uncertainty was higher for the larger decay coefficients (smaller correlation) for both components. In case of highly non-stationary recordings, the confidence intervals were usually larger.

## 5. Buffeting response of the bridge deck

The dynamic response of the HB deck was measured using seven accelerometer pairs located along the bridge span (Table 1). The lateral and vertical accelerations were taken as the average of the signals from two sensors at either side of the girder, and torsional acceleration was obtained by dividing the difference of the two signals by the distance between them (13 meters). The acceleration signals were then low-pass filtered with a cut-off of 1 Hz to remove the high-frequency response, which is considered not important when the wind-induced vibrations are concerned. The continuous acceleration measurements from the sensor pair H3 (120 meters from the midspan) during the entire storm are given in Fig. 30. It is seen that in the beginning of the storm, when the mean wind speed was around 5 m/s, the acceleration response was very low. With the increase in wind speed around 12:30, the amplitude of vibrations rapidly increased. For all the response components, the highest sustained vibrations seem to have occurred between 17:00–19:30, where the wind was the strongest (Fig. 9). Two distinct, rather sudden peaks were also observed in all components, one around 14:50 and another around 16:50, which correspond to two strong gusts (Fig. 9). For a 10-minute recording, the probability distributions of accelerations are shown in Fig. 31. It is observed that all components follow a Gaussian distribution; therefore, the assumption of a zero-mean Gaussian response process seems fair.

In order to have a more elaborate look at the frequency content of the signals, short time Fourier transforms of the signals were carried out using 10-minute windows with 80% overlap between them, and the resulting spectrograms are presented in Fig. 32 for the three response components. Several frequency contributions, which were consistent throughout the storm, are apparent in the plots. The continuous horizontal lines in the plots for lateral (0.05 Hz, 0.1 Hz, 0.18 Hz), vertical (0.14 Hz, 0.21 Hz, 0.27 Hz, 0.33 Hz) and torsional (0.37 Hz, 0.42 Hz, 0.55 Hz) yield similar frequencies as the natural vibration frequencies of the bridge extracted through finite element analysis (Table 2). No significant change in vibration frequencies during the storm can be detected. The regions where the wind speed increases and decreases are distinguishable from the plots. Two vertical lines are also recognized, coinciding with the locations of the jumps in acceleration signals (Fig. 30).

Moreover, the root-mean-squares (RMSs) of the three response components were calculated for 10-minute recordings at each sensor pair location. The results are used to obtain contour plots of RMS acceleration and displacement responses, which are given in Fig. 33 and Fig. 34, respectively. Measurement locations are indicated on the plots as dots. According to the contour plots, the largest lateral response occurred around 16:30–16:50. Although this was not the interval with the highest wind speed, the wind was quite gusty, which can be seen from the plots of

**Table 2**
Mode shapes and natural frequencies from FEM.

| Lateral | | | Vertical | | | Torsional | | |
|---|---|---|---|---|---|---|---|---|
| mode no | freq. (Hz) | description | mode no | freq. (Hz) | description | mode no | freq. (Hz) | description |
| 1 | 0.05 | 1st symm. | 3 | 0.11 | 1st asymm. | 15 | 0.36 | 1st symm. |
| 2 | 0.098 | 1st asymm. | 4 | 0.14 | 1st symm. | 26 | 0.52 | 1st asymm. |
| 5 | 0.169 | 2nd symm. | 6 | 0.197 | 2nd symm. | | | |
| 10 | 0.233 | 2nd asymm. | 7 | 0.21 | 2nd asymm. | | | |
| 11 | 0.244 | 3rd symm. | 12 | 0.272 | 3rd symm. | | | |
| 13 | 0.293 | 3rd asymm. | 14 | 0.33 | 3rd asymm. | | | |

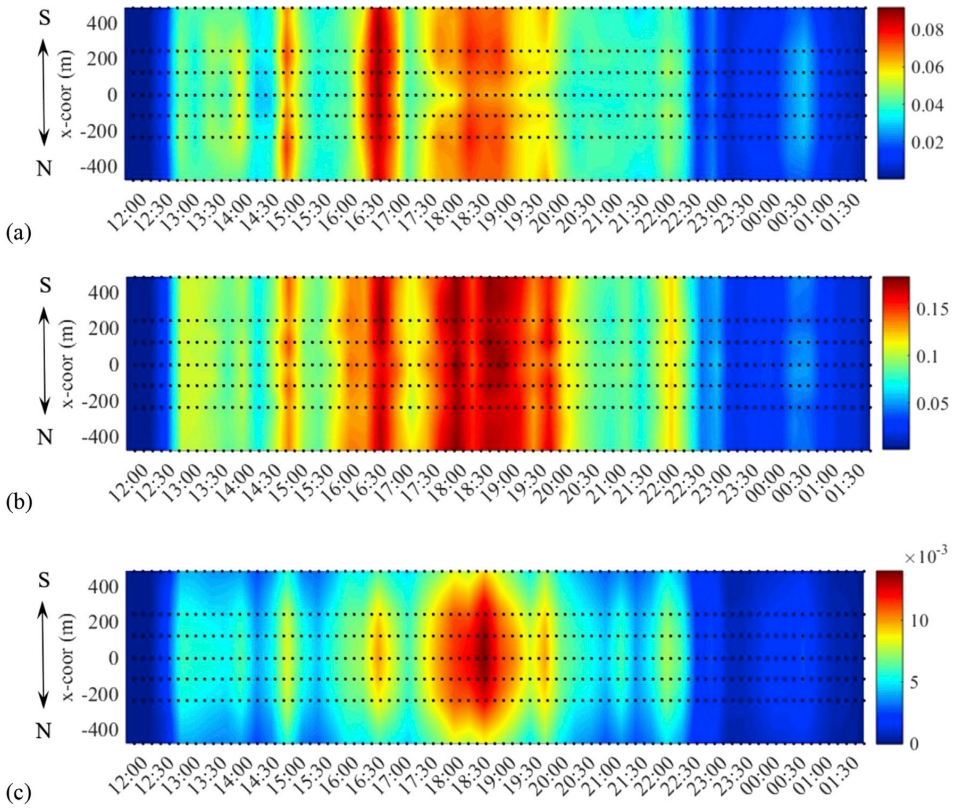


**Fig. 33.** RMS acceleration response during the storm (a) lateral (m/s$^2$), (b) vertical (m/s$^2$) and (c) torsional acceleration (rad/s$^2$).

gust factor (Fig. 10) or turbulence intensity (Fig. 11). It can also be seen that higher modes are more important for the acceleration response, where displacement response is usually dominated by a few lower modes. For the lateral and torsional modes, first modes of vibration, which are symmetrical modes, dominated the responses, resulting in maximum displacements at the midspan. However, the vertical displacement response was maximum around the quarter-span rather than the midspan. This is because the first vertical mode is antisymmetric and more vibration modes contribute to the vertical response.

It is also interesting to compare the results from this study on an extratropical cyclone to the results obtained from previous tropical cyclone measurements. Xu et al. (2001) studied the wind field characteristics and the dynamic response of the Tsing Ma Suspension Bridge in Hong Kong during the passage of typhoon Victor. The main span of the bridge is 1377 meters long, which is very similar to HB; however, the bridge girder is much wider (41 meters) and the bridge accommodates train passage. The topography surrounding the bridge is also complex, including sea, islands and mountains reaching up to 500 meters. From the wind measurements at the girder level, the typhoon was characterized with mean speeds up to 20 m/s and highly variable turbulence intensity. Along-wind length scales of 200–300 meters were reported, which are much lower than what was measured at the HB. Other differences include presence of skew-winds, high cross-wind turbulence, changing wind direction (due to passage of the eye of the typhoon) and variable angle-of-attack ($-6^\circ$ to $+6^\circ$). The turbulence spectra could not be modeled well with von Karman or Kaimal spectra. The results suggest that it can be more challenging to model tropical storm winds. The maximum RMS accelerations of the bridge girder, on the other hand, were in general smaller than the case of HB under similar wind speeds, presumably due to its stiffer girder.

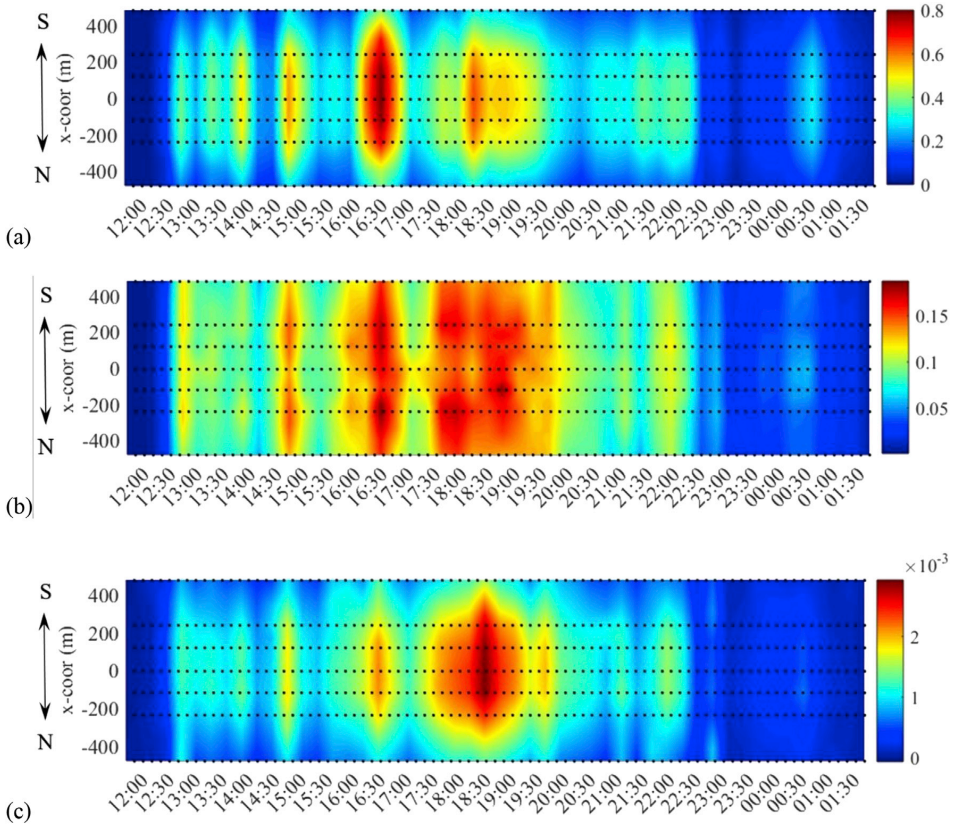


**Fig. 34.** RMS displacement response during the storm (a) lateral (m), (b) vertical (m) and (c) torsional displacement (rad).

**Table 3**
Steady-state force coefficients for the Hardanger Bridge section (Siedziako et al., 2017).

| $\overline{C}_{D*}$ | $C'_D$ | $\overline{C}_{L*}$ | $C'_L$ | $\overline{C}_{M*}$ | $C'_M$ |
|---|---|---|---|---|---|
| 1.05 | 0 | −0.363 | 2.22 | −0.017 | 0.786 |

*D = drag, L = lift, M = moment (bar denotes mean value and apostrophe denotes derivative).

## 6. Comparison with analytical predictions

The buffeting response of the HB during Storm Tor was also evaluated analytically using a multimode approach. The fully coupled system of equations of motion including the aeroelastic terms were solved in the frequency domain using the procedure given in Øiseth et al. (2010), where the bridge displacements are written in terms of generalized coordinates of the still-air vibration modes. Detailed formulation of the procedure can be found elsewhere (Katsuchi et al., 1998; Øiseth et al., 2010) and, therefore, will not be repeated here. The first 80 still-air vibration modes of the bridge (0.05 Hz – 1.3 Hz), which were obtained via finite element analysis, were included in the analysis, excluding the tower and cable modes. Petersen and Øiseth (2017) conducted sensitivity-based finite element model updating of the HB using monitoring data. It was seen that the discrepancy between identified and analytical natural frequencies were in an acceptable range for the applications in the current study. It should also be noted that the RMS response is more sensitive to damping, rather than minor shifts in the response frequencies. Information regarding the first few still-air modes is given in Table 2. A structural damping of 0.5% was assigned to all modes. The so-called self-excited forces, which are induced by the motion of the bridge deck, were modeled using aerodynamic derivatives (ADs). The ADs of the HB deck section were obtained by Siedziako et al. (2017) through forced vibration tests in the wind tunnel. The resulting ADs exhibited exceptionally low scatter, increasing confidence on the modeling of the self-excited forces. The ADs for the entire reduced velocity range were obtained by fitting rational functions to the experimental data by nonlinear least squares approximation. The identified ADs and the corresponding fits were presented in Figs. 17 and 18 in Fenerci and Øiseth (2017). The steady-state force coefficients were also obtained using the tests by Siedziako et al. (2017) in the wind tunnel (Table 3). The cross-sectional aerodynamic admittance functions were set to unity due to lack of experimental data, and the spanwise correlation of the buffeting forces was assumed the same as those of the incoming turbulence.

Neglecting the cross terms, the cross-spectral density matrix of turbulence used in the analysis can be written as

$$S_{turb}(\Delta x,f)=\begin{bmatrix} S_{uu}(\Delta x,f) & 0 \\ 0 & S_{ww}(\Delta x,f)\end{bmatrix},\quad S_{uu,ww}(\Delta x,f) = S_{u,w}(f)C_{uu,ww}(f,\Delta x) \tag{7}$$

where $S_{u,w}(f)$ are given in Eqn. (3) and $C_{uu,ww}(f,\Delta x)$ in Eqn. (5). The values of the spectral parameter $A_{u,w}$ and the decay coefficient $K_{u,w}$ in the equations were taken from Figs. 20 and 29, respectively, for each 10-minute recording. It should be noted that this formulation assumes

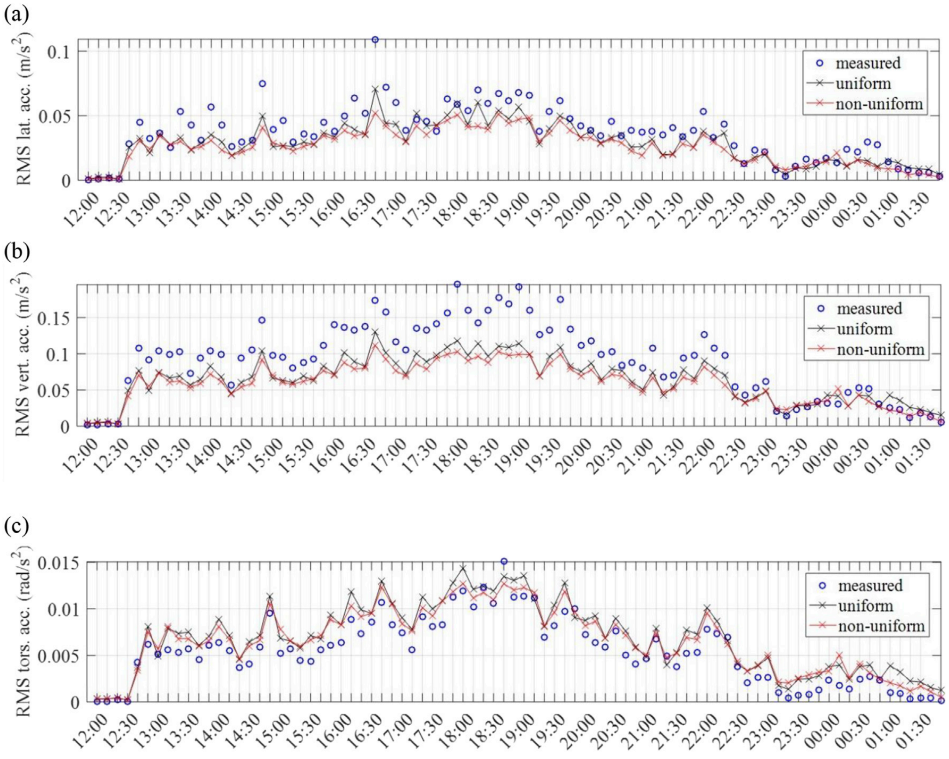


**Fig. 35.** RMS acceleration response comparison (a) lateral, (b) vertical and (c) torsional acceleration.

spanwise uniform turbulence characteristics, which is not the case for the HB. The spanwise non-uniformity of the mean wind speed, turbulence intensities and spectral parameters can be implemented by modifying the cross-spectral density matrix in Eqn. (7) as follows:

$$\tilde{S}_{turb}(x_1, x_2, f) = \begin{bmatrix} S_{uu}(x_1, x_2, f) & 0 \\ 0 & S_{ww}(x_1, x_2, f) \end{bmatrix}, \\ S_{uu,ww}(x_1, x_2, f) = \sqrt{S_{u,w}(x_1, f) S_{u,w}(x_2, f)} C_{uu,ww}(f, \Delta x) \tag{8}$$

where $S_{u,w}(x_1, f)$and $S_{u,w}(x_2, f)$are the auto-spectral densities of turbulence components at two points $x_1$ and $x_2$, separated by $\Delta x$. The buffeting response of the HB was calculated using both spanwise uniform and non-uniform wind profiles. In the non-uniform case, the mean wind speed, turbulence intensities and spectral parameters $A_{u,w}$ were interpolated between sensor locations to obtain the profiles, where the normalized cross-spectra of turbulence was kept constant.

The comparisons of measured and predicted responses are given in Fig. 35 and Fig. 36 for the RMS acceleration response and Fig. 37 and Fig. 38 for the RMS displacement response at the midspan. It should be noted that for a fair comparison between RMS responses, the analytical response spectra was integrated up to a frequency of 1 Hz. The comparisons yield similar results for the RMS acceleration and displacement responses; therefore, a common discussion is possible. The lateral and torsional RMS responses were predicted with reasonable accuracy, although the variability in the lateral response was not fully captured with the analytical method. This can be attributed to the lack of wind

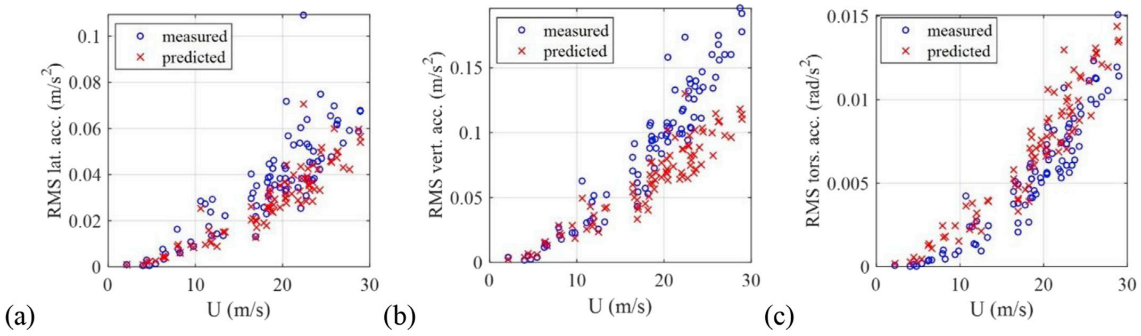


**Fig. 36.** RMS acceleration vs. mean wind speed comparison (a) lateral, (b) vertical and (c) torsional acceleration.

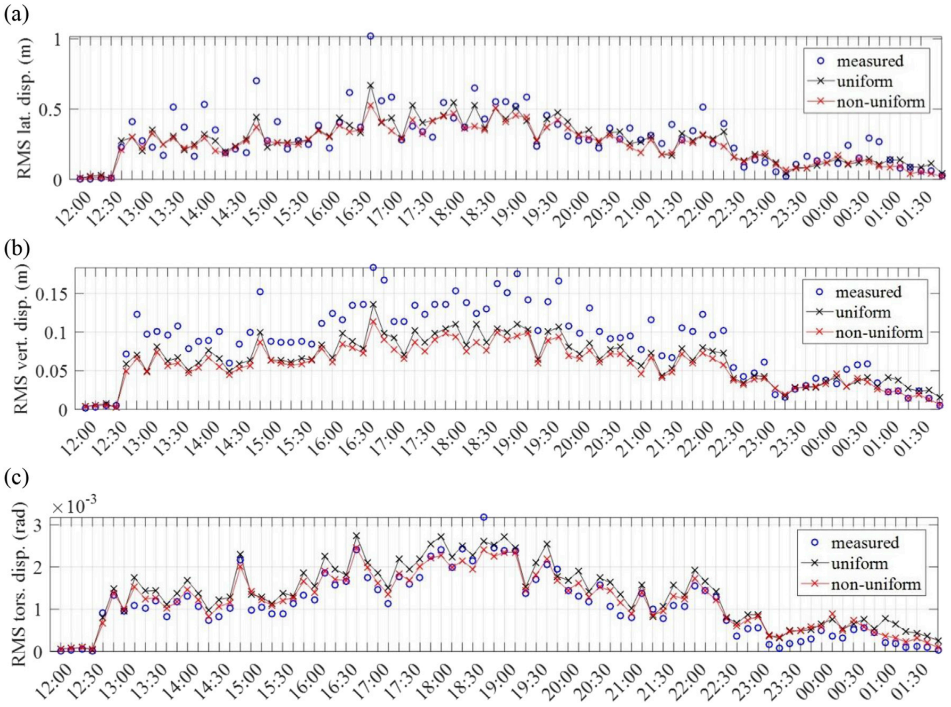


**Fig. 37.** RMS displacement response comparison (a) lateral, (b) vertical and (c) torsional displacement.

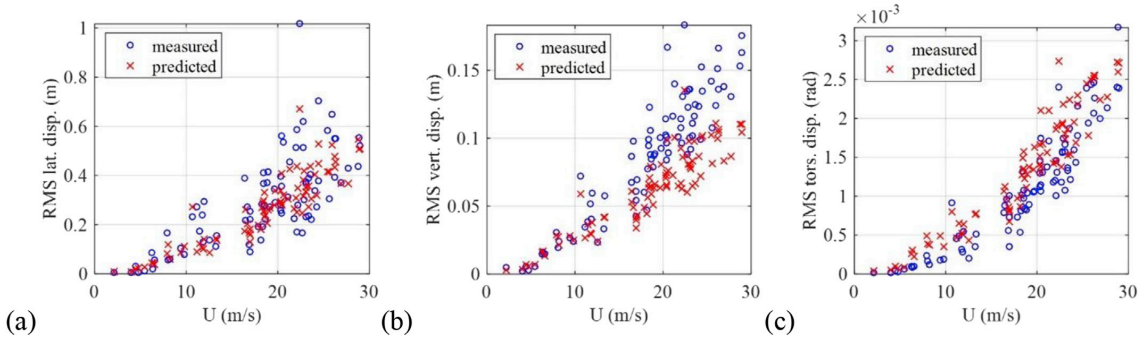


**Fig. 38.** RMS displacement vs. mean wind speed comparison (a) lateral, (b) vertical and (c) torsional displacement.

forces on bridge cables and towers in the analysis. This issue was also addressed in Fenerci and Øiseth (2017). The vertical response, on the other hand, was severely underestimated by the analysis for the whole storm. The source of this discrepancy cannot be easily identified since many sources of uncertainty are present in the analysis. However, the analysis seems to capture the variability in response reasonably well (Figs. 36 and 38). Considering this and given that the turbulence field was modeled with maximum possible accuracy, it is unlikely that the discrepancy is due to uncertainties in the wind field model. The difference between uniform and non-uniform analyses were negligible, especially compared to the overall uncertainty involved in the predictions.

The total modal damping ratios utilized in the analysis are presented in Fig. 39. Petersen and Øiseth (2017) developed an operational modal analysis (OMA) framework to identify the natural frequencies of HB based on covariance-driven stochastic subspace identification (SSI) method (Peeters and De Roeck, 2001). Applying the same framework here, total modal damping ratios during two one-hour segments of the storm were identified. The comparison of identified damping ratios and damping ratios utilized in the analysis are given in Table 4. To distinguish between structural and aerodynamic damping, SSI was performed on a low wind speed (≈3 m/s) recording (recorded on 20/12/2015 01.30–2.30) and identified damping ratios were assumed as structural damping. Looking at the comparison, it is seen that the horizontal and torsional damping were modeled with reasonable accuracy, where the damping in vertical modes were underestimated in the analysis. This implies even higher discrepancy between measured and calculated vertical response, which is contradictory and indicates further problems in prediction of the vertical response.

When the analyses were repeated to take into account the angle-of-attack shown in Fig. 16 using steady-state force coefficients for an

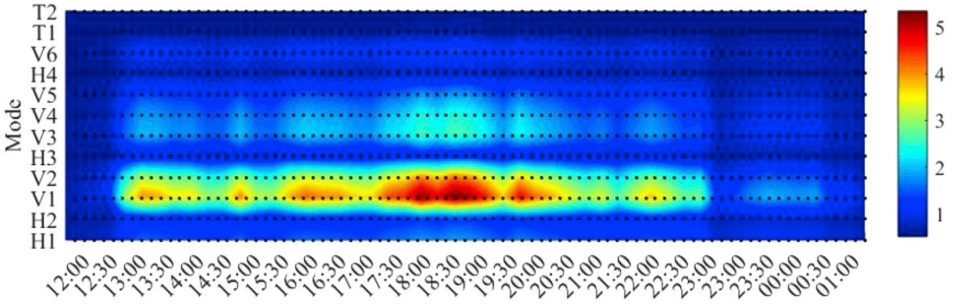


**Fig. 39.** Modal total damping ratio utilized in the analysis (%).

**Table 4**
Identified vs. analytical modal damping ratios.

| | 16.00–17.00 | | | | | | 18.00–19.00 | | | | | |
|---|---|---|---|---|---|---|---|---|---|---|---|---|
| | $\zeta_{str*}$ (%) | | $\zeta_{aero*}$ (%) | | $\zeta_{tot*}$ (%) | | $\zeta_{str}$ (%) | | $\zeta_{aero}$ (%) | | $\zeta_{tot}$ (%) | |
| Mode | ANA* | SSI* | ANA | SSI | ANA | SSI | ANA | SSI | ANA | SSI | ANA | SSI |
| H1* | 0.50 | 0.88 | 1.01 | 0.27 | 1.51 | 1.15 | 0.50 | 0.88 | 1.25 | 0.53 | 1.75 | 1.41 |
| H2 | 0.50 | 0.79 | 0.64 | 0.37 | 1.14 | 1.16 | 0.50 | 0.79 | 0.75 | 0.49 | 1.25 | 1.28 |
| V1* | 0.50 | 1.70 | 3.59 | 3.48 | 4.09 | 5.18 | 0.50 | 1.70 | 4.67 | 5.07 | 5.17 | 6.77 |
| V2 | 0.50 | 0.16 | 2.57 | 4.19 | 3.07 | 4.35 | 0.50 | 0.16 | 3.42 | 6.24 | 3.92 | 6.40 |
| H3 | 0.50 | 0.47 | 0.39 | 0.08 | 0.89 | 0.55 | 0.50 | 0.47 | 0.46 | 0.68 | 0.96 | 1.15 |
| V3 | 0.50 | 0.14 | 1.51 | 3.00 | 2.01 | 3.14 | 0.50 | 0.14 | 2.05 | 3.80 | 2.55 | 3.94 |
| V4 | 0.50 | 0.33 | 1.34 | 1.99 | 1.84 | 2.32 | 0.50 | 0.33 | 1.82 | 3.03 | 2.32 | 3.36 |
| V5 | 0.50 | 0.19 | 0.90 | 1.67 | 1.40 | 1.86 | 0.50 | 0.19 | 1.21 | 1.96 | 1.71 | 2.15 |
| H4 | 0.50 | 0.22 | 0.24 | 0.38 | 0.74 | 0.60 | 0.50 | 0.22 | 0.28 | 0.53 | 0.78 | 0.75 |
| V6 | 0.50 | 0.22 | 0.67 | 1.28 | 1.17 | 1.50 | 0.50 | 0.22 | 0.90 | 1.38 | 1.40 | 1.60 |
| T1* | 0.50 | 0.25 | 0.08 | 0.85 | 0.58 | 1.10 | 0.50 | 0.25 | 0.11 | 0.58 | 0.61 | 0.83 |
| T2 | 0.50 | 0.76 | 0.05 | 0.74 | 0.55 | 1.50 | 0.50 | 0.76 | 0.06 | 0.89 | 0.56 | 1.65 |

*H: Horizontal mode, V: vertical mode, T: torsional mode, $\zeta_{str}$: structural modal damping ratio, $\zeta_{aero}$: aerodynamic modal damping ratio, $\zeta_{tot}$: total modal damping ratio, ANA: analysis, SSI: stochastic subspace identification.

**Table 5**
Steady-state force coefficients for the Hardanger Bridge section for an angle-of-attack of 3° (Siedziako et al., 2017).

| $\overline{C}_{D*}$ | $C'_D$ | $\overline{C}_{L*}$ | $C'_L$ | $\overline{C}_{M*}$ | $C'_M$ |
|---|---|---|---|---|---|
| 1.082 | 0.94 | −0.267 | 1.302 | 0.021 | 0.698 |

*D = drag, L = lift, M = moment (bar denotes mean value and apostrophe denotes derivative).

inclined section of 3° (Table 5), no significant change was observed in the lateral and torsional responses. The vertical response, however, was found to be even smaller, resulting into an even larger discrepancy when compared with the measurements. Unfortunately, the section of Siedziako et al. (2017) were not tested to obtain ADs for an angle-of-attack. However, ADs corresponding to a 3° angle-of-attack was obtained through free vibration tests of Hansen et al. (2006) on the HB section in a different wind tunnel prior to the design of the bridge. The analyses were repeated using the ADs of Hansen et al. (2006) for the cases of 0° and 3° angle-of-attack. Again, the change in the predicted responses between the two cases were not significant.

Although the RMS response at the midspan is a good indicator of the accuracy of the predictions from a global point of view, it is also of interest to see how the spectral densities and responses at different locations along the bridge correspond between measurement data and analytical results. Therefore, a 10-minute recording with high wind speed and response was selected, and its acceleration response spectra at the span and spanwise RMS acceleration response were compared to the analytical predictions in Fig. 40 and Fig. 41, respectively. It is seen that the discrepancy in the vertical RMS response mainly arises from the underestimation of both magnitude and bandwidth of the first mode spectral response. It is also

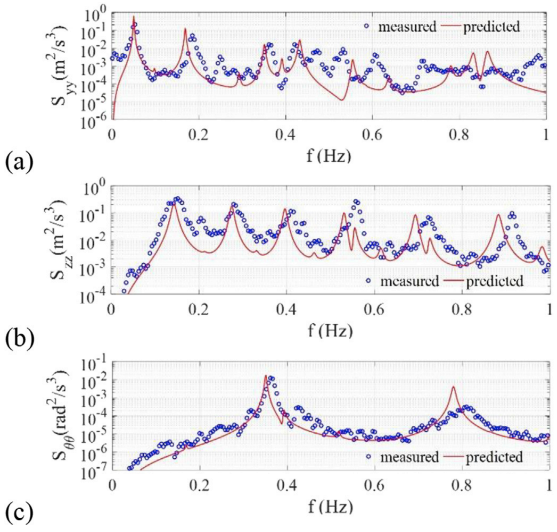


**Fig. 40.** Comparison of spectral density of the acceleration response at the midspan for a 10-minute recording recoded on 29/01/2016 between 18:40 and 18:50: (a) lateral, (b) vertical and (c) torsional acceleration.

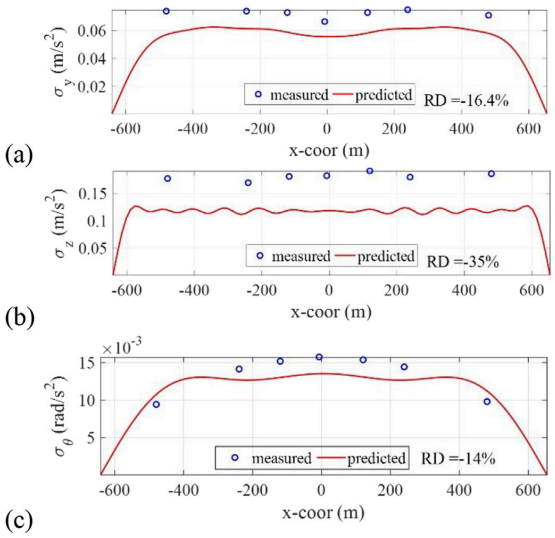


**Fig. 41.** Comparison of RMS acceleration response along the bridge span for a 10-minute recording recoded on 29/01/2016 between 18:40 and 18:50: (a) lateral, (b) vertical and (c) torsional acceleration. (RD = relative discrepancy).

observed that even though the RMS responses of lateral and torsional responses were predicted with reasonable accuracy, significant discrepancies were present in the high frequency range of the two spectra. Furthermore, the peaks of the response spectra were also not matched well by the analysis, especially beyond 0.5 Hz. Thus, the prediction of higher frequency response (>0.5 Hz) appears to be more challenging in the absence of aerodynamic admittance information and a more accurate description of the modal properties corresponding to such modes.

## 7. Conclusions

Strong wind characteristics and dynamic response of a long-span suspension bridge located in mountainous terrain were studied in this paper using full-scale monitoring data acquired during a storm. The dynamic response of the bridge deck was predicted analytically and compared with the measured response. The following conclusions were reached for this specific case:

- The wind recordings showed non-stationary features, especially in the beginning and the end of the strong wind part of the storm. The along-wind and vertical turbulence components exhibited a nearly Gaussian distribution, where the cross-wind turbulence did not.
- Length scale estimations using Taylor's hypothesis showed significant variability and did not agree with the code recommendations. The use of length scales as deterministic design parameters should be avoided when possible, especially in complex terrain and non-stationary wind.
- It was shown that the one-point spectra of the turbulence could be represented reasonably well by a Kaimal-type of spectral formula. Despite its well-known weaknesses, Davenport's formula was found satisfactory in representing the normalized cross-spectra of turbulence in the important reduced frequency range.
- Comparisons between measured and predicted responses yielded significant discrepancies in case of the vertical response component. Reasonable agreement was achieved in case of lateral and torsional response predictions. Moreover, it was found more challenging to match the spectral response compared to the RMS response.
- The use of spanwise non-uniform profiles for the turbulence statistics did not improve the results significantly, considering the overall uncertainty in the predictions.

## Acknowledgments

The research described in this paper was financially supported by the Norwegian Public Roads Administration. The authors also thank PhD candidate Øyvind Wiig Petersen for his valuable help in damping identification.

## References

Bendat, J.S., Piersol, A.G., 2000. Random Data: Analysis and Measurement Procedures, fourth ed. Wiley.
Bietry, J., Delaunay, D., Conti, E., 1995. Comparison of full-scale measurement and computation of wind effects on a cable-stayed bridge. J. Wind Eng. Ind. Aerod. 57 (2–3), 225–235.
Brownjohn, J.M.W., Bocciolone, M., Curami, A., Falco, M., Zasso, A., 1994. Humber bridge full-scale measurement campaigns 1990-1991. J. Wind Eng. Ind. Aerod. 52 (C), 185–218.
Cao, S., Tamura, Y., Kikuchi, N., Saito, M., Nakayama, I., Matsuzaki, Y., 2009. Wind characteristics of a strong typhoon. J. Wind Eng. Ind. Aerod. 97 (1), 11–21.
Cao, S., Tamura, Y., Kikuchi, N., Saito, M., Nakayama, I., Matsuzaki, Y., 2015. A case study of gust factor of a strong typhoon. J. Wind Eng. Ind. Aerod. 138, 52–60.
Chen, J., Hui, M.C.H., Xu, Y.L., 2007. A comparative study of stationary and non-stationary wind models using field measurements. Boundary-Layer Meteorol. 122 (1), 105–121.
Chen, X., 2015. Analysis of multimode coupled buffeting response of long-span bridges to nonstationary winds with force parameters from stationary wind. J. Struct. Eng. (United States) 141 (4), 1–14.
Chen, X., Kareem, A., Matsumoto, M., 2001. Multimode coupled flutter and buffeting analysis of long span bridges. J. Wind Eng. Ind. Aerod. 89 (7–8), 649–664.
Cheynet, E., Jakobsen, J.B., Snæbjørnsson, J., 2016. Buffeting response of a suspension bridge in complex terrain. Eng. Struct. 128, 474–487.
Choi, E.C.C., 1978. Characteristics of typhoons over the south China sea. J. Wind Eng. Ind. Aerod. 3 (4), 353–365.
Choi, E.C.C., 1983. Wind Loading in Hong Kong—Commentary on the Code of Practice on Wind Effects Hong Kong. Hong Kong Institute of Engineers, Hong Kong.
Cross, E.J., Koo, K.Y., Brownjohn, J.M.W., Worden, K., 2013. Long-term monitoring and data analysis of the Tamar Bridge. Mech. Syst. Signal Process. 35 (1–2), 16–34.
Davenport, A.G., 1961. The spectrum of horizontal gustiness near the ground in high winds. Q. J. R. Meteorol. Soc. 87 (372), 194–211.
Davenport, A.G., 1962. Buffeting of a suspension bridge by storm winds. J. Struct. Div. 88 (3), 233–268.
Ellevset, O., Skorpa, L., 2011. A Feasibility Study – How to Cross the Wide and Deep Sognefjord, Summary. Norwegian Public Roads Administration - Western Region Projects Division, Norway.
ESDU 086010, 2001a. Characteristics of Atmospheric Turbulence Near the Ground Part 3: Variations in Space and Time for Strong Winds (Neutral Atmosphere). ESDU International plc, London.
ESDU 85020, 2001b. Characteristics of Atmospheric Turbulence Near Groud Part 2: Signle Point Data for Strong Winds (Neutral Atmosphere). ESDU International plc, London.
Fenerci, A., Øiseth, O., 2016a. Wind field characteristics at the Hardanger bridge site. Proc. 12th U. K. Conf. Wind Eng. Nottm. U. K. 163–166.
Fenerci, A., Øiseth, O., 2016b. Full-scale measurements on the Hardanger bridge during strong winds. In: Pakzad, S., Juan, C. (Eds.), Dynamics of Civil Structures, Volume 2: Proceedings of the 34th IMAC, a Conference and Exposition on Structural Dynamics 2016. Springer International Publishing, Cham, pp. 237–245.
Fenerci, A., Øiseth, O., 2017. Measured buffeting response of a long-span suspension bridge compared with numerical predictions based on design wind spectra. J. Struct. Eng. (United States) 143 (9).
Fenerci, A., Øiseth, O., Rønnquist, A., 2017. Long-term monitoring of wind field characteristics and dynamic response of a long-span suspension bridge in complex terrain. Eng. Struct. 147, 269–284.
Hansen, S., Lollesgaard, M., Rex, S., Jacobsen, J., Hansen, E., 2006. The Hardanger Bridge: Static and Dynamic Wind Tunnel Tests with a Section Model (Copenhagen).
Harstveit, K., 1996. Full scale measurements of gust factors and turbulence intensity, and their relations in hilly terrain. J. Wind Eng. Ind. Aerod. 61 (2–3), 195–205.
He, Y.C., Chan, P.W., Li, Q.S., 2013. Wind characteristics over different terrains. J. Wind Eng. Ind. Aerod. 120.
Holmes, J., 2007. Wind Loading on Structures. Taylor&Francis, New york.
Hu, J., Ou, J., 2013. Wind field characteristics analysis at a long-span suspension bridge based on long-term monitoring data. Zhongnan Daxue Xuebao (Ziran Kexue Ban)/J. Central South Univ. Sci. Technol. 44 (7).
Hu, L., Xu, Y.-L., Huang, W.-F., 2013. Typhoon-induced non-stationary buffeting response of long-span bridges in complex terrain. Eng. Struct. 57 (0), 406–415.
Hu, L., Xu, Y.-L., Zhu, Q., Guo, A., Kareem, A., June 2017. Tropical storm–induced buffeting response of long-span bridges: enhanced nonstationary buffeting force model. J. Struct. Eng. 143 (6).

Hui, M.C.H., Larsen, A., Xiang, H.F., 2009a. Wind turbulence characteristics study at the Stonecutters Bridge site: Part I-Mean wind and turbulence intensities. J. Wind Eng. Ind. Aerod. 97 (1), 22–36.
Hui, M.C.H., Larsen, A., Xiang, H.F., 2009b. Wind turbulence characteristics study at the Stonecutters Bridge site: Part II: wind power spectra, integral length scales and coherences. J. Wind Eng. Ind. Aerod. 97 (1), 48–59.
Ishizaki, H., 1983. Wind profiles, turbulence intensities and gust factors for design in typhoon-prone regions. J. Wind Eng. Ind. Aerod. 13 (1–3), 55–66.
Jain, A., Jones, N.P., Scanlan, R.H., 1996. Coupled flutter and buffeting analysis of long-span bridges. J. Struct. Eng. 122 (7), 716–725.
Kaimal, J.C.J., Wyngaard, J.C.J., Izumi, Y., Coté, O.R., Cote, O.R., 1972. Spectral characteristics of surface-layer turbulence. Q. J. … 98 (417), 563–589.
von Karman, T., 1948. Progress in the statistical theory of turbulence. Proc. Natl. Acad. Sci. U. S. A. 34 (11), 530–539.
Katsuchi, H., Jones, N.P., Scanlan, R.H., Akiyama, H., 1998. Multi-mode flutter and buffeting analysis of the Akashi-Kaikyo bridge. J. Wind Eng. Ind. Aerod. 77–78, 431–441.
Kimura, K., Tanaka, H., 1992. Bridge buffeting due to wind with yaw angles. J. Wind Eng. Ind. Aerod. 42 (1–3), 1309–1320.
Krayer, W.R., Marshall, R.D., 1992. Gust factors applied to hurricane winds. Bull. Am. Meteorol. Soc. 73, 613–618.
Krenk, S., 1996. Wind Field Coherence and Dynamic Wind Forces. In: Naess, A., Krenk, S. (Eds.), IUTAM Symposium on Advances in Nonlinear Stochastic Mechanics: Proceedings of the IUTAM Symposium Held in Trondheim, Norway, 3–7 July 1995. Springer Netherlands, Dordrecht, pp. 269–278.
Kristensen, L., Jensen, N.O., 1979. Lateral coherence in isotropic turbulence and in the natural wind. Boundary-Layer Meteorol. 17 (3), 353–373.
Kristiansen, S., Mamen, J., Szewczyk-Bartincka, H., 2016. Weather in Norway: Monthly Climatological Report: January 2016 (In Norwegian). Norwegian Meteorological Institute, Oslo.
Kwon, D.K., Kareem, A., 2014. Revisiting gust averaging time and gust effect factor in ASCE 7. J. Struct. Eng. 140 (11), 6014004.
Li, L., Kareem, A., Xiao, Y., Song, L., Zhou, C., 2015. A comparative study of field measurements of the turbulence characteristics of typhoon and hurricane winds. J. Wind Eng. Ind. Aerod. 140.
Macdonald, J.H.G., 2003. Evaluation of buffeting predictions of a cable-stayed bridge from full-scale measurements. J. Wind Eng. Ind. Aerod. 91 (12–15), 1465–1483.
Mann, J., 2006. The spatial structure of neutral atmospheric surface-layer turbulence. J. Fluid Mech. 273 (1), 141.
McCullough, M., Kwon, D.K., Kareem, A., Wang, L., 2014. Efficacy of averaging interval for nonstationary winds. J. Eng. Mech. 140 (1).
Miyata, T., Yamada, H., Katsuchi, H., Kitagawa, M., 2002. Full-scale measurement of Akashi-Kaikyo bridge during typhoon. J. Wind Eng. Ind. Aerod. 90 (12–15), 1517–1527.
Norwegian Meteoroligical Institute, 2016. Extreme Weather Report: Storm Tor 29–30 January 2016 (Oslo).
Øiseth, O., Rönnquist, A., Sigbjörnsson, R., 2010. Simplified prediction of wind-induced response and stability limit of slender long-span suspension bridges, based on modified quasi-steady theory: a case study. J. Wind Eng. Ind. Aerod. 98 (12), 730–741.
Pagnini, L.C., Solari, G., 2002. Gust buffeting and turbulence uncertainties. J. Wind Eng. Ind. Aerod. 90 (4–5), 441–459.
Park, J., Kim, H.-K., Lee, H.S., Koh, H.-M., Cho, S., 2012. Buffeting Responses of a Cable-stayed Bridge during the Typhoon Kompasu. Bridge Maintenance, Safety, Management, Resilience and Sustainability, Bridge Maintenance, Safety and Management, CRC Press, pp. 1158–1161.
Peeters, B., De Roeck, G., 2001. Stochastic system identification for operational modal analysis: a review. J. Dyn. Syst. Meas. Control 123 (4), 659.
Peng, H., Xu, W., Ming, G., 2013. Study on near-ground wind characteristics of a strong typhoon-wind speed, turbulence intensities, gust factors and peak factors. Disaster Adv. 6 (5).
Petersen, Ø.W., Øiseth, O., 2017. Finite element model updating of a long span suspension bridge. In: The International Conference on Earthquake Engineering and Structural Dynamics (Reykjavik, Iceland).
Scanlan, R.H., 1978. The action of flexible bridges under wind, II: buffeting theory. J. Sound Vib. 60 (2), 187–199.
Scanlan, R.H., Tomko, J.J., 1971. Airfoil and bridges deck flutter derivatives. J. Eng. Mech. Div. (ASCE) 97, 1717–1737.
Shu, Z.R., Li, Q.S., He, Y.C., Chan, P.W., 2015. Gust factors for tropical cyclone, monsoon and thunderstorm winds. J. Wind Eng. Ind. Aerod. 142, 1–14.
Siedziako, B., Øiseth, O., Rønnquist, A., 2017. An enhanced forced vibration rig for wind tunnel testing of bridge deck section models in arbitrary motion. J. Wind Eng. Ind. Aerod. 164, 152–163.
Simiu, E., Scanlan, R.H., 1996. Winds Effects on Structures: Fundamentals and Applications to Design. Wiley.
Solari, G., Piccardo, G., 2001. Probabilistic 3-D turbulence modeling for gust buffeting of structures. Probabilist. Eng. Mech. 16 (1), 73–86.
Statens-Vegvesen, 2009. N400 Handbook for Bridge Design.
Tao, T., Wang, H., Wu, T., 2017. Comparative study of the wind characteristics of a strong wind event based on stationary and nonstationary models. J. Struct. Eng. Am. Soc. Civ. Eng. 143 (5).
Toriumi, R., Katsuchi, H., Furuya, N., 2000. A study on spatial correlation of natural wind. J. Wind Eng. Ind. Aerod. 87 (2–3), 203–216.
Wang, H., Hu, R., Xie, J., Tong, T., Li, A., 2013. Comparative study on buffeting performance of sutong bridge based on design and measured spectrum. J. Bridge Eng. 18 (7), 587–600.
Wang, H., Li, A., Guo, T., Xie, J., 2009. Field measurement on wind characteristic and buffeting response of the Runyang Suspension Bridge during typhoon Matsa, 52 (5), 1354–1362.
Wang, H., Li, A., Hu, R., 2011. Comparison of ambient vibration response of the runyang suspension bridge under skew winds with time-domain numerical predictions. J. Bridge Eng. 16 (4), 513.
Wang, H., Wu, T., Tao, T., Li, A., Kareem, A., 2016. Measurements and analysis of non-stationary wind characteristics at sutong bridge in typhoon Damrey. J. Wind Eng. Ind. Aerod. 151, 100–106.
Wang, X., Chen, B., Sun, D., Wu, Y., 2014. Study on typhoon characteristic based on bridge health monitoring system. Sci. World J. 2014.
Wang, X., Huang, P., Yu, X.-F., Wang, X.-R., Liu, H.-M., 2017. Wind characteristics near the ground during typhoon Meari. J. Zhejiang Univ. Sci. A 18 (1).
Welch, P.D., 1967. The use of fast fourier transform for the estimation of power spectra: a method based on time averaging over short, modified periodograms. IEEE Trans. Audio Electroacoust. 15 (2), 70–73.
Xie, J., Tanaka, H., Wardlaw, R.L., Savage, M.G., 1991. Buffeting analysis of long span bridges to turbulent wind with yaw angle. J. Wind Eng. Ind. Aerod. 37 (1), 65–77.
Xu, Y.-L., 2013. Wind Effects on Cable-Supported Bridges. John Wiley & Sons.
Xu, Y.L., Chen, J., 2004. Characterizing nonstationary wind speed using empirical mode decomposition. J. Struct. Eng. Asce 130 (6), 912–920.
Xu, Y.L., Sun, D.K., Ko, J.M., Lin, J.H., 2000. Fully coupled buffeting analysis of Tsing Ma suspension bridge. J. Wind Eng. Ind. Aerod. 85 (1), 97–117.
Xu, Y.L., Zhu, L.D., 2005a. Buffeting response of long-span cable-supported bridges under skew winds. Part 2: case study. J. Sound Vib. 281 (3–5), 675–697.
Xu, Y.L., Zhu, L.D., 2005b. Buffeting Response of Long-span Cable-supported Bridges under Skew Winds. Part 2: Case Study. J. Sound Vib. Acad. Press vol. 281 (3–5), 675–697.
Xu, Y.L., Zhu, L.D., Wong, K.Y., Chan, K.W.Y., 2001. Field measurement results of Tsing Ma suspension bridge during typhoon Victor. Struct. Eng. Mech. 10 (6), 545–559.
Xu, Y.L., Zhu, L.D., Xiang, H.F., 2003. Buffeting response of long suspension bridges to skew winds. Wind Struct. Int. J. 6 (3), 179–196.
Zhu, L.D., Xu, Y.L., 2005. Buffeting response of long-span cable-supported bridges under skew winds. Part 1: theory. J. Sound Vib. 281 (3–5), 647–673.

# Paper V

Aksel Fenerci, Ole Øiseth

*Site-specific data-driven probabilistic wind field modeling for wind-induced response prediction of cable-supported bridges*

*Submitted for journal publication*

# Site-specific data-driven probabilistic wind field modeling for the wind-induced response prediction of cable-supported bridges

Aksel Fenerci[1], Ph.D. candidate, Department of Structural Engineering, Norwegian University of Science and Technology, Trondheim, Norway

Ole Øiseth, Ph.D., Department of Structural Engineering, Norwegian University of Science and Technology, Trondheim, Norway

*Keywords: suspension bridge, buffeting response, probabilistic turbulence model, turbulence characteristics, cross-spectral density*

## Abstract

In this study, full-scale wind velocity measurements are conducted at eight locations on the Hardanger Bridge girder to investigate the possibility of a probabilistic representation of the turbulence field along the bridge span. Using appropriate assumptions, the two-dimensional turbulence field along the structure is reduced to six turbulence parameters, which are considered as correlated lognormally distributed random variables. The directionality and wind speed dependence of the parameters are demonstrated by means of wind roses and scatter diagrams. Depending on the wind speed and direction, simulations of the turbulence field were carried out using random number generators. The performance of simulated wind fields in capturing the variability and correlation structures of an actual wind field at a site is tested by detailed comparisons with the measurement data. For the sake of illustration, simulations were also performed for the design wind speed of the Hardanger Bridge using the current model and another model from the literature. The resulting probabilistic model is suitable for implementation in reliability-based frameworks and long-term extreme response analysis.

## Introduction

There is an increasing global demand for long-span cable-supported bridges around the world, as the world population and urbanization grow rapidly. Although the nearly 20-year-old Akashi-Kaikyo suspension bridge still holds the world record for the longest span, during the last two decades a large number of long-span bridge projects were realized. The possibility of building super long-span suspension bridges (greater than 3000 m spans) has also been considered for long and deep straits such as the Gibraltar Strait or the Messina Strait. Recently, a similar effort was initiated by the Norwegian government (Dunham, 2016; Ellevset and Skorpa, 2011). As the span lengths of cable-supported bridges increase, wind-induced effects become of primary importance. In addition to potentially destructive phenomena such as flutter, the buffeting response of such structures is also critical and may govern design, especially for the serviceability and fatigue limit states (Xu, 2013). The buffeting response of cable-supported bridges have been analyzed using a stochastic dynamics framework (Davenport, 1962; Jain et al., 1996; Scanlan, 1978), which relies on an accurate description of the turbulent wind loads acting on the structure. This description is commonly achieved using the cross-spectral densities of the turbulence components, which are assumed to be zero-mean stationary Gaussian stochastic processes. Over the years, many spectral formulae have been suggested by researchers in this regard (Busch and Panofsky, 1968; Davenport, 1961; ESDU 086010, 2001; ESDU 85020, 2001; Kaimal et al., 1972; Krenk, 1996; Kristensen and Jensen, 1979; Mann, 2006; Simiu and Scanlan, 1996; Solari, 1987; Tieleman, 1995; Toriumi et al., 2000; von Karman, 1948). Most of the formulae are restricted to flat homogenous terrain and neutral atmospheric conditions. Several attempts have also been made for spectra in complex terrain (ESDU 85020, 2001; Mann, 2000; Nielsen et al., 2007; Panofsky et al., 1982; Tieleman, 1992).

[1] Corresponding author: aksel.fenerci@ntnu.no

In bridge design, such spectral formulae are commonly used. Regardless of the spectral form adopted, the spectral parameters are deterministic where the mean wind speed remains as the only design parameter. This approach ignores any uncertainty in turbulence parameters, which might arise due to the intrinsic variable nature of the wind. However, Solari and Piccardo showed that the parameters of the turbulence spectra exhibited vast variability between measurements at different sites (Solari and Piccardo, 2001). A large variability was also reported in field measurement results at specific bridge sites identified with complex terrain (Fenerci et al., 2017; Hui et al., 2009a, 2009b). Moreover, it was also reported that this variability has implications on the buffeting response analysis of long-span cable-supported bridges and should not be ignored during the design (Fenerci et al., 2017; Fenerci and Øiseth, 2017).

Modern approaches to structural design and assessment suggest consideration of uncertainties in the structural and aerodynamic properties of structures, as well as in the environmental loading. The effect of these uncertainties on the dynamic response can be taken into account in previously established frameworks such as probabilistic response analysis (Kareem, 1988; Minciarelli et al., 2001; Solari, 1997), reliability analysis (Davenport, 1983a, 1983b; Kareem, 1987; Pagnini, 2010; Xu, 2013; Zhang et al., 2008) or performance-based design (Ciampoli et al., 2011; Spence and Kareem, 2014). In such analyses, a probabilistic turbulence model is often needed to propagate the parametric uncertainties due to the inherent variability of the wind turbulence field into the response estimates. A probabilistic model of this sort is also useful for the estimation of a long-term extreme response, when a full long-term approach is adopted (Giske et al., 2017; Xu et al., 2017). In an estimation of the long-term extreme response in this manner, a joint probability distribution of all parameters governing the turbulence field, such as turbulence intensities, integral length scales or parameters defining one-point and two point correlation structures of the turbulence, has to be defined (Naess and Moan, 2012; Xu et al., 2017). Thereby, with the available response analysis and design tools at hand, a good probabilistic description of the variable turbulence field at the considered site is needed.

Although the need for a probabilistic description of a wind field has been stressed extensively during the past years, little work has been performed towards development of such models. The only probabilistic model, to the authors' knowledge is of Solari and Piccardo (2001), which is based on a large amount of measurement data from different sites reported in the literature. Although its performance is yet to be tested, such a model includes the variability between the different sites and measurement campaigns, which might result in overly conservative uncertainty estimates for a specific site.

In the present study, a probabilistic description of the turbulence field along the Hardanger Bridge (HB) in Norway is carried out using long-term monitoring data. The turbulence spectra are modeled with simple expressions with only a few parameters, which are frequently used in practice. The probability distributions and correlation structure of the turbulence parameters, conditional on the mean wind speed and direction, are deduced using measurement data. Using a random number generator, simulations of the turbulent wind field are generated and compared with measurement data to assess the validity of the model. Finally, simulations for the design wind speed of the HB are conducted using both the current model and the model developed by Solari and Piccardo.

## Wind conditions at the Hardanger Bridge site

In Western Norway, the Hardanger Bridge (HB) crosses the Hardangerfjord and today it remains the longest suspension bridge in Norway with its main span of 1308 meters. The bridge is situated in a mountainous and complex terrain (Fig. 1) in the Norwegian fjords and is exposed to strong European windstorms. As part of a research project funded by the Norwegian Public Roads Administration (NPRA), wind velocities at several locations along the bridge girder have been monitored since December 2013 by the Norwegian University of Science and Technology (NTNU). Detailed information on the instrumentation and the workings of the monitoring system can be found in (Fenerci et al., 2017; Fenerci and Øiseth, 2017). The layout of the wind sensors on the bridge are shown schematically in (Fig. 2) and the coordinates of the sensors are given in Table 1. The monitoring system, which has been permanently installed on the bridge since 2013, records data in a discontinuous manner with a predefined trigger wind speed of 15 m/s. This means that a recording with a 30-

minute duration is taken each time the trigger value is exceeded by a 1-minute mean speed in any of the anemometers. The system is also triggered manually from time to time in a random manner to include recordings with low mean speeds in the database and avoid excessive storage demand at the same time.

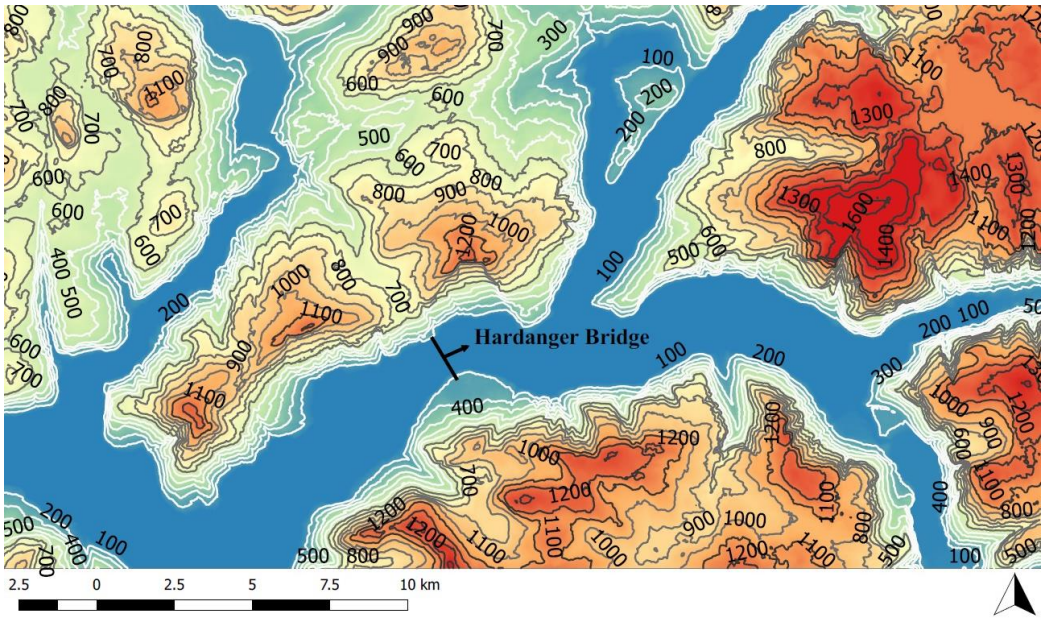


Fig. 1. Local topographical map of the Hardanger Bridge site

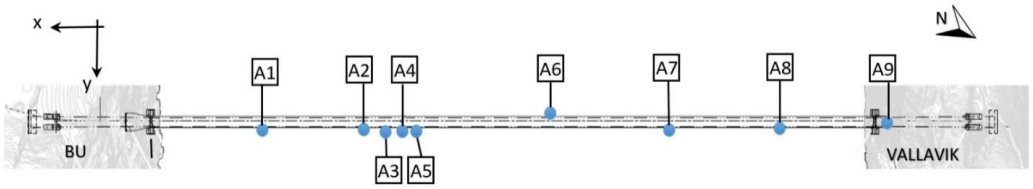


Fig. 2. Layout of the wind sensors

Table 1 Coordinates of the wind sensors (the origin of the coordinate system is at the midspan of the bridge)

| | A1 | A2 | A3 | A4 | A5 | A6 | A7 | A8 | A9 |
|---|---|---|---|---|---|---|---|---|---|
| x (m) | 460 | 280 | 240 | 200 | 180 | -10 | -180 | -420 | -655 |
| y (m) | 7.25 | 7.25 | 7.25 | 7.25 | 7.25 | -7.25 | 7.25 | 7.25 | 4.5 |
| z (m) | 0.3 | 3.2 | 3.9 | 4.6 | 4.9 | 8 | 5.2 | 1.2 | 140 |

Then, the acquired wind velocity data from the anemometers are collected into a dataset to study the long-term wind characteristics, and an averaging interval of 10 minutes is adopted to obtain the turbulence statistics. This resulted in 15386 recordings with a 10-minute duration each in the dataset. Fig. 3 shows a histogram of all 10-minute recordings collected over each month since the start of the project. The wind velocity data were first recorded in polar coordinates and then decomposed into a mean (static) part in the horizontal plane and three fluctuating (turbulent) components. In a cartesian coordinate system directed along the along-wind direction

(mean wind direction), three orthogonal turbulence components were defined, namely, the along-wind (u), cross-wind (v) and vertical (w) turbulences. A histogram of the mean wind speed for all recordings is given in Fig. 4. Using these turbulence components, three turbulence intensity components can be defined accordingly as

$$I_u = \frac{\sigma_u}{U}, I_v = \frac{\sigma_v}{U}, I_w = \frac{\sigma_w}{U} \tag{1}$$

where $\sigma_{u,v,w}$ denote the standard deviations of the three turbulence components and U denotes the mean wind speed. The turbulence intensity provides an elegant measure of the intensity of the wind speed fluctuations and is one of the most descriptive statistics of turbulence since it directly relates to the energy content of the turbulence.

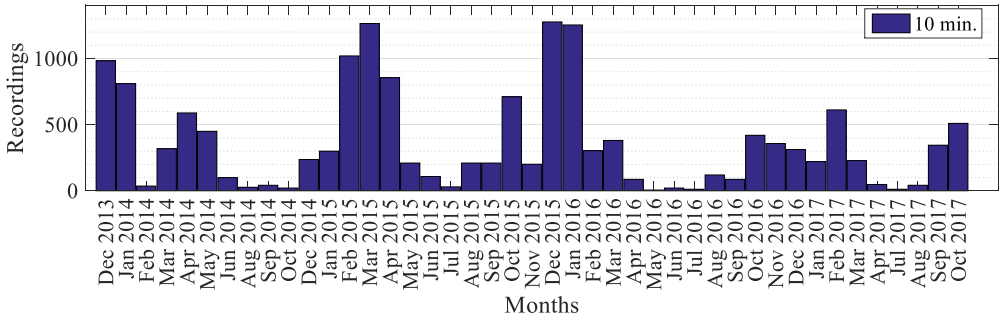


Fig. 3. Overview of the 10-minute recordings

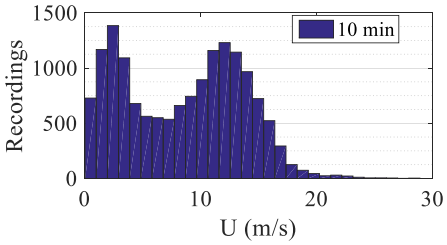


Fig. 4. Histogram of the mean wind speed for all the recordings

For the 10-minute recordings in the dataset, using the data from the midspan sensor (A6) only, wind rose scatter plots of the mean wind speed and the three turbulence intensities are presented in Fig. 5 to provide an overview of the general wind conditions at the site. The recordings with mean wind speeds lower than 3 m/s were discarded from the data set. Due to high number of data points in the plots, the relative data density was calculated for a fine rectangular grid in the plotting area, and the relative density was assigned to each point by means of color-coding. It should be noted that the density for the easterly and westerly winds were calculated separately. This allows a visualization of how the data are distributed according to the upwind direction and along a particular direction. The distinct spreading of the mean wind speed was observed for the easterly and westerly winds. It is also noticed that the turbulence intensity is higher for the winds approaching from the mountain side on the north, whereas it is smaller for winds blowing along the fjord.

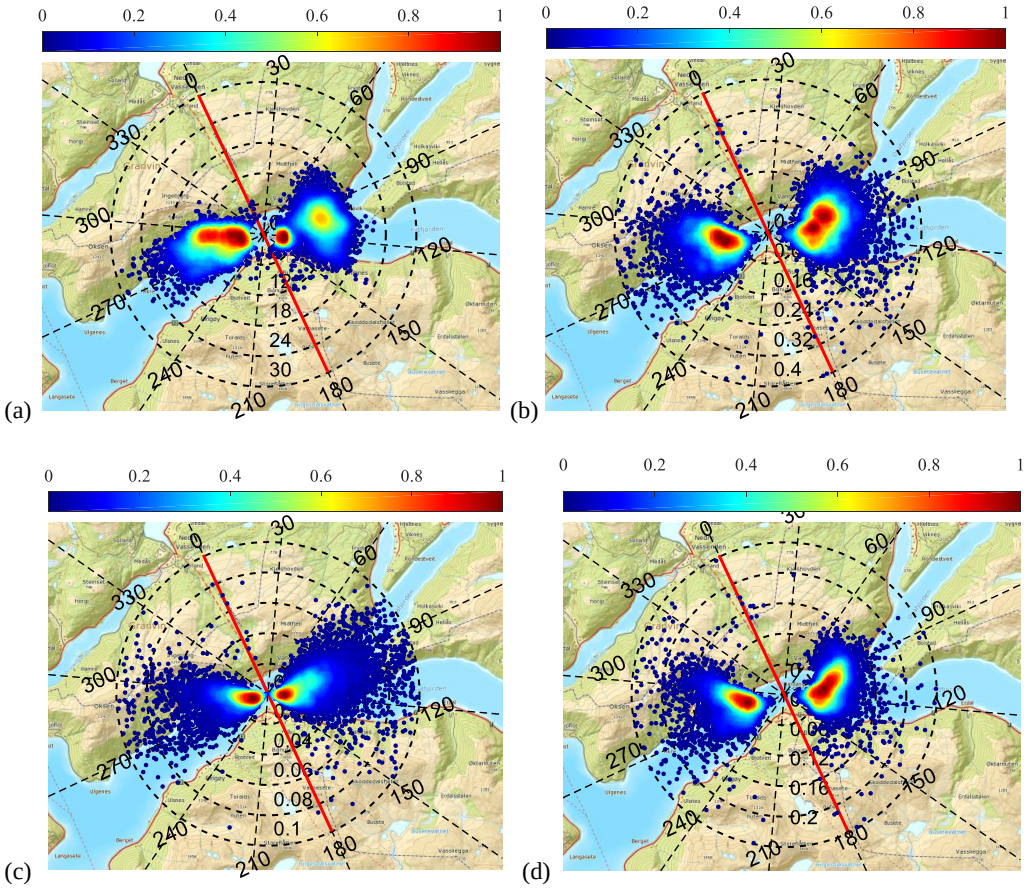


Fig. 5. Wind rose scatter plots: the (a) mean wind speed; (b) along-wind; (c) cross-wind and (d) vertical turbulence intensities at the midspan of the bridge (the color bar indicates the relative density of data points in the area, and red line highlights the bridge longitudinal axis)

## Wind Field modeling

Modeling the relevant atmospheric turbulence field is of outmost importance in prediction of the wind-induced dynamic response of long-span bridges, since it is used to model the environmental dynamic loads acting on the structure. In the frequency domain, for a horizontal line-like structure, the turbulence field can be represented by a cross-spectral density tensor such as

$$S_{turb} = \begin{bmatrix} S_{uu}(\Delta x, f) & S_{uw}(\Delta x, f) \\ S_{wu}(\Delta x, f) & S_{ww}(\Delta x, f) \end{bmatrix} \tag{2}$$

Here, the cross terms are usually neglected since they have little influence on the dynamic response (Cheynet, 2016; Øiseth et al., 2013). The diagonal terms can be written as

$$S_{uu}(\Delta x, f) = S_u(f)C_u(\Delta x, f)$$
$$S_{ww}(\Delta x, f) = S_w(f)C_w(\Delta x, f) \tag{3}$$

where $S_{u,w}(f)$ are the auto power spectral densities of the u and w turbulence components, $C_{u,w}$ are the normalized cross-spectral densities and f is the frequency. The normalized cross-spectra is a frequency dependent correlation coefficient, providing the spatial correlation of the turbulence components along the bridge longitudinal axis. For two points, $x_1$ and $x_2$, separated by a distance $\Delta x$, the normalized cross-spectra read

$$C_i(\Delta x, f) = \frac{S_i^{x_1 x_2}(\Delta x, f)}{\sqrt{S_i^{x_1}(f) S_i^{x_2}(f)}}, \quad i = u, w \tag{4}$$

where $S_{u,w}^{x_1 x_2}(\Delta x, f)$ are the cross-power spectral densities of the same turbulence component at points $x_1$ and $x_2$ separated by $\Delta x$. The cross-power spectral density has a real part and a complex part as usual, where the complex part contains phase information. In the case of separations in the horizontal plane perpendicular to the along-wind direction, the phase is usually small and often neglected (ESDU 086010, 2001; Simiu and Scanlan, 1996). The normalized spectra containing only the real part is also referred to as the normalized co-spectra. In summary, a modeling of the turbulence field for a horizontal line-like structure requires the definition of two auto-spectral densities and two normalized co-spectra for the u and w turbulence components.

The literature is rich on formulae for the spectral densities of the turbulence components, which were derived both on empirical and theoretical bases. However, most models rely on the assumption of a flat and homogenous terrain and neutral atmospheric stability. Moreover, the models are based on deterministic coefficients or simple variables as functions of the height above the ground or the roughness length, which makes it difficult to reflect the variability in the turbulence characteristics due to complex topographical effects. In previous papers by the authors (Fenerci and Øiseth, 2018, 2017), it was shown that the auto-spectra and normalized co-spectra of turbulence component at the HB site could be represented well with two simple expressions commonly used in the literature when the parameters of these expressions were fitted to the measured data. The expressions for the auto-spectra are of a Kaimal-type (Kaimal et al., 1972; Simiu and Scanlan, 1996), where the normalized co-spectra is of a Davenport type (Davenport, 1961), which read

$$\frac{S_{u,w} f}{\sigma_{u,w}} = \frac{A_{u,w} f_z}{(1+1.5A_{u,w} f_z)^{5/3}}, \quad f_z = \frac{fz}{U}$$
$$C_{u,w} = \exp(-K_{u,w} \frac{f \Delta x}{U}) \tag{5}$$

where z is the height above ground level (68 meters above sea level for the HB), which ensures dimensional consistency. The non-dimensional parameters $A_{u,w}$ and $K_{u,w}$ are to be fitted to the 10-minute measurements and are referred to as the spectral parameter and the decay coefficient, respectively. Adopting the above expressions, for a particular mean wind speed and direction, the turbulence field for the entire structure can be defined with just six parameters ($\sigma_{u,w}$, $A_{u,w}$, $K_{u,w}$), which can be treated as random variables. In sequence, these parameters relate to the energy content and correlation lengths of the turbulence components along the along-wind and bridge longitudinal axes. Nevertheless, to use these parameters in a probabilistic framework, an elaborate investigation of their underlying probability distributions, dependence on the mean wind speed or direction and correlation structures is needed.

Using the data from the midspan sensor (A6) the one-point statistics and the data from the closely spaced sensor pairs (A3-A4, A4-A5) for the two-point statistics, the six turbulence parameters were calculated for all 10-minute recordings above 3 m/s mean wind speed. The parameters are presented in Fig. 6 in terms of wind rose scatter plots using the same manner as in Fig. 5. The power spectral densities of the 10-minute signals were estimated using Welch's method of averaged periodograms (Welch, 1967), where 8 segments with 50% overlap were

averaged to reduce the variance in the Fast Fourier Transform (FFT) estimates. The expressions of Eqn. (5) were then fitted to the estimated auto and normalized co-spectra of the turbulence components using a nonlinear least-squares approximation to obtain the $A_{u,w}$ and $K_{u,w}$ parameters. Observing the plots, the distinct distribution of data for the easterly and westerly winds and dependence of the parameters on the upwind direction are noted. A mountainous upwind terrain was associated with high turbulence ($\sigma_{u,w}$), where the spectral parameter $A_{u,w}$ was higher for the fjord exposure. The decay coefficient $K_{u,w}$ seems less sensitive to the wind direction, as it shows approximately uniform scatter with respect to the mean wind direction.

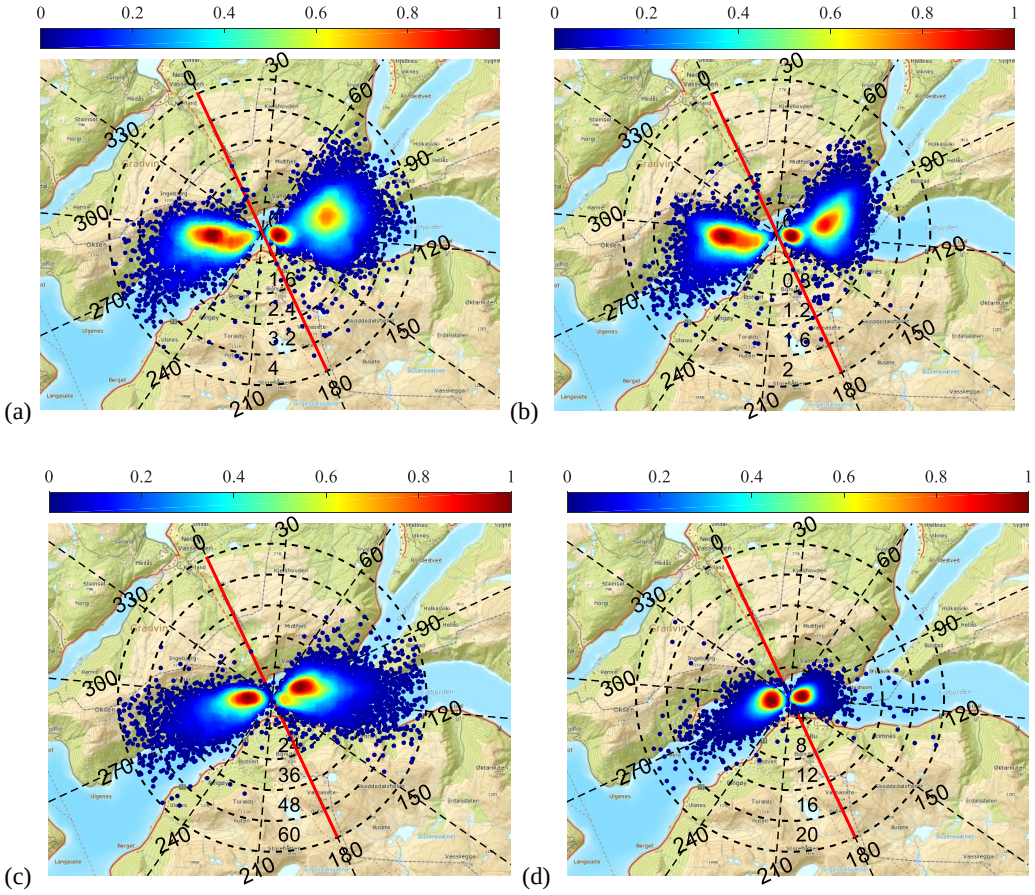


(a) (b) (c) (d)

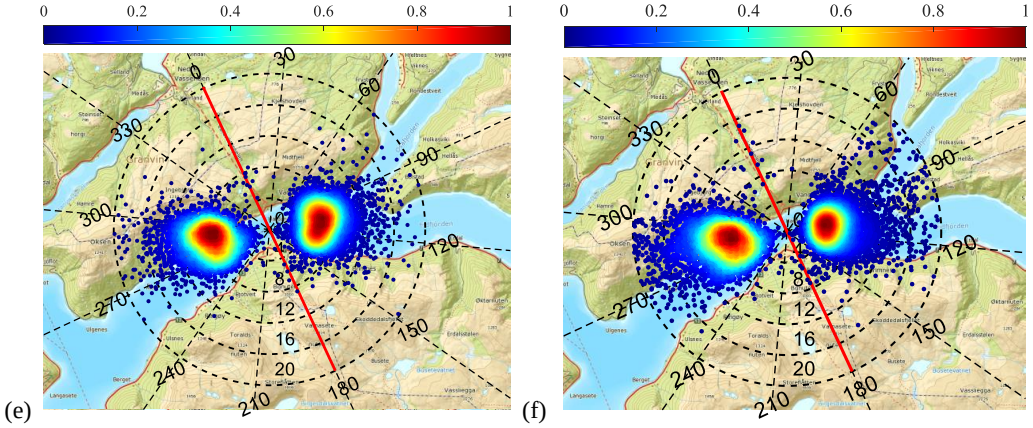


Fig. 6. Wind rose scatter plots of the turbulence parameters: (a) $\sigma_u$; (b) $\sigma_w$; (c) $A_u$; (d) $A_w$; (e) $K_u$ and (f) $K_w$ (the color bar indicates the relative data density; the red line indicates the bridge longitudinal axis)

In addition to the wind direction, it is deemed important to investigate the dependence of the turbulence parameters on the mean wind speed. Scatter plots are presented for each of the six parameters against the mean wind speed to reveal their dependence on the wind speed (Fig. 7 and Fig. 8). The data were plotted for the east and west winds separately. For each scatter diagram, the linear regression fits were plotted on top of the data to show the linear dependence on the variables. From the figures, a clear linear dependence was observed for the parameters $\sigma_u$, $\sigma_w$ and $A_u$, where no significant dependence was detected for the three remaining parameters.

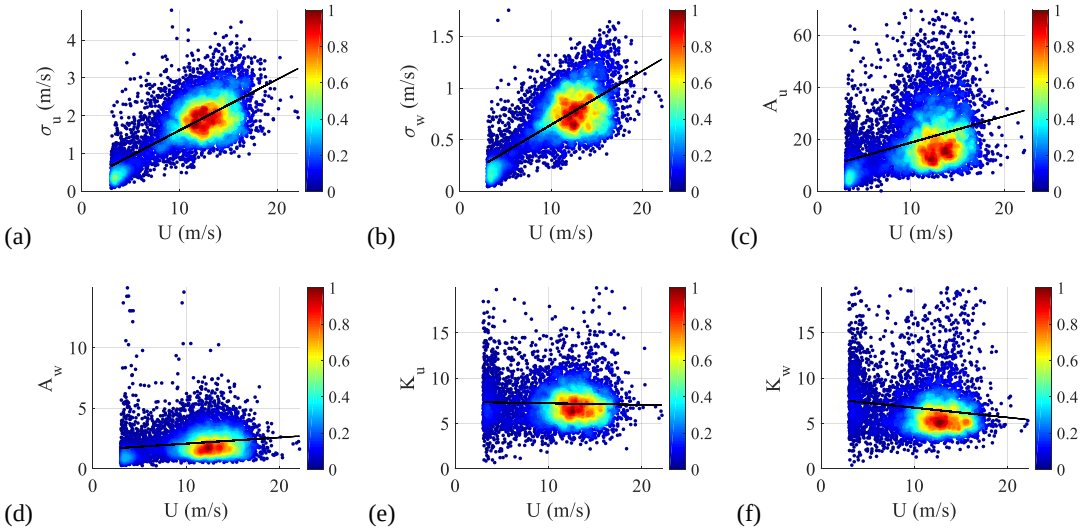


Fig. 7. Turbulence parameters against the mean wind speed for the easterly winds: (a) $\sigma_u$; (b) $\sigma_w$; (c) $A_u$; (d) $A_w$; (e) $K_u$ and (f) $K_w$ (the color bar shows the relative data density; the straight line is a linear regression fit)

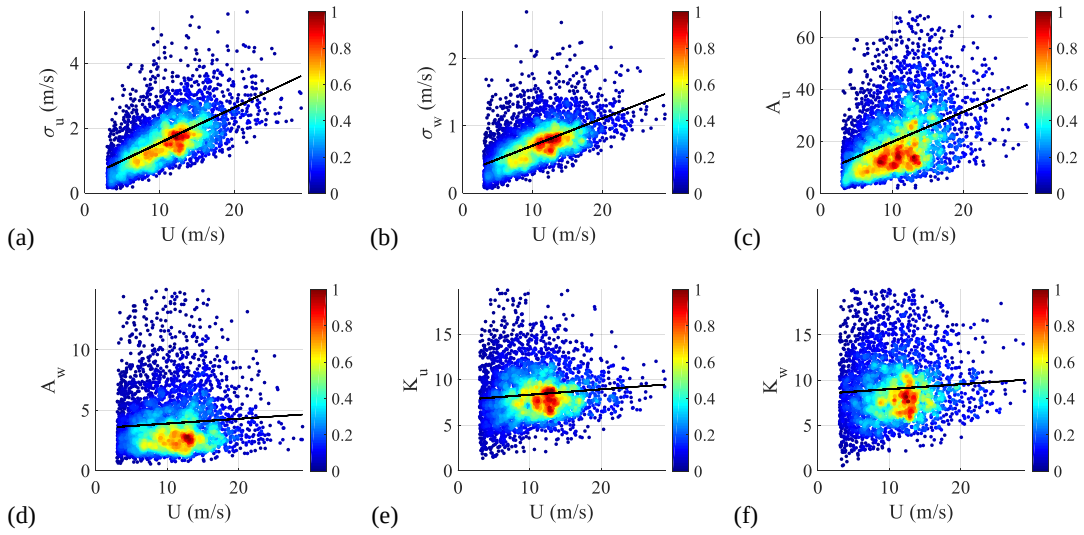


Fig. 8. Turbulence parameters against the mean wind speed for the westerly winds: (a) $\sigma_u$; (b) $\sigma_w$; (c) $A_u$; (d) $A_w$; (e) $K_u$ and (f) $K_w$ (the color bar shows the relative data density; the straight line is a linear regression fit)

## Statistical properties of the turbulence parameters

Having established that the turbulence field at the HB site can be modeled with the six turbulence parameters dependent on the mean wind speed and the wind direction, their statistical properties, such as the underlying probability distributions and correlation structures, can now be established. To that extent, using all recordings with mean wind speeds above 10 m/s, the scatter diagrams of the six turbulence parameters were plotted against each other in a matrix form. The results are shown in Fig. 9 and Fig. 10 for the easterly and westerly winds, respectively. In the diagonal, histograms of the turbulence parameters are plotted, showing the probability density. The lognormal probability distributions were then fitted to the data and shown on top of the histograms. The probability density function (pdf) of the lognormal distribution can be written for a random variable x as

$$P(x \mid \tilde{\mu}, \tilde{\sigma}) = \frac{1}{x\tilde{\sigma}\sqrt{2\pi}} \exp\left( \frac{-(\ln x - \tilde{\mu})^2}{2\tilde{\sigma}^2} \right) \tag{6}$$

where $\tilde{\mu}$ and $\tilde{\sigma}$ are the parameters of the distribution, which are the mean and the standard deviation of the associated normal distribution, respectively. Note that for a lognormally distributed random variable x, the natural logarithm of x is normally distributed with the mean $\tilde{\mu}$ and the standard deviation $\tilde{\sigma}$. Therefore, the parameters of the lognormal distribution can simply be estimated by calculating the mean and the standard deviation of the natural logarithm of the random variable from available data. The lognormal distribution parameters are given in Table 2. In the off-diagonals, scatter plots of turbulence parameters were plotted against each other, showing their correlation structures. Linear regression curves were also plotted along with the scatter diagrams to highlight the trends present in the plots, which are not apparent due to the large number of data points and large scatter. A strong linear dependence between the turbulence standard deviations $\sigma_u$ and $\sigma_w$ is immediately evident after a first look at the matrix plots. For the easterly and westerly winds, the matrices of the correlation coefficients of the turbulence parameters are tabulated in Table 3. Examining the table and the scatter diagrams, the correlations between $\sigma_u$ and $\sigma_w$, $A_u$ and $A_w$, $K_u$ and $K_w$, $\sigma_u$ and $A_u$ and $\sigma_w$ and $A_w$ are considered significant, where the other

pairs are assumed as uncorrelated. Note that different correlation structures are observed for the winds from two directions.

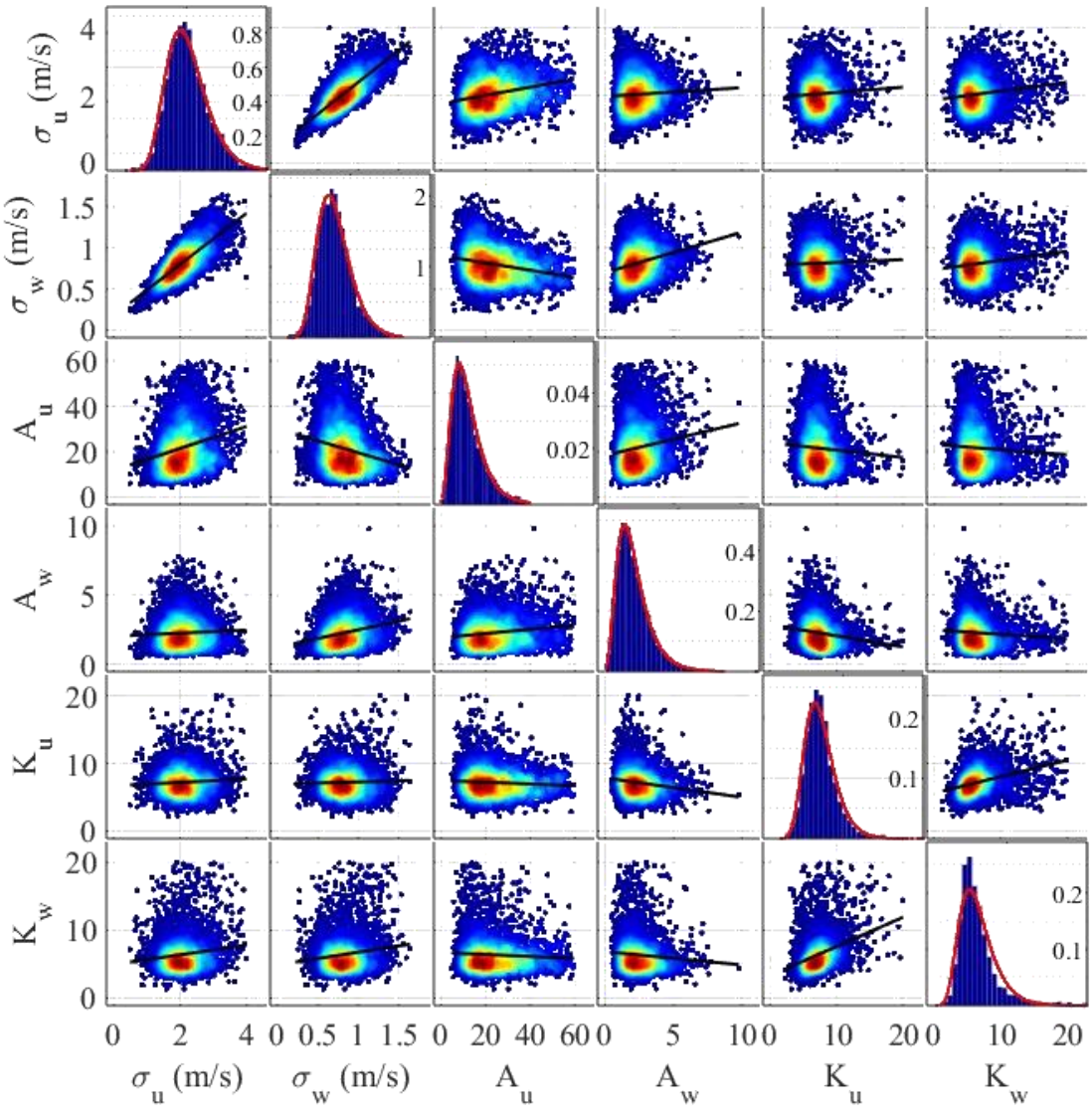


Fig. 9. The scatter plot matrix of the turbulence parameters for the easterly winds (the y-axis for the histograms indicating the probability density is shown on the right side of the plotting area)

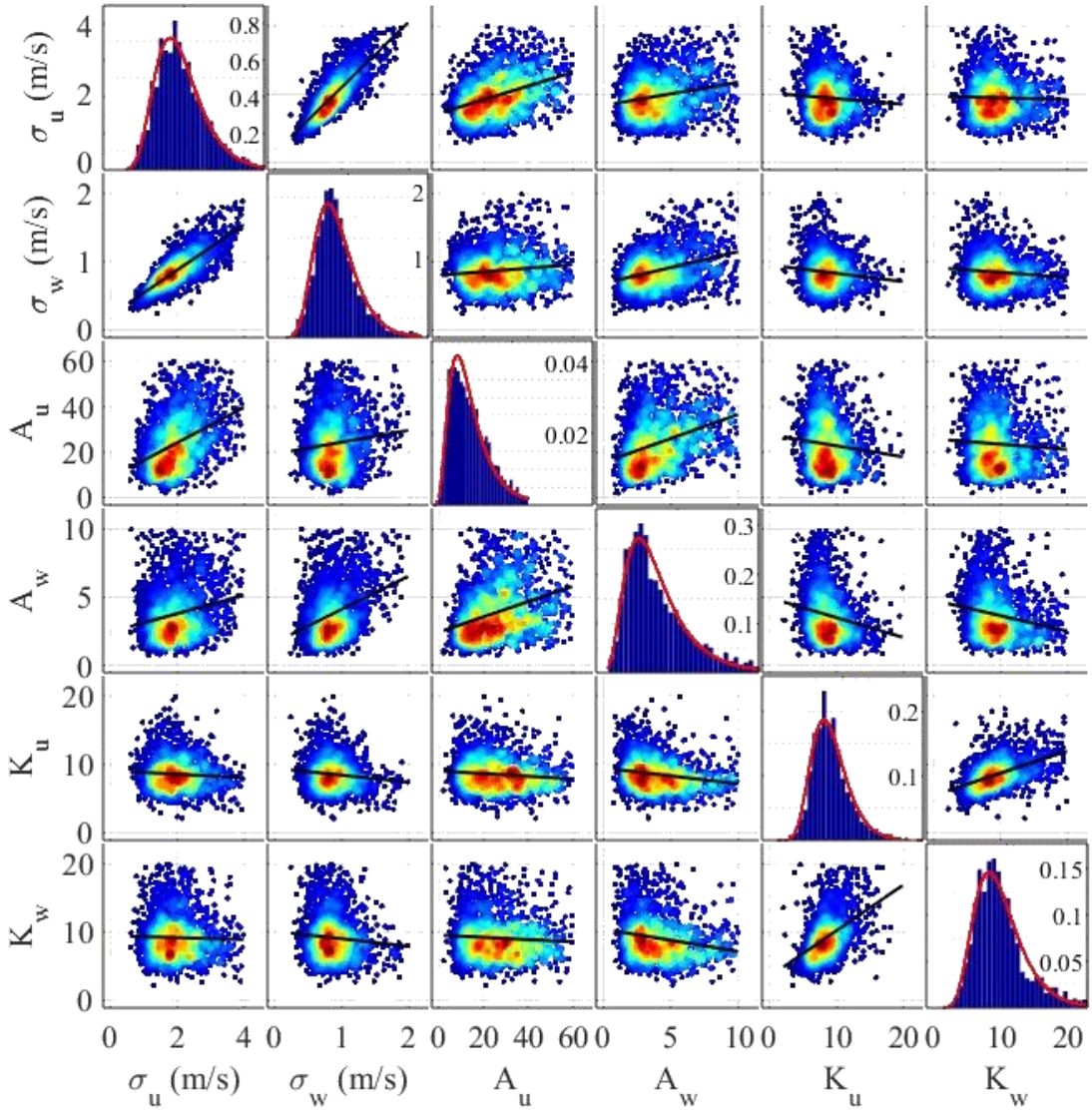


Fig. 10. The scatter plot matrix of the turbulence parameters for the westerly winds (the y-axis for the histograms indicating the probability density is shown on the right side of the plotting area)

Table 2 Lognormal distribution parameters for the easterly and westerly winds

| | | $\sigma_u$ | $\sigma_w$ | $A_u$ | $A_w$ | $K_u$ | $K_w$ |
|---|---|---|---|---|---|---|---|
| EAST | $\tilde{\mu}$ | 0.6753 | -0.2468 | 2.9669 | 0.7076 | 1.9385 | 1.7932 |
| | $\tilde{\sigma}$ | 0.2566 | 0.2632 | 0.4538 | 0.4466 | 0.2652 | 0.3423 |
| WEST | $\tilde{\mu}$ | 0.6104 | -0.1932 | 3.0364 | 1.2075 | 2.1093 | 2.1633 |
| | $\tilde{\sigma}$ | 0.3159 | 0.3021 | 0.5282 | 0.4943 | 0.268 | 0.3322 |

Table 3 Correlation coefficients matrix for the easterly and westerly winds

| | | $\sigma_u$ | $\sigma_w$ | $A_u$ | $A_w$ | $K_u$ | $K_w$ |
|---|---|---|---|---|---|---|---|
| | $\sigma_u$ | 1 | 0.7608 | 0.2641 | 0.045 | 0.0458 | 0.1289 |
| | $\sigma_w$ | 0.7608 | 1 | -0.2056 | 0.2571 | 0.0044 | 0.1338 |
| | $A_u$ | 0.2641 | -0.2056 | 1 | 0.1633 | -0.0678 | -0.0564 |
| | $A_w$ | 0.045 | 0.2571 | 0.1633 | 1 | -0.1706 | -0.0843 |
| | $K_u$ | 0.0458 | 0.0044 | -0.0678 | -0.1706 | 1 | 0.3261 |
| EAST | $K_w$ | 0.1289 | 0.1338 | -0.0564 | -0.0843 | 0.3261 | 1 |
| | $\sigma_u$ | 1 | 0.8148 | 0.4087 | 0.1712 | -0.0559 | -0.0199 |
| | $\sigma_w$ | 0.8148 | 1 | 0.053 | 0.2851 | -0.1036 | -0.0656 |
| | $A_u$ | 0.4087 | 0.053 | 1 | 0.3065 | -0.0525 | -0.0385 |
| | $A_w$ | 0.1712 | 0.2851 | 0.3065 | 1 | -0.2059 | -0.2002 |
| | $K_u$ | -0.0559 | -0.1036 | -0.0525 | -0.2059 | 1 | 0.4725 |
| WEST | $K_w$ | -0.0199 | -0.0656 | -0.0385 | -0.2002 | 0.4725 | 1 |

It was previously stated that some of the parameters ($\sigma_u$, $\sigma_w$, $A_u$) were also dependent on the mean wind speed (Fig. 7 and Fig. 8). Consequently, the probability distributions given in Fig. 9 and Fig. 10 and the corresponding lognormal distributions parameters given in Table 2 do not represent the true distribution of these parameters, since the dataset is not complete in the entire wind speed range. To overcome this problem and obtain a true statistical representation of these parameters, the probability distributions of these parameters should be established conditional to the mean wind speed. Accordingly, the data were divided into 1 m/s intervals, and the corresponding lognormal parameters were calculated for each interval. In each interval, a minimum number of 70 recordings were sought because the distribution is not apparent otherwise. The estimated lognormal distribution parameters and the correlation coefficients were then plotted against the mean wind speed (c). It is found that the parameters $\tilde{\mu}_{\sigma_u}$, $\tilde{\mu}_{\sigma_w}$ and $\tilde{\mu}_{A_u}$ linearly vary with the mean wind speed, where the remaining $\tilde{\mu}$ and $\tilde{\sigma}$ parameters and the correlation coefficients ρ remain constant. It is also seen that the behavior of the statistical parameters stabilize after the mean wind speed exceeds 10 m/s. This is thought to arise due to the nonstationarity of the signals below 10 m/s, where trends in the wind speed and rapid changes in the wind direction are common. Therefore, the linear curves were fitted to the estimates of $\tilde{\mu}_{\sigma_u}$, $\tilde{\mu}_{\sigma_w}$ and $\tilde{\mu}_{A_u}$ in the range above 10 m/s to model the conditional distributions of these parameters. For the others, average of values above 10 m/s were taken. A summary of the results is shown in Table 4.

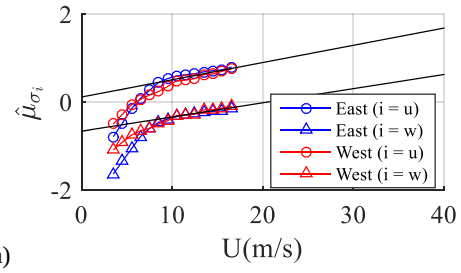


(a)

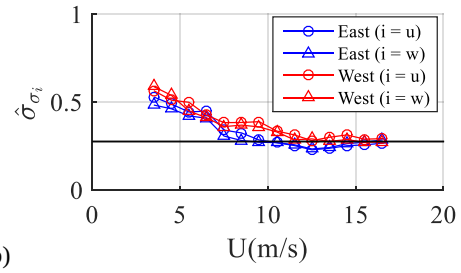


(b)

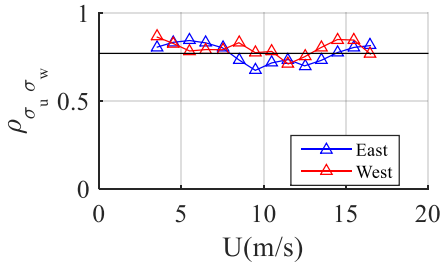


(c)

Fig. 11. Statistical parameters for the turbulence standard deviations: the (a) lognormal parameter $\tilde{\mu}$; (b) lognormal parameter $\tilde{\sigma}$ and (c) correlation coefficient $\rho$

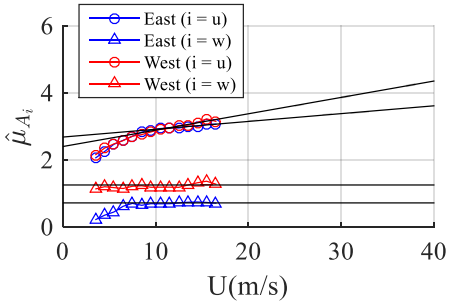


(a)

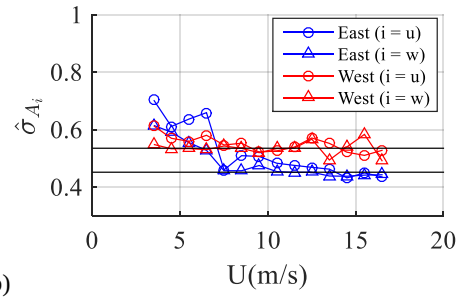


(b)

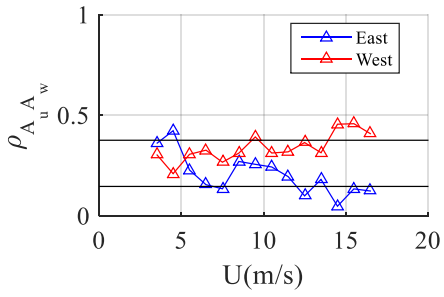


(c)

Fig. 12. Statistical parameters for the spectral parameter A: the (a) lognormal parameter $\tilde{\mu}$; (b) lognormal parameter $\tilde{\sigma}$ and (c) correlation coefficient $\rho$

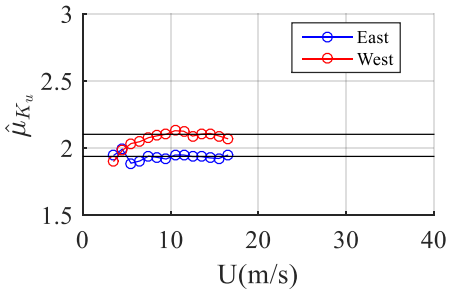


(a)

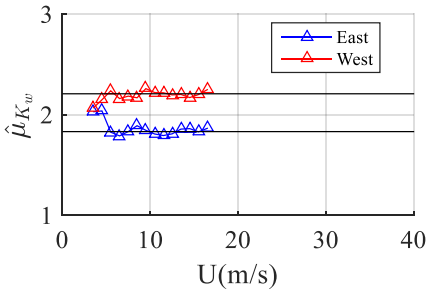


(b)

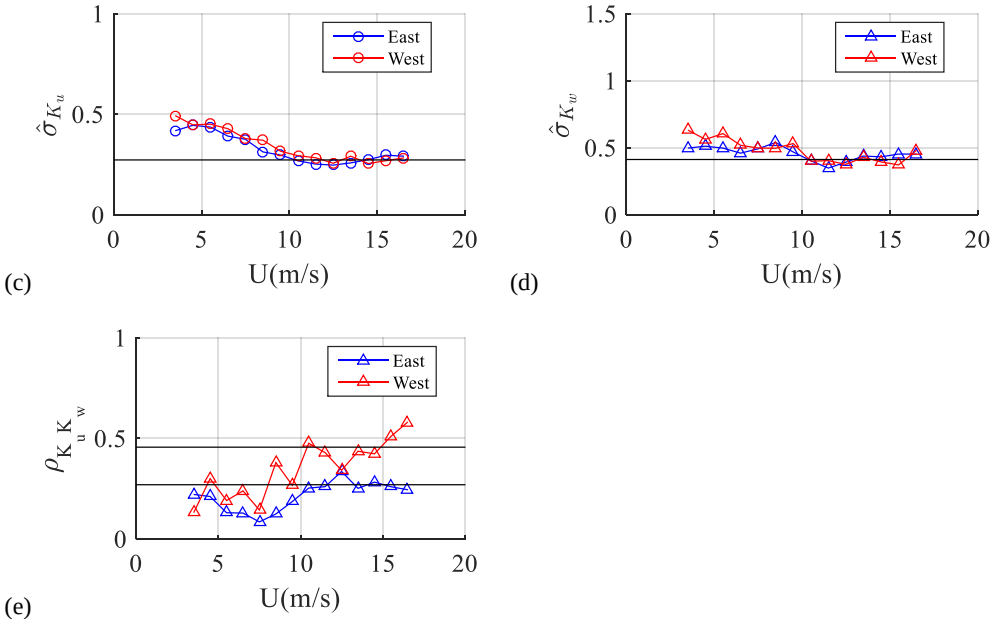


Fig. 13. Statistical parameters for the decay coefficient K: the (a) lognormal parameter $\tilde{\mu}_{K_u}$; (b) lognormal parameter $\tilde{\mu}_{K_w}$; (c) lognormal parameter $\tilde{\sigma}_{K_u}$; (d) lognormal parameter $\tilde{\sigma}_{K_u}$ and (e) correlation coefficient $\rho$

Table 4 Statistical properties of the turbulence parameters conditional to mean wind speed

| | East | | | West | | |
|---|---|---|---|---|---|---|
| | $\tilde{\mu}$ | $\tilde{\sigma}$ | $\rho$ | $\tilde{\mu}$ | $\tilde{\sigma}$ | $\rho$ |
| $\sigma_u$ | 0.122+0.039U | 0.28 | 0.754 | 0.122+0.039U | 0.28 | 0.772 |
| $\sigma_w$ | -0.657+0.032U | 0.278 | | -0.657+0.032U | 0.278 | |
| $A_u$ | 2.67+0.0248U | 0.456 | 0.15 | 2.407+0.048U | 0.556 | 0.327 |
| $A_w$ | 0.725 | 0.456 | | 1.247 | 0.556 | |
| $K_u$ | 1.938 | 0.275 | 0.267 | 2.11 | 0.275 | 0.459 |
| $K_w$ | 1.833 | 0.415 | | 2.213 | 0.415 | |

Ultimately, it was found appropriate to model $\tilde{\mu}_{\sigma_u}$, $\tilde{\mu}_{\sigma_w}$ and $\tilde{\mu}_{A_u}$ as functions of the mean wind speed and all the remaining parameters as constants. For an estimation of the constant parameters, all the data above a 10 m/s mean wind speed was used, as displayed in Table 2. The final lognormal distribution parameters and the correlation coefficient matrix are summarized in Table 5 and Table 6, respectively. As can be observed in Fig. 11 and Fig. 13, due to limited number of data points in the high wind speed range, the statistical parameters had to be extrapolated based on the data in the lower wind speed range. Therefore, it is important to ensure that these extrapolations are reasonable. For this purpose, the data in the high wind speed range were plotted along with the extrapolated probability distributions, and the correspondence between the measured data with the extrapolated distributions was assessed visually. The results are shown in Fig. 14 and Fig. 16. Here, note that the recordings with high wind speeds usually belong to the same storm events and therefore are not independent. Nevertheless, it is seen that the measured data remains in the reasonable margin even in the extrapolated wind speed range.

Table 5 Final lognormal parameters

| | | $\sigma_u$ | $\sigma_w$ | $A_u$ | $A_w$ | $K_u$ | $K_w$ |
|---|---|---|---|---|---|---|---|
| EAST | $\tilde{\mu}$ | 0.122+0.039U | -0.657+0.032U | 2.67+0.0248U | 0.7076 | 1.9385 | 1.7932 |
| | $\tilde{\sigma}$ | 0.2566 | 0.2632 | 0.4538 | 0.4466 | 0.2652 | 0.3423 |
| WEST | $\tilde{\mu}$ | 0.122+0.039U | -0.657+0.032U | 2.407+0.048U | 1.2075 | 2.1093 | 2.1633 |
| | $\tilde{\sigma}$ | 0.3159 | 0.3021 | 0.5282 | 0.4943 | 0.268 | 0.3322 |

Table 6 Final correlation matrix

| | | $\sigma_u$ | $\sigma_w$ | $A_u$ | $A_w$ | $K_u$ | $K_w$ |
|---|---|---|---|---|---|---|---|
| EAST | $\sigma_u$ | 1 | 0.7608 | 0.2641 | 0 | 0 | 0 |
| | $\sigma_w$ | 0.7608 | 1 | 0 | 0.2571 | 0 | 0 |
| | $A_u$ | 0.2641 | 0 | 1 | 0.1633 | 0 | 0 |
| | $A_w$ | 0 | 0.2571 | 0.1633 | 1 | 0 | 0 |
| | $K_u$ | 0 | 0 | 0 | 0 | 1 | 0.3261 |
| | $K_w$ | 0 | 0 | 0 | 0 | 0.3261 | 1 |
| WEST | $\sigma_u$ | 1 | 0.8148 | 0.4087 | 0 | 0 | 0 |
| | $\sigma_w$ | 0.8148 | 1 | 0 | 0.2851 | 0 | 0 |
| | $A_u$ | 0.4087 | 0 | 1 | 0.3065 | 0 | 0 |
| | $A_w$ | 0 | 0.2851 | 0.3065 | 1 | 0 | 0 |
| | $K_u$ | 0 | 0 | 0 | 0 | 1 | 0.4725 |
| | $K_w$ | 0 | 0 | 0 | 0 | 0.4725 | 1 |

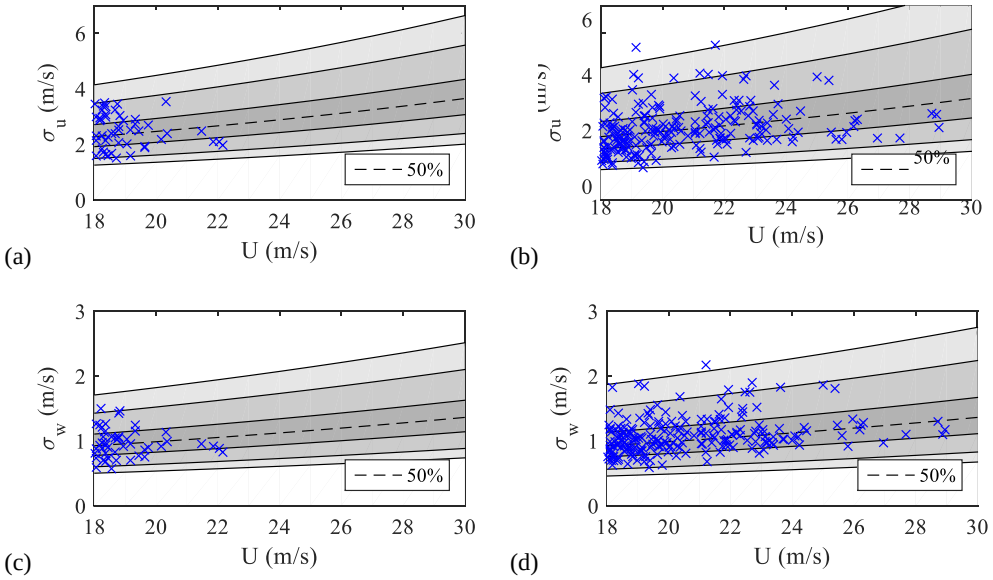

Fig. 14. Extrapolation of the probability distributions of the turbulence standard deviations: (a) $\sigma_u$ –East (b) $\sigma_u$ –West (c) $\sigma_w$ –West and (d) $\sigma_w$ –West (the continuous curves show the 1, 5, 25, 75, 95 and 99 percentiles of the distribution in order)

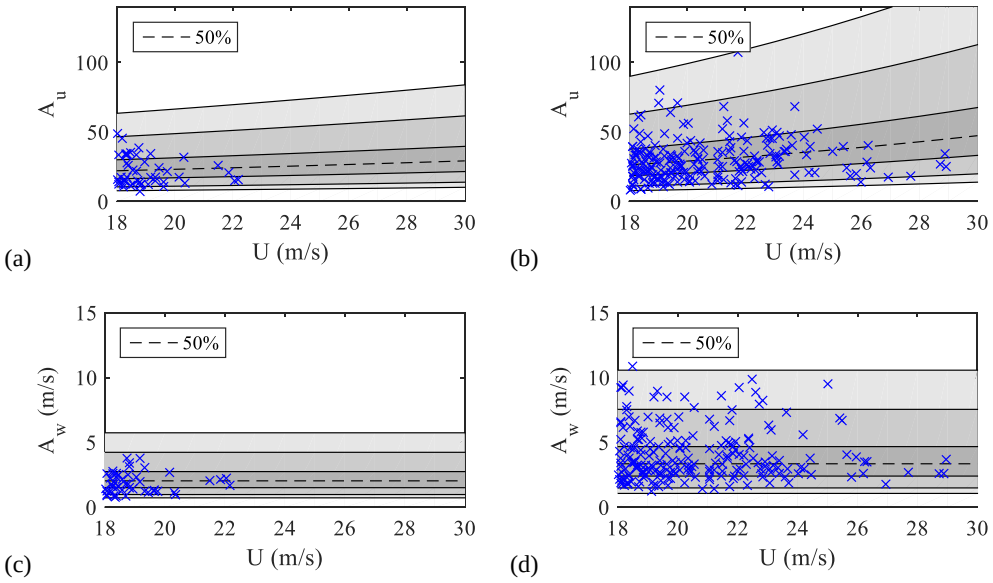


Fig. 15. Extrapolation of the probability distributions of the spectral parameters: (a) $A_u$ –East; (b) $A_u$ –West; (c) $A_w$ –West and (d) $A_w$ –West (the continuous curves show the 1, 5, 25, 75, 95 and 99 percentiles of the distribution in order)

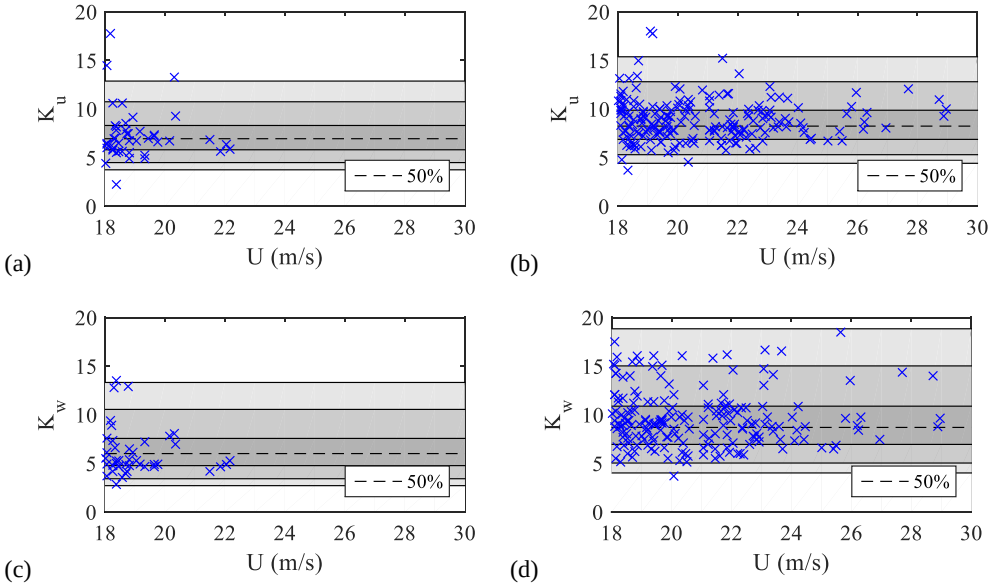


Fig. 16. Extrapolation of the probability distributions of the decay coefficients: (a) $K_u$ –East; (b) $K_u$ –West; (c) $K_w$ –West and (d) $K_w$ –West (the continuous curves show the 1, 5, 25, 75, 95 and 99 percentiles of the distribution in order)

## Simulations of random wind fields

A probabilistic turbulence field was formulated in the previous section that consisted of six correlated and lognormally distributed random variables. This model was validated by comparing the simulations from the model with the measured data. For this purpose, correlated lognormally distributed random parameters were generated. Parameter generation was achieved using a standard normally distributed number generator (The Mathworks Inc., 2015) and then taking their exponent. Given the vector of lognormally distributed random variables

$$Y = \begin{bmatrix} \sigma_u & \sigma_w & A_u & A_w & K_u & K_w \end{bmatrix} \tag{7}$$

the natural logarithm of the elements of Y forms a vector of normally distributed random variables

$$X = \ln(Y) \tag{8}$$

The mean values and standard deviations of the elements of the vectors Y and X are denoted as $(m_i, v_i)$ and $(\tilde{\mu}_i, \tilde{\sigma}_i),\ i = 1..6$, respectively, where the latter pair also represents the lognormal distribution parameters, as mentioned earlier. The two sets of statistical moments are related to each other as

$$\begin{aligned} m &= \exp(\tilde{\mu} + \tilde{\sigma}^2 / 2) \\ v &= \sqrt{\left(\exp(\tilde{\sigma}^2) - 1\right)\exp(2\tilde{\mu} + \tilde{\sigma}^2)} \end{aligned} \tag{9}$$

The covariance matrix of vector X can be written in terms of the covariance matrix of Y using (Zerovnik et al., 2012)

$$\operatorname{cov}(X_i, X_j) = \ln\left[\frac{\operatorname{cov}(Y_i, Y_j)}{m_i m_j} + 1\right],\ i = 1..6,\ j = 1..6 \tag{10}$$

which can be rewritten in terms of the correlation coefficient matrix of vector Y ( $\rho_y$ ) and the vector $\tilde{\sigma}$ as

$$\operatorname{cov}(X_i, X_j) = \ln\left[(\rho_y)_{ij}\sqrt{\exp(\tilde{\sigma}_i^2 - 1)}\sqrt{\exp(\tilde{\sigma}_j^2 - 1)} + 1\right],\ i = 1..6,\ j = 1..6 \tag{11}$$

Using Eqn. (11), the covariance matrix of the vector X of the normally distributed random variables can be calculated. Using this covariance matrix and knowing the mean value vector $\tilde{\mu}$, a set of multivariate correlated normally distributed random variables can be obtained. Then, the corresponding lognormal random variables can obtained by taking their natural exponents.

Using above formulations along with the vectors of $\tilde{\mu}$, $\tilde{\sigma}$ given in Table 5 and the correlation coefficient matrix $\rho$ given in Table 6, the random turbulence fields were generated for each 10 minute recording in the dataset. The conditional distributions for each simulation were established according to the mean wind speed and direction (east or west) of each individual recording. The simulated turbulence parameters were then compared with the measurement data in terms of scatter plots. The scatter plots with both measured and simulated turbulence components are shown in Fig. 17 and Fig. 19, respectively, for different mean wind velocity intervals. A brief look at the plots suggest that the target variability of the data is matched reasonably well by the simulations.

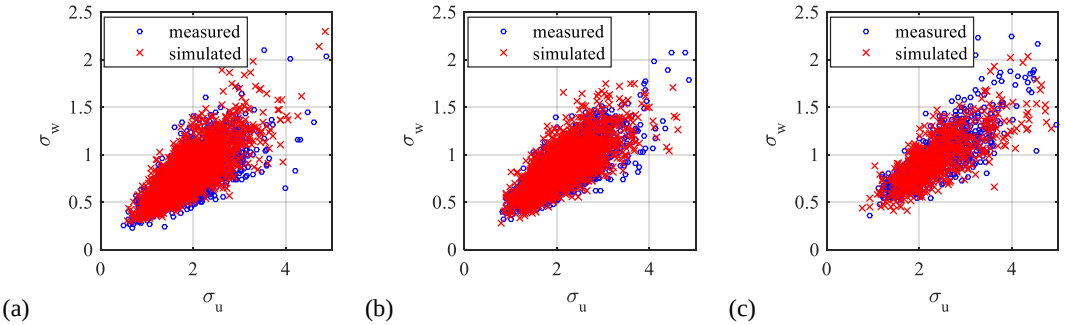


Fig. 17. Scatter plots of the measured and simulated turbulence standard deviations: (a) $10 \leq U < 13$ m/s; (b) $13 \leq U < 16$ m/s and (c) $U \geq 16$ m/s

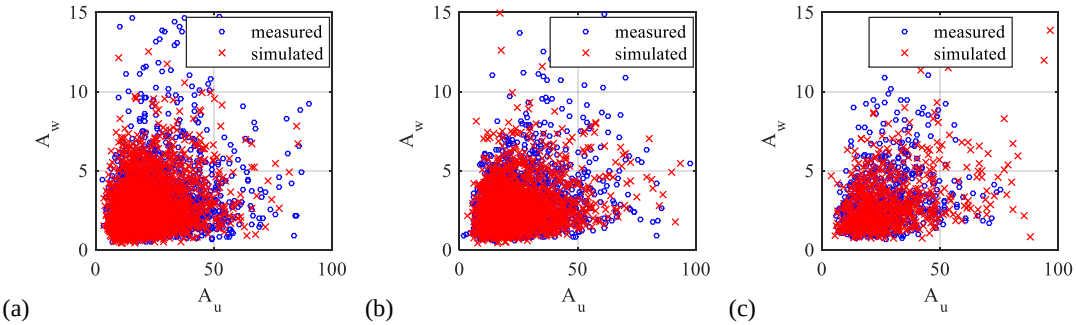


Fig. 18. Scatter plots of the measured and simulated turbulence spectral parameters: (a) $10 \leq U < 13$ m/s; (b) $13 \leq U < 16$ m/s and (c) $U \geq 16$ m/s

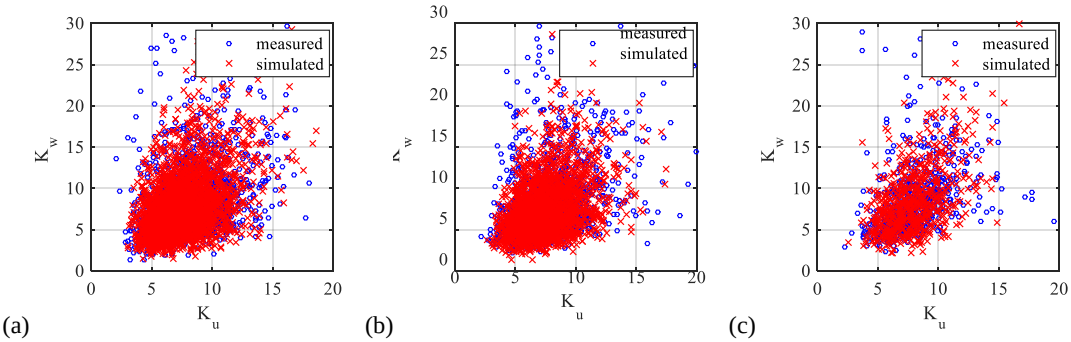


Fig. 19. Scatter plots of the measured and simulated decay coefficients: (a) $10 \leq U < 13$ m/s; (b) $13 \leq U < 16$ m/s and (c) $U \geq 16$ m/s

To have a more detailed look at the simulated wind field data and their correspondence with the measurements, the auto-spectral density and normalized co-spectra of the u and w turbulence, which are more familiar to engineers, are presented in Fig. 20 and Fig. 23, respectively. Only recordings with mean wind speeds above 10 m/s were considered. The simulated and measured spectra display a reasonable agreement. The relative data density is once again shown using color-coded data points. It is observed that for a given frequency, the auto-spectral density also follows a lognormal distribution. Fitting the lognormal distributions to the measured and simulated data, the peak of the distribution (mode) and the 95 percentile values for the auto-spectra were obtained and included in the same figures. For a clearer comparison, the measured and simulated auto-spectra were plotted

on top of each other, as shown in Fig. 24. Excellent agreement is observed between the percentile values, implying that the simulations are statistically representative of the measurements.

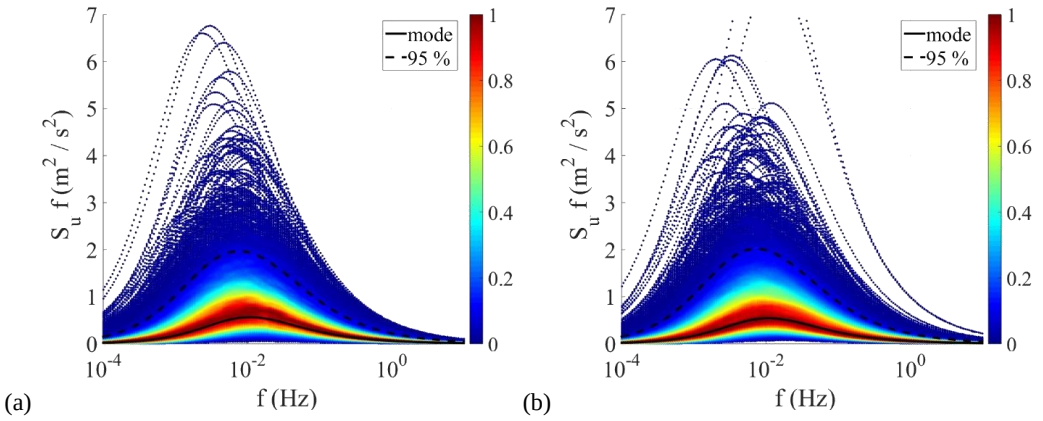


Fig. 20. Auto-spectral density of the along-wind turbulence: (a) measured and (b) simulated

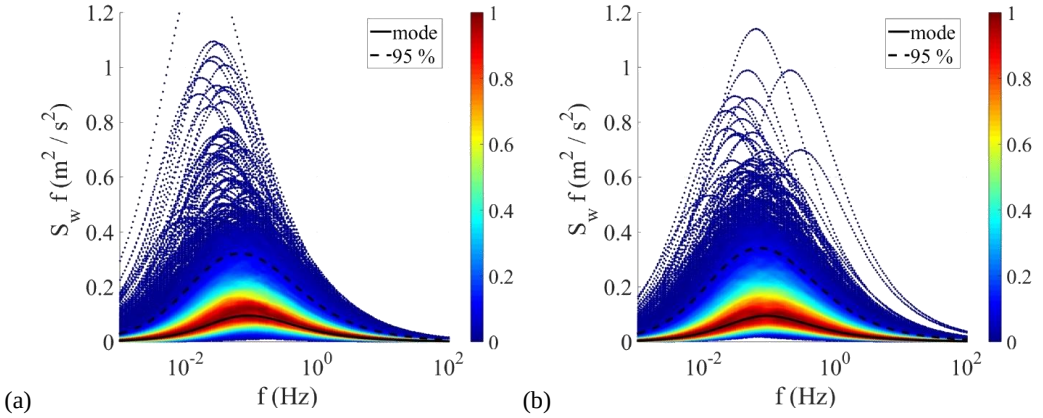


Fig. 21. Auto-spectral density of the vertical turbulence: (a) measured and (b) simulated

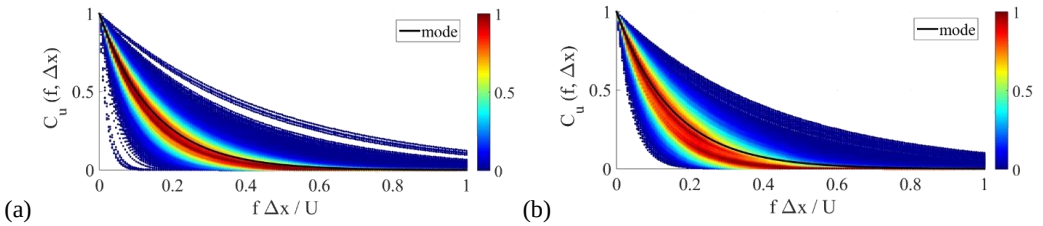


Fig. 22. Normalized co-spectra of the along-wind turbulence: (a) measured and (b) simulated

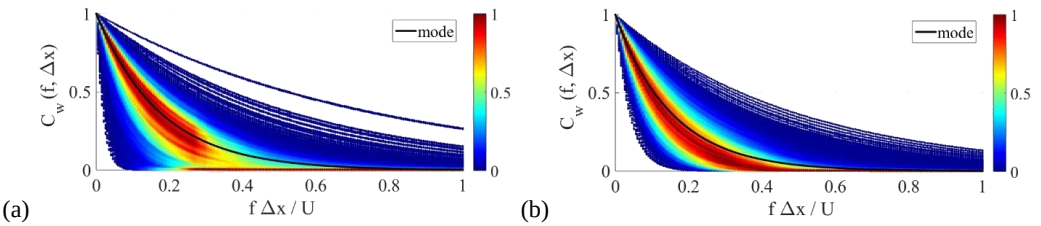


Fig. 23. Normalized co-spectra of the vertical turbulence: (a) measured and (b) simulated

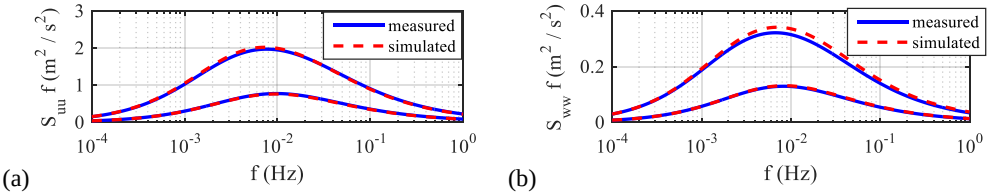


Fig. 24. Comparison of measured and simulated auto-spectra: (a) along-wind and (b) vertical turbulence (the curves show 50 and 95 percentile values)

Unlike the auto-spectra, the normalized co-spectra do not follow a lognormal distribution, since it is simply the exponential of a lognormally distributed random variable. Therefore, the spectral density tensors for both turbulence components deviate from the lognormal distribution, when the separation distance is larger. Note that the amplitude of the spectra becomes rather small in that case. This result is illustrated in Fig. 25 and Fig. 26. by showing the probability distributions of the spectral tensors at few important natural frequencies of the HB. Those natural frequencies, obtained through finite element analysis (Fenerci and Øiseth, 2017), are listed in Table 7 with their associated mode shape.

Table 7 First few fundamental natural frequencies and mode shapes of the Hardanger Bridge

| Mode | Frequency (Hz) | Period (seconds) | Description of the dominant motion |
|---|---|---|---|
| 1 | 0.05 | 20.00 | Symmetric lateral vibration of the deck |
| 2 | 0.098 | 10.20 | Asymmetric lateral vibration of the deck |
| 3 | 0.11 | 9.09 | Asymmetric vertical vibration of the deck |
| 4 | 0.14 | 7.14 | Symmetric vertical vibration of the deck |
| 15 | 0.36 | 2.78 | Symmetric torsional vibration of the deck |

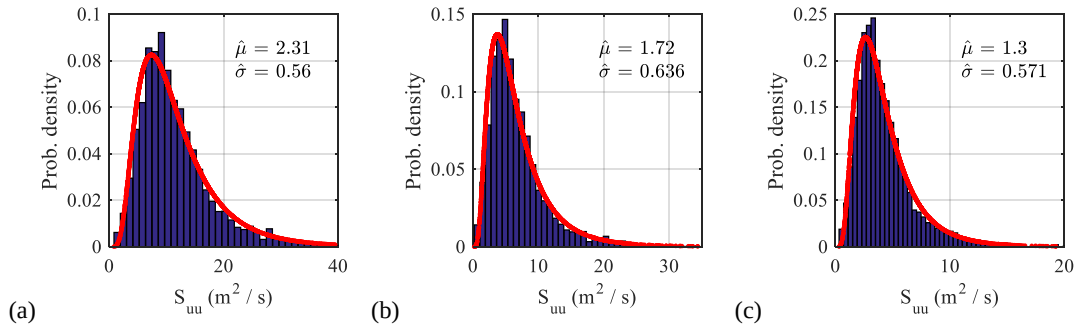

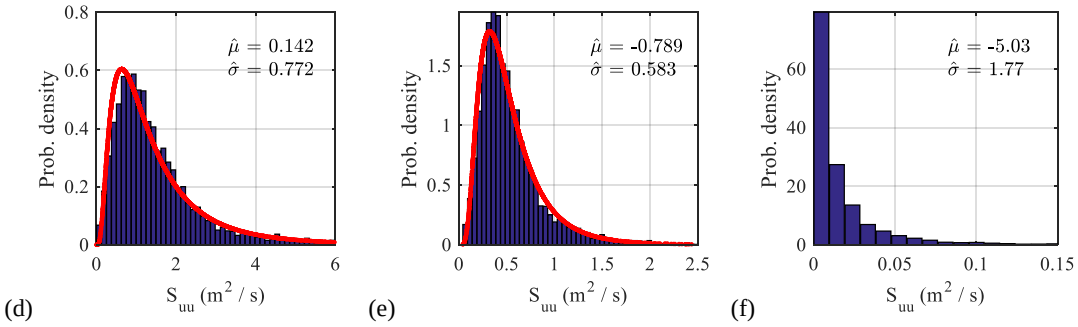


Fig. 25. Probability distributions of the spectral densities of the along-wind turbulence: (a) f = 0.05 Hz, Δx = 0 (b); f = 0.05 Hz, Δx = 20 m; (c) f = 0.098, Hz Δx = 0; (d) f = 0.098, Hz Δx = 20 m; (e) f = 0.36 Hz, Δx = 0 and (f) f = 0.36 Hz, Δx = 20 m (red curves show the lognormal fit)

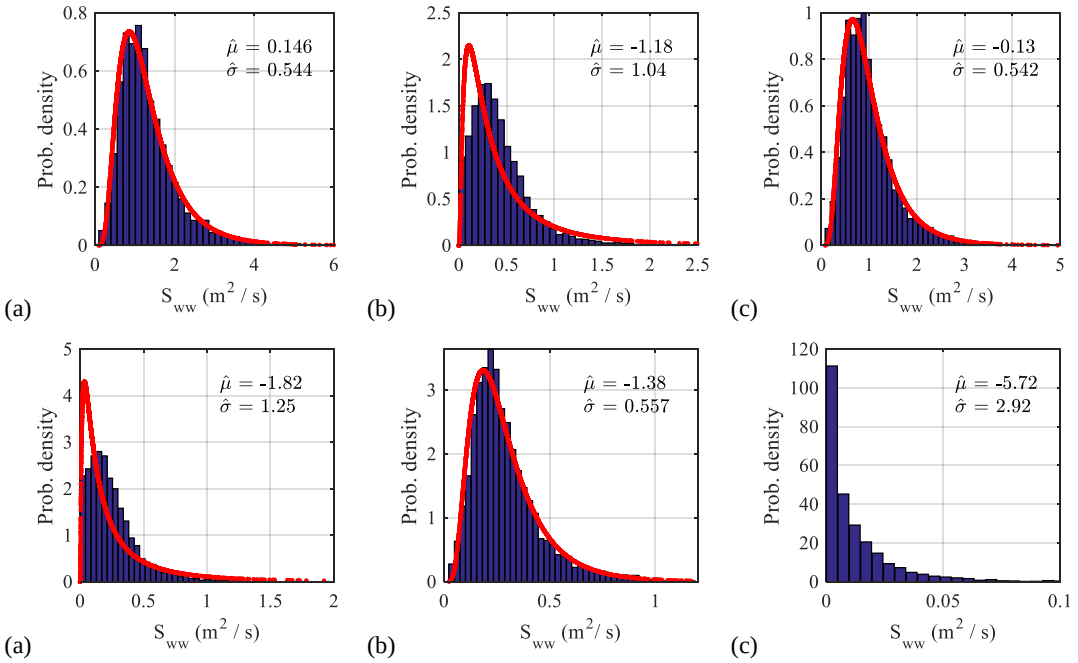


Fig. 26. Probability distributions of the spectral densities of the vertical turbulence: (a) f = 0.11 Hz, Δx = 0; (b) f = 0.11 Hz, Δx = 20 m; (c) f = 0.14 Hz, Δx = 0; (d) f = 0.14 Hz, Δx = 20 m; (e) f = 0.36 Hz, Δx = 0 and (f) f = 0.36 Hz, Δx = 20 m (red curves show the lognormal fit)

The probability distributions showed that it is possible to model the measured spectra with a lognormal distribution, at least for small separations. This allows further and more elaborate comparisons of the distributions of the measured and simulated spectral densities. To that extent, the correlation coefficients and lognormal distribution parameters were estimated for the measured and simulated spectral tensors and presented in Fig. 27 - Fig. 31 for the sake of comparison. A good overall agreement can be observed between the contour plots. Since it is difficult to observe the agreement in detail, especially for the important range of small separation distances and low frequencies, a numerical comparison is sought. For this purpose, surfaces were fitted to both data, where

the coefficients were obtained through a least-squares approximation. The equations of the surfaces, the estimated coefficients and the $R^2$ values as a measure of the goodness of the fits, are presented in Table 8 for the correlation coefficients and in Table 9 for the lognormal distribution parameters. Finally, the measured and simulated spectral tensors were compared at few important natural frequencies of the bridge (Fig. 32 and Fig. 33). Excellent agreement is observed except for the parameter $\tilde{\sigma}_{S_{ww}}(f,\Delta x)$, where the discrepancy increases with increasing separation distance. In the important range of separation where the magnitude of the spectra is large, the discrepancy remains within a reasonable margin.

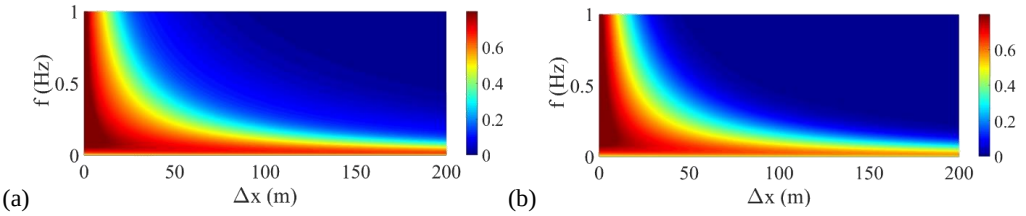


Fig. 27. Correlation coefficients $\rho_{S_{uu}S_{ww}}(f,\Delta x)$: (a) measured and (b) simulated

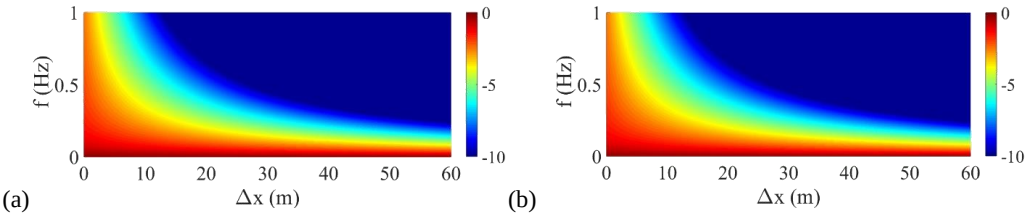


Fig. 28. Parameters $\tilde{\mu}_{S_{uu}}(f,\Delta x)$: (a) measured and (b) simulated

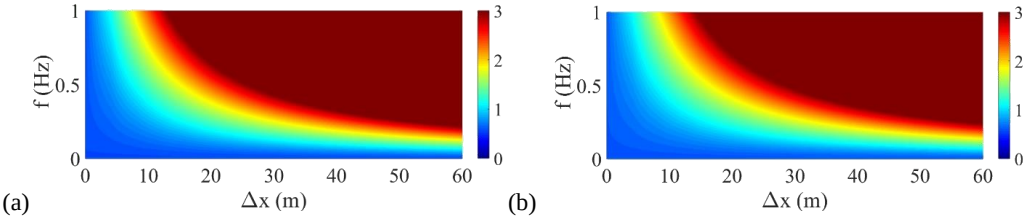


Fig. 29. Parameters $\tilde{\sigma}_{S_{uu}}(f,\Delta x)$ : (a) measured and (b) simulated

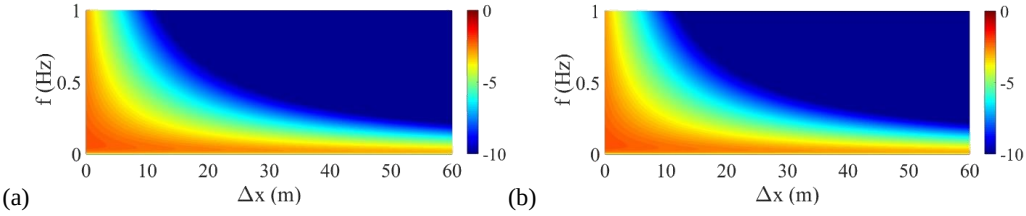


Fig. 30. Parameters $\tilde{\mu}_{S_{ww}}(f,\Delta x)$: (a) measured and (b) simulate

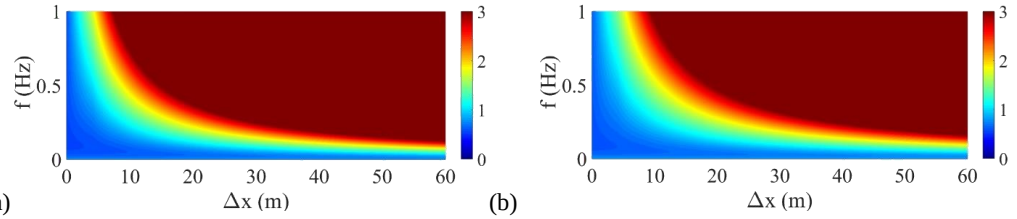


Fig. 31. Parameters $\hat{\rho}_{S_{ww}}(f,\Delta x)$: (a) measured and (b) simulated

Table 8 Surface fit to the correlation coefficients of the along-wind and vertical spectra

| surface equation | $\rho_{S_{uu}S_{ww}}(f,\Delta x)=p_0+p_x f+p_y(\Delta x)+p_{xy} f(\Delta x)+p_{xx} f^2+p_{yy}(\Delta x)^2$ | | | | | | |
|---|---|---|---|---|---|---|---|
| coefficients | $p_0$ | $p_x$ | $p_y$ | $p_{xy}$ | $p_{xx}$ | $p_{yy}$ | $R^2$ |
| measured | 1.126 | -1.464 | -0.00888 | 0.9121 | 0.000621 | 2.89E-05 | 0.87 |
| simulated | 1.08 | -1.404 | -0.00943 | 0.848 | 0.001138 | 3.11E-05 | 0.86 |

Table 9 Surface fits to the lognormal distribution parameters of the along-wind and vertical spectra

| surface equation | | $p_0+p_x f+p_y(\Delta x)+p_{xy} f(\Delta x)+p_{xx} f^2+p_{yy}(\Delta x)^2$ | | | |
|---|---|---|---|---|---|
| parameter | coefficients | $p_0$ | $p_x$ | $p_{xy}$ | $R^2$ |
| $\hat{\mu}_{S_{uu}}(f,\Delta x)$ | measured | 1.522 | -4.751 | -0.5886 | 0.999 |
| | simulated | 1.498 | -4.754 | -0.5992 | 0.999 |
| $\hat{\sigma}_{S_{uu}}(f,\Delta x)$ | measured | 0.2299 | -0.03733 | 0.2183 | 0.999 |
| | simulated | 0.2179 | -0.04053 | 0.2335 | 0.999 |
| $\hat{\mu}_{S_{ww}}(f,\Delta x)$ | measured | 0.3553 | -3.852 | -0.6029 | 0.999 |
| | simulated | 0.3973 | -3.804 | -0.6016 | 0.999 |
| $\hat{\sigma}_{S_{ww}}(f,\Delta x)$ | measured | 0.263 | 0.1371 | 0.3873 | 0.999 |
| | simulated | 0.2308 | -0.01032 | 0.236 | 0.999 |

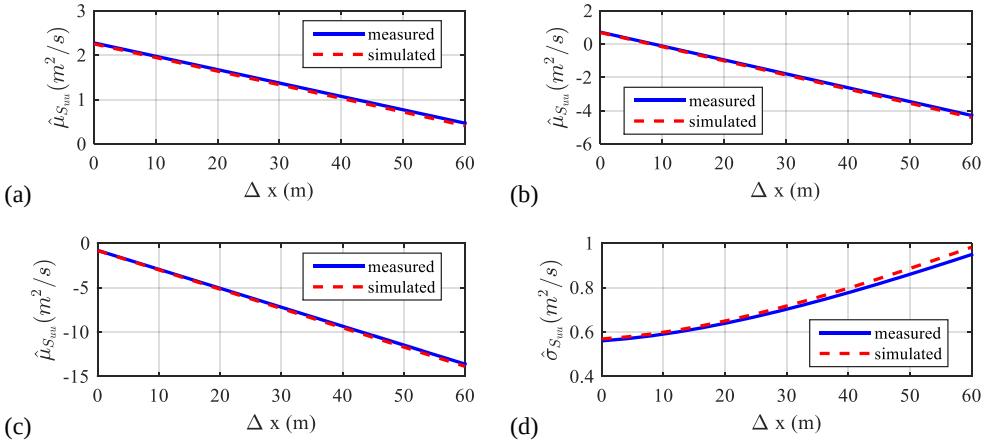

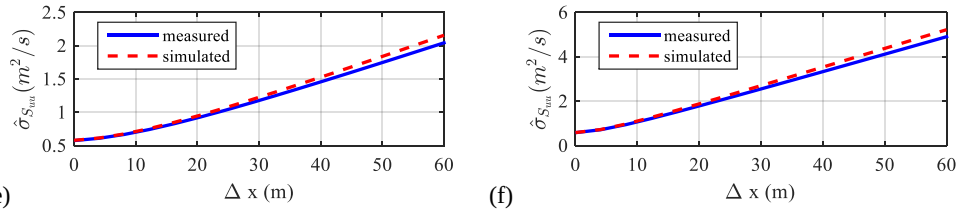


Fig. 32. Parameters for the spectral density of the along-wind turbulence: (a) f = 0.05 Hz; (b) f = 0.098 Hz; (c) f = 0.36 Hz; (d) f = 0.05 Hz; (e) f = 0.098 Hz and (f) f = 0.36 Hz

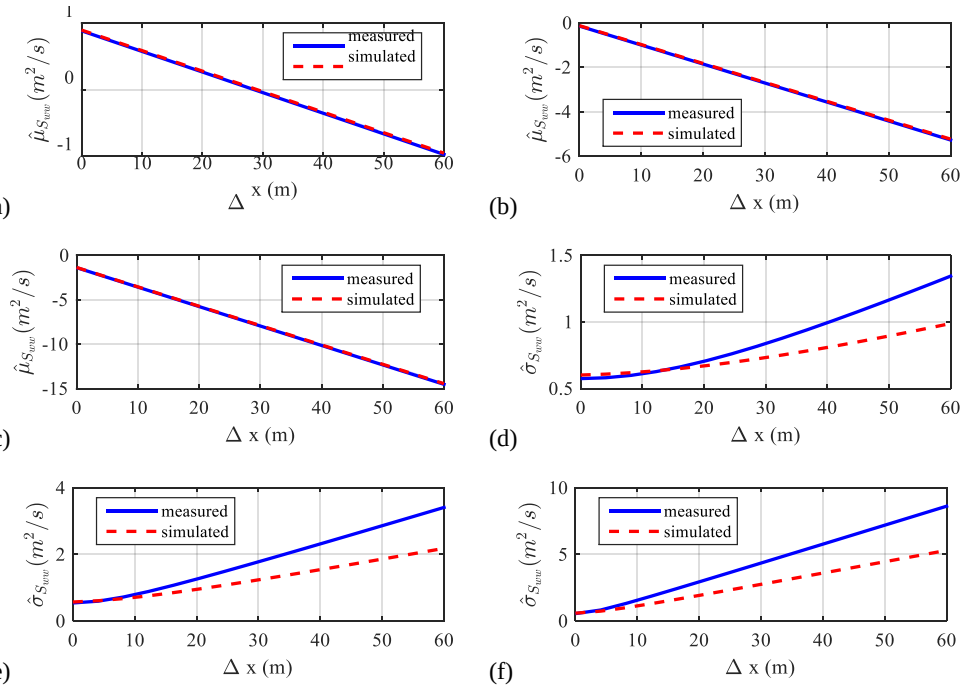


Fig. 33. Parameters for the spectral density of the vertical turbulence: (a) f = 0.11 Hz; (b) f = 0. 14 Hz; (c) f = 0.36 Hz; (d) f = 0.11 Hz; (e) f = 0. 14 Hz and (f) f = 0.36 Hz

## Simulations for the design wind speed

Previous investigations provided a probabilistic model with good confidence in describing the variability and statistical properties of the turbulence field at the Hardanger Bridge site. Now, using the established model, simulations of the turbulence field can be conducted for the design wind speed of the bridge. The design wind speed of the HB for a 10-minute averaging interval, which is the short-term extreme wind speed for a 50-year return period (0.02 annual probability of exceedance), was provided as 39 m/s (Statens-Vegvesen, 2006). Given the design wind speed, 1000 wind turbulence fields were generated for the east and west directions separately. The first 10 simulations of the parameters are listed in Table 10. The resulting autospectra and normalized co-spectra are presented in Fig. 34 and Fig. 35, respectively. On the same plots, the design spectra are also indicated. It is seen that for the along-wind turbulence, the design spectra provides slightly higher values than the mode,

where for the vertical turbulence it is on the higher side, closer to the 95$^{th}$ percentile. The design normalized co-spectra are also almost in the middle of the scatter. However, it is obvious that both spectra were exceeded by many of the simulations. Therefore, it can be stressed again that a deterministic description of the variable turbulence fields causes an oversimplification of the phenomenon, and it is not unexpected that this approach results into unconservative designs.

Table 10 First 10 simulations of the turbulence parameters for a design wind speed U = 39 m/s

| Sim. No. | EAST | | | | | | WEST | | | | | |
|---|---|---|---|---|---|---|---|---|---|---|---|---|
| | $\sigma_u$ | $\sigma_w$ | $A_u$ | $A_w$ | $K_u$ | $K_w$ | $\sigma_u$ | $\sigma_w$ | $A_u$ | $A_w$ | $K_u$ | $K_w$ |
| 1 | 5.24 | 2.06 | 35.74 | 3.71 | 13.90 | 10.37 | 4.72 | 1.88 | 75.48 | 5.31 | 8.61 | 11.79 |
| 2 | 8.19 | 2.47 | 99.77 | 2.40 | 8.01 | 4.96 | 4.95 | 1.77 | 38.89 | 1.75 | 4.87 | 6.77 |
| 3 | 4.51 | 1.37 | 102.65 | 3.94 | 9.29 | 11.28 | 9.13 | 2.99 | 177.62 | 7.27 | 10.38 | 8.69 |
| 4 | 6.80 | 2.25 | 50.48 | 3.73 | 7.64 | 4.44 | 6.78 | 2.29 | 75.51 | 3.06 | 7.66 | 11.18 |
| 5 | 3.86 | 1.54 | 27.15 | 3.11 | 5.74 | 6.56 | 4.03 | 1.58 | 30.74 | 1.79 | 9.08 | 5.79 |
| 6 | 4.24 | 1.61 | 24.09 | 2.68 | 6.35 | 8.69 | 3.83 | 1.93 | 29.81 | 3.94 | 8.64 | 5.53 |
| 7 | 5.16 | 1.94 | 47.34 | 2.84 | 2.93 | 5.26 | 4.97 | 2.11 | 69.05 | 5.85 | 10.72 | 9.79 |
| 8 | 3.95 | 1.24 | 29.38 | 1.60 | 6.22 | 8.12 | 5.25 | 1.68 | 93.77 | 3.35 | 4.45 | 8.10 |
| 9 | 4.76 | 2.02 | 30.57 | 3.58 | 4.80 | 7.83 | 9.38 | 4.16 | 87.62 | 8.56 | 12.49 | 11.32 |
| 10 | 5.66 | 1.80 | 32.91 | 1.17 | 7.32 | 10.91 | 6.11 | 2.03 | 92.89 | 3.68 | 11.92 | 13.18 |

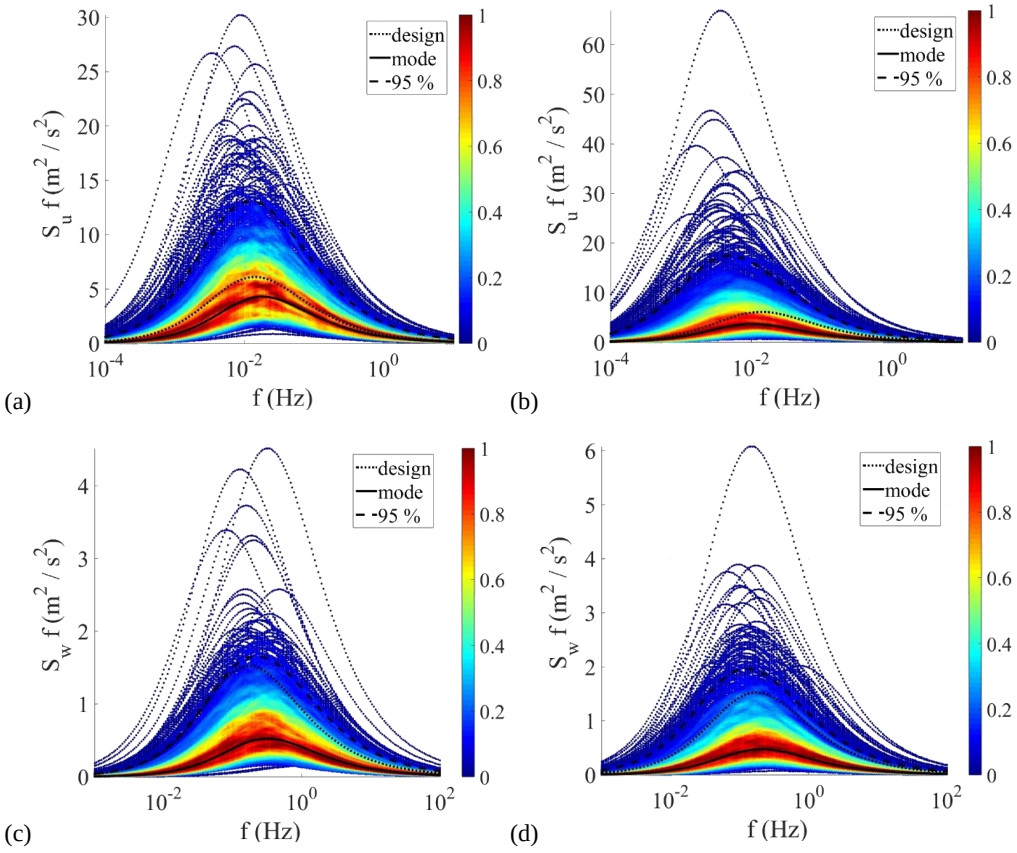

Fig. 34. Simulations of the autospectral density of the turbulence for a design wind speed of 39 m/s: the (a) along-wind turbulence for the easterly winds; (b) along-wind turbulence for the westerly winds; (c) vertical turbulence for the easterly winds and (d) vertical turbulence for the westerly winds (1000 simulations, the color bar shows the relative data density in the plotting area)

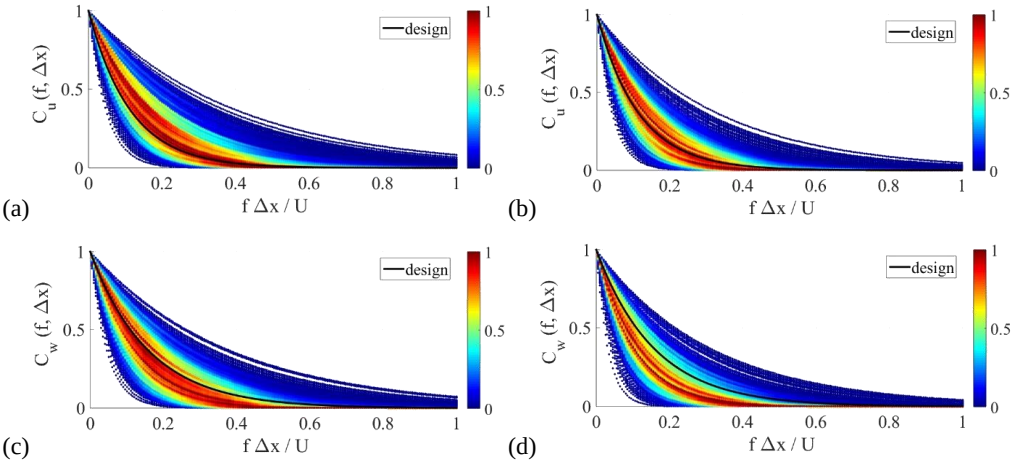


Fig. 35. Simulations of the normalized co-spectra of the turbulence for the design wind speed of 39 m/s: the (a) along-wind turbulence for the easterly winds; (b) along-wind turbulence for the westerly winds; (c) vertical turbulence for the easterly winds and (d) vertical turbulence for the westerly winds (1000 simulations, the color bar shows the relative data density in the plotting area)

Finally, as an illustrative and comparative exercise, simulations were conducted using a probabilistic model formulated by Solari and Piccardo (2001) almost two decades ago. In their study, the researchers adopted two simple parametric expressions for the autospectra and the normalized co-spectra. Neglecting the cross-spectral densities of the *u* and *w* components and discarding the *v* turbulence component as before, the spectra can be written as

$$\frac{S_{u,w}\,f}{{\sigma_{u,w}}^2} = \frac{6.868\ fL_{u,w}/U}{\left(1+1.5(6.868)\ fL_{u,w}/U\right)^{5/3}}$$
$$C_{u,w} = \exp\left(-K_{u,w}\frac{fz}{U}\right) \tag{12}$$

where $L_{u,w}$ are the integral length scales of turbulence. The length scales and standard deviations of turbulence components are estimated through

$$\sigma_{u,w} = \beta_{u,w}u_*$$
$$L_{u,w} = 300\lambda_{u,w}(z/200)^{\upsilon} \tag{13}$$
$$\upsilon = 0.67 + 0.05\ln(z_0)$$

where $u_*$ is the friction velocity and $z_0$ is the roughness length. Assuming that the coefficients $\beta_{u,w}$, $\lambda_{u,w}$ and $K_{u,w}$ are normally distributed random variables, Solari and Piccardo collected an extensive amount of

measurement data from literature to obtain their first and second statistical moments. The resulting mean values and covariance matrices for the coefficients were given as

$$\mu_\beta = \begin{bmatrix} 1 \\ 0.25 \end{bmatrix},\ \mathrm{cov}(\beta) = E\left[\beta_u\right]^2 \begin{bmatrix} 0.0625 & 0.0155 \\ 0.0155 & 0.0065 \end{bmatrix},\ E\left[\beta_u\right] = 6 - 1.1\arctan\left(\ln(z_0) + 1.75\right)$$
$$\mu_\lambda = \begin{bmatrix} 1 \\ 0.1 \end{bmatrix},\ \mathrm{cov}(\lambda) = \begin{bmatrix} 0.0625 & 0.006 \\ 0.006 & 0.0015 \end{bmatrix} \tag{14}$$
$$\mu_K = \begin{bmatrix} 10 \\ 6.5 \end{bmatrix},\ \mathrm{cov}(K) = \begin{bmatrix} 16 & 5.2 \\ 5.2 & 6.76 \end{bmatrix}$$

For the HB, $z_0$ can be taken as 0.01 m using the design basis (Statens-Vegvesen, 2006). The friction velocity is taken as 1.77 m/s following the ESDU 85020 (2001) guidelines. Using the above statistical properties, 1000 simulations of correlated normally distributed variables were obtained. Note that if the roughness coefficient can be defined for different directions, the model can account for the wind direction. Here, with the available design values, common spectra were obtained for all wind directions. The resulting simulated autospectra and normalized co-spectra are presented in Fig. 36. The design curves are also shown in the figures. Considering that the model is actually limited to a flat homogenous terrain and neutral atmospheric conditions, which is far from the conditions at the HB site, the simulated spectra do not provide results that are far off the measurements but rather present a more conservative version of the site-specific simulations, as shown in the figure. The overestimation of the along-wind turbulence spectra might be considered severe. It should also be noted that the model is quite sensitive to the friction velocity and the roughness coefficient. The scatter is also higher, which results from the use of Gaussian parameters rather than lognormal parameters. In summary, it seems that the model by Solari and Piccardo can be a good alternative in cases where no data are available. It is also likely that the model performs better in less complex terrain, given that the friction velocity is estimated correctly. More investigations that use data from such sites are needed.

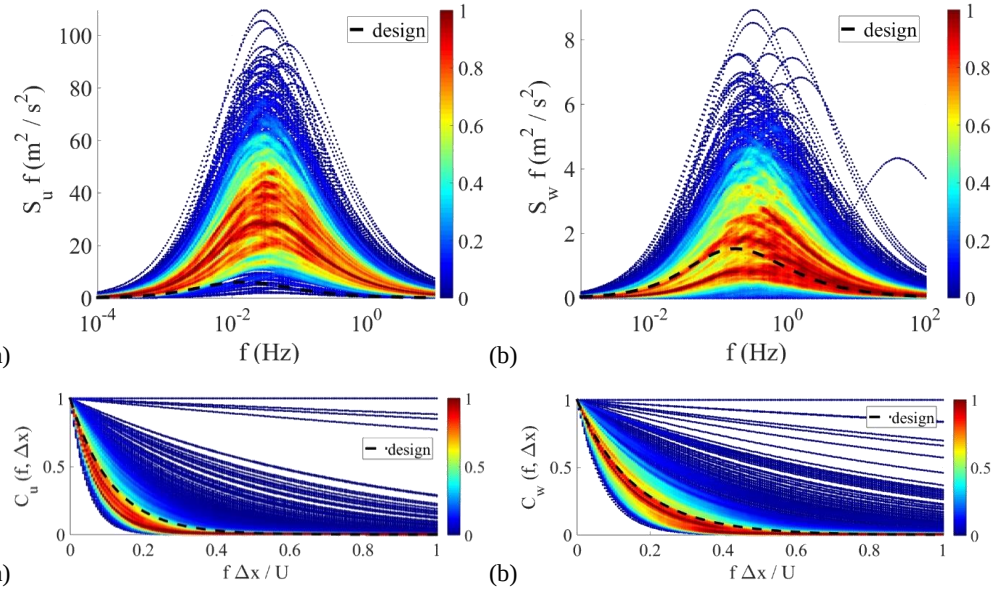


Fig. 36. Simulations of the autospectra and normalized co-spectra of the turbulence for the design wind speed using Solari and Piccardo's probabilistic model: the (a) autospectral density of the along-wind turbulence; (b)

autospectral density of the vertical turbulence; (c) normalized co-spectra of the along-wind turbulence and (d) normalized co-spectra of the vertical turbulence

## Concluding Remarks

The turbulence field along the single span of the Hardanger Bridge was modeled here in a probabilistic manner using the lognormal distribution coefficients and correlation coefficients of the turbulence parameters, which were obtained from an analysis of the long-term monitoring data. The following conclusions were reached for the specific case considered:

- For a 10-minute averaging interval, neglecting the cross-wind turbulence and cross-spectral density of the *u*-*w* turbulence, the wind field along the structure was defined by just six parameters, which were then treated as random variables.
- Conditional on the mean wind speed and direction, the turbulence parameters approximately followed a lognormal distribution.
- Detailed comparisons between the simulations of the turbulence parameters and the corresponding turbulence spectra with the measurement data provided confidence in the probabilistic model in representing the site-specific variability.
- As a next step, the performance of such a model in accurately propagating the uncertainty into the response prediction shall be assessed. As noted in the paper, the model is suitable for use in reliability-based or performance-based frameworks or long-term extreme response predictions.
- The probabilistic model here was derived for the specific site of the Hardanger Bridge and relies on a large amount of data, which may not always be available to design engineers. To develop a more general procedure, analyses of additional data from different sites are necessary.

## Acknowledgements

The research described in this paper was financially supported by the Norwegian Public Roads Administration as part of the Ferry-Free Coastal E39 project. The authors appreciate this support.

## References

Busch, N.E., Panofsky, H.A., 1968. Recent spectra of atmospheric turbulence. Q. J. R. Meteorol. Soc. 94, 132–148. doi:10.1002/qj.49709440003

Cheynet, E., 2016. Wind-induced vibrations of a suspension bridge. Univ. Stavanger.

Ciampoli, M., Petrini, F., Augusti, G., 2011. Performance-Based Wind Engineering: Towards a general procedure. Struct. Saf. 33, 367–378. doi:https://doi.org/10.1016/j.strusafe.2011.07.001

Davenport, A.G., 1983a. The relationship of reliability to wind loading. J. Wind Eng. Ind. Aerodyn. 13, 3–27. doi:https://doi.org/10.1016/0167-6105(83)90125-3

Davenport, A.G., 1983b. On the assessment of the reliability of wind loading on low buildings. J. Wind Eng. Ind. Aerodyn. 11, 21–37. doi:https://doi.org/10.1016/0167-6105(83)90088-0

Davenport, A.G., 1962. Buffeting of a suspension bridge by storm winds. J. Struct. Div. 88, 233–268. doi:10.4319/lo.2013.58.2.0489

Davenport, A.G., 1961. The spectrum of horizontal gustiness near the ground in high winds. Q. J. R. Meteorol. Soc. 87, 194–211. doi:10.1002/qj.49708737208

Dunham, K.K., 2016. Coastal Highway Route E39 - Extreme Crossings, in: Transportation Research Procedia. pp. 494–498. doi:10.1016/j.trpro.2016.05.102

Ellevset, O., Skorpa, L., 2011. A feasibility study – How to cross the wide and deep Sognefjord, summary.

Norwegian Public Roads Administration - Western Region Projects Division, Norway.

ESDU 086010, 2001. Characteristics of atmospheric turbulence near the ground Part 3: variations in space and time for strong winds (neutral atmosphere), 2008th ed. ESDU International plc, London.

ESDU 85020, 2001. Characteristics of atmospheric turbulence near groud Part 2: signle point data for strong winds (neutral atmosphere). ESDU International plc, London.

Fenerci, A., Øiseth, O., 2018. Strong wind characteristics and dynamic response of a long-span suspension bridge during a storm. J. Wind Eng. Ind. Aerodyn. 172, 116–138.

Fenerci, A., Øiseth, O., 2017. Measured Buffeting Response of a Long-Span Suspension Bridge Compared with Numerical Predictions Based on Design Wind Spectra. J. Struct. Eng. (United States) 143. doi:10.1061/(ASCE)ST.1943-541X.0001873

Fenerci, A., Øiseth, O., Rønnquist, A., 2017. Long-term monitoring of wind field characteristics and dynamic response of a long-span suspension bridge in complex terrain. Eng. Struct. 147, 269–284. doi:10.1016/j.engstruct.2017.05.070

Giske, F.-I.G., Leira, B.J., Øiseth, O., 2017. Full long-term extreme response analysis of marine structures using inverse FORM. Probabilistic Eng. Mech. 50, 1–8. doi:https://doi.org/10.1016/j.probengmech.2017.10.007

Hui, M.C.H., Larsen, A., Xiang, H.F., 2009a. Wind turbulence characteristics study at the Stonecutters Bridge site: Part I-Mean wind and turbulence intensities. J. Wind Eng. Ind. Aerodyn. 97, 22–36. doi:10.1016/j.jweia.2008.11.002

Hui, M.C.H., Larsen, A., Xiang, H.F., 2009b. Wind turbulence characteristics study at the Stonecutters Bridge site: Part II: Wind power spectra, integral length scales and coherences. J. Wind Eng. Ind. Aerodyn. 97, 48–59. doi:10.1016/j.jweia.2008.11.003

Jain, A., Jones, N.P., Scanlan, R.H., 1996. Coupled Flutter and Buffeting Analysis of Long-Span Bridges. J. Struct. Eng. 122, 716–725. doi:10.1061/(ASCE)0733-9445(1996)122:7(716)

Kaimal, J.C.J., Wyngaard, J.C.J., Izumi, Y., Coté, O.R., Cote, O.R., 1972. Spectral Characteristics of Surface-Layer Turbulence. Q. J. … 98, 563–589. doi:10.1002/qj.49709841707

Kareem, A., 1988. Aerodynamic response of structures with parametric uncertainties. Struct. Saf. 5, 205–225. doi:10.1016/0167-4730(88)90010-0

Kareem, A., 1987. Wind effects on structures: a probabilistic viewpoint. Probabilistic Eng. Mech. 2, 166–200. doi:10.1016/0266-8920(87)90009-9

Krenk, S., 1996. Wind Field Coherence And Dynamic Wind Forces, in: Naess, A., Krenk, S. (Eds.), IUTAM Symposium on Advances in Nonlinear Stochastic Mechanics: Proceedings of the IUTAM Symposium Held in Trondheim, Norway, 3--7 July 1995. Springer Netherlands, Dordrecht, pp. 269–278. doi:10.1007/978-94-009-0321-0_25

Kristensen, L., Jensen, N.O., 1979. Lateral coherence in isotropic turbulence and in the natural wind. Boundary-Layer Meteorol. 17, 353–373. doi:10.1007/BF00117924

Mann, J., 2006. The spatial structure of neutral atmospheric surface-layer turbulence. J. Fluid Mech. 273, 141. doi:10.1017/S0022112094001886

Mann, J., 2000. The spectral velocity tensor in moderately complex terrain. J. Wind Eng. Ind. Aerodyn. 88, 153–169. doi:https://doi.org/10.1016/S0167-6105(00)00046-5

Minciarelli, F., Gioffrè, M., Grigoriu, M., Simiu, E., 2001. Estimates of extreme wind effects and wind load factors: influence of knowledge uncertainties. Probabilistic Eng. Mech. 16, 331–340. doi:https://doi.org/10.1016/S0266-8920(01)00024-8

Naess, A., Moan, T., 2012. Stochastic Dynamics of Marine Structures. Cambridge University Press, Cambridge.

doi:DOI: 10.1017/CBO9781139021364

Nielsen, M., Larsen, G.C., Hansen, K.S., 2007. Simulation of inhomogeneous, non-stationary and non-Gaussian turbulent winds, in: Journal of Physics: Conference Series. doi:10.1088/1742-6596/75/1/012060

Øiseth, O., Rönnquist, A., Sigbjörnsson, R., 2013. Effects of co-spectral densities of atmospheric turbulence on the dynamic response of cable-supported bridges: A case study. J. Wind Eng. Ind. Aerodyn. 116, 83–93. doi:10.1016/j.jweia.2013.03.001

Pagnini, L., 2010. Reliability analysis of wind-excited structures. J. Wind Eng. Ind. Aerodyn. 98, 1–9. doi:https://doi.org/10.1016/j.jweia.2009.08.010

Panofsky, H.A., Larko, D., Lipschutz, R., Stone, G., Bradley, E.F., Bowen, A.J., H??jstrup, J., 1982. Spectra of velocity components over complex terrain. Q. J. R. Meteorol. Soc. 108, 215–230. doi:10.1002/qj.49710845513

Scanlan, R.H., 1978. The action of flexible bridges under wind, II: Buffeting theory. J. Sound Vib. 60, 187–199. doi:10.1016/S0022-460X(78)80029-7

Simiu, E., Scanlan, R.H., 1996. Winds Effects on Structures: Fundamentals and Applications to Design, 3rd ed. Wiley.

Solari, G., 1997. Wind-excited response of structures with uncertain parameters. Probabilistic Eng. Mech. 12, 75–87. doi:10.1016/S0266-8920(96)00027-6

Solari, G., 1987. Turbulence Modeling for Gust Loading. J. Struct. Eng. 113, 1550–1569. doi:10.1061/(ASCE)0733-9445(1987)113:7(1550)

Solari, G., Piccardo, G., 2001. Probabilistic 3-D turbulence modeling for gust buffeting of structures. Probabilistic Eng. Mech. 16, 73–86. doi:10.1016/S0266-8920(00)00010-2

Spence, S.M.J., Kareem, A., 2014. Performance-based design and optimization of uncertain wind-excited dynamic building systems. Eng. Struct. 78, 133–144. doi:https://doi.org/10.1016/j.engstruct.2014.07.026

Statens-Vegvesen, 2006. The Hardanger Bridge design basis - wind characteristics.

The Mathworks Inc., 2015. MATLAB (R2015a). MathWorks Inc. doi:10.1007/s10766-008-0082-5

Tieleman, H.W., 1995. Universality of velocity spectra. J. Wind Eng. Ind. Aerodyn. 56, 55–69. doi:10.1016/0167-6105(94)00011-2

Tieleman, H.W., 1992. Wind characteristics in the surface layer over heterogeneous terrain. J. Wind Eng. Ind. Aerodyn. 41, 329–340. doi:10.1016/0167-6105(92)90427-C

Toriumi, R., Katsuchi, H., Furuya, N., 2000. A study on spatial correlation of natural wind. J. Wind Eng. Ind. Aerodyn. 87, 203–216. doi:10.1016/S0167-6105(00)00037-4

von Karman, T., 1948. Progress in the statistical theory of turbulence. Proc. Natl. Acad. Sci. U. S. A. 34, 530–539. doi:10.1073/pnas.34.11.530

Welch, P.D., 1967. The Use of Fast Fourier Transform for the Estimation of Power Spectra: A Method Based on Time Averaging Over Short, Modified Periodograms. IEEE Trans. Audio Electroacoust. 15, 70–73. doi:10.1109/TAU.1967.1161901

Xu, Y.-L., 2013. Wind Effects on Cable-Supported Bridges. John Wiley & Sons.

Xu, Y., Øiseth, O., Naess, A., Moan, T., 2017. Prediction of long-term extreme load effects due to wind for cable-supported bridges using time-domain simulations. Eng. Struct. 148, 239–253. doi:10.1016/j.engstruct.2017.06.051

Zerovnik, G., Trkov, A., Kodeli, I.A., 2012. Correlated random sampling for multivariate normal and log-normal distributions. Nucl. Instruments Methods Phys. Res. Sect. A Accel. Spectrometers, Detect. Assoc. Equip.

690, 75–78. doi:10.1016/j.nima.2012.06.036

Zhang, L., Li, J., Peng, Y., 2008. Dynamic response and reliability analysis of tall buildings subject to wind loading. J. Wind Eng. Ind. Aerodyn. 96, 25–40. doi:https://doi.org/10.1016/j.jweia.2007.03.001

**DEPARTMENT OF STRUCTURAL ENGINEERING**
**NORWEGIAN UNIVERSITY OF SCIENCE AND TECHNOLOGY**

N–7491 TRONDHEIM, NORWAY
Telephone: +47 73 59 47 00 Telefax: +47 73 59 47 01

"Reliability Analysis of Structural Systems using Nonlinear Finite Element Methods",
C. A. Holm, 1990:23, ISBN 82-7119-178-0.

"Uniform Stratified Flow Interaction with a Submerged Horizontal Cylinder",
Ø. Arntsen, 1990:32, ISBN 82-7119-188-8.

"Large Displacement Analysis of Flexible and Rigid Systems Considering Displacement-Dependent Loads and Nonlinear Constraints",
K. M. Mathisen, 1990:33, ISBN 82-7119-189-6.

"Solid Mechanics and Material Models including Large Deformations",
E. Levold, 1990:56, ISBN 82-7119-214-0, ISSN 0802-3271.

"Inelastic Deformation Capacity of Flexurally-Loaded Aluminium Alloy Structures",
T. Welo, 1990:62, ISBN 82-7119-220-5, ISSN 0802-3271.

"Visualization of Results from Mechanical Engineering Analysis",
K. Aamnes, 1990:63, ISBN 82-7119-221-3, ISSN 0802-3271.

"Object-Oriented Product Modeling for Structural Design",
S. I. Dale, 1991:6, ISBN 82-7119-258-2, ISSN 0802-3271.

"Parallel Techniques for Solving Finite Element Problems on Transputer Networks",
T. H. Hansen, 1991:19, ISBN 82-7119-273-6, ISSN 0802-3271.

"Statistical Description and Estimation of Ocean Drift Ice Environments",
R. Korsnes, 1991:24, ISBN 82-7119-278-7, ISSN 0802-3271.

“Properties of concrete related to fatigue damage: with emphasis on high strength concrete”,
G. Petkovic, 1991:35, ISBN 82-7119-290-6, ISSN 0802-3271.

"Turbidity Current Modelling",
B. Brørs, 1991:38, ISBN 82-7119-293-0, ISSN 0802-3271.

"Zero-Slump Concrete: Rheology, Degree of Compaction and Strength. Effects of Fillers as Part Cement-Replacement",
C. Sørensen, 1992:8, ISBN 82-7119-357-0, ISSN 0802-3271.

"Nonlinear Analysis of Reinforced Concrete Structures Exposed to Transient Loading",
K. V. Høiseth, 1992:15, ISBN 82-7119-364-3, ISSN 0802-3271.

"Finite Element Formulations and Solution Algorithms for Buckling and Collapse Analysis of Thin Shells",
R. O. Bjærum, 1992:30, ISBN 82-7119-380-5, ISSN 0802-3271.

"Response Statistics of Nonlinear Dynamic Systems",
J. M. Johnsen, 1992:42, ISBN 82-7119-393-7, ISSN 0802-3271.

"Digital Models in Engineering. A Study on why and how engineers build and operate digital models for decisison support",
J. Høyte, 1992:75, ISBN 82-7119-429-1, ISSN 0802-3271.

"Sparse Solution of Finite Element Equations",
A. C. Damhaug, 1992:76, ISBN 82-7119-430-5, ISSN 0802-3271.

"Some Aspects of Floating Ice Related to Sea Surface Operations in the Barents Sea",
S. Løset, 1992:95, ISBN 82-7119-452-6, ISSN 0802-3271.

"Modelling of Cyclic Plasticity with Application to Steel and Aluminium Structures",
O. S. Hopperstad, 1993:7, ISBN 82-7119-461-5, ISSN 0802-3271.

"The Free Formulation: Linear Theory and Extensions with Applications to Tetrahedral Elements
with Rotational Freedoms",
G. Skeie, 1993:17, ISBN 82-7119-472-0, ISSN 0802-3271.

"Høyfast betongs motstand mot piggdekkslitasje. Analyse av resultater fra prøving i Veisliter'n",
T. Tveter, 1993:62, ISBN 82-7119-522-0, ISSN 0802-3271.

"A Nonlinear Finite Element Based on Free Formulation Theory for Analysis of Sandwich Structures",
O. Aamlid, 1993:72, ISBN 82-7119-534-4, ISSN 0802-3271.

"The Effect of Curing Temperature and Silica Fume on Chloride Migration and Pore Structure of High Strength Concrete",
C. J. Hauck, 1993:90, ISBN 82-7119-553-0, ISSN 0802-3271.

"Failure of Concrete under Compressive Strain Gradients",
G. Markeset, 1993:110, ISBN 82-7119-575-1, ISSN 0802-3271.

"An experimental study of internal tidal amphidromes in Vestfjorden",
J. H. Nilsen, 1994:39, ISBN 82-7119-640-5, ISSN 0802-3271.

"Structural analysis of oil wells with emphasis on conductor design",
H. Larsen, 1994:46, ISBN 82-7119-648-0, ISSN 0802-3271.

"Adaptive methods for non-linear finite element analysis of shell structures",
K. M. Okstad, 1994:66, ISBN 82-7119-670-7, ISSN 0802-3271.

"On constitutive modelling in nonlinear analysis of concrete structures",
O. Fyrileiv, 1994:115, ISBN 82-7119-725-8, ISSN 0802-3271.

"Fluctuating wind load and response of a line-like engineering structure with emphasis on motion-induced wind forces",
J. Bogunovic Jakobsen, 1995:62, ISBN 82-7119-809-2, ISSN 0802-3271.

"An experimental study of beam-columns subjected to combined torsion, bending and axial actions",
A. Aalberg, 1995:66, ISBN 82-7119-813-0, ISSN 0802-3271.

"Scaling and cracking in unsealed freeze/thaw testing of Portland cement and silica fume concretes",
S. Jacobsen, 1995:101, ISBN 82-7119-851-3, ISSN 0802-3271.

"Damping of water waves by submerged vegetation. A case study of laminaria hyperborea",
A. M. Dubi, 1995:108, ISBN 82-7119-859-9, ISSN 0802-3271.

"The dynamics of a slope current in the Barents Sea",
Sheng Li, 1995:109, ISBN 82-7119-860-2, ISSN 0802-3271.

"Modellering av delmaterialenes betydning for betongens konsistens",
Ernst Mørtsell, 1996:12, ISBN 82-7119-894-7, ISSN 0802-3271.

"Bending of thin-walled aluminium extrusions",
Birgit Søvik Opheim, 1996:60, ISBN 82-7119-947-1, ISSN 0802-3271.

"Material modelling of aluminium for crashworthiness analysis",
Torodd Berstad, 1996:89, ISBN 82-7119-980-3, ISSN 0802-3271.

"Estimation of structural parameters from response measurements on submerged floating tunnels",
Rolf Magne Larssen, 1996:119, ISBN 82-471-0014-2, ISSN 0802-3271.

“Numerical modelling of plain and reinforced concrete by damage mechanics”,
Mario A. Polanco-Loria, 1997:20, ISBN 82-471-0049-5, ISSN 0802-3271.

“Nonlinear random vibrations - numerical analysis by path integration methods”,
Vibeke Moe, 1997:26, ISBN 82-471-0056-8, ISSN 0802-3271.

"Numerical prediction of vortex-induced vibration by the finite element method",
Joar Martin Dalheim, 1997:63, ISBN 82-471-0096-7, ISSN 0802-3271.

"Time domain calculations of buffeting response for wind sensitive structures",
Ketil Aas-Jakobsen, 1997:148, ISBN 82-471-0189-0, ISSN 0802-3271.

"A numerical study of flow about fixed and flexibly mounted circular cylinders",
Trond Stokka Meling, 1998:48, ISBN 82-471-0244-7, ISSN 0802-3271.

"Estimation of chloride penetration into concrete bridges in coastal areas",
Per Egil Steen, 1998:89, ISBN 82-471-0290-0, ISSN 0802-3271.

"Stress-resultant material models for reinforced concrete plates and shells",
Jan Arve Øverli, 1998:95, ISBN 82-471-0297-8, ISSN 0802-3271.

"Chloride binding in concrete. Effect of surrounding environment and concrete composition",
Claus Kenneth Larsen, 1998:101, ISBN 82-471-0337-0, ISSN 0802-3271.

"Rotational capacity of aluminium alloy beams",
Lars A. Moen, 1999:1, ISBN 82-471-0365-6, ISSN 0802-3271.

"Stretch Bending of Aluminium Extrusions",
Arild H. Clausen, 1999:29, ISBN 82-471-0396-6, ISSN 0802-3271.

"Aluminium and Steel Beams under Concentrated Loading",
Tore Tryland, 1999:30, ISBN 82-471-0397-4, ISSN 0802-3271.

"Engineering Models of Elastoplasticity and Fracture for Aluminium Alloys",
Odd-Geir Lademo, 1999:39, ISBN 82-471-0406-7, ISSN 0802-3271.

"Kapasitet og duktilitet av dybelforbindelser i trekonstruksjoner",
Jan Siem, 1999:46, ISBN 82-471-0414-8, ISSN 0802-3271.

"Etablering av distribuert ingeniørarbeid; Teknologiske og organisatoriske erfaringer fra en norsk ingeniørbedrift",
Lars Line, 1999:52, ISBN 82-471-0420-2, ISSN 0802-3271.

"Estimation of Earthquake-Induced Response",
Símon Ólafsson, 1999:73, ISBN 82-471-0443-1, ISSN 0802-3271.

"Coastal Concrete Bridges: Moisture State, Chloride Permeability and Aging Effects"
Ragnhild Holen Relling, 1999:74, ISBN 82-471-0445-8, ISSN 0802-3271.

"Capacity Assessment of Titanium Pipes Subjected to Bending and External Pressure",
Arve Bjørset, 1999:100, ISBN 82-471-0473-3, ISSN 0802-3271.

“Validation of Numerical Collapse Behaviour of Thin-Walled Corrugated Panels”,
Håvar Ilstad, 1999:101, ISBN 82-471-0474-1, ISSN 0802-3271.

“Strength and Ductility of Welded Structures in Aluminium Alloys”,
Miroslaw Matusiak, 1999:113, ISBN 82-471-0487-3, ISSN 0802-3271.

“Thermal Dilation and Autogenous Deformation as Driving Forces to Self-Induced Stresses in High Performance Concrete”,
Øyvind Bjøntegaard, 1999:121, ISBN 82-7984-002-8, ISSN 0802-3271.

“Some Aspects of Ski Base Sliding Friction and Ski Base Structure”,
Dag Anders Moldestad, 1999:137, ISBN 82-7984-019-2, ISSN 0802-3271.

"Electrode reactions and corrosion resistance for steel in mortar and concrete",
Roy Antonsen, 2000:10, ISBN 82-7984-030-3, ISSN 0802-3271.

"Hydro-Physical Conditions in Kelp Forests and the Effect on Wave Damping and Dune Erosion. A case study on Laminaria Hyperborea",
Stig Magnar Løvås, 2000:28, ISBN 82-7984-050-8, ISSN 0802-3271.

"Random Vibration and the Path Integral Method",
Christian Skaug, 2000:39, ISBN 82-7984-061-3, ISSN 0802-3271.

"Buckling and geometrical nonlinear beam-type analyses of timber structures",
Trond Even Eggen, 2000:56, ISBN 82-7984-081-8, ISSN 0802-3271.

”Structural Crashworthiness of Aluminium Foam-Based Components”,
Arve Grønsund Hanssen, 2000:76, ISBN 82-7984-102-4, ISSN 0809-103X.

“Measurements and simulations of the consolidation in first-year sea ice ridges, and some aspects of mechanical behaviour”,
Knut V. Høyland, 2000:94, ISBN 82-7984-121-0, ISSN 0809-103X.

”Kinematics in Regular and Irregular Waves based on a Lagrangian Formulation”,
Svein Helge Gjøsund, 2000-86, ISBN 82-7984-112-1, ISSN 0809-103X.

”Self-Induced Cracking Problems in Hardening Concrete Structures”,
Daniela Bosnjak, 2000-121, ISBN 82-7984-151-2, ISSN 0809-103X.

"Ballistic Penetration and Perforation of Steel Plates",
Tore Børvik, 2000:124, ISBN 82-7984-154-7, ISSN 0809-103X.

"Freeze-Thaw resistance of Concrete. Effect of: Curing Conditions, Moisture Exchange and Materials",
Terje Finnerup Rønning, 2001:14, ISBN 82-7984-165-2, ISSN 0809-103X

"Structural behaviour of post tensioned concrete structures. Flat slab. Slabs on ground",
Steinar Trygstad, 2001:52, ISBN 82-471-5314-9, ISSN 0809-103X.

"Slipforming of Vertical Concrete Structures. Friction between concrete and slipform panel",
Kjell Tore Fosså, 2001:61, ISBN 82-471-5325-4, ISSN 0809-103X.

"Some numerical methods for the simulation of laminar and turbulent incompressible flows",
Jens Holmen, 2002:6, ISBN 82-471-5396-3, ISSN 0809-103X.

“Improved Fatigue Performance of Threaded Drillstring Connections by Cold Rolling”,
Steinar Kristoffersen, 2002:11, ISBN: 82-421-5402-1, ISSN 0809-103X.

"Deformations in Concrete Cantilever Bridges: Observations and Theoretical Modelling",
Peter F. Takâcs, 2002:23, ISBN 82-471-5415-3, ISSN 0809-103X.

"Stiffened aluminium plates subjected to impact loading",
Hilde Giæver Hildrum, 2002:69, ISBN 82-471-5467-6, ISSN 0809-103X.

"Full- and model scale study of wind effects on a medium-rise building in a built up area",
Jónas Thór Snæbjørnsson, 2002:95, ISBN82-471-5495-1, ISSN 0809-103X.

“Evaluation of Concepts for Loading of Hydrocarbons in Ice-infested water”,
Arnor Jensen, 2002:114, ISBN 82-417-5506-0, ISSN 0809-103X.

”Numerical and Physical Modelling of Oil Spreading in Broken Ice”,
Janne K. Økland Gjøsteen, 2002:130, ISBN 82-471-5523-0, ISSN 0809-103X.

”Diagnosis and protection of corroding steel in concrete”,
Franz Pruckner, 20002:140, ISBN 82-471-5555-4, ISSN 0809-103X.

“Tensile and Compressive Creep of Young Concrete: Testing and Modelling”,
Dawood Atrushi, 2003:17, ISBN 82-471-5565-6, ISSN 0809-103X.

“Rheology of Particle Suspensions. Fresh Concrete, Mortar and Cement Paste with Various Types of Lignosulfonates”,
Jon Elvar Wallevik, 2003:18, ISBN 82-471-5566-4, ISSN 0809-103X.

“Oblique Loading of Aluminium Crash Components”,
Aase Reyes, 2003:15, ISBN 82-471-5562-1, ISSN 0809-103X.

“Utilization of Ethiopian Natural Pozzolans”,
Surafel Ketema Desta, 2003:26, ISSN 82-471-5574-5, ISSN:0809-103X.

“Behaviour and strength prediction of reinforced concrete structures with discontinuity regions”, Helge Brå, 2004:11, ISBN 82-471-6222-9, ISSN 1503-8181.

“High-strength steel plates subjected to projectile impact. An experimental and numerical study”, Sumita Dey, 2004:38, ISBN 82-471-6282-2 (printed version), ISBN 82-471-6281-4 (electronic version), ISSN 1503-8181.

“Alkali-reactive and inert fillers in concrete. Rheology of fresh mixtures and expansive reactions.”
Bård M. Pedersen, 2004:92, ISBN 82-471-6401-9 (printed version), ISBN 82-471-6400-0 (electronic version), ISSN 1503-8181.

“On the Shear Capacity of Steel Girders with Large Web Openings”.
Nils Christian Hagen, 2005:9 ISBN 82-471-6878-2 (printed version), ISBN 82-471-6877-4 (electronic version), ISSN 1503-8181.

”Behaviour of aluminium extrusions subjected to axial loading”.
Østen Jensen, 2005:7, ISBN 82-471-6873-1 (printed version), ISBN 82-471-6872-3 (electronic version), ISSN 1503-8181.

”Thermal Aspects of corrosion of Steel in Concrete”.
Jan-Magnus Østvik, 2005:5, ISBN 82-471-6869-3 (printed version), ISBN 82-471-6868 (electronic version), ISSN 1503-8181.

”Mechanical and adaptive behaviour of bone in relation to hip replacement.” A study of bone remodelling and bone grafting.
Sébastien Muller, 2005:34, ISBN 82-471-6933-9 (printed version), ISBN 82-471-6932-0 (electronic version), ISSN 1503-8181.

“Analysis of geometrical nonlinearities with applications to timber structures”.
Lars Wollebæk, 2005:74, ISBN 82-471-7050-5 (printed version), ISBN 82-471-7019-1 (electronic version), ISSN 1503-8181.

“Pedestrian induced lateral vibrations of slender footbridges”,
Anders Rönnquist, 2005:102, ISBN 82-471-7082-5 (printed version), ISBN 82-471-7081-7 (electronic version), ISSN 1503-8181.

“Initial Strength Development of Fly Ash and Limestone Blended Cements at Various Temperatures Predicted by Ultrasonic Pulse Velocity”,
Tom Ivar Fredvik, 2005:112, ISBN 82-471-7105-8 (printed version), ISBN 82-471-7103-1 (electronic version), ISSN 1503-8181.

“Behaviour and modelling of thin-walled cast components”,
Cato Dørum, 2005:128, ISBN 82-471-7140-6 (printed version), ISBN 82-471-7139-2 (electronic version), ISSN 1503-8181.

“Behaviour and modelling of selfpiercing riveted connections”,
Raffaele Porcaro, 2005:165, ISBN 82-471-7219-4 (printed version), ISBN 82-471-7218-6 (electronic version), ISSN 1503-8181.

”Behaviour and Modelling og Aluminium Plates subjected to Compressive Load”,
Lars Rønning, 2005:154, ISBN 82-471-7169-1 (printed version), ISBN 82-471-7195-3 (electronic version), ISSN 1503-8181.

”Bumper beam-longitudinal system subjected to offset impact loading”,
Satyanarayana Kokkula, 2005:193, ISBN 82-471-7280-1 (printed version), ISBN 82-471-7279-8 (electronic version), ISSN 1503-8181.

“Control of Chloride Penetration into Concrete Structures at Early Age”,
Guofei Liu, 2006:46, ISBN 82-471-7838-9 (printed version), ISBN 82-471-7837-0 (electronic version), ISSN 1503-8181.

“Modelling of Welded Thin-Walled Aluminium Structures”,
Ting Wang, 2006:78, ISBN 82-471-7907-5 (printed version), ISBN 82-471-7906-7 (electronic version), ISSN 1503-8181.

”Time-variant reliability of dynamic systems by importance sampling and probabilistic analysis of ice loads”,
Anna Ivanova Olsen, 2006:139, ISBN 82-471-8041-3 (printed version), ISBN 82-471-8040-5 (electronic version), ISSN 1503-8181.

“Fatigue life prediction of an aluminium alloy automotive component using finite element analysis of surface topography”.
Sigmund Kyrre Ås, 2006:25, ISBN 82-471-7791-9 (printed version), ISBN 82-471-7791-9 (electronic version), ISSN 1503-8181.

”Constitutive models of elastoplasticity and fracture for aluminium alloys under strain path change”,
Dasharatha Achani, 2006:76, ISBN 82-471-7903-2 (printed version), ISBN 82-471-7902-4 (electronic version), ISSN 1503-8181.

“Simulations of 2D dynamic brittle fracture by the Element-free Galerkin method and linear fracture mechanics”,
Tommy Karlsson, 2006:125, ISBN 82-471-8011-1 (printed version), ISBN 82-471-8010-3 (electronic version), ISSN 1503-8181.

“Penetration and Perforation of Granite Targets by Hard Projectiles”,
Chong Chiang Seah, 2006:188, ISBN 82-471-8150-9 (printed version), ISBN 82-471-8149-5 (electronic version), ISSN 1503-8181.

"Deformations, strain capacity and cracking of concrete in plastic and early hardening phases",
Tor Arne Hammer, 2007:234, ISBN 978-82-471-5191-4 (printed version), ISBN 978-82-471-5207-2 (electronic version), ISSN 1503-8181.

"Crashworthiness of dual-phase high-strength steel: Material and Component behaviour", Venkatapathi Tarigopula, 2007:230, ISBN 82-471-5076-4 (printed version), ISBN 82-471-5093-1 (electronic version), ISSN 1503-8181.

"Fibre reinforcement in load carrying concrete structures",
Åse Lyslo Døssland, 2008:50, ISBN 978-82-471-6910-0 (printed version), ISBN 978-82-471-6924-7 (electronic version), ISSN 1503-8181.

"Low-velocity penetration of aluminium plates",
Frode Grytten, 2008:46, ISBN 978-82-471-6826-4 (printed version), ISBN 978-82-471-6843-1 (electronic version), ISSN 1503-8181.

"Robustness studies of structures subjected to large deformations",
Ørjan Fyllingen, 2008:24, ISBN 978-82-471-6339-9 (printed version), ISBN 978-82-471-6342-9 (electronic version), ISSN 1503-8181.

"Constitutive modelling of morsellised bone",
Knut Birger Lunde, 2008:92, ISBN 978-82-471-7829-4 (printed version), ISBN 978-82-471-7832-4 (electronic version), ISSN 1503-8181.

"Experimental Investigations of Wind Loading on a Suspension Bridge Girder",
Bjørn Isaksen, 2008:131, ISBN 978-82-471-8656-5 (printed version), ISBN 978-82-471-8673-2 (electronic version), ISSN 1503-8181.

"Cracking Risk of Concrete Structures in The Hardening Phase",
Guomin Ji, 2008:198, ISBN 978-82-471-1079-9 (printed version), ISBN 978-82-471-1080-5 (electronic version), ISSN 1503-8181.

"Modelling and numerical analysis of the porcine and human mitral apparatus",
Victorien Emile Prot, 2008:249, ISBN 978-82-471-1192-5 (printed version), ISBN 978-82-471-1193-2 (electronic version), ISSN 1503-8181.

"Strength analysis of net structures",
Heidi Moe, 2009:48, ISBN 978-82-471-1468-1 (printed version), ISBN 978-82-471-1469-8 (electronic version), ISSN1503-8181.

"Numerical analysis of ductile fracture in surface cracked shells",
Espen Berg, 2009:80, ISBN 978-82-471-1537-4 (printed version), ISBN 978-82-471-1538-1 (electronic version), ISSN 1503-8181.

"Subject specific finite element analysis of bone – for evaluation of the healing of a leg lengthening and evaluation of femoral stem design",
Sune Hansborg Pettersen, 2009:99, ISBN 978-82-471-1579-4 (printed version), ISBN 978-82-471-1580-0 (electronic version), ISSN 1503-8181.

"Evaluation of fracture parameters for notched multi-layered structures",
Lingyun Shang, 2009:137, ISBN 978-82-471-1662-3 (printed version), ISBN 978-82-471-1663-0 (electronic version), ISSN 1503-8181.

"Modelling of Dynamic Material Behaviour and Fracture of Aluminium Alloys for Structural Applications"
Yan Chen, 2009:69, ISBN 978-82-471-1515-2 (printed version), ISBN 978-82 471-1516-9 (electronic version), ISSN 1503-8181.

"Nanomechanics of polymer and composite particles"
Jianying He 2009:213, ISBN 978-82-471-1828-3 (printed version), ISBN 978-82-471-1829-0 (electronic version), ISSN 1503-8181.

"Mechanical properties of clear wood from Norway spruce"
Kristian Berbom Dahl 2009:250, ISBN 978-82-471-1911-2 (printed version) ISBN 978-82-471-1912-9 (electronic version), ISSN 1503-8181.

"Modeling of the degradation of $TiB_2$ mechanical properties by residual stresses and liquid Al penetration along grain boundaries"
Micol Pezzotta 2009:254, ISBN 978-82-471-1923-5 (printed version) ISBN 978-82-471-1924-2 (electronic version) ISSN 1503-8181.

"Effect of welding residual stress on fracture"
Xiabo Ren 2010:77, ISBN 978-82-471-2115-3 (printed version) ISBN 978-82-471-2116-0 (electronic version), ISSN 1503-8181.

"Pan-based carbon fiber as anode material in cathodic protection system for concrete structures"
Mahdi Chini 2010:122, ISBN 978-82-471-2210-5 (printed version) ISBN 978-82-471-2213-6 (electronic version), ISSN 1503-8181.

"Structural Behaviour of deteriorated and retrofitted concrete structures"
Irina Vasililjeva Sæther 2010:171, ISBN 978-82-471-2315-7 (printed version) ISBN 978-82-471-2316-4 (electronic version) ISSN 1503-8181.

"Prediction of local snow loads on roofs"
Vivian Meløysund 2010:247, ISBN 978-82-471-2490-1 (printed version) ISBN 978-82-471-2491-8 (electronic version) ISSN 1503-8181.

"Behaviour and modelling of polymers for crash applications"
Virgile Delhaye 2010:251, ISBN 978-82-471-2501-4 (printed version) ISBN 978-82-471-2502-1 (electronic version) ISSN 1503-8181.

"Blended cement with reducted $CO_2$ emission – Utilizing the Fly Ash-Limestone Synergy",
Klaartje De Weerdt 2011:32, ISBN 978-82-471-2584-7 (printed version) ISBN 978-82-471-2584-4 (electronic version) ISSN 1503-8181.

"Chloride induced reinforcement corrosion in concrete" Concept of critical chloride content – methods and mechanisms.
Ueli Angst 2011:113, ISBN 978-82-471-2769-9 (printed version) ISBN 978-82-471-2763-6 (electronic version) ISSN 1503-8181.

"A thermo-electric-Mechanical study of the carbon anode and contact interface for Energy savings in the production of aluminium".
Dag Herman Andersen 2011:157, ISBN 978-82-471-2859-6 (printed version) ISBN 978-82-471-2860-2 (electronic version) ISSN 1503-8181.

"Structural Capacity of Anchorage Ties in Masonry Veneer Walls Subjected to Earthquake". The implications of Eurocode 8 and Eurocode 6 on a typical Norwegain veneer wall.
Ahmed Mohamed Yousry Hamed 2011:181, ISBN 978-82-471-2911-1 (printed version) ISBN 978-82-471-2912-8 (electronic ver.) ISSN 1503-8181.

"Work-hardening behaviour in age-hardenable Al-Zn-Mg(-Cu) alloys".
Ida Westermann , 2011:247, ISBN 978-82-471-3056-8 (printed ver.) ISBN 978-82-471-3057-5 (electronic ver.) ISSN 1503-8181.

"Behaviour and modelling of selfpiercing riveted connections using aluminium rivets".
Nguyen-Hieu Hoang, 2011:266, ISBN 978-82-471-3097-1 (printed ver.) ISBN 978-82-471-3099-5 (electronic ver.) ISSN 1503-8181.

"Fibre reinforced concrete".
Sindre Sandbakk, 2011:297, ISBN 978-82-471-3167-1 (printed ver.) ISBN 978-82-471-3168-8 (electronic ver) ISSN 1503:8181.

"Dynamic behaviour of cablesupported bridges subjected to strong natural wind".
Ole Andre Øiseth, 2011:315, ISBN 978-82-471-3209-8 (printed ver.) ISBN 978-82-471-3210-4 (electronic ver.) ISSN 1503-8181.

"Constitutive modeling of solargrade silicon materials"
Julien Cochard, 2011:307, ISBN 978-82-471-3189-3 (printed ver). ISBN 978-82-471-3190-9 (electronic ver.) ISSN 1503-8181.

"Constitutive behavior and fracture of shape memory alloys"
Jim Stian Olsen, 2012:57, ISBN 978-82-471-3382-8 (printed ver.) ISBN 978-82-471-3383-5 (electronic ver.) ISSN 1503-8181.

“Field measurements in mechanical testing using close-range photogrammetry and digital image analysis”
Egil Fagerholt, 2012:95, ISBN 978-82-471-3466-5 (printed ver.) ISBN 978-82-471-3467-2 (electronic ver.) ISSN 1503-8181.

“Towards a better under standing of the ultimate behaviour of lightweight aggregate concrete in compression and bending”,
Håvard Nedrelid, 2012:123, ISBN 978-82-471-3527-3 (printed ver.) ISBN 978-82-471-3528-0 (electronic ver.) ISSN 1503-8181.

“Numerical simulations of blood flow in the left side of the heart”
Sigrid Kaarstad Dahl, 2012:135, ISBN 978-82-471-3553-2 (printed ver.) ISBN 978-82-471-3555-6 (electronic ver.) ISSN 1503-8181.

“Moisture induced stresses in glulam”
Vanessa Angst-Nicollier, 2012:139, ISBN 978-82-471-3562-4 (printed ver.) ISBN 978-82-471-3563-1 (electronic ver.) ISSN 1503-8181.

“Biomechanical aspects of distraction osteogensis”
Valentina La Russa, 2012:250, ISBN 978-82-471-3807-6 (printed ver.) ISBN 978-82-471-3808-3 (electronic ver.) ISSN 1503-8181.

“Ductile fracture in dual-phase steel. Theoretical, experimental and numerical study”
Gaute Gruben, 2012:257, ISBN 978-82-471-3822-9 (printed ver.) ISBN 978-82-471-3823-6 (electronic ver.) ISSN 1503-8181.

“Damping in Timber Structures”
Nathalie Labonnote, 2012:263, ISBN 978-82-471-3836-6 (printed ver.) ISBN 978-82-471-3837-3 (electronic ver.) ISSN 1503-8181.

“Biomechanical modeling of fetal veins: The umbilical vein and ductus venosus bifurcation”
Paul Roger Leinan, 2012:299, ISBN 978-82-471-3915-8 (printed ver.) ISBN 978-82-471-3916-5 (electronic ver.) ISSN 1503-8181.

“Large-Deformation behaviour of thermoplastics at various stress states”
Anne Serine Ognedal, 2012:298, ISBN 978-82-471-3913-4 (printed ver.) ISBN 978-82-471-3914-1 (electronic ver.) ISSN 1503-8181.

“Hardening accelerator for fly ash blended cement”
Kien Dinh Hoang, 2012:366, ISBN 978-82-471-4063-5 (printed ver.) ISBN 978-82-471-4064-2 (electronic ver.) ISSN 1503-8181.

“From molecular structure to mechanical properties”
Jianyang Wu, 2013:186, ISBN 978-82-471-4485-5 (printed ver.) ISBN 978-82-471-4486-2 (electronic ver.) ISSN 1503-8181.

“Experimental and numerical study of hybrid concrete structures”
Linn Grepstad Nes, 2013:259, ISBN 978-82-471-4644-6 (printed ver.) ISBN 978-82-471-4645-3 (electronic ver.) ISSN 1503-8181.

“Mechanics of ultra-thin multi crystalline silicon wafers”
Saber Saffar, 2013:199, ISBN 978-82-471-4511-1 (printed ver.) ISBN 978-82-471-4513-5 (electronic ver). ISSN 1503-8181.

“Through process modelling of welded aluminium structures”
Anizahyati Alisibramulisi, 2013:325, ISBN 978-82-471-4788-7 (printed ver.) ISBN 978-82-471-4789-4 (electronic ver.) ISSN 1503-8181.

“Combined blast and fragment loading on steel plates”
Knut Gaarder Rakvåg, 2013:361, ISBN978-82-471-4872-3 (printed ver.) ISBN 978-82-4873-0 (electronic ver.). ISSN 1503-8181.

“Characterization and modelling of the anisotropic behaviour of high-strength aluminium alloy”
Marion Fourmeau, 2014:37, ISBN 978-82-326-0008-3 (printed ver.) ISBN 978-82-326-0009-0 (electronic ver.) ISSN 1503-8181.

“Behaviour of threated steel fasteners at elevated deformation rates”
Henning Fransplass, 2014:65, ISBN 978-82-326-0054-0 (printed ver.) ISBN 978-82-326-0055-7 (electronic ver.) ISSN 1503-8181.

“Sedimentation and Bleeding”
Ya Peng, 2014:89, ISBN 978-82-326-0102-8 (printed ver.) ISBN 978-82-326-0103-5 (electric ver.) ISSN 1503-8181.

“Impact against X65 offshore pipelines”
Martin Kristoffersen, 2014:362, ISBN 978-82-326-0636-8 (printed ver.) ISBN 978-82-326-0637-5 (electronic ver.) ISSN 1503-8181.

“Formability of aluminium alloy subjected to prestrain by rolling”
Dmitry Vysochinskiy, 2014:363,, ISBN 978-82-326-0638-2 (printed ver.) ISBN 978-82-326-0639-9 (electronic ver.) ISSN 1503-8181.

“Experimental and numerical study of Yielding, Work-Hardening and anisotropy in textured AA6xxx alloys using crystal plasticity models”
Mikhail Khadyko, 2015:28, ISBN 978-82-326-0724-2 (printed ver.) ISBN 978-82-326-0725-9 (electronic ver.) ISSN 1503-8181.

“Behaviour and Modelling of AA6xxx Aluminium Alloys Under a Wide Range of Temperatures and Strain Rates”
Vincent Vilamosa, 2015:63, ISBN 978-82-326-0786-0 (printed ver.) ISBN 978-82-326-0787-7 (electronic ver.) ISSN 1503-8181.

“A Probabilistic Approach in Failure Modelling of Aluminium High Pressure Die-Castings”
Octavian Knoll, 2015:137, ISBN 978-82-326-0930-7 (printed ver.) ISBN 978-82-326-0931-4 (electronic ver.) ISSN 1503-8181.

“Ice Abrasion on Marine Concrete Structures”
Egil Møen, 2015:189, ISBN 978-82-326-1034-1 (printed ver.) ISBN 978-82-326-1035-8 (electronic ver.) ISSN 1503-8181.

“Fibre Orientation in Steel-Fibre-Reinforced Concrete”
Giedrius Zirgulis, 2015:229, ISBN 978-82-326-1114-0 (printed ver.) ISBN 978-82-326-1115-7 (electronic ver.) ISSN 1503-8181.

“Effect of spatial variation and possible interference of localised corrosion on the residual capacity of a reinforced concrete beam”
Mohammad Mahdi Kioumarsi, 2015:282, ISBN 978-82-326-1220-8 (printed ver.) ISBN 978-82-1221-5 (electronic ver.) ISSN 1503-8181.

“The role of concrete resistivity in chloride-induced macro-cell corrosion”
Karla Horbostel, 2015:324, ISBN 978-82-326-1304-5 (printed ver.) ISBN 978-82-326-1305-2 (electonic ver.) ISSN 1503-8181.

“Flowable fibre-reinforced concrete for structural applications”
Elena Vidal Sarmiento, 2015-335, ISBN 978-82-326-1324-3 (printed ver.) ISBN 978-82-326-1325-0 (electronic ver.) ISSN 1503-8181.

“Development of chushed sand for concrete production with microproportioning”
Rolands Cepuritis, 2016:19, ISBN 978-82-326-1382-3 (printed ver.) ISBN 978-82-326-1383-0 (electronic ver.) ISSN 1503-8181.

“Withdrawal properties of threaded rods embedded in glued-laminated timer elements”
Haris Stamatopoulos, 2016:48, ISBN 978-82-326-1436-3 (printed ver.) ISBN 978-82-326-1437-0 (electronic ver.) ISSN 1503-8181.

“An Experimental and numerical study of thermoplastics at large deformation”
Marius Andersen, 2016:191, ISBN 978-82-326-1720-3 (printed ver.) ISBN 978-82-326-1721-0 (electronic ver.) ISSN 1503-8181.

“Modeling and Simulation of Ballistic Impact”
Jens Kristian Holmen, 2016:240, ISBN 978-82-326-1818-7 (printed ver). ISBN 978-82-326-1819-4 (electronic ver.) ISSN 1503-8181.

“Early age crack assessment of concrete structures”
Anja B. Estensen Klausen, 2016:256, ISBN 978-82-326-1850-7 (printed ver). ISBN 978-82-326-1851-4 (electronic ver.) ISSN 1503-8181.

“Uncertainty quantification and sensitivity analysis for cardiovascular models”
Vinzenz Gregor Eck, 2016:234, ISBN 978-82-326-1806-4 (printed ver.) ISBN 978-82-326-1807-1 (electronic ver.) ISSN 1503-8181.

“Dynamic behaviour of existing and new railway catenary systems under Norwegain conditions”
Petter Røe Nåvik, 2016:298, ISBN 978-82-326-1935-1 (printed ver.) ISBN 978-82-326-1934-4 (electronic ver.) ISSN 1503-8181.

“Mechanical behaviour of particle-filled elastomers at various temperatures”
Arne Ilseng, 2016-295, ISBN978-82-326-1928-3 (printed ver.) ISBN 978-82-326-1929-0 (electronic ver.) ISSN 1503-8181.

“Nanotechnology for Anti-Icing Application”
Zhiwei He, 2016:348, ISBN 978-82-326-2038-8 (printed ver.) ISBN 978-82-326-2019-5 (electronic ver.) ISSN 1503-8181.

“Conduction Mechanisms in Conductive Adhesives with Metal-Coated Polyer Spheres”
Sigurd Rolland Pettersen, 2016:349, ISBN 978-326-2040-1 (printed ver,) ISBN 978-82-326-2041-8 (electronic ver.) ISSN 1503-8181.

“The interaction between calcium lignosulfonate and cement”
Alessia Colombo, 2017:20, ISBN 978-82-326-2122-4 (printed ver.) ISBN 978-82-326-2123-1 (electronic ver.) ISSN 1503-8181.

“Behaviour and Modelling of Flexible Structures Subjected to Blast Loading”
Vegard Aune, 2017:101, ISBN 978-82-326-2274-0 (printed ver.) ISBN 978-82-326-2275-7 (electronic ver.) ISSN 1503-8181.

“Behaviour of steel connections under quasi-static and impact loading”
Erik Løhre Grimsmo, 2017:159, ISBN 978-82-326-2390-7 (printed ver.) ISBN 978-82-326-2391-4 (electronic ver.) ISSN 1503-8181.

“An experimental and numerical study of cortical bone at he macro and Nano-scale”
Masoud Ramenzanzadehkoldeh,, 2017:208, ISBN 978-82-326-2488-1 (printed ver.) ISBN 978-82-326-2489-8 (electronic ver.) ISSN 1503-8181.

“Optoelectrical Properties of a Novel Organic Semiconductor: 6,13-Dichloropentacene”
Mao Wang, 2017:130, ISBN 978-82-326-2332-7 (printed ver.) ISBN 978-82-326-2333-4) (electronic ver.) ISSN 1503-8181.

“Core-shell structured microgels and their behavior at oil and water interface”
Yi Gong, 2017:182, ISBN 978-82-326-2436-2 (printed. ver.) ISBN 978-82-326-2437-9 (electronic ver.) ISSN 1503-8181.

“Aspects of design of reinforced concrete structures using nonliear finite element analyses”
Morten Engen, 2017:149, ISBN 978-82-326-2370-9 (printed ver.) ISBN 978-82-326-2371-6 (electronic ver.) ISSN 1503-8181.

“Numerical studies on ductile failure of aluminium alloys”
Lars Edvard Dæhli, 2017:284, ISBN 978-82-326-2636-6 (printed ver.) ISBN 978-82-326-2637-3 (electronic ver.) ISSN 1503-8181.

“Modelling and Assessment of Hydrogen Embrittlement in Steels and Nickel Alloys”
Haiyang Yu, 2017:278, ISBN 978-82-326-2624-3 (printed. ver.) ISBN 978-82-326-2625-0 (electronic ver.) ISSN 1503-8181.

“Network arch timber bridges with light timber deck on transverse crossbeams”
Anna Weronika Ostrycharczyk, 2017:318, ISBN 978-82-326-2704-2 (printed ver.) ISBN 978-82-326-2705-9 (electronic ver.) ISSN 1503-8181.

“Splicing of Large Glued Laminated Timber Elements by Use of Long Threated Rods”
Martin Cepelka, 2017:320, ISBN 978-82-326-2708-0 (printed ver.) ISBN 978-82-326-2709-7 (electronic ver.) ISSN 1503-8181.

“Thermomechanical behaviour of semi-crystalline polymers: experiments, modelling and simulation”
Joakim Johnsen, 2017-317, ISBN 978-82-326-2702-8 (printed ver.) ISBN 978-82-326-2703-5 (electronic ver.) ISSN 1503-8181.

“Small-Scale Plasiticity under Hydrogen Environment”
Kai Zhao, 2017:356, ISBN 978-82-326-2782-0 (printed ver.) ISBN 978-82-326-2783-7 (electronic er.) ISSN 1503-8181.

“Risk and Reliability Based Calibration of Structural Design Codes”
Michele Baravalle, 2017:342, ISBN 978-82-326-2752-3 (printed ver,) ISBN 978-82-326-2753-0 (electronic ver.) ISSN 1503-8181.

“Dynamic behaviour of floating bridges exposed to wave excitation”
Knut Andreas Kvåle, 2017:365, ISBN 978-82-326-2800-1 (printed ver.) ISBN 978-82-326-2801-8 (electronic ver.) ISSN 1503-8181.

“Dolomite calcined clay composite cement – hydration and durability”
Alisa Lydia Machner, 2018:39, ISBN 978-82-326-2872-8 (printed ver.). ISBN 978-82-326-2873-5 (electronic ver.) ISSN 1503-8181.

“Modelling of the self-excited forces for bridge decks subjected to random motions: an experimental study”
Bartosz Siedziako, 2018:52, ISBN 978-82-326-2896-4 (printed ver.). ISBN 978-82-326-2897-1 (electronic ver.) ISSN 1503-8181.

“A probabilistic-based methodology for evaluation of timber facade constructions”
Klodian Gradeci, 2018:69, ISBN 978-82-326-2928-2 (printed ver.) ISBN 978-82-326-2929-9 (electronic ver.) ISSN 1503-8181.

“Behaviour and modelling of flow-drill screw connections”
Johan Kolstø Sønstabø, 2018:73, ISBN 978-82-326-2936-7 (printed ver.) ISBN 978-82-326-2937-4 (electronic ver.) ISSN 1503-8181.